

Università degli Studi di Cagliari

Università degli Studi di Sassari

DOTTORATO DI RICERCA

In Scienze e Tecnologie Chimiche

Ciclo XXXV

UniCa-UniSS

Growth, characterization and functional properties of thin films on metal and ceramic substrates

CHIM/01 Chimica Analitica

Presentata da: Deborah Biggio

Coordinatore Dottorato: Prof. ssa Carla Cannas

Tutor: Prof. ssa Marzia Fantauzzi

Prof. ssa Antonella Rossi

Esame finale anno accademico 2021 – 2022



MINISTERO DELL'ISTRUZIONE,
DELL'UNIVERSITÀ E DELLA RICERCA



Unione europea
Fondo sociale europeo



REGIONE AUTONOMA DE SARDIGNA
REGIONE AUTONOMA DELLA SARDEGNA



Contents

Abstract.....	7
Chapter 1. Introduction	10
1.1. Functional properties of surface films on materials.....	10
1.2. Scope and outline of the thesis.....	11
References.....	13
Chapter 2. Literature Review	14
2.1. Thin films and functional properties of materials.....	14
2.2. The role of surface thin films in corrosion.....	15
2.3. Anti-wear and lubrication properties of thin films.....	16
2.4. Analytical techniques for characterizing thin films.....	17
2.4.1. <i>In-situ</i> : Electrochemical and tribological techniques.....	18
<i>Electrochemical Techniques</i>	18
<i>Tribological Techniques</i>	19
2.4.2. <i>Ex-situ</i> techniques for characterizing thin films.....	20
X-Ray photoelectron spectroscopy (XPS) [54,61].....	20
<i>Scanning Electron microscopy (SEM)</i>	21
Atomic force microscopy (AFM).....	22
Static secondary ion mass spectroscopy (SSIMS).....	23
References.....	26
Chapter 3. Techniques	30
3.1. Fundamentals of Corrosion [1-12].....	30
3.2. Electrochemical techniques.....	34
3.2.1. Open Circuit potential (OCP).....	35
3.2.2. Linear polarization resistance (LPR) and potentiodynamic polarization (<i>Tafel</i> Plot).....	35
3.3. Tribological methods.....	38
3.3.1. Fundamentals of tribology and lubrication [13-23].....	38
3.2.2. <i>Lubricants and Regimes of Lubrication: The Stribeck curve</i>	41
3.2.3. Lubricants and Lubricant Additives.....	43
<i>Ionic liquids</i>	43
3.2.4. Tribological test: Pin on disk tribometer [13].....	45
3.4. X-ray photoelectron spectroscopy (XPS) [30-43].....	46
3.4.2. Spectral interpretation.....	50
References.....	57
Chapter 4. Thin Films on CuZn37	59
4.1. Introduction.....	59

4.2.	Experimental	60
4.2.1.	Materials and surface preparation	60
4.2.2.	Model solutions	61
4.2.3.	Optical microscopy (OM)	62
4.2.4.	XRF analysis	62
4.2.5.	Electrochemical tests	63
	<i>Open Circuit Potential (OCP) and Linear Polarization resistance (LPR)</i>	63
	<i>Cathodic and anodic polarization curves</i>	64
4.2.6.	XPS surface analysis	64
4.3.	Results.....	66
4.3.1.	Morphology.....	66
4.3.2.	Electrochemical results	67
	<i>Open circuit potential (OCP)</i>	67
	<i>Potentiodynamic polarization curves (Tafel plot)</i>	69
	<i>Linear Polarization resistance (LPR) and corrosion rate</i>	71
4.3.3.	XPS results	72
	<i>CuZn37 mechanically polished</i>	72
	<i>CuZn37 exposed to saliva formulations</i>	80
4.4.	Discussion	89
4.4.1.	Effect of exposure time	89
4.4.2.	Dissolution mechanism	89
4.4.3.	Practical implications - corrosion rate	90
4.4.4.	Influence of saliva composition	91
4.4.5.	Effect of citrate on film composition	92
4.4.6.	Effect of uric acid	94
4.4.7.	Wagner plots	96
4.5.	Conclusions	100
	References.....	101
	Chapter 5. Thin Films on stainless steel DIN 1.4456	104
5.1.	Introduction	104
5.2.	Experimental	105
5.2.1.	Materials and surface preparation	105
5.2.2.	Model solutions	106
5.2.3.	Optical microscopy (OM)	107
5.2.4.	XRF analysis	107
5.2.5.	Electrochemical tests	107

<i>Open Circuit Potential (OCP) and Linear Polarization resistance (LPR)</i>	108
<i>Cathodic and anodic polarization curves</i>	108
5.2.6. XPS surface analysis	108
5.3.2. Electrochemical Results	111
<i>Open circuit potential (OCP)</i>	111
<i>Potentiodynamic polarization curves (Tafel plot)</i>	112
<i>Linear Polarization resistance (LPR) and corrosion rate</i>	114
5.3.3. XPS results	115
<i>Stainless steel DIN 1.4456 mechanically polished</i>	115
<i>Stainless steel DIN 1.4456 exposed to saliva solutions</i>	118
5.4. Discussion	127
<i>Influence of exposure time</i>	128
<i>Effect of model solutions on the film composition</i>	130
<i>Estimated weight loss</i>	132
5.5. Conclusions	133
References.....	134
Chapter 6. Thin films on Si_3N_4	136
6.1. Introduction	136
6.2. Experimental.....	137
6.2.2. Materials	137
6.2.3. Surface preparation.....	138
6.2.4. Optical microscopy and Profilometry	138
6.2.5. Tribological tests.....	139
6.2.6. XPS surface analysis.....	141
6.3. Results.....	142
The ionic liquids characterization for its use in the tribotest are presented in this section.	142
6.3.1. Viscosity.....	142
6.3.2. Morphology	143
<i>Si_3N_4 mechanically polished</i>	143
<i>Si_3N_4 disk and the pin after Stribeck Tests in the presence of [EMIM]EtSO₄</i>	144
<i>Si_3N_4 disk and the pin after Stribeck Tests in the presence of [EMIM]EtSO₄ + 2 wt % Oleic acid/[EMIM]oleate 50/50</i>	147
6.3.3. Tribological results.....	149
<i>Stribeck curves in the presence of dried and equilibrated [EMIM]EtSO₄</i>	149
<i>Stribeck curves in the presence of dried and equilibrated [EMIM]EtSO₄ + 2 wt% Oleic acid/[EMIM]oleate 50/50</i>	149
6.3.4. XPS results	151

<i>Si₃N₄ disk mechanically polished</i>	151
<i>Si₃N₄ disk and pin after the test in the presence of equilibrated [EMIM]EtSO₄</i>	154
<i>Si₃N₄ disk and pin after the test in the presence of equilibrated [EMIM]EtSO₄ + 2 wt % Oleic acid/[EMIM]oleate 50/50</i>	159
6.4. Discussion	166
6.4.1. Effect of the water content on lubrication.....	166
6.4.2. Effect of the blend composition on lubrication.....	167
6.4.3. Slow tests: tribochemical film effect	168
6.5. Conclusions	169
References.....	171
Conclusions and outlooks	172
Appendix A	175
<i>Curriculum Vitae</i>	185
Acknowledgments	187

Abstract

Functional properties are mechanical, physical and chemical characteristics of the material that make it suitable for its intended function, such as resistance to wear, corrosion and biocompatibility. These functions can be afforded by the bulk of the material and especially by functional surface films. An example is the corrosion resistance of metals and alloys that is often attributable to the presence of thin layers, few nanometres thick, with a different composition from the bulk. In this work, an analytical method was developed for studying the growth and characterization of such thin layers (used to improve the functional properties of materials such as ceramics, brass and steel), combining electrochemical and tribological techniques with the X-ray photoelectron spectroscopy (XPS) and X-ray induced Auger electron spectroscopy (XAES). The data quality in the XPS analysis was controlled and evaluated by periodic calibrations according to ISO 15472:2014 protocol and by using reference materials for an accurate qualitative and quantitative analysis.

The first part of this thesis is focussed on the study of the corrosion behaviour of the brass CuZn37 and the DIN 1.4456 Ni-free stainless-steel alloys exposed to different model saliva formulations, Darvell (D), Carter-Brugirard(C-B) and SALMO (S). Since real saliva has variable and non-reproducible composition, these corrosion studies are performed with model solutions i.e., simulating the biofluids. Their compositions mainly differ for the organic compounds content: in addition to urea present in all formulations, uric acid, lactic acid, and citrate are present in the case of D and the amino acid glycine in the case of SALMO. The corrosion behaviour of the CuZn37 and of the Ni-free stainless steel in contact with the artificial saliva was evaluated with electrochemical measurements (open circuit potential and polarization resistance) at different exposure times (1h, 3h and 16 h). The corrosion rate ($\mu\text{m} / \text{year}$) decreased with exposure time from 48 (11) after 1 h to 15 (2) after 16 h for D, from 27 (12) after 1 h to 1.8 (0.7) after 16 h for C-B and from 3.0 (0.3) after 1 h to 0.8 (0.2) after 16 h for SALMO. The corrosion rate was found higher in Darvell solution. These differences can be explained by the results of X-ray electron spectroscopy (XPS) analyses, that allowed obtaining the chemical state of the elements, the composition and thickness of the thin films formed after the contact with the different formulations. On the CuZn37 brass alloy following the contact with C-B and Salmo solutions a protective film composed of zinc phosphate was formed. In Darvell solution the phosphorus signal, ascribed to the presence of $\text{Zn}_3(\text{PO}_4)_2$ in the samples exposed to the other solutions, is absent. In addition to the component ascribed to CuSCN on the S 2p high-resolution spectra, a second sulphur component at low binding energy is also revealed. The

surface film after the exposure to D solution is depleted in zinc, in respect with the bulk composition, with a Zn/Cu atomic percentage ratio of about ten times lower than those in the samples in contact with the other model solutions. Moreover, the thickness of the film of the sample exposed to D, determined by angle-resolved XPS, is lower than for those observed in other solutions.

In the case of Ni-free stainless steel, the corrosion behaviour is similar for the three saliva formulations. The corrosion rate values in this case are significantly lower than the values obtained with CuZn37 due to the formation of a passive film on the steel. The composition of the passive film on the surface of the samples exposed to the D solution is enriched in chromium oxi-hydroxide and depleted in iron oxide in respect to the bulk composition. This can be explained by the presence of organic compounds such as uric acid, lactic acid and citrate in the Darvell formulation, which could form complexes with iron, promoting its dissolution from the surface of 1.4556 stainless steel.

The results obtained for both brass and steel suggest that the presence of organic compounds in the model solutions influences the composition of the film formed on the surface and controls the corrosion behaviour of the materials.

In the second part of this thesis, the focus is on the lubrication mechanism of 1-ethyl-3-methyl imidazolium ethyl sulfate [EMIM] EtSO₄ and a mixture of [EMIM] EtSO₄ + 2 wt % of an equimolar ratio of oleic acid and [EMIM] oleate for the sliding of a Si₃N₄ tribopair. The experiments were carried out after the running-in procedure, to achieve a conformal contact between the surfaces of the tribological pair and were performed in a speed range from 200 mm/s to 0.1 mm/s, in order to evaluate the different lubrication regimes. The influence of the water uptake during the experiment carried out with a relative humidity (RH) of 43.5-55% and the effect of the additive are evaluated. The water content influences the lubrication mechanism: the decrease in viscosity of the lubricant and consequently an increase of the coefficient of friction (CoF) are observed. In the presence of additive, a marked decrease of CoF is measured in comparison with the one in the presence of pure IL. The combination with the XPS analysis allows the elucidation of the possible mechanism: in the presence of [EMIM] EtSO₄ + 2 wt % of equimolar ratio of oleic acid / [EMIM] oleate blend XPS results provide evidence of the formation of a tribofilm, while in the presence of the pure IL and in humid air the mechanism is likely a smoothing of asperities.

This work confirms that the analytical approach based on combination of *in-situ* (electrochemical and tribological) techniques and *ex-situ* (XPS) techniques following a careful calibration and the

analysis of reference materials allow the rationalization of the results, the understanding of the mechanisms, and the role played by the surface film composition both in corrosion and in tribology.

Chapter 1. Introduction

1.1. Functional properties of surface films on materials

Functional coatings have been used by humans throughout history, and their origin can be traced back to the use of natural materials such as beeswax, vegetable oils, animal fat, and clay minerals used to protect metallic tools from corrosion and wear, to improve water repellence, and as lubricants [1]. 'Functional materials' are designed to perform a specific function, essential for various applications, such as medical diagnostics, chemical and process control, and automotive. The properties of these materials depend on the chemical composition, structure, and manufacturing process. In fact, different studies based on theoretical models have been widely conducted on the bulk properties of functional materials and their description in the recent past. [2-5] Nowadays, the approach has changed in order to optimise the materials for current and future needs, considering the relationships between composition, microstructure, processing and macroscopic properties.

The functional properties of materials such as corrosion resistance, wear resistance and friction reduction, are not only dependent on bulk properties (e.g. tensile strength, elasticity, hardness, density, etc.) but also, on the morphology, the composition, and the structure of the surface films formed after the contact of the material with the environment: air, aqueous solutions, lubricants, additives, or other media. [6] In fact, several examples are reported in the literature [7-14] concerning the protective function of surface films against materials corrosion.

Although the surface of a material is a tiny part of the material itself, it plays a crucial role in terms of materials properties. [15] The surface of a material defines how the material interacts with the surrounding environment and plays a fundamental role in many processes, phenomena, and in designing innovative materials and devices. Thin-film lithium batteries are an example: they have application in electronic devices, like cellular phones and laptops and in medical devices, as implant materials. These batteries have the same properties of the bulk counterpart, but their small size allows their application in miniaturized systems. [16]

In recent times, in fact, surface functionalisation of materials has become an increasingly important area. The functional coatings studies have been evolving for a very long time and nowadays a variety of surface functionalisation pathways are available. The growth of films on materials, whether thin or thick, has several advantages as the production of complex structures, compatibility with a wide variety of materials (ceramics, metals, polymers), and low processing temperatures. [1, 17-18]

The surface films and their properties are widely investigated and are of considerable industrial importance: the preservation of monuments, food and health safety, pollution monitoring, anti-wear and lubrication depend on functional properties of the surfaces. [19,20] The surface of a material may be altered by surrounding medium either unwittingly (corrosion) or on purpose due to technological demands. Films and surface coatings can be applied to a variety of materials, from organic (polymer), to inorganic (metal, ceramics), and to hybrid materials (functionalized nanoparticles), in order to tailor their properties for the current challenges related not only to healthcare and medicine, but also to energy production, pollution detection and to long-term exposure with the environment and with biological systems. [21]

An analytical strategy aiming at surface films characterization is, therefore, crucial for understanding and tuning the functional properties of materials.

1.2. Scope and outline of the thesis

The scope of this thesis is to develop an analytical method aimed to characterize thin films formed on three different substrates and media:

- Two metallic substrates (a CuZn37 brass alloy and a stainless-steel DIN 1.4456) following the contact with various solutions simulating human saliva.
- A ceramic substrate (Si_3N_4) before and after sliding tests of a tribopair in contact with a room-temperature ionic liquid (IL) and a blend of IL plus an additive.

The composition of the chemical species in the films and the correlation with corrosion resistance, anti-wear, and lubrication properties were investigated. For this purpose, *in-situ* analysis, as electrochemical and tribological measurements, and *ex-situ* analysis, as surface analysis by x-ray photoelectron spectroscopy, were performed.

This thesis is divided into 7 chapters: the first chapter provides a brief introduction on the functional properties of thin films on materials, followed by the second chapter that deals more specifically with the role of films in corrosion and lubrication, reporting a literature review. The third chapter provides an overview of the physical principles and the *in-situ* and *ex-situ* techniques adopted for the measurements carried out in this PhD work. The fourth chapter focuses on the corrosion behaviour of CuZn37 brass alloy in contact with different saliva formulations and on the composition of the surface films formed on brass following the contact with the model solutions. In the fifth chapter, the corrosion behaviour of the stainless steel 1.4456 in contact with different saliva

formulations and the surface films characterization are reported. The synergistic combination of electrochemical and surface analyses is highlighted for the comprehension of the corrosion mechanism and for correlating it with the functional properties of the film.

The sixth chapter reports the investigation of the lubrication mechanism following the sliding test of a Si₃N₄ tribopair in the presence of a room temperature ionic liquid also with the addition of an additive (1-ethyl-3-methyl imidazolium ethyl sulphate, [EMIM] EtSO₄ + 2 wt % of an equimolar ratio of oleic acid and [EMIM] oleate). It is shown that a combination of the tribological data and the surface investigations following the tribological test allows a clarification of the mechanism and the rationalization of the tribological behaviour.

Then, in the seventh chapter a comprehensive conclusion on this work is drawn and the outlooks are given.

References

- [1] “M.F. Montemor, Functional and smart coatings for corrosion protection: A review of recent advances, *Surface and Coatings Technology*, 258, 17-37, 2014, ISSN 0257-8972.
- [2] J. Valasek, “Piezoelectric and Allied Phenomena in Rochelle Salt,” *Physical Review*, 17, No. 4, 475-481, 1921.
- [3] G. Zhang, C. Viney, 1.2.3 - Bulk Properties of Materials, *Biomaterials Science (Fourth Edition)*, Academic Press, 2020, 41-51, ISBN 9780128161371.
- [4] A. Cigada, T. Pastore, *Struttura e proprietà dei materiali metallici*, McGraw-Hill Education (Italy) srl, 2012, ISBN 978-88-386-6733-6.
- [5] C. Viney, 1.1.3 - Bulk Properties of Materials, *Biomaterials Science, (Third Edition)*, Elsevier, Oxford (UK), 9–21, 2013.
- [6] M. Mozetič, Surface Modification to Improve Properties of Materials. *Materials (Basel)*, 12(3), 441, 2019.
- [7] F. Cocco, M. Fantauzzi, B. Elsener B., A. Rossi, Dissolution of brass alloys naturally aged in neutral solutions – an electrochemical and surface analytical study, *RSC Adv.*, 6, 90654, 2016.
- [8] B. Elsener, F. Cocco, M. Fantauzzi, S. Palomba and A. Rossi, Determination of the corrosion rate inside historical brass wind instruments – Proof of concept, *Materials and Corrosion*, 67, No. 12, 1336, 2016.
- [9] F. Cocco, PhD thesis, Sustainability in cultural heritage: from diagnosis to the development of innovative systems for monitoring and understanding corrosion inside ancient brass wind, Università di Cagliari, 2016.
- [10] M. Fantauzzi, B. Elsener, F.Cocco, C.Passiu, A.Rossi, Model Protective Films on Cu-Zn Alloys Simulating the Inner Surfaces of Historical Brass Wind Instruments by EIS and XPS, *Front. Chem.*, 8, 272, 2020.
- [11] B. Elsener, D. Addari, S. Coray, A. Rossi, Nickel-free manganese bearing stainless steel in alkaline media— Electrochemistry and surface chemistry, *Electrochimica Acta*, 56, Issue 12, 4489-4497, 2011.
- [12] D. Addari, B. Elsener, A. Rossi, Electrochemistry and surface chemistry of stainless steels in alkaline media simulating concrete pore solutions, *Electrochimica Acta*, 53, Issue 27, 8078-8086, 2008.
- [13] A. Rossi, R. Tulifero, B. Elsener, Surface analytical and electrochemical study on the role of adsorbed chloride ions in corrosion of stainless steels. *Materials and Corrosion*, 52, 175-180, 2001.
- [14] B. Elsener, M. Pisu, M. Fantauzzi, D. Addari, A. Rossi, Electrochemical and XPS surface analytical study on the reactivity of Ni-free stainless steel in artificial saliva. *Materials and Corrosion*, 67, 591-599, 2016.
- [15] K. Wandelt, *Surface and Interface Science. 4- Solid-Solid Interfaces and Thin Films*. Weinheim: Wiley-VCH, 2014.
- [16] M. C. Rao, M. S. Shekhawat, A brief survey on basic properties of thin films for device application, *Intern. J. of Modern Physics: Conference Series*, 22, 576, 2013.
- [17] P.M. Vilarinho, *Functional Materials: Properties, Processing and Applications*. In: Vilarinho, P.M., Rosenwaks, Y., Kingon, A. (eds) *Scanning Probe Microscopy: Characterization, Nanofabrication and Device Application of Functional Materials*, NATO Science Series II: Mathematics, Physics and Chemistry, vol 186. Springer, 2005.
- [18] E. Ostroff, K.Parekh, A.Prominski, B.Tian, *Biocompatible and Nanoenabled Technologies for Biological Modulation*. *Adv. Mater. Technol.*, 7, 2100216, 2022.
- [19] J.C Scully, *Treatise on materials science and technology, corrosion: aqueous processes and passive films*, Academic Press inc, London ltd, Vol. 23, 1983, ISBN: 0-12-633670-9.
- [20] Shibe, & Chawla, Vikas, A Review of Surface Modification Techniques in Enhancing the Erosion Resistance of Engineering Components 1. *International Journal of Research in Mechanical Engineering & Technology*, 4, 2249-5762, 2014.
- [21] K.Wieszczycka, K.Staszak, M. J. Woźniak-Budych, J. Litowczenko, B. M. Maciejewska, S. Jurga, Surface functionalization – The way for advanced applications of smart materials, *Coordination Chemistry Reviews*, 436, 213846, 2021.”

Chapter 2. Literature Review

This chapter starts with a general description of thin films, and provides an overview on their functional properties and applications. In section 2.2 and 2.3 the role of the surface films in corrosion and tribology is described. Then, the analytical approaches used in the characterization of thin films are presented.

2.1. Thin films and functional properties of materials

The IUPAC definition of thin film is *“a film whose thickness is of the order of a characteristic scale or smaller. Since a film may 'look' operationally thin or thick, according to the procedure applied, it is also recommended that the measurement procedure employed be specified (e.g. ellipsometrically thin film, optically thin film, etc.). It is recommended that the physical specification of the film thickness be used, whenever possible (e.g. thick compared to the electron mean free path, thin compared to the optical wavelength, etc.)”* [1] Mechanical, optical, electrical and magnetic properties of thin films generally differ from those of bulk materials [2-4]. The evolution of surface films technology, with the development of vacuum technology and electric power facilities, has led to an increase in a wide range of industrial applications due to the improved properties of materials. Indeed, thin films are used for wear and corrosion protection, and for advanced applications such as photovoltaics, microelectronics and antireflective coatings. [5] Thin films were first employed for optical applications: for example, the reflecting properties of metallic films were used for improving the accuracy of the interferometer. The production of anti-reflective coatings for optical lenses was developed in the 1950s, starting from the studies of Rayleigh and Fraunhofer on the atmospheric corrosion of the lens surfaces of their instruments resulting in the increase in transmission rather than to decreased performance. [6] Nowadays, new applications of optical films, consisting in metal, dielectric, and semiconductor alone and/or in layered combinations, have emerged to produce anti-reflective coatings for solar cells, films for energy storage systems, mirrors for lasers. The electrical properties of thin films are also of current interest given the ongoing development of more efficient and reliable electrical components, such as systems with microscopic thin-film integrated circuit chips and photovoltaic converters. Metal oxides films are commonly employed in photovoltaic cells and one of the most used oxides is TiO_2 due to its adhesion properties, chemical stability, such as tuneable electrical conductivity, and photocatalytic properties [7-9]. The literature reports other different applications of thin films spacing from the improvement of mechanical properties, as in

the case of Al and W deposited on glass, aluminium, silicon, and sapphire substrates, where the value of hardness and Young's modulus change according to the different composition, properties and the thickness of the film [10], to the improvement of the antibacterial properties of materials, used for implants, by depositing silver, copper and zinc oxides. [1-16]

Thin films are acknowledged to play a very important role both in corrosion and in tribochemistry: they improve the stability of the metal and of alloys due to their properties. These important aspects will be discussed in the next section.

2.2. The role of surface thin films in corrosion

Parallel to the great development of thin-film technology in microelectronics, there have been remarkable advances in the field of protective coatings of metals. It is well-known that most metals and alloys are thermodynamically unstable in air and in aqueous environments [17] and, in these conditions, they are corroding mainly forming oxides and hydroxides as products. Thus, protective coatings are used to protect these metallic materials from gaseous or aqueous environments that cause corrosive attacks. [2, 18]. Different kinds of materials are used as protective coatings; among them, ceramic oxides (e.g., Al_2O_3 , TiO_2), covalent materials (e.g., diamond, SiC), transition metal compounds (e.g., TiC, WC) and metal alloys (e.g., CoCrAlY) can be mentioned. It is well-known that many metals and alloys are thermodynamically unstable in air and in aqueous solutions [17] and, in these conditions, they usually tend to passivate.

An example of the widespread use of coatings is the automotive industry that for several years exploited coating technologies to improve the corrosion resistance of automotive bodies, typically made of steel. Steel sheets are treated by phosphating in order to improve corrosion resistance and ensure the adhesion of organic paints.

Another significant example of the role of surface films, only few nanometers thick, in corrosion protection is the passivity of stainless steels, aluminium and its alloys and titanium. Thin oxide films are formed spontaneously on their surface as a result of contact with the ambient and are responsible for their corrosion resistance. Stainless steels are used in various applications, such as in the chemical industry, in the transport of chemicals, in architecture and civil engineering and are also used in medicine and in dentistry [19-21]. In the literature [22-25], both in alkaline and saliva model solutions, it is reported that on the stainless steels surface, after few hours of exposure to

the various solutions, a passive film mainly composed of oxi-hydroxide of chromium and iron is present that protects the material from further dissolution.

The same behaviour was observed for brass alloys, used in different applications as in water and steam systems to fabricate various cast components in ocean engineering [26]. In natural seawater, brass showed a layered dezincification corrosion with the loss of Zn and the deposition of Cu on metal surface.[27] The use of organic films as the deposition of a PropS-SH silane film was found to be effective in reducing this dissolution. It was reported a decrease of dezincification coefficient from 4.45 to 0.47, for bare brass and covered brass respectively, inhibiting the dezincification process and improving the corrosion resistance of brass in natural seawater. [28]

Brass alloys were also utilized in the fabrication of wind instruments and in this case the corrosion of the inner surfaces might occur due to the contact with saliva. An investigation carried out on the stability of brasses following the contact with a saliva model solution [29-31] demonstrated the growth of a protective film mainly composed of CuSCN and $\text{Zn}_3(\text{PO}_4)_2$. The authors reported that the longer the brass was exposed to the solution, the less dissolution of the material was observed: the corrosion rate in $\mu\text{m} / \text{year}$ significantly decreased from 1 to 16 hours of exposure.

Thus, the corrosion resistance and the stability of a metal and its alloys depends on various parameters: the bulk composition of the alloy, the chemical composition of the film formed after the contact with the environment and its thickness and the duration of the interaction with the ambient [32]

2.3. Anti-wear and lubrication properties of thin films

In tribological systems, the interactions between the lubricant and the various surfaces of materials are complex and usually result in the formation of a surface film. In engine-oils field, additives are commonly added to lubricants with the purpose of increasing the anti-wear properties. One of the most used anti-wear additives is zinc dialkyl dithiophosphate (ZDTP), which forms a tribological multi-layered film [33]. During the use, at the rubbing interface, the ZDTP molecule degrades rapidly to produce a variety of products as organo-thiophosphates, soluble organic sulphides (e.g. dialkyl sulphide), and in addition an oil insoluble component (zinc polyphosphate); these products have a significant role on wear protection. [34-35] Recently, the growing awareness of the ecological and economic impact of the use of oils and additives in industrial processes has led industries and governments to promote sustainability. In tribology field, this trend led to the so-called 'green

tribology' [36], which indicates “the science and technology of the tribological aspects of ecological balance and of environmental and biological impacts” .[36] For these reasons and for their physical and chemical properties, the ionic liquids (ILs) have been recently proposed as substitutes of the common oils or in combination with them as additives. Indeed, ILs are highly tuneable due to the variety of available combinations of anions and cations that can be used for a specific application. In addition, the incorporation of elements (F, P or B) into the cation and/or anion, allow designing an IL that can react with the surface of particular material and/or can be miscible with a specific base oil. [37-38] Steel/steel and steel/aluminum tribopairs are the most investigated materials for examining ILs as lubricants, such as imidazolium tetrafluoroborates and hexafluorophosphates that exhibited lower friction and wear than traditional lubricants for different systems [38-40]. Metal fluorides, phosphates and B_2O_3 were detected by XPS analysis on the wear scar lubricated with these ILs [41-42]. It was demonstrated that IL reacted with exposed metal surfaces: the formation of degradation products, formed due to local temperatures and high pressures developed during rubbing between metal surfaces, led to the formation of a protective tribo-film. ILs have been also used as additives in aqueous lubrication of ceramics, but another interesting and promising approach is to use water-soluble brush-like copolymers. [43] For example, the adsorption of poly(L-lysine)-graft-poly (ethylene glycol) (PLL-g-PEG) on ceramics substrates lead to a formation of a thick film that not only reduce the wear and friction but also preserves the lubricating effect through the self-healing mechanism. This mechanism allows preventing the protein adsorption on ceramic surface too. [44]

2.4. Analytical techniques for characterizing thin films

Analytical techniques for the characterisation of thin films can be divided into *in-situ* and *ex-situ* techniques. *In-situ* techniques provide information on growth and formation mechanism of the film present on surfaces, and the *ex-situ* techniques allow determining the chemical composition at the surface after the tests. [18] Thus, the combination of *in-situ* and *ex-situ* techniques allow analysing and correlating the growth mechanism to the composition of the film formed after the contact with the environment [45]. Nowadays, it is also possible to obtain the chemical composition during the tests, for example by using Raman spectroscopy and confocal Raman mapping during corrosion test and characterize the products formed in electrochemical reactions [46].

In the following paragraphs, a critical review of the main techniques used for characterizing thin films and their advantages and disadvantages will be given.

2.4.1. *In-situ*: Electrochemical and tribological techniques

Electrochemical and tribological techniques are commonly used as *in-situ* and real-time analyses for characterizing thin films growth during the interaction with aqueous solution, oils, and lubricants.

Electrochemical Techniques

Electrochemical techniques, such as open circuit potential (OCP) measurements, provide information on film formation over time. More details on OCP and corrosion rate measurements are reported in chapter 3, and here a brief overview on Electrochemical Impedance Spectroscopy (EIS) studies on protective films on metallic substrates is provided.

EIS is employed to investigate mass-transfer, charge-transfer, and diffusion processes [47]. It is a non-destructive electrochemical method for evaluating a wide variety of materials: it provides not only information about the electric properties of materials and of the processes taking place at the electrode – solution interface, but also about electrochemical mechanisms, reaction kinetics and corrosion phenomena.

From EIS measurements it is possible to obtain different important parameters that allow evaluating the properties and thickness of the film formed: the solution resistance (or ohmic resistance) R_s , the film resistance, R_{film} , the oxide film capacitance, CPE_{film} , the charge transfer resistance (R_{ct}) and the capacitance of the double layer, CPE_{dl} .

EIS was exploited for example in corrosion studies of brass in artificial saliva and in neutral buffer solutions: [30-31] the authors reported that for the brass exposed to artificial saliva the resistive component associated to the thick film is high, while in the brass exposed to buffer solution the charge transfer resistance is much higher than the film resistance, thus in the artificial saliva the film resistance governs the dissolution rate. EIS spectroscopy is also used for characterizing organic films (amines) used as protective films on carbon steel [48] in terms of permittivity, resistivity profile, inhibitive efficiency, and also thickness, combining EIS as *in-situ* technique and XPS as *ex-situ* technique.

Thus, electrochemical techniques are useful for investigating the corrosion rate and film formation in a metal/ solution system, but do not provide any direct chemical information. For this reason, these techniques are usually combined with surface analysis methods.

Tribological tests provide information on wear and friction mechanisms of a specific tribosystem. It is essential to plan a test to perform model testing that reproduces a real application. The contact geometry is crucial in tribological tests and it has to be taken into account the shape of the contacting bodies and whether the contact is conformal or nonconformal. There are several contact configurations for model tests that evaluate sliding wear: pin-on-disk configuration (Figure 2a), ball-on-disk configuration (Figure 2b), reciprocating pin against a fixed plate (Figure 2c) and reciprocating cylinder against a fixed plate (Figure 2d). [49]

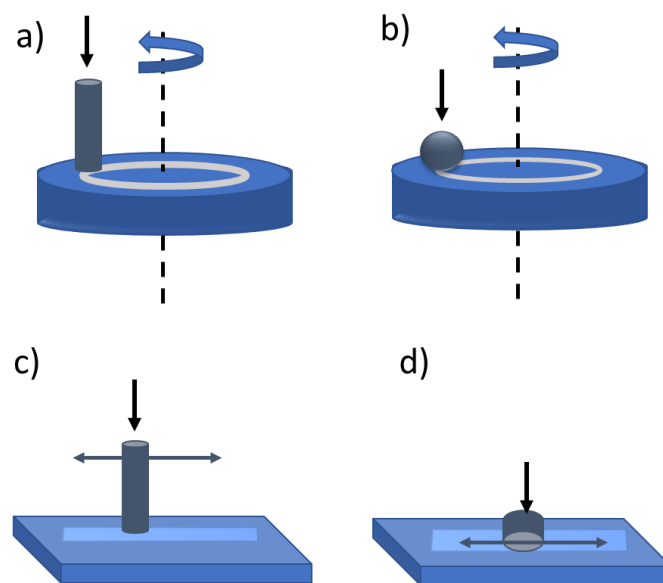


Figure 2: Contact configurations for model tests: a) pin-on-disk configuration (uniform motion), b) ball-on-disk configuration (uniform motion), c) reciprocating pin against a fixed plate and d) reciprocating cylinder against a fixed plate, adapted from [49]

The configuration most commonly used is pin-on-disk since it is versatile and allows examining both dried and lubricated contacts. (More details are reported in chapter 3). The sliding motion in pin on disk test is unidirectional. The sliding velocity is changed when the track radius or the rotating velocity are altered. Also, the applied load can also change, and tests can be also performed with pin and disk immersed in the lubricant. During the test, the friction force is measured, and the rotational speed can be varied, for example by an increase sliding velocity. The output obtained with such a test is the friction force versus time, but also the coefficient of friction versus sliding velocity can be measured.

To obtain information on the film thickness variation during testing, optical interferometry can be combined with the tribological techniques. It is an *in-situ*, non-contact and non-destructive technique based on the basic optical interference principle. The film thickness in the contact area can be determined by the light intensity value between the minimum and the maximum values, called the relative light intensity (eq.1). [50]

$$h = \frac{\lambda}{4\pi k} \left[\left(n + \left| \sin \frac{n\pi}{2} \right| \right) * \pi + \arccos(\bar{I}) * \cos n\pi - \arccos(\bar{I}_0) \right] \quad \text{eq. 1}$$

where λ , k , and n are the wavelength of the incident light, reflective index of lubricant and interference order respectively. I , I_{\max} and I_{\min} are the light intensity, and the maximum and minimum interference light intensity, respectively, I is used as the relative interference light intensity $\bar{I} = (2I - I_{\max} - I_{\min}) / (I_{\max} - I_{\min})$ and \bar{I}_0 represents the relative light intensity of zero film thickness.

The main disadvantage of optical interferometry is that the materials with low reflective properties cannot be measured and the highly reflective materials produce artificial spikes. [51,52]

Although tribological techniques provide information on friction, lubrication and the wear mechanism in a specific tribological system, they do not provide information on the surface topography and chemical composition of the surface of the counterparts. For these reasons, *ex-situ* techniques or their combination are necessary to fully understand what is happening in a real system in service. It is reported in the literature [53] that the combination of Raman and XPS analysis has enabled the understanding of the wear mechanism at different speeds for SiO₂/Si tribopairs lubricated with fluorinated ionic liquids under anhydrous conditions and with [EMIM] and [HMIM] TFSI in a pin-disk configuration.

2.4.2. *Ex-situ* techniques for characterizing thin films

X-Ray photoelectron spectroscopy (XPS) [54,61]

One of the most common *ex-situ* techniques is the X-ray photoelectron spectroscopy (XPS). It is a surface analytical technique widely used for characterizing thin films, that allow determining not only the chemical composition but also the thickness of the surface films, by using depth profile analyses. An in-depth discussion on this technique is reported in the next chapter (Chapter 3).

In the following paragraphs an overview on other the *ex-situ* techniques is discussed.

Scanning Electron microscopy (SEM)

The characterization of the material surface and thus of the related thin films is possible by scanning electron microscopy (SEM). [2, 62 -65] As the name suggest, SEM uses an electron focused beam. The interaction of the electron beam with the surface of the sample affects the images received. The electrons ejected from the sample are used to create a detailed image, revealing information on topography, chemical composition, crystalline structure, and material orientation. As a result of the electron-sample interaction, different signals are produced: secondary electrons (SE), back-scattered electrons (BSEs), characteristic X-rays and light (cathodoluminescence) (CL), absorbed specimen current and transmitted electrons. Usually, SEs, BSEs, and emitted X-rays are detected with appropriate detectors. SEs are inelastically scattered and have a very low energy (~ 50 eV), thus they derive from the outermost layer of the surface specimen no larger than several angstroms. SEs give information about the topography of the sample and with the SEs detector it is possible to obtain a 3D well-defined image with an image resolution of about 0.5 nm. BSEs are elastically scattered and have a high energy as the incident electrons. They provide information about the elemental composition of the surface: the measured intensity depends on the element and the BSE increase with increasing the atomic number Z . The lighter elements reveal a lighter backscattering, thus the areas appear darker in the BSE image, whereas heavier elements appear brighter. The characteristic X-rays were exploited in SEM analysis to obtain the elemental composition. The combination of SEM with Energy Dispersive Spectroscopy (EDS) allows identifying and quantifying elements. SEM technique is commonly used for characterizing the topography and chemical composition of thin films, and it is used in different research fields. [62-65] In literature [66-67] it is reported that the SEM-EDS allows also determining the film thickness. The thickness of ZnO thin films on glass substrate has been determined by a cross-sectional SEM image. [66] Indeed, the use of EDS allow to determine the thickness by using the intensity ratio of an X-ray peak of the thin film to one of the substrates. Some authors [67] reported also the results of thickness measurements by SEM EDS for copper and CdTe films on glass substrates: according to their results the accuracy of the measured thickness is strongly affected by the film composition, since they reported a relative error lower than 11% in the case of copper film and of about 40% for the CdTe film.

Atomic force microscopy (AFM)

Atomic force microscopy is one of the most popular scanning probe microscopies and it is a high-resolution technique that provides information on topographical, electrical, magnetic, chemical, optical, mechanical, etc. properties of a sample surface. Unlike the light or electron microscopes, AFM is based on the measurement of different forces (e.g., repulsive, attractive, magnetic, electrostatic, van der Waals) between a sharp tip, usually Si or Si₃N₄, and the sample surface. [68-69] The force probe of AFM technique could remain stationary while the sample is moving or could move over a stationary sample. The AFM operation relies on a tip mounted at the end of cantilever with a known spring constant. The tip is positioned at a specific distance from the sample and is scanned over the surface by means of a piezo actuator. Little deflections due to the attractive interaction forces between the tip and the substrate of the cantilever can be monitored. The small deflection can be approximated in terms of Hook's law which estimate an upward restoring force proportional to the cantilever deflection [70]. A laser beam is focused on the cantilever and the reflected light is directed onto a four-segment photo-detector that detected the lateral and normal deflection of the cantilever. AFM can operate in different modes: contact mode, when the tip is raster scanned across the surface, always touching the sample, and it can be either constant force or height mode, and non-contact mode (also known as tapping or dynamic mode), which allows obtaining a 3D topographic map of the sample by measuring the change in amplitude of the oscillation at a constant frequency or by measuring the change in resonant frequency, in this case the tip is driven sinusoidally close to the resonance value of the cantilever. The non-contact mode is preferred for investigating soft material and in this case the tip is quite close to the sample and does not touch the surface. This technique is one of the principal tools for imaging, measuring and manipulating matter at the nanoscale. Moreover, it is an important technique for studying the morphology and properties of thin films, measuring their small and deep structures. [71] Furthermore, the principal advantage of AFM is that it can work in ambient air or even a liquid environment. AFM is applied in various scientific fields, such as functional coatings, or polymer engineering and in pharmaceutical applications as highlighted in the study about how specific drugs or drug dosages affect cells, due to the fact that it can be used in aqueous conditions. [70-72] AFM is commonly used in tribology after tribotests to detect topography at the nanometer scale [73-74]. Recently, some researchers are exploiting the possibility to use the cantilevers as tribometers in order to investigate the single asperity contact, friction, and wear. [75].

AFM and AFM-based techniques are also exploited in corrosion studies and in studies on corrosion inhibition. A recent review reports a number of examples of application of scanning probe techniques showing the importance of localized studies in understanding the corrosion mechanism of metallic substrates. [76]

Static secondary ion mass spectroscopy (SSIMS)

Static secondary ion mass spectrometry (SSIMS) emerged as a technique of importance for surface analysis. The prefix *static* is used to distinguish the technique from *dynamic* SIMS. The difference between the two lies in the current density of ion incident (or primary) used, higher for dynamic SIMS and thus, in the information that it can be obtained: SSIMS provides information on surface composition, surface contaminants present, as a function of lateral position for all types of material, and can also be used to study surface phenomena such as adhesion, chemisorption and physisorption, chemical reactivity, wettability, wear, corrosion, lubrication, surface diffusion, and segregation. Dynamic SIMS is related to the sputtering process and it is usually used for depth profile analysis. [54]

During the SIMS experiment the sample is bombarded with a beam of positive ions and positive and negative secondary ions that are emitted together with other secondary particles (e.g. Auger electrons, neutrals, positive secondary ions, and negative secondary ions, etc.) are considered. By a mass spectrometer the emitted ions are analysed and in a mass spectra, that can be positive or negative, the intensity of the parent and fragment peaks from the surface is plotted against m/z ratio. Different mass analysers are available: magnetic sector, quadrupole, and time-of-flight (ToF). The last one is the standard analyser for the SSIMS. ToF-SIMS and SSIMS are widely used various fields, including corrosion studies in combination with XPS and AES [77] with electrochemical measurements and XPS [78], with SEM, SEM-EDX and AFM [79]. ToF SIMS is also exploited for the characterization of tribofilms [80-83]; it was also used for the characterization of polyphosphate glasses [84] that are thought to be responsible for anti-wear properties of phosphorus-based engine-oil additives.

Due to the inherently destructive nature of ion bombardment, the use of the SSIM technique alone must be considered with caution. For this reason, it is used in combination with other surface techniques, usually XPS.

In table 1 disadvantages and advantages of common *ex-situ* techniques used for characterizing thin films are reported.

Table 1: Advantages and disadvantages of different *ex-situ* techniques.

Technique	Advantages	Disadvantages
OM [85]	<ul style="list-style-type: none"> • Non-destructive • Colour differentiation • No vacuum needed • Low magnification (usually <1,500 x) allows for rapid, coarse examination • Easy and quick use • Information about morphology 	<ul style="list-style-type: none"> • Limited resolution • Smaller depth of field, compared to SEM • No chemical composition information
SEM [2, 62-67]	<ul style="list-style-type: none"> • High magnification (500,000 X) • Great depth of focus compared OM • Information about the topography, chemical composition, and film thickness (combined with EDS) • 2D detailed images 	<ul style="list-style-type: none"> • Vacuum needed • Grey scales only • Expensive
AFM [68-76]	<ul style="list-style-type: none"> • Can work in liquid or air environment • Information about topography • 3D images 	<ul style="list-style-type: none"> • No chemical composition information • Damage to soft sample • Slow scan speed
XPS (XAES, ARXPS) [54-61]	<ul style="list-style-type: none"> • Information about chemical composition, chemical state identification and film thickness • Qualitative and quantitative analysis • Depth resolution 0.5-10 nm • Can detect all elements, except H and He • Imaging / mapping 	<ul style="list-style-type: none"> • Vacuum needed • Expensive • Samples must be compatible with high vacuum environment in traditional instruments • Non-conductive sample must be analysed by using a charge compensation system

SIMS [54,77-84]	<ul style="list-style-type: none"> • Can detect all elements and isotopes can be distinguish • Elemental and molecular analysis • High sensitivity for trace elements (ppm to ppb) • 2D e 3D Imaging and mapping 	<ul style="list-style-type: none"> • Destructive analysis • Complex quantitative analysis • Expensive • Vacuum needed
IR (FTIR; RAIRS) [86-89]	<ul style="list-style-type: none"> • Information about molecular composition and structure of thin film • can be used in both high vacuum and ambient pressure environments • Non-destructive 	<ul style="list-style-type: none"> • water interference • several considerations are necessary when analysing films
Raman [54]	<ul style="list-style-type: none"> • Information about chemical composition • Non-destructive • don't require any sort of sample preparation 	<ul style="list-style-type: none"> • Many compounds are not Raman active • More expensive than IR • several considerations are necessary when analysing films
XRF[90]	<ul style="list-style-type: none"> • Information about chemical composition • Quantitative analysis • Film thickness determination with FP calculation • Non-destructive 	<ul style="list-style-type: none"> • Low sensitivity for low atomic number

References

- [1] "UPAC. Compendium of Chemical Terminology, 2nd ed. (the "Gold Book"). Compiled by A. D. McNaught and A. Wilkinson. Blackwell Scientific Publications, Oxford (1997). Online version (2019-) created by S. J. Chalk. ISBN 0-9678550-9-8. <https://doi.org/10.1351/goldbook>.
- [2] A. Jilani, M. S. Abdel-wahab, A. H. Hammad, *Advance Deposition Techniques for Thin Film and Coating, Modern Technologies for Creating the Thin-film Systems and Coatings*, 2017.
- [3] M. Ohring, *The Materials science of Thin Films: Deposition and Structure* (2nd ed.). San Diego, CA: Academic Press., 2002.
- [4] M. C. Rao, M. S. Shekhawat, A brief survey on basic properties of thin films for device application, *Intern. J. of Modern Physics: Conference Series*, Vol. 22, pp. 576, 2013.
- [5] E. Acosta, *Thin Films/Properties and Applications*, Intechopen, 2021. DOI: 10.5772/intechopen.95527
- [6] L. Rayleigh, "Polish," *Nature* (London), **64**, p. 385, 1901.
- [7] V.V. Brus, I.G. Orletsky, M.I. Ilashchuk, P.D. Mar'yanchuk, Electrical properties of thin film semiconductor heterojunctions n-TiO₂/p-CuInS₂., *Semiconductors* Vol. 48, No. 8, pp. 1046, 2014.
- [8] A. Goossens, J. Hofhuis, Spray-deposited CuInS₂ solar cells, *Nanotechnology*, Vol. **19**, 2008.
- [9] U. Diebold, The surface science of titanium dioxide, *Surf. Science Reports*, Vol. 48, p. 53, 2003.
- [10] R. Saha, W. D. Nix, Effects of the substrate on the determination of thin film mechanical properties by nanoindentation, *Acta Materialia*, Vol. 50, p. 23, 2002.
- [11] M. Basiaga, W. Walke, M. Antonowicz, W. Kajzer, J. Szewczenko, A. Domanowska, A. Michalewicz, M. Szindler, M. Staszuk, M. Czajkowski, Impact of Surface Treatment on the Functional Properties Stainless Steel for Biomedical Applications, *Materials*, Vol. 13, p. 4767, 2020.
- [12] M. Basiaga, W. Kajzer, W. Walke, A. Kajzer, M. Kaczmarek, Evaluation of physicochemical properties of surface modified Ti6Al4V and Ti6Al7Nb alloys used for orthopedic implants., *Mater. Sci. Eng. C*, Vol. 68, p. 851, 2016.
- [13] M. Basiaga, M. Staszuk, W. Walke, Z. Opilski, Mechanical properties of atomic layer deposition (ALD) TiO layers on stainless steel substrates. *Mater. Werkst.*, Vol. 47, p. 512, 2016.
- [14] B. Senthil, T. Devasena, B. Prakash, A. Rajasekar, Non-cytotoxic effect of green synthesized silver nanoparticles and its antibacterial activity. *J. Photochem. Photobiol. B Biol.*, 177, p., 2017.
- [15] M. Baláž, Bio-mechanochemical synthesis of silver nanoparticles with antibacterial activity. *Adv. Powder Technol.*, Vol. 28, p. 3307, 2017.
- [16] A. Kiro, J. Bajpai, A. Bajpai, Designing of silk and ZnO based antibacterial and noncytotoxic bionanocomposite films and study of their mechanical and UV absorption behavior. *J. Mech. Behav. Biomed. Mater.*, Vol. 65, p. 281, 2017.
- [17] M. Pourbaix, *Atlas of Electrochemical Equilibria in aqueous solution*, Pergamon, London, 1966.
- [18] J.S.Llewelyn Leach, The role of surface films in corrosion and oxidation, *Surface Science*, Vol. 53, p. 257, 1975.
- [19] S. Jäggi, H. Böhni, B. Elsener, Microcell corrosion of steel in concrete – experiments and numerical modelling, ed. M. Raupach, *Int European Federation of Corrosion (EFC) Series, Corrosion of Reinforcement in Concrete*, Woodhead Publishing, p.75, 2007.
- [20] P. Boillot, J. Peultier, Use of Stainless Steels in the Industry: Recent and Future Developments, *Procedia Engineering*, Vol. 83, p. 309, 2014.
- [21] U. Eduok, J. Szpunara, In vitro corrosion studies of stainless-steel dental substrates during *Porphyromonas gingivalis* biofilm growth in artificial saliva solutions: providing insights into the role of resident oral bacterium, *RSC Adv.*, Vol. 10, p. 31280, 2020.
- [22] D. Addari, PhD thesis, Nanosized films on the surface of stainless steels. A combined electrochemical and XPS analytical investigation on their formation and stability in alkaline environments, University of Cagliari, 2004.
- [23] B. Elsener, D. Addari, S. Coray, A. Rossi, Nickel-free manganese bearing stainless steel in alkaline media— Electrochemistry and surface chemistry, *Electrochimica Acta*, Vol. 56, Issue 12, 2011.
- [24] M. Pisu, PhD thesis, Stability of dental alloys in artificial saliva: an electrochemical and XPS investigation, University of Cagliari, 2012.
- [25] B. Elsener, M. Pisu, M. Fantauzzi, D. Addari, A. Rossi, Electrochemical and XPS surface analytical study on thereactivity of Ni-free stainless steel in artificial saliva, *Materials and Corrosion*, Vol. 67, No. 6, 2016.

- [26] L. Yohai, M. Vázquez, M.B. Valcarce, Brass corrosion in tap water distribution systems inhibited by phosphate ions, *Corros. Sci.*, 53, 1130-1136, 2011.
- [27] P. Zhou, M.J. Hutchison, J.W. Erning, J.R. Scully, K. Ogle, An in situ kinetic study of brass dezincification and corrosion, *Electrochim. Acta*, 229, 141-154, 2017.
- [28] Hong-Qiang Fan, Dong-Dong Shi, Meng-Meng Ding, Mou-Cheng Li, Y. Frank Cheng, Qian Li, Preparation of (3-mercaptopropyl)trimethoxysilane film on brass and its corrosion resistance in natural seawater, *Progress in Organic Coatings*, 138, 105392, 2020.
- [29] F.Cocco, PhD Thesis, Sustainability in cultural heritage: from diagnosis to the development of innovative systems for monitoring and understanding corrosion inside ancient brass wind instruments, University of Cagliari, 2013.
- [30] F. Cocco, M. Fantauzzi, B. Elsener and A. Rossi, Dissolution of brass alloys naturally aged in neutral solutions – an electrochemical and surface analytical study, *RSC Adv.*, Vol.6, p. 90654, 2016.
- [31] M. Fantauzzi, B. Elsener, F.Cocco, C.Passiu, A.Rossi, Model Protective Films on Cu-Zn Alloys Simulating the Inner Surfaces of Historical Brass Wind Instruments by EIS and XPS, *Front. Chem.*, 8, 272, 2020.
- [32] Y. Sun, Surface Engineering and Coating Technologies for Corrosion and Tribocorrosion Resistance. *Materials*, Vol.15, p. 2885, 2022.
- [33] Graham C Smith, Surface analytical science and automotive lubrication, *J. Phys. D: Appl. Phys.* 33 R187, 2000.
- [34] R.B. Jones, R.C. Coy, The chemistry of the thermal degradation of zinc dialkyldithiophosphate additives, *ASLE Trans.* Vol. 24, p. 9, 1979.
- [35] R.J. Bird, G.D. Galvin, The application of photoelectron spectroscopy to the study of e. p. films on lubricated surfaces, *Wear*, Vol. 37, Issue 1, p. 143, 1976.
- [36] M. Nosonovsky, B. Bhushan, Green tribology: principles, research areas and challenges. *Phil. Trans. Of the Royal Society of London A: Mathematical, Physical and Engineering Sciences*, Vol. 368, p. 4677, 2010.
- [37] A. E. Somers, P. C. Howlett, D.R. MacFarlane, M. Forsyth, A review of ionic liquid lubricants, *Lubricants*, Vol.1, p.3, 2013.
- [38] D.S. Silvester, R.G. Compton, Electrochemistry in room temperature ionic liquids: A review and some possible applications. *Z. Phys. Chem.*, Vol. 220, p. 1247, 2006.
- [39] C. Ye, W. Liu, Y. Chen, L. Yu, Room-Temperature ionic liquids: A novel versatile lubricant. *Chem. Commun.*, Vol. 21, p. 2244, 2001.
- [40] W. Liu, C. Ye, Q. Gong, H. Wang, P. Wang, Tribological performance of room-temperature ionic liquids as lubricant. *Tribol. Lett.*, Vol. 13, p. 81, 2002.
- [41] H. Wang, Q. Lu, C. Ye, W. Liu, Z. Cui, Friction and wear behaviours of ionic liquid of alkylimidazolium hexafluorophosphates as lubricants for steel/steel contact. *Wear*, Vol. 256, p. 44, 2004.
- [42] A.E. Jiménez, M.D. Bermúdez, P. Iglesias, F.J. Carrión, G. Martínez-Nicolás, 1-*N*-alkyl-3-methylimidazolium ionic liquids as neat lubricants and lubricant additives in steel-aluminium contacts. *Wear*, Vol. 260, p. 766, 2006.
- [43] W. Hartung, A. Rossi, S. Lee, N.D, Spencer, Aqueous Lubrication of SiC and Si₃N₄ Ceramics Aided by a Brush-like Copolymer Additive, Poly(L-lysine)-*graft*-poly(ethylene glycol). *Tribol Lett*, Vol. 34, p. 201, 2009.
- [44] Hartung, W., PhD thesis, Aqueous lubrication of ceramics by means of brush-forming graft copolymers, 2009.
- [45] A. J. Davenport, M. Sanson, High Resolution *In Situ* XANES Investigation of the Nature of the Passive Film on Iron in a pH 8.4 Borate Buffer, *J. Electrochem. Soc.*, 142, 725, 1995.
- [46] Alina Maltseva, Viacheslav Shkirskiy, Grégory Lefèvre, Polina Volovitch, Effect of pH on Mg(OH)₂ film evolution on corroding Mg by in situ kinetic Raman mapping (KRM), *Corrosion Science*, 153, 272-282, 2019.
- [47] H.S. Magar, R.Y.A Hassan, A. Mulchandani, Electrochemical Impedance Spectroscopy (EIS): Principles, Construction, and Biosensing Applications. *Sensors*, Vol.21, p.6578, 2021.
- [48] J. Baux, N. Caussé, J. Esvan, S. Delaunay, J. Tireau, M. Roy, D.You, N. Pèbère, Impedance analysis of film-forming amines for the corrosion protection of a carbon steel. *Electrochimica Acta*, 283, pp.699-707, 2018.
- [49] M.Torbacke, A. K. Rudolphi, E. Kassfeldt, *Lubricants: Introduction to Properties and Performance*, First Edition. John Wiley & Sons, 2014. LtdH.
- [50] H. Liang, D. Guo, J. Luo, Film forming behavior in thin film lubrication at high speeds. *Friction*, Vol. 6, p. 156, 2018.
- [51] J. Luo, S. Wen, P. Huang, Thin film lubrication. Part I. Study on the transition between EHL and thin film lubrication using a relative optical interference intensity technique, *Wear*, Vol. 194, Issues 1–2, p. 107, 1996.
- [52] L. Ma, C. Zhang, Discussion on the technique of relative optical interference intensity for the measurement of lubricant film thickness. *Tribol Lett*, Vol. 36(3), p. 239–245, 2009.

- [53] A. Arcifa, A. Rossi, N. D. Spencer, Adsorption and Tribochemical Factors Affecting the Lubrication of Silicon-Based Materials by (Fluorinated) Ionic Liquids *J. Phys. Chem. C*, 121, 7259–7275, 2017.
- [54] G. Friedbecher, H. Bubert, *Surface and Thin Film Analysis. A compendium of Principles, Instrumentation and Applications*, Wiley-VCH, 2011.
- [55] D. Briggs, J.T. Grant, *Surface Analysis by Auger and X-ray photoelectron spectroscopy*, IM publications and SurfaceSpectra, 2003.
- [56] D. Briggs, M.P. Seah, *Practical surface analysis*, second edition, vol.1, Wiley, 1990.
- [57] P.J. Cumpson, M.P. and Seah, Elastic Scattering Corrections in AES and XPS. II. Estimating Attenuation Lengths and Conditions Required for their Valid Use in Overlayer/Substrate Experiments. *Surf. Interface Anal.*, Vol.25, p. 430, 1997.
- [58] U. Vogel, T. Gemming, J. Eckert, S. Oswald, Analysis of surface pre-treatment for SAW-substrate material (LiNbO₃) and deposited thin films of Ta/Ti using ARXPS. *Surface and Interface Analysis*, Vol. 46(10-11), p.1033, 2014.
- [59] D.R. Baer, M. H. Engelhard, XPS analysis of nanostructured materials and biological surfaces. *Journal of Electron Spectroscopy and Related Phenomena*, Vol. 178, p.415, 2010.
- [60] I. Milošev, M. Metikoš-Huković, H.H. Strehblow, Passive film on orthopaedic TiAlV alloy formed in physiological solution investigated by X-ray photoelectron spectroscopy. *Biomaterials*, Vol. 21(20), 2103, 2000.
- [61] R.W. Paynter, Degradation during ARXPS measurements of polystyrene treated with an oxygen plasma. *Surface and Interface Analysis: An International Journal devoted to the development and application of techniques for the analysis of surfaces, interfaces and thin films*, Vol. 33(10-11), p. 862, 2002.
- [62] J. Goldstein, D.E. Newbury, D.C. Joy, C.E. Lyman, P. Echlin, E. Lifshin, L. Sawyer, J. Michael, *Scanning Electron Microscopy and X-ray Microanalysis*, ed. Springer Science + Business Media New York, 2007.
- [63] L. Hans, *Solid surfaces, interfaces and thin films*, Springer, 2001.
- [64] M.W. Alam, M.Z. Ansari, M. Aamir, M. Waheed-Ur-Rehman, N. Parveen, S.A. Ansari, Preparation and Characterization of Cu and Al Doped ZnO Thin Films for Solar Cell Applications. *Crystals*, Vol. 12, p.128, 2022.
- [65] V. Kazmiruk, *Scanning Electron Microscopy*, IntechOpen, 2012.
- [66] D. Aryanto, W. N. Jannah, Masturi, T Sudiro, A. S. Wismogroho, P. Sebayang, Sugianto, P. Marwoto, Preparation and structural characterization of ZnO thin films by sol-gel method, *J. Phys.: Conf. Ser.* 817 012025, 2017.
- [67] R. Pascual, L.R. Cruz, C.L. Ferreira, D.T. Gomes, Thin film thickness measurement using the energy-dispersive spectroscopy technique in a scanning electron microscope, *Thin Solid Films*, Vol. 185, p. 279, 1990.
- [68] G. Haugstad, *Atomic Force Microscopy: Understanding Basic Modes and Advanced Applications*, John Wiley & Sons, 2012.
- [69] R. Reifengerger, *Fundamentals of Atomic Force Microscopy: Part I: Foundations*, ed. World Scientific, 2016.
- [70] M. Ramzan, E. Ahmed, N.A. Niaz, A.M. Rana, A.S. Bhatti, N.R. Khalid, M.Y. Nadeem, AFM applications to study the morphology of HfO₂ multilayer thin films, Superlattices and Microstructures, Vol. 82, p. 399, 2015.
- [71] P. Nguyen-Tri, P. Ghassemi, P. Carriere, S. Nanda, A.A. Assadi, D.D. Nguyen, Recent applications of advanced atomic force microscopy in polymer science: A review. *Polymers*, Vol. 12(5), p.1142, 2020.
- [72] P. Lemoine, C. Dooley, A. Morelli, E. Harrison, D. Dixon, AFM study of organic ligand packing on gold for nanoparticle drug delivery applications. *Applied Surface Science*, Vol. 574, p. 151386, 2022.
- [73] F. Spadaro, A. Rossi, Shivaprakash N. Ramakrishna, E. Lainé, P. Woodward, and N. D. Spencer, *Langmuir*, Understanding Complex Tribofilms by Means of H₃BO₃–B₂O₃ Model Glasses, 34 (6), 2219-2234, 2018.
- [74] F. Spadaro, A. Rossi, E. Lainé, J. Hartley, N.D. Spencer, Mechanical and tribological properties of boron oxide and zinc borate glasses, *Physics & Chemistry of Glasses: European Journal of Glass Science & Technology Part B.*, Vol. 57 Issue 6, p233-244, 2016.
- [75] M. Reichelt M, B. Cappella B, Micro- and Nanowear of Self-Mated Steel Generated and Studied With an AFM at the Single Asperity Level. *Front. Mech. Eng* 7:722434, 2021.
- [76] K. Yasakau, Application of AFM-Based Techniques in Studies of Corrosion and Corrosion Inhibition of Metallic Alloys. *Corros. Mater. Degrad*, 1, 345-372, 2020.
- [77] A. Rossi, B. Elsener, G. Hähner, M. Textor, N. D. Spencer, XPS, AES and ToF-SIMS investigation of surface films and the role of inclusions on pitting corrosion in austenitic stainless steels. *Surf. Interface Anal.*, 29: 460-467, 2000.

- [78] L. Wang, D. Mercier, S. Zanna, A. Seyeux, M. Laurent-Brocq, L. Perrière, I. Guillot, P. Marcus, Study of the surface oxides and corrosion behaviour of an equiatomic CoCrFeMnNi high entropy alloy by XPS and ToF-SIMS, *Corrosion Science*, 167, 108507, 2020.
- [79] M. Esmaily, P. Malmberg, M. Shahabi-Navid, J.E. Svensson, L.G. Johansson, A ToF-SIMS investigation of the corrosion behavior of Mg alloy AM50 in atmospheric environments, *Applied Surface Science*, 360 (Part A), 98-106, 2016.
- [80] F. Spadaro, A. Rossi, E. Lainé, P. Woodward, N.D. Spencer, Elucidating the resistance to failure under tribological tests of various boron-based films by XPS and ToF-SIMS, *Applied Surface Science*, 425, 948-964, 2017.
- [81] C. Minfray, J.M. Martin, M.I. De Barros, T. Le Mogne, R. Kersting & B. Hagenhoff, Chemistry of ZDDP Tribofilm by ToF-SIMS. *Tribology Letters* 17, 351–357, 2004.
- [82] F. Cyriac, T. Xin Yi, S. K. Poornachary, P. Shan Chow, Effect of temperature on tribological performance of organic friction modifier and anti-wear additive: Insights from friction, surface (ToF-SIMS and EDX) and wear analysis, *Tribology International*, 157, 106896, 2021.
- [83] F. Pape, Nano- and Micro-Tribological Investigations of Boundary Layers on Axial Bearing Washers Tested under WEC Critical Conditions. *Lubricants*, 10, 198, 2022.
- [84] M. Crobu, A. Rossi, F. Mangolini, N. D. Spencer, Chain-length-identification strategy in zinc polyphosphate glasses by means of XPS and ToF-SIMS. *Anal Bioanal Chem* 403, 1415–1432, 2012.
- [85] M. Douglas B., *Fundamentals of light microscopy and electronic imaging*, Wiley-Liss, 2001.
- [86] V.P. Tolstoy, I. Chernyshova, V.A. Skryshevsky, *Handbook of infrared spectroscopy of ultrathin films*. John Wiley & Sons, 2003.
- [87] D. Allara, J. Stapleton, *Methods of IR Spectroscopy for Surfaces and Thin Films*, Vol.51, p.59, 2013.
- [88] M. Trenary, Reflection Absorption Infrared Spectroscopy and the Structure of Molecular Adsorbates on Metal Surfaces, *Annual Review of Physical Chemistry*, Vol. 51, p. 381, 2000.
- [89] D. W. Berreman, Infrared Absorption at Longitudinal Optic Frequency in Cubic Crystal Films, *Phys. Rev.* Vol.130, p. 2193, 1963.
- [90] J.A.M. Vrielink, R.M. Tiggelaar, J.G.E. Gardeniers, L. Lefferts, Applicability of X-ray fluorescence spectroscopy as method to determine thickness and composition of stacks of metal thin films: A comparison with imaging and profilometry, *Thin Solid Films*, Vol. 520, Issue 6, p. 1740, 2012.”

Chapter 3. Techniques

In this chapter an overview of the physical principles and on the *in-situ* and *ex-situ* techniques employed during this PhD work is presented.

First, the *in-situ* techniques as electrochemical and tribological techniques, are addressed. The principles of corrosion and how to evaluate the corrosion rate are presented. A paragraph dedicated to tribology follows where the most important definitions are provided together with the technique used to measure various parameters such as friction and wear coefficients. It is also described, in the body of the paragraph, the instrument used for simulating the in-service conditions. In the last part of the chapter, the principles of x-ray photoelectron spectroscopy (XPS) (*ex-situ* technique) and a spectrometer overview are given.

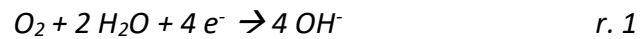
3.1. Fundamentals of Corrosion [1-12]

Introduction: Corrosion is a natural phenomenon that occurs as a result of the chemical-physical interaction between a metal/alloy and the surrounding environment. This process alters the composition of the metal and its functionality. Corrosive processes occur when the metal, being in an aggressive environment, tends to reach its energetically most stable state. A classification of corrosion processes is not easy, due to the huge variety of possible corrosive environments and corrosion reactions. The classification into '*dried corrosion*' and '*wet corrosion*' is now accepted. The first one usually occurs at high temperatures and without water. On the contrary, wet corrosion occurs when a metal is in contact with aqueous electrolytes: redox reactions can take place at the metal-solution interface causing the dissolution of the metal and the reduction of oxygen. As a result, the metal ions can be dissolved in the electrolyte or form oxides. Since corrosion processes are electrochemical reactions, they can be investigated by electrochemical techniques. During the corrosion process of a metal or an alloy, the following reactions occur:

- Cathodic reactions, where the reduction reactions involving electrons gain take place.
- Anodic reactions, where the oxidation reactions take place: the metal oxidises to M^{n+} , losing electrons.

Thermodynamics: If the corrosion reaction occurs spontaneously, there is a decrease in the free energy of the system ($G < 0$). Since corrosion is an electrochemical reaction, it is possible to consider it as the result of reduction and oxidation half-reactions.

In an alkaline or neutral environment, oxygen reduction occurs following the reaction (r.1):



$$E_{cat.} = E^0 + \left(\frac{RT}{4F}\right) \ln \frac{P_{O_2}}{a_{OH^-}} \quad eq. 1$$

Where E_0 is the standard reduction potential (V), T is the absolute temperature (K), F is the Faraday constant (96486 C/mol), R is the universal gas constant (8.314 JK⁻¹mol), 4 is the number of electrons exchanged, P is the partial pressure of oxygen and a_{OH^-} is the activity of the OH⁻ ion. Being $E^0 = 1.23$ V, for $P_{O_2} = 1$ atm the equation becomes:

$$E_{O_2} = 1.23 - 0.059 pH \quad eq. 1.2$$

In acidic environments the hydrogen reduction occurs according to the reaction (r.2):



$$E_{cat.} = E^0 - 0.059 pH + \frac{0.059}{2} \log P_{H_2} \quad eq. 2$$

For $P_{H_2} = 1$ atm and $E^0 = 0$ V the equation becomes:

$$E_{H^+} = -0.059 pH \quad eq. 2.1$$

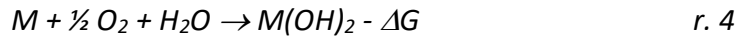
The anodic reaction is the oxidation of the metal:



According to Nernst's law, the equilibrium potential E is:

$$E_{anod.} = E^0 + \frac{RT}{nF} \ln a_{M^{n+}} \quad \text{eq. 3}$$

Thus, the overall reaction of the corrosion process in a neutral or alkaline environment, if ΔG were negative, would then be equal to:



Such a reaction occurs spontaneously if the change in Gibbs' free energy is $\Delta G < 0$. Being,

$$\Delta G = -nF\Delta E = -nF(E_{cat.} - E_{anod.}) \quad \text{eq.4}$$

With $\Delta E = E_{cat} - E_{an}$ a spontaneous corrosion process can occur if $E_{cat} > E_{an}$.

Once the thermodynamic conditions have been defined, it is important to consider the kinetics of the corrosion processes.

Kinetics: The current flow, generated by the electron exchange between an anodic and cathodic reaction, causes an electrode polarization i.e. the shift of electrode potential E from its equilibrium value. This polarization can be measured as an overpotential η by the potentiodynamic polarization test and it is defined by the Tafel's law:

$$\eta_c = E_c - E_{eq,c} = -\beta_c \ln \frac{i_c}{i_{0,c}} \quad \text{eq. 5}$$

$$\eta_a = E_a - E_{eq,a} = -\beta_a \ln \frac{i_a}{i_{0,a}} \quad \text{eq. 6}$$

Where $E_{c,a}$ are the actual potentials of the electrodes (c: cathode; a: anode), $E_{eq,c,a}$ are the electrodes equilibrium potentials, $\beta_{c,a}$ are the Tafel constants (volts/decade), $i_{c,a}$ are the current densities and $i_{0,c,a}$ are the exchange current densities referring to the cathode and anode reactions (Figure 1).

The anodic and cathodic currents have to be identical: the electrons released by the anodic reaction (r.3) are immediately consumed by the cathodic reaction (r.1 or r.2). Thus, the corrosion potential E_{corr} (or open circuit potential) is determined by the electroneutrality condition between the anodic and cathodic reactions, so the corrosion current is $i_{corr} = i_a = |i_c|$.

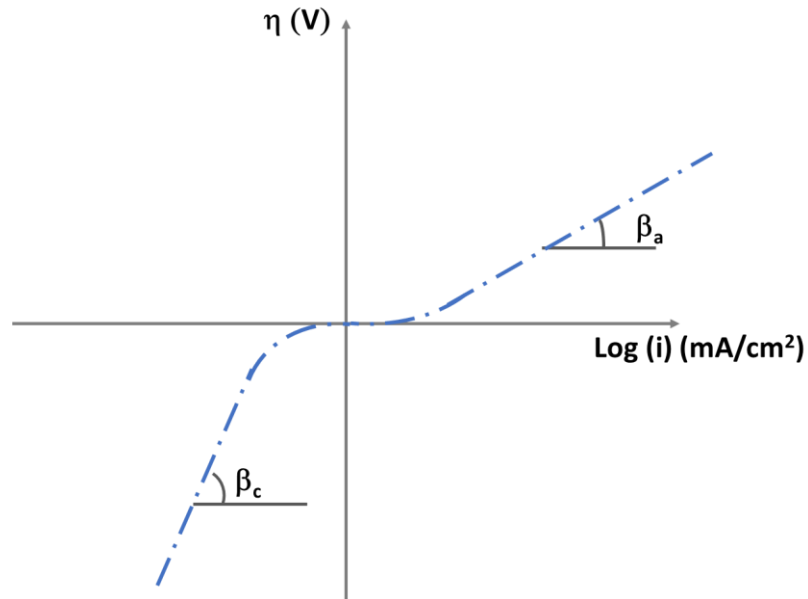


Figure 1: Polarization curves plot, overpotential η vs current density ($\log(i)$), adapted from [11]

Passivation: the passivation process occurs when a metal surface is exposed to an environment under conditions favouring the growth of a protective film on the surface. [11-12]

In order to study the passivation of a metal or alloy, the current density can be measured at different predetermined potentials applied by means of an external electromotive force (emf) source: in this way the potentiostatically determined E-i curves are obtained. If a metal in contact with a solution is considered, e.g., iron in contact with H_2SO_4 , the E vs i curve shows three regions (Figure 2). In the active region, the oxidation of the metal ($\text{M} \rightarrow \text{M}^{n+} + n\text{e}^-$) is occurring and a linear increase of the current density with the applied E is observed (A-B region in Figure 2). For applied potentials higher than the potential in B, a further increase of E does not produce any significant increase in the current density (B-C region in figure 2). At the applied potential C, the current density drastically decreases. The current and potential at point C are the critical current density (i_{crit}) and passivation potential (E_{pp}) respectively. Increasing the applied potential, passivation is occurring. The transition from active to passive region can be justified with the change in the composition of the metal surface due to the formation of a thin film. In this region of the graph the current density (i_{pass}) remains constant if the potential increases from E_{pp} . The i_{pass} starts to increase in the transpassive region (D-E). This region can be associated to gas evolution or to the corrosion of the metal, or both, depending on the nature of metal/solution system.

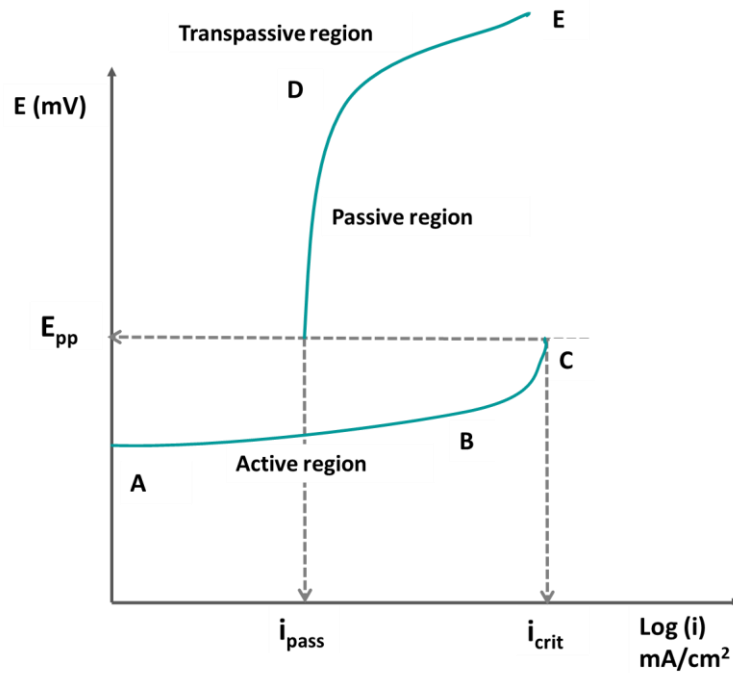


Figure 2: anodic E vs i curve for the metal that shows active and passive transition, adapted from [12].

3.2. Electrochemical techniques

In order to evaluate the corrosion resistance of a material various approaches can be exploited. One is based on the direct measurement of the mass of the specimen before and after its exposure to the corrosive medium. The corrosion rate can be calculated by the weight loss using the equation 7:

$$R = \frac{KW}{AtD} \quad \text{eq. 7}$$

Where R is the corrosion rate, $K = 8.76 \cdot 10^4$ is a constant that allows obtaining the corrosion rate in mm/year, t is the time of exposure of the sample to the solution in hours, W is the weight loss in grams, A is the area of the sample exposed in cm^2 , and D is the density g/cm^3 .

Another approach exploits the electrochemical techniques that were adopted in this work. The measurements are carried out using a potentiostat connected to an electrochemical cell where the working electrode is the metal or the alloy under investigation, the reference electrode is a saturated calomel electrode (SCE) and the counter electrode is a platinum grid. A scheme is given in Figure 3.

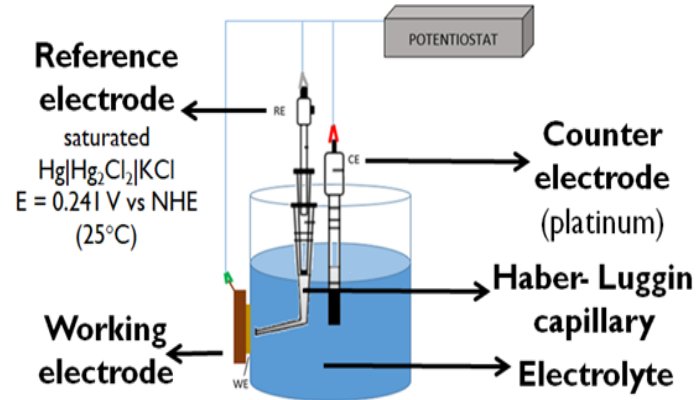


Figure 3: Scheme of electrochemical cell used in this work.

3.2.1. Open Circuit potential (OCP)

The electrochemical techniques can be used for the investigation of the electrochemical reactions that take place when the metallic sample is immersed in a solution, which simulates the solution that might be in contact with the material in the real applications. The relation between current and potential can provide information on the corrosion rate and film formation on the material surface. Electrochemical reactions occurring at the metal-solution interface give rise to an electrochemical potential, the so-called corrosion potential E_{corr} or open circuit potential, E_{OCP} . Since the corrosion potential depends on the chemical/electrochemical properties of the system, this value is characteristic of each metal-solution system. The corrosion potential E_{corr} is experimentally measured by a high-impedance voltmeter (in the potentiostat) as the potential difference between a reference electrode and the working electrode (the tested metal or alloy). During an OCP measurement no current is applied to the sample and the variation of the potential with time is registered: indicatively, if E_{corr} decreases with time, a corrosion process is taking place, whereas if E_{corr} increases upon time to more positive values, a passive film is growing at the sample surface.

3.2.2. Linear polarization resistance (LPR) and potentiodynamic polarization (*Tafel* Plot)

The corrosion current density (i_{corr}) and, consequently, the corrosion rate (v_{corr}) can be calculated by measuring the polarization resistance. After the OCP measurement, a small polarization potential (± 20 mV vs OCP) is applied to promote the oxidation and reduction reactions. This results in a plot showing the current density as a function of the applied potential as in figure 4.

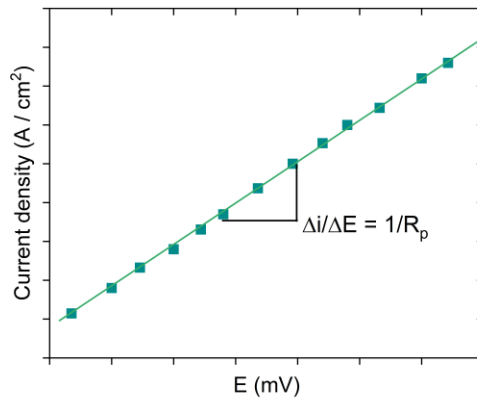


Figure 4: Example of linear polarisation curve, current density vs applied potential.

There is a linear relationship between current density and potential in a small range of potential around E_{corr} . The slope of the straight line of the polarisation curve in i_{corr} vs E_{corr} plot corresponds to the inverse of the polarisation resistance (R_p). The polarisation resistance is related to the corrosion current by the following equation:

$$\frac{1}{R_p} = \frac{1}{i_{corr}} \cdot \frac{\beta_a \beta_c}{2.3 (\beta_a + \beta_c)} \quad \text{eq.7}$$

Where β_c and β_a are the anodic and cathodic constants, which are the slopes of the polarization curve, called Tafel slopes, determined by scanning the potential of ± 250 mV starting from the OCP (Figure 5). The Tafel slopes are related to the kinetics of the oxidation – reduction reactions involved during the corrosion reaction. [9] (eq. 5, eq. 6).

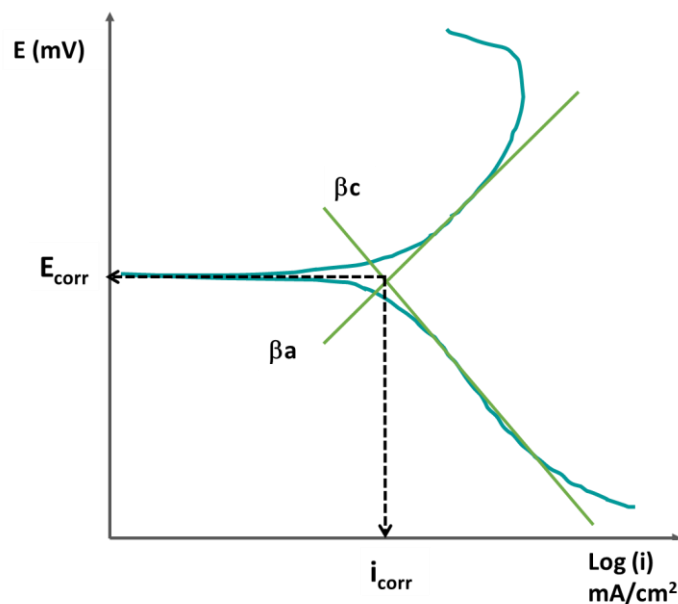


Figure 5: Example of Tafel Plot, adapted from [9]

From the polarization resistance it is possible to calculate the i_{corr} when the sample undergoes to uniform corrosion. For a brass alloy, the Tafel constant of the anodic partial reaction can be assumed to be 60 mV and for the cathodic partial reaction can be assumed to be 120 mV. The corrosion rate v_{corr} ($\mu\text{m}/\text{year}$) can be calculated by using Faraday 's law, as:

$$v_{\text{corr}} = \frac{M}{nFd} \cdot i_{\text{corr}} \quad \text{eq.8}$$

Where M is the molar mass of the metal, d is the density (g/cm^3), n is the number of electrons exchanged during the reaction and F is the Faraday constant.

3.3. Tribological methods

3.3.1. Fundamentals of tribology and lubrication [13-23]

Tribology, from the Greek words *τρίβω* (tribo-) and *λογία* (-logia), literally means “*the science of rubbing and technology of interacting surfaces in relative motion*” [13] and includes friction, wear and lubrication.

The interaction of two bodies in relative motion leads to energy dissipation, friction, and might damage them with loss of material: this phenomenon is known as *wear*. A *lubricant* is a substance placed between the counterparts for reducing the friction and wear [13-14]. The importance of investigating the tribological systems refers to numerous applications as automotive industry, bearings, space, sports, food, health and biomedical, renewable energy, and many others. The research in tribology aims to prolong the lifetime of the mechanical parts involved for saving energy and for improving safety [13].

Friction – the friction force describes the resistance encountered by one body when is moving over another. Friction can be quantified in terms of coefficient of friction that is dependent on different parameters as:

- The structure of the system, i.e. the materials and its properties.
- The operating conditions as load, temperature, time, and kinematics.
- The interaction among the system components.

Whenever two bodies are in contact under a normal load, L , a force is required to initiate and maintain them in relative motion. This force is known as frictional force. In order to describe this interaction, before the 20th century, three empirical laws of friction were established [13-15]:

1. The tangential friction force (F) is proportional to the normal force on the contact (L) in sliding
2. F is independent of the apparent contact area and of the sliding velocity.
3. F always acts in an opposite direction to the relative displacement between the counterparts.

These laws can be summarized as follows:

$$F = \mu L \qquad \text{eq. 9}$$

Where μ is the proportionality between normal load L and tangential force, F ; μ is nowadays indicated as coefficient of friction (CoF). These three statements constitute the knowledge of sliding

friction under dried conditions. The friction derives from interactions between contacting bodies as the effects of adhesion and of surface asperity deformation, plastic deformation of a softer material by hard surface, etc. Thus, several aspects, such as the mechanical and physical-chemical properties of the materials in contact, the environment (i.e. T, RH%) and their surface topography define the relative importance of each component in the friction process. According to the model of Bowden and Tabor [16], energy dissipation derives from the shear strengths of the junctions formed by the asperities that adhere and deform plastically during the relative movement of the counterparts:

$$F_{adh} = s \cdot A \quad \text{eq.10}$$

Where, F_{adh} is the adhesive friction, A is the contact area (m^2) and s (N/m^2) is the mean value of shear strength of the junctions. A is proportional to the load (L) and H (N/mm^2) is the hardness of the softer surface (under static conditions and in the presence of plastically deformed asperities):

$$L = A \cdot H \quad \text{eq.11}$$

Considering the eq. 9:

$$\mu_{adh} = \frac{s}{H} \quad \text{eq. 12}$$

So, the coefficient of friction is dependent on the mechanical properties of the counterpart-surfaces. This model (eq. 12) forecasts that the coefficient of friction for dried sliding and homogenous samples would be always in the range of 0.2-0.3, but in the case of clean ceramics and metallic parts it is found to be 0.3-0.9: higher than what it is expected [16-17]. These variations from the estimated values can be ascribed to the effect of tangential forces on the actual contact area, resulting in higher predicted values. Despite the simplicity of the Bowden and Tabor model, a significant qualitative prediction is achieved: when the material is covered by a layer of a material with a low shear strength and hardness, a coefficient of friction below the estimated range for the bulk material can be measured. This general principle is applied in the presence of additives in oil formulations that are able to form low- share-strength surface layers following the physisorption or mechano-chemical reactions. The *third-body approach* [18-19], proposed in the late 1970s to unify the view of tribology, extends the concept of tribological layers: *third-body* is any layer of material sited at the interface between the two counterparts in relative motion that differ in terms of chemical composition and structure from the bulk material.

Wear - Another important concept in tribology is wear. During the contact between the counterparts in relative motion, different phenomena can occur as plastic deformation, tribochemical reactions, phase transformation, etc. leading to the removal of material as debris. The specific wear coefficient can be calculated as:

$$k = \frac{V}{Ld} [\text{mm}^3\text{N}^{-1}\text{m}^{-1}] \quad \text{eq.13}$$

Where V is the wear volume, L is the applied load and d is the sliding distance. The *wear coefficient* is also reported as dimensionless value and it is equal to:

$$K = k \cdot H \quad \text{eq.14}$$

Where H is the hardness of the softer material.

It is possible to identify four wear mechanisms [20]:

1. **Adhesive wear:** occurs when adhesive junctions are formed between surface asperities that are in relative motion with each other.
2. **Abrasive wear:** results in material removal on the surface which in the case of two-body abrasion, it is due to the asperities of the harder counterpart, while in third-body abrasion, it is due to loose particles entering the contact.
3. **Fatigue wear:** deriving from surface damage of the material with the strain-induced on the surface during repeat contact cycles.
4. **Tribochemical wear:** resulting in alteration of chemical composition and mechanical properties of the interface, following the tribochemical reactions. The material removal is governed by the kinetics of growth and removal of reaction layer.

Running-in [21] is the common procedure used in order to obtain an optimal shape and topography of the moving counterparts' surface. After the running-in, a steady state is achieved and a low wear rate is observed.

3.2.2. *Lubricants and Regimes of Lubrication: The Stribeck curve*

Lubricants are used to control and to minimise the wear and the friction in a mechanical system. When the lubricant, may be fluid or solid, is used in a tribological system, it is possible to observe different lubrication regimes: hydrodynamic, mixed and boundary regime. [13,22-23]

The plot of the coefficient of friction vs the fluid-film thickness is reported as Stribeck curve. This name is also used when plotting the coefficient of friction against the parameters that influence the lubricant film thickness as the dynamic viscosity of the fluid (Pa*s), the applied load (N/m) and the speed (m/s) of the two counterparts. This is a convenient representation of the lubrication regimes (Figure 6).

Referring to figure 6 the various regimes can be identified:

- **Boundary lubrication regime:** It occurs at the lowest speeds and when the applied load is high. In this situation the lubricant is squeezed out of the contact area and the normal load is carried out by the asperities present in the contact area (Sketch 1a in Figure 6).
- **Mixed lubrication regime:** this regime is characterized by the presence of the lubricant but the film is thin and even if the solid surfaces are better separated by the fluid compared to the boundary regime, it does not avoid the contact among the asperities of the tribo-surfaces as it is schematized in sketch 1b of Figure 6. In this regime elastic deformation may occur. It is the transition region between the hydrodynamic/elastohydrodynamic and boundary lubrication regimes.
- **Hydrodynamic (HD) lubrication regime:** Also called full fluid-film or thick-film lubrication. It occurs when at high speed the hydrodynamic pressure increases and the liquid entirely separates the two conformal counterparts' surfaces as it is depicted in the sketch 1c of Figure 6. The hydrodynamic lubrication is also defined as the ideal lubricated contact condition: no solid contact occurs because of the thickness of the lubricating films usually greater than the height of the asperities on the bearing surface. The coefficient of friction is low and depends on the shear forces in the viscous lubricant.
- The transition from HD to mixed lubrication can be predicted by using the λ ratio defined as:

$$\lambda = \frac{h_0}{\sqrt{\sigma_A^2 + \sigma_B^2}} \quad \text{eq.15}$$

Where h_0 is the minimum film thickness, σ_A and σ_B are the roughness of the surface of the two bodies A and B.

When the ratio is close to 1, the transition is expected.

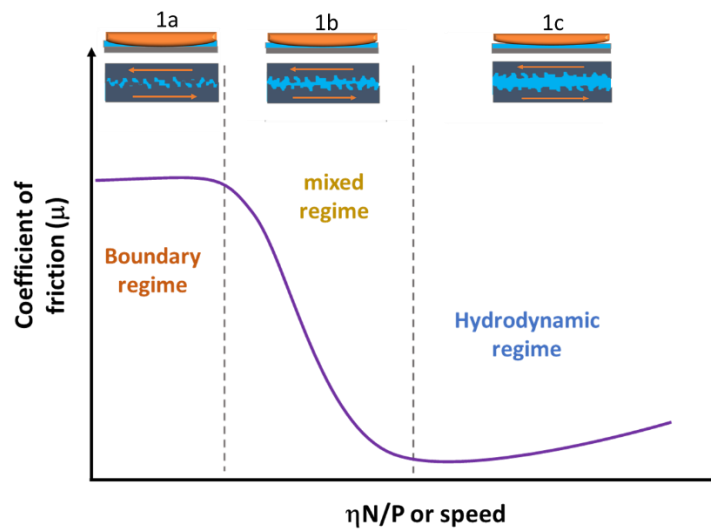


Figure 6: example of Stribeck curve, In the upper part of the figure three situations are depicted: 1a, boundary regime, 1b mixed regime, 1c hydrodynamic regime. [13,23]

From the hydrodynamic theory derives another lubrication regime: the **Elastohydrodynamic lubrication (EHL)**. [22] It occurs in the case of bearings and gear, with non-conformal lubricated surfaces. This regime considers the elastic deformation of the bodies and the increase in viscosity of the liquid with the raise in pressure at the inlet. A schematic representation of the EHL is reported in Figure 7. The pressure initially rises slowly and reaches a maximum value in the contact area. In correspondence of the spike, the minimum value of the thickness of the film (h_0) is reached. Consequently, high pressures can occur during contact, which can increase the viscosity of the lubricant.

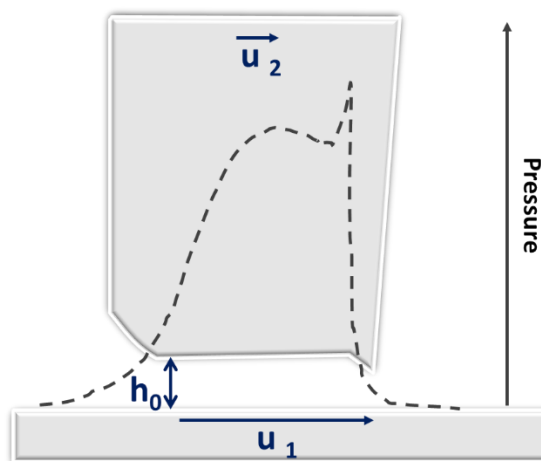


Figure 7: Scheme of elastohydrodynamic lubrication and pressure profile, adapted from [22].

3.2.3. Lubricants and Lubricant Additives

The traditional lubricants are based on mineral oils. Their wide use is mainly related to their relatively high abundance, as they are obtained directly from crude oil. [23] To improve their performance, the antiwear additives, as the zinc dialkyldithiophosphate (ZDDP), or extreme pressure additives, as molybdenum disulfide, [24] are usually added to the oil formulations. Another class is that of the organic friction modifiers that are also known as boundary additives used for reducing friction. To this class belong fatty acids, as the oleic acid. For examples, oleic acid is reported [25 and 25bis] achieving superlubrication in boundary lubrication regime (CoF lower than 0.01) in the case of diamond-like coated (DLC) - bearing steel pairs.

The increase of the demand of lubricants with specific applications has led to the development of a new large lubricants liquid class: the ionic liquids. These compounds have been proposed as lubricants, due to their physical and chemical properties that are interesting in lubrication because of their melting point lower than 100°C, their low flammability and low volatility. [26]

Ionic liquids

Room temperature ionic liquids (RTILs) are usually composed of an organic cation and a coordinating anion. Based on this combination, it can obtain a lubricant suited for specific purposes. They can also be used as pure lubricants or as lubricant additives in the mineral oils. [23]

Several examples of their use and combination are reported in the literature: 1-ethyl-3-methylimidazolium tris(perfluoroethyl)trifluorophosphate ([EMIM] FAP), 1-ethyl-3-methylimidazolium bis(trifluoromethylsulfonyl)imide ([EMIM] TFSI) and 1-hexyl-3-methylimidazolium bis(trifluoromethylsulfonyl)imide ([HMIM] TFSI) were used for the silicon-based samples lubrication. [27]. The authors reported that both the aliphatic chain length bonded to the imidazolium unit and the type of anion affect the onset of film failure. This was interpreted as the ability of the interfacial IL layer to prevent contact between the sliding surfaces. In fact, the onset of film failure, in EHL regime, with [EMIM] FAP is appreciably higher than the value observed with the TFSI salt having the same cation, indicating that the robustness of the interfacial layer is affected by the aliphatic chain and the type of anion. The 1-hexyl-3-methylimidazolium ethylsulfate ([HMIM] EtSO₄) was used in the lubrication studies of mica tribopair [28]. The authors reported how the water content significantly influences the lubrication mechanism, by changing the chemical and physical

properties of the IL. The significant water absorption of the ([EMIM]EtSO₄) was also studied by Espinosa et al. [29]

In this work, the effect of the water content on the lubrication mechanism for Si₃N₄ tribopair in the presence of [EMIM]EtSO₄ will be considered together with the effect of the oleic acid [EMIM oleate] as lubricant additive in the lubrication of Si₃N₄ tribopairs. [Chapter 6] The literature on the lubrication of Si₃N₄ in the presence of IL and IL + additives is scarce. The most common traditional lubricants, ILs and additives are reported in Table 1.

Table 1: Most common lubricants and additives [23-29]

Lubricants	Additives
<ul style="list-style-type: none"> Minerals oils (divided into chemical forms: paraffin, naphthene, aromatic, sulphur content and viscosity) Synthetic lubricants: (hydrocarbon-based, as esters, polyglycols, or silicones, or organohalogens, as perfluoro-polyethers) 	<ul style="list-style-type: none"> Absorption or boundary additives: Fatty acids, ammine and esters of fatty acids. Antiwear additives: zinc dithiophosphate, zinc dialkyl dithio phosphate and Tricresyl phosphate. Extreme-pressure additives: Polysulfides, molybdenum disulfide, chlorinated hydrocarbons, Polymer esters, chlorinated paraffins, etc. RT-ILs
<ul style="list-style-type: none"> ILs: as [EMIM] FAP, [HEMIM] FAP, ([EMIM] TFSI), [EMIM]EtSO₄, [HMIM]EtSO₄ [26-29] 	

3.2.4. Tribological test: Pin on disk tribometer [13]

Tribological tests provides information on the friction mechanisms of a specific tribosystem. The tribological tests are performed to simulates the real working conditions by an instrument, called tribometer. it is essential to plan a test with the best configuration to simulate a real application. The first important step is to assess the geometry of the contact, i.e. the shape of the counterparts and whether the contact is conformal or nonconformal. Among the various contact configurations for model tests assessing sliding wear, the most commonly used tribotest is the pin-on-disk, due to its versatility. In this work the UMT-2 tribometer (Bruker Nano Inc., Campbell, CA, USA) operating in pin-on-disk mode was used. A scheme of the instrument is shown in figure 8.

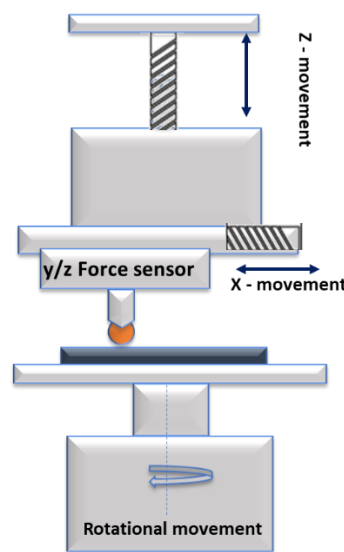


Figure 8: Scheme of the UMT-2 tribometer in a pin-on-disk configuration, adapted from [13].

In the upper side of the tribometer, the Z and X carriage and stages are present. The Z carriage allows the movement in the vertical direction, the X stage is connected to the vertical stage and the carriage allows the horizontal movement of the force sensor. The Y/Z sensor is a load cell, in this case with a maximum capacity of 20 N and a resolution of 0.001 N in both directions. The calibration of the load cell is performed using a standard weight. For the rotary movement, a rotary motor with a rotational speed from 0.1 to 3000 rpm was used. The pin holder is connected to the load cell and it is used to mount the sphere, while the disk holder is connected to the rotary drive. The disk is clamped to the metallic ring, between the metallic ring and the sample, a ring of Teflon or PET is commonly interposed, in order to prevent the leakage of the lubricant. Aluminium foils are placed between the base of disk holder and the rotary drive so that surface sample is brought as close as possible to the plane normal to the rotation axes of the rotary drive.

3.4. X-ray photoelectron spectroscopy (XPS) [30-43]

3.4.1. Basic Principles

X-ray photoelectron spectroscopy (XPS) is a surface sensitive analytical technique used to analyse the chemical composition of the samples' surface. It is based on the photoelectric effect. Emission of photoelectrons can be observed from solids, liquids and gases. The most common application is from solid samples. [30-33]

The photoelectric effect: Provided that the electrons in an atom have quantized energies thus the emitted electrons have discrete kinetic energy values, which are characteristic for each atom. Following the absorption of an X-ray photon of adapt energy $h\nu$ an electron is ejected from an energy level. The kinetic energy (KE) distribution of the photoemitted electrons $N(KE)$ is experimentally measured by the spectrometer, and the spectrum consists of a series of discrete bands that correspond to the electronic structure of the atoms of the sample. The binding energy of the photoemitted electron (BE), which is defined by ISO 18115-1:2013 as the “*energy that shall be expended in removing an electron from a given electronic level to the Fermi level of a solid or to the vacuum level of a free atom or molecule*”, is a parameter that depends on the emitting atom to which the electron is bound, thus it allows the identification of the elements and also to recognise their chemical state. The kinetic energy (KE) and the binding energy (BE) are related by the Einstein relation:

$$BE = E_f - E_i = h\nu - KE - \phi_{spectr.}$$

Where $h\nu$ is the photon energy and $\phi_{spectr.}$ is the spectrometer work function, that is measured during the calibration of the spectrometer; $h\nu$ and $\phi_{spectr.}$ are known, KE is measured thus the BE of the photoelectron can be easily calculated. Note that the photoelectron binding energy is measured considering the sample Fermi level (not the vacuum level), which is the reason of the inclusion of $\phi_{spectr.}$

In the case of conductive sample, the sample is grounded, thus the Fermi level of the sample coincides with that of the spectrometer (Figure 9); the kinetic energy of the photoemitted electron referred to the sample Fermi level is equal to $KE_1 = h\nu - BE^F - \phi^s$, where ϕ^s is the sample work function and BE^F is the binding energy of the photoelectron referred to the Fermi level (Figure 9 – left). The kinetic energy of the electron reaching the detector, thus the kinetic energy measured by the

instrument, is $KE_2 = h\nu - BE^F - \phi^s - (\phi^{sp} - \phi^s)$, where ϕ^{sp} is the spectrometer work function that can be experimentally determined during calibration, as said above.

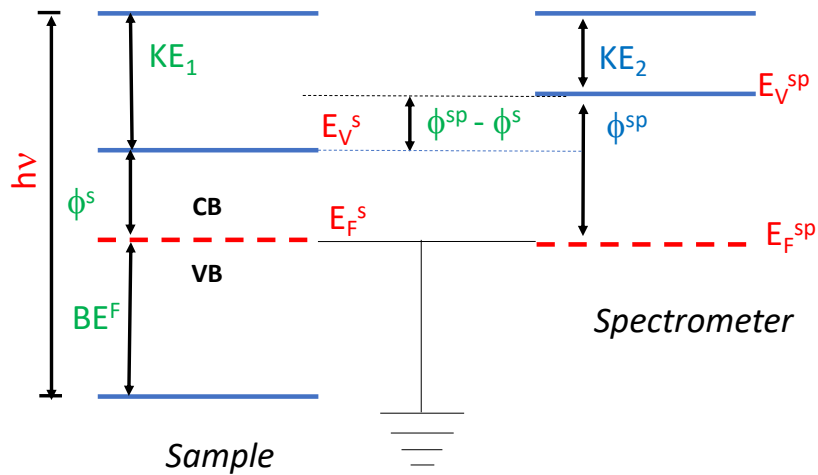


Figure 9: Diagram of the energy levels in conductive samples during an XPS experiment. $h\nu$: radiation energy; KE_1 : kinetic energy of the photoemitted electron; KE_2 : kinetic energy of the detected electron; VB: valence band; CB: conduction band; E_F^s : sample Fermi level; E_F^{sp} : spectrometer Fermi level; E_V^s : sample vacuum level; E_V^{sp} : spectrometer vacuum level; ϕ^s sample work function; ϕ^{sp} spectrometer work function. Adapted from [33].

For an insulating sample, no conduction mechanism exists and a compensation with a flood low-energy electrons is needed. Thus, in this case the measured kinetic energy is $KE = h\nu - BE^F - \phi^s + E_e$. Where E_e is the effective energy of the flooding electrons relative to the instrument Fermi level. [32]

The electron photoemission is schematized in Figure 10; this process is possible if the energy of the incident photon is greater than the BE of the electron.

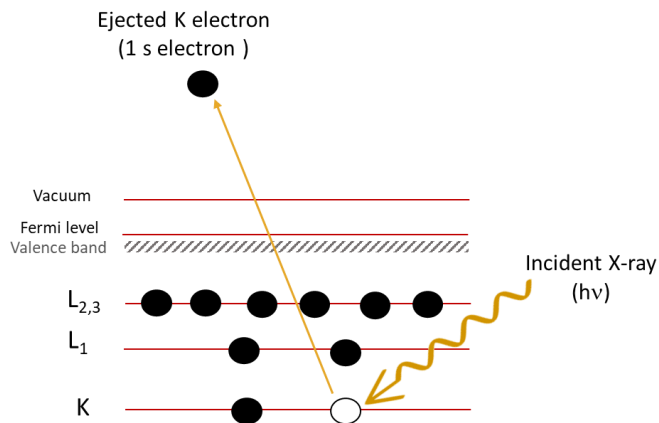


Figure 10: Scheme of the photoemission process. Adapted from [31].

Once an electron has been photoemitted, a vacancy is generated and this excited ionized state will relax by filling the hole with an electron from a higher energy level. The atom may relax following two competing mechanisms: by X-ray fluorescence emission or by the emission of an Auger secondary electron (Figure 11). The Auger emission is the dominant relaxation process for elements with low atomic number, with the increase of Z the X-ray fluorescence is the most probable relaxation process.

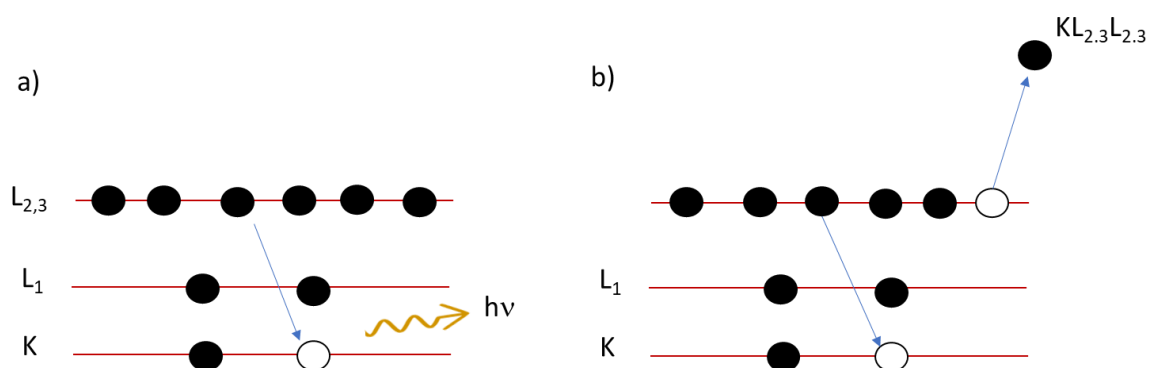


Figure 11: Schematic diagram of the relaxation mechanisms after the photoemission process: a) X-ray fluorescence, b) Auger secondary electron emission. Adapted from [31].

X-ray fluorescence does not contribute to XP spectra since a radiation of energy $h\nu'$ and no electrons are produced. In the case of the emission of a secondary electron (called Auger electron) the kinetic energy is equal to the difference of the energy levels involved in the relaxation process and these electrons will be detected and contribute with various signals to the spectrum. They are often used in XPS analysis. Unlike the photoelectrons, the kinetic energy of the Auger electrons is independent from the energy of the X-ray source since it only depends on the energy of the levels involved in the electron transfer. For this reason, while the BE values are typically given for photoelectron lines, the KE is usually provided for the Auger ones.

The photoionization cross section: the relative intensity of a peak in a XPS spectrum is basically determined by the cross-section σ , that depends on the atomic number, quantum numbers and on the proximity of the photon energy to the photoemission threshold [26]. Its value depends also on the X-rays source, however the cross-section values for the two common laboratory source, Al $\kappa\alpha$ and Mg $\kappa\alpha$, are similar. [30-32] The photoionization cross sections for elements with atomic number from 1 to 101 and for photon energies from 1 to 1500 keV were calculated by Scofield [34].

The sampling depth: The depth of analysis varies with the kinetic energy of the electrons and it is determined by the attenuation length (Λ) that is a quantity related to the inelastic mean free path (λ , IMFP) and it depends on material, on the kinetic energy of the emitted electron and on the take-off angle [31]. IMFP is defined as “the average distance an electron with a certain kinetic energy can travel before inelastically scattering” as reported in [31-32]. According to the definition provided in ISO 18115-1:2013, the take-off angle ϕ is “the angle between the trajectory of the photoemitted electron as it leaves a surface and the local or average surface plane”. Thus, $\Lambda = \lambda \sin \phi$.

The intensity of the photoelectron signal measured as function of the depth d can be described by the equation:

$$I = I_0 \exp\left(\frac{-d}{\lambda \sin \phi}\right) \quad \text{eq.16}$$

where I_0 is the peak intensity originated from depth d , ϕ is the take-off angle.

The sampling depth is estimated to be given by: $d = 3 \lambda \sin \phi$.

An empirical approach to calculate the IMFP calculation was proposed by Seah and Dench in 1979 [35]. According to their paper, λ (nm) can be calculated by using the equation:

$$\lambda = \frac{A}{KE^2} + B\sqrt{KE} \quad \text{eq. 17}$$

where A and B are empirically derived parameters depending on the type of material and KE is the kinetic energy (eV) of the emitted photoelectron (Table 2).

Table 2: A and B values for the eq.16.

	A	B
Element	143	0.054
Organic compounds	31	0.087
Inorganic compounds	641	0.096

95% of the information obtained by XPS is originated from within sampling depth ($3 \lambda \sin \phi$). Although the X-ray can penetrate deep into the solid, only photoelectrons deriving from about 10 nm can be detect without loss of energy. Electrons emitted from the bulk of the material lose their energy through inelastic collisions with other atoms. This is why XPS is a surface sensitive technique.

3.4.2. Spectral interpretation

The survey spectrum: The elemental characterization of the surface chemistry of a sample is possible acquiring a survey spectrum, recorded from 0 to 1400 eV. The spectrum consists of photoelectron and Auger signals and their height depends on the photoionisation cross section [34]. The elements are identified by comparing the experimentally obtained BE values with reference tables and electronic database. [36-37]

High-resolution spectra: the high-resolution spectra, also known as narrow-scan or detailed spectra, of each element of interest are acquired. The high-resolution spectra are processed by adapting the synthetic curves determined on reference standard elements and/or compounds to the spectra of the analysed sample (curve fitting) in order to obtain information on the chemical state of the elements present on the sample surfaces. Typically, the first step of the curve fitting procedure is the background subtraction, then a model from a set of Gaussian/Lorentzian line-shape is created. After the curve-fitting procedure, the chemical state can be assessed on the basis of the BE values of the different components.

Initial state effects and final state effects: The BE of an electron depends not only on the level from which the electron is ejected, but also on the oxidation state of the atom and its surroundings. The variation of the BE values generates a small shift of the peaks in the spectrum. This variation is so-called chemical shift and it can vary from a fraction up to several eVs. The chemical shift, ΔBE , could be also expressed considering the initial state effects (i.e. changes in the core potential due to the alteration of the local environment) and the final state effects (relaxation effect following the photoemission); according to the potential model [38] it can be described by the equation:

$$\Delta BE = \Delta V + \Delta\Phi - \Delta R \quad \text{eq. 18}$$

Where ΔV is the environmentally induced change in the ground state core potential, ΔR is the change in relaxation energy and $\Delta\Phi$ the change of reference potential.

The relaxation energy contributions depend both on the intra-atomic and extra-atomic relaxations. The significant component in the intra-atomic relaxation refers to the rearrangement of outer shell electrons, that have a smaller BE than the photoemitted electron, in fact, the contribution of the inner shell electrons rearrangement is negligible. The extra-atomic relaxation depends on the material analysed: in the case of conducting sample, such as metals, the core hole is screened by the valence band electrons that move from one atom to the next. For ionically bonded solids as the

alkali halides, the electrons can be polarized by the presence of the core hole, due to the fact that they are not free to move among the atoms. [33]

The Auger spectrum and the Auger parameter: In some cases, no chemical shift on XP lines of the same atom in different compounds is observed. The most well-known examples are those of copper and zinc. In fact, from their photoelectron signals it is not possible to distinguish between Cu (I) and Cu (0) and between Zn (0) and Zn (II). Only the Auger signals allow an unambiguous identification of the species. Combining the information obtained by the Auger and the XPS spectra, by using the chemical state plot, it is possible an unambiguous differentiation of the species. This analytical strategy is exploited in this work and the results are provided in Chapter 4.

The fine structure of the XP-spectra: Other chemical information can be obtained by analysing other spectrum features as the *spin – orbit coupling*, shake-up and shake-off satellites and the multiplet splitting. These features, if they are present, can give more details useful for the chemical investigation.

The *spin-orbit coupling* is responsible of the split of peaks originated from orbitals with angular momentum quantum number greater than zero. The peak splits into two components due to the interaction of the spin angular momentum ($s = \pm \frac{1}{2}$) and the orbital angular momentum (l). The two resulting states have a different total angular momentum. The relative intensity of the two peaks is dependent on their relative populations and their ratio is equal to the ratio of their multiplicity; the binding energy difference between the doublet components depends upon the spin-orbit coupling constant ξ_{nl} which depends on $1/r^3$ of the orbital involved, where r is the radius. [31] In this work examples are given by the S2p and the Si2p signals (chapter4 and chapter 6 respectively)

Shake-up and shake-off are due to electronic rearrangement effects after the photoemission process. Shake-up satellites are present when a valence electron is excited to a higher level by the energy relaxation of the core-hole level; shake-off satellites are originated when the photo-ionization is followed by the excitation of an electron to a free level state.

The XPS instrument [32] consists of an X-ray source, a sample stage, the lens system, an analyser, and a detector housed in an ultra-high vacuum environment. The most common X-ray sources employed in a XPS spectrometer are the Al $K\alpha$ (1486.6 eV) and the Mg $K\alpha$ (1253.6 eV). The analyser allows discriminating the ejected electrons on the basis of their KE and the number of emitted photoelectrons at a specific KE is counted by the detector. Two other essential accessories are the

electron flood gun, used for the charge compensation generated in the case of the insulating samples when using a monochromatic source, and the ion gun (usually Ar⁺ ion) used to remove contaminants from the surface of the samples, for example organic contamination layers, by sputtering or to perform the sputtering depth-profile analysis. A detailed description of the spectrometer and of the experimental set up used in this work is provided in the next chapters.

XPS provides not only qualitative information about the chemical composition of the surface, but it is also a quantitative technique (see paragraph 4.2.6). Moreover, it is possible to obtain information about the thickness of the layer by XPS, and for these reasons it is a very useful technique for the investigation of thin films. Different methods exist to estimate both the thickness and the composition of thin films: angle resolved analysis (ARXPS), depth profiling and the three-layers model.

Angle resolved XPS, [31,32] also known as angle-dependent XPS, or ADXPS, is a method that allows the determination of the thickness of thin films and recognizing the in-depth homogeneity or non-homogeneity of the uppermost layers of the samples. ARXPS has several advantages, the two most valuable are:

- It is a non-destructive analysis; indeed, the rate of damage is usually sufficiently slow to allow obtaining the chemical state information of the outermost part of the surface more easily than depth profiling methods that involves sputtering.
- Good absolute depth resolution.

A disadvantage is that the analysed layers cannot be deeper than two or three times the attenuation length (52ca. 4-6 nm) since a signal from the substrate is required to estimate the film thickness; for thicker layers the substrate peak is typically too small to be accurately measured. The intensity of the photoelectron signal measured as function of the depth d can be describe by the equation:

$$I = I_0 \exp\left(\frac{-d}{\lambda \cos\theta}\right) \quad \text{eq.19}$$

where I_0 is the peak intensity originated from depth d , θ is the emission angle that, according to ISO:18115-1:2013 is "*the angle between the trajectory of the photoelectron as it leaves a surface and the local or average surface normal*" and λ is the attenuation length. High-resolution spectra are used to measure the intensities of a photoelectron peak from the substrate with the one from the same element in the overlayer (e.g. oxide and elements from a thin oxide layer on a metal).

Thus, considering a thin layer, with a thickness d , of a material A on a substrate B and integrating the eq. 18 between 0 and d , the equation becomes:

$$I_A = I_A^\infty [1 - \exp(\frac{-d}{\lambda_{A,A} \cos \theta})] \quad \text{eq. 19}$$

Where, I_A is the measured intensity of the photoelectron signal from element A in specific chemical state and from a specific transition.

I_A^∞ is the intensity of the photoelectron signal from an element A in a specific chemical state and from a specific transition from a thick layer of material A, and $\lambda_{A,A}$ is the attenuation length for a photoelectron emitted in layer A for electrons emitted from A. θ is the emission angle.

The signal from B arriving at the B-A interface is I_B^∞ , assuming that the layer B is thick in comparison with $\lambda_{B,B}$. This signal is then attenuated by passing through the layer A:

$$I_B = I_B^\infty \exp(\frac{-d}{\lambda_{B,A} \cos \theta}) \quad \text{eq. 20}$$

Where $\lambda_{B,A}$ is the attenuation length of the electrons emitted from B and passing in the layer A. θ is the emission angle.

The intensity ratio R of these signals has to be considered:

$$\frac{I_A}{I_B} = R = R^\infty \frac{[1 - \exp(\frac{-d}{\lambda_{A,A} \cos \theta})]}{\exp(\frac{-d}{\lambda_{B,A} \cos \theta})} \quad \text{eq. 21}$$

Where $R^\infty = \frac{I_A^\infty}{I_B^\infty}$; R could be calculated taking into account the atom number density (atom per unit volume) and the attenuation length in the two materials. The atom number density σ is given by ratio of the density, D, of the material and the formula weight, F. For example, for the system ZnO/Zn, R^∞ will be:

$$R^\infty = \sigma_{Zn,ZnO} \lambda_{Zn,ZnO} / \sigma_{Zn,Zn} \lambda_{Zn,Zn} = (D_{ZnO} F_{Zn} / D_{Zn} F_{ZnO}) (\lambda_{Zn,ZnO} / \lambda_{Zn,Zn}).$$

Assuming that $\lambda_{A,A} = \lambda_{B,A} = \lambda_A$, eq. 21 can be rearranged and taking the natural logarithm, it is possible to calculate the equivalent thickness of an overlayer d by the Hill equation [25,26]:

$$d = \lambda \cos \theta \ln \left(1 + \frac{R}{R^\infty} \right)$$

This approach could be applied to the data recorded at one angle assuming the attenuation of the substrate from a discrete overlayer. A more rigorous approach to obtain the thickness of an overlayer is to carry out an ARXPS measurement at different emission angles and to plot $\ln \left(1 + \frac{R}{R^\infty} \right)$ vs $1/\cos \theta$: a straight line is obtained and its slope is equal to d/λ_A (Figure 12).

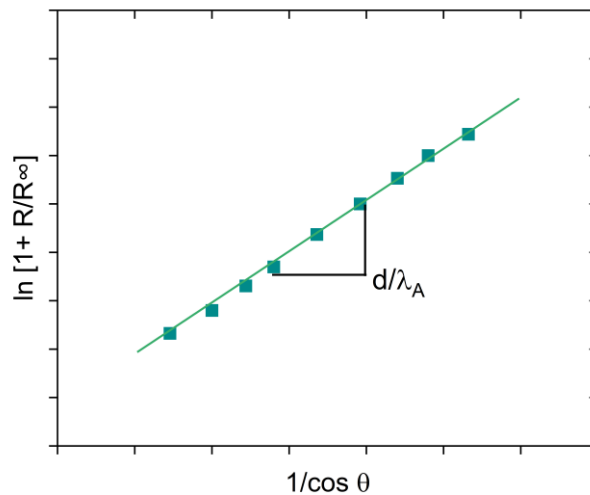


Figure 12: Example of a graph $\ln\left(1 + \frac{R}{R^\infty}\right)$ vs $1/\cos\theta$. Adapted from [30].

It is important to stress that the methods here presented for the thickness estimation by ARXPS can be applied only if $\lambda_{A,A} = \lambda_{B,A} = \lambda_A$ assumption holds, thus if the difference in the binding energy of the signals from the substrate and from the film is negligible.

Furthermore, from ARXPS data, the surface composition vs emission angle is obtained. In the case of multi-layered systems, if the thickness of the layers has to be estimated, the reconstruction of the depth profiles from ARXPS data can be obtained by the maximum entropy method (MEM). [39-41]

Elastic scattering affects ARXPS measurements: at larger emission angles more intensity from the substrate than expected is observed (often greater than 50 %), this effect can be avoided by using emission angle no greater than $\theta = 63^\circ$. [42] At small emission angles, close to the surface normal, less intensity from substrate is observed than expected. This is a smaller effect, typically 5-10 % depending on the material and it is minimised at around $\theta = 45^\circ$.

The lower limit in terms of the estimation of the thickness is about 0.2 nm.

I. Depth profiling

Non-destructive methods such as ARXPS are limited to an assessment of the chemical profile within depths of less than about 10 nm. To obtain the in-depth information for thicker layers, destructive methods using ion bombardment, i.e. sputtering, are required. Sputtering describes a process where primary ions are accelerated onto a sample resulting in an etching of the sample surface.

Typically, a positively charged argon ion at energies between 0.5 and 10 keV is used and focused into a beam of 2 – 5 μm , with a current density between 5 and 50 μA . This primary ion collides with the surface and lose energy through interactions with atoms and electrons of the target material. The XP spectra are recorded in the standard mode before the sputtering and after each sputtering cycle.

The data obtained can be plot in a graph of atomic percentage of elements as function of sputtering time (s). If the sputtering rate is known, it is possible to obtain the thickness of the layer. For the determination of the sputtering rate, a sample with a known thickness is used as reference. The typical sample for this determination is a Ta_2O_5 on Ta (0) sample. When the interface between the oxide film and the substrate is reached, the sputtering rate can be calculated considering the sputtering time and the film thickness. In this work the Au/Si (20 nm) and SiO_2 /Si (1.45 nm) are used as references. More details are reported in Chapter 4 and Appendix A.

The main disadvantage of the sputtering depth-profile analysis is that during the sputtering process, many artefacts can affect the chemical composition and the thickness determination; these artefacts can derive from the nature of the sample itself, as electrical conductivity, roughness, phase distribution, crystalline structure, and others are radiation – induced (e.g., atomic mixing, preferential sputtering, compound reduction, sputter – induced topography). [43-44]

II. Three-layer model [45]

For the quantitative analysis of nanometer-thick surface films and the film/substrate interface, the three-layer model can be applied. This model assumes the absence of concentration gradients and the lateral homogeneity of each layer. The photo-emitted electrons deriving from the bulk are exponentially attenuated by the oxide and the contamination layer, while the electrons emitted in the oxide layer are attenuated by the contamination layer. By the following equations, according to these assumptions, it is possible to determine the thickness and chemical composition of the layers:

$$I_i^{ox} = \left[\frac{(g_i \sigma_i^{ox} C_i^{ox} \rho_i^{ox} \Lambda_i^{ox})}{A_i} \right] \cdot \left[1 - \exp\left(-t/\Lambda_i^{ox}\right) \right] \cdot \exp^{-l_c/\Lambda_i^{con}} \quad \text{eq. A}$$

$$I_j^m = \left[\frac{(g_j \sigma_j^m C_j^m \rho_j^m \Lambda_j^m)}{A_j} \right] \cdot \left[1 - \exp\left(-t/\Lambda_j^{ox}\right) \right] \cdot \exp^{-l_c/\Lambda_i^{con}} \quad \text{eq. B}$$

Where A is the atomic weight, g is the transmission function of the spectrometer, t is film thickness, l_c is the thickness of the contamination layer and ρ is the density (g/cm^3). Equations A and B must be written for each element present in the system being analyzed. T and l_c can be calculated as follows:

$$f_1(t, l_c) = (\rho^m / \rho_{oc}) \sum_j I_j^m k_j^m \left[\exp\left(-t / \Lambda_j^{ox}\right) \right] \cdot \left[\exp^{-l_c / \Lambda_i^{con}} \right] - \sum_{ox}$$

$$f_2(t, l_c) = \left[l_c^{con} k_c \rho^{ox} / (1 - \exp(-l_c / \Lambda^{con})) \right] - \sum_{ox}$$

Where k are calculated as:

$$k_j^m = \left[\frac{(g_o \sigma_o \Lambda_o A_j)}{(g_j \sigma_j \Lambda_j^m A_o)} \right]$$

$$k_j^{ox} = \left[\frac{(g_o \sigma_o \Lambda_o A_j)}{(g_j \sigma_j \Lambda_j^{ox} A_o)} \right]$$

$$k_c = \left[\frac{(g_o \sigma_o \Lambda_o A_j)}{(g_c \sigma_c \Lambda_c^{ox} A_o)} \right]$$

$$\Sigma^{ox} = \sum I_j^{ox} k_j^{ox} \exp(-l_c / \Lambda^{con}) / (1 - \exp(-t / \Lambda_j^{ox}))$$

And O refers to oxygen.

The film and the interface compositions as well as the film thickness t and l_c are calculated simultaneously and the acquisition of the spectra at a single emission angle is required.

In chapter 4.2.6 and 5.2.5 data processing and quantitative analysis applied to the XPS experimental results obtained in this work will be detailed.

References

- [1] "Hilti_Corrosion-Handbook_W4412_it,
https://www.hilti.it/content/dam/documents/pdf/e4/engineering/manuals/Hilti_Corrosion-Handbook_W4412_it.pdf.
- [2] 1.1- Appendix- classification of corrosion processes, Corrosion, Metal/Environment reactions, Vol.1, Newnes-Butterworths, 1976.
- [3] B. Elsener, Corrosione dei metalli: introduzione. Laboratorio Corrosione e protezione dei metalli. 2015.
http://dipcia.unica.it/superf/Corrosione/Elsener_Cap2.pdf.
- [4] G.Bianchi, F.Mazza, Corrosione e protezione dei metalli, third ed. Masson,1989.
- [5] K. E. Heuslerl, D. Landolt, S. Trasatti, Electrochemical Corrosion Nomenclature, Pure & Appl. Chem., Vol. 61(1), 19, 1989.
- [6] F.Cocco, PhD Thesis, Sustainability in cultural heritage: from diagnosis to the development of innovative systems for monitoring and understanding corrosion inside ancient brass wind instruments, University of Cagliari,2013.
- [7] L. Lazzari, Aspetti generali della Corrosione, Enciclopedia degli idrocarburi, Vol V, pag.486.
http://www.treccani.it/export/sites/default/Portale/sito/altre_aree/Tecnologia_e_Scienze_applicate/enciclopedia/italiano_vol_5/485_506__x9_1_Aspetti_x_ita.pdf
- [8] Application note corr-1, Basics of Corrosion Measurements, Princeton Applied Research.
https://www.ameteksi.com/-/media/ameteksi/download_links/documentations/library/princetonappliedresearch/application_note_corr-1.pdf?la=en.
- [9] M. Stern and A.L. Geary, Electrochemical Polarization, Journal of the Electrochemical Society, 104 (1957) p.56
- [10] Application Note CORR-4, Electrochemistry and Corrosion: Overview and Techniques, Princeton Applied Research.
https://www.ameteksi.com/-/media/ameteksi/download_links/documentations/library/princetonappliedresearch/application_note_corr-4.pdf?la=en.
- [11] G. Bianchi, T. Mussini, Elettrochimica, Tamburini Masson editori, 1976.
- [12] L.L. Shreir, Corrosion, Metal/environment reactions, Vol. 1, Newnes-Butterworths, 1976.
- [13] B. Bharat, Introduction to tribology – Second edition. 1949.
- [14] A. Arcifa, PhD thesis, On the Mechanism of Ionic-Liquid-Mediated Lubrication of Silicon-Based Materials: A Combined Tribological and Spectroscopic Investigation ETH Zuerich, 2016.
- [15] T.A. Stolarski, 2 – Basic principles of tribology, Tribology in Machine Design, Newnes, 13-63, 1990.
- [16] F.P. Bowden, D. Tabor, The friction and lubrication of solids. Oxford university press, Vol. 1., 2001.
- [17] D. Dowson, History of tribology. Second edition, Professional Engineering Publishing Limited, 1998.
- [18] M. Godet, Third bodies in tribology, Wear, 136 (1), 29-45, 1990.
- [19] D. Dowson, Tribology Series, 31, Elsevier, 1996.
- [20] H.C. Meng, K.C. Ludema, Wear models and predictive equations: their form and content, Wear, Volumes 181–183, Part 2, 443-457, 1995.
- [21] P. J. Blau, On the nature of running-in, Tribology International, Vol. 38, 1007-1012, 2005.
- [22] H. Spikes, Basics of EHL for practical application, Lubrication Science, 27(1), 45-67, 2015.
- [23] W. G. Stachowiak, A. W Batchelor, Engineering Tribology, Butterworth-Heinemann, 2013.
- [24] A. M. Barnes, K. D. Bartle, V.R.A Thibon, A review of zinc dialkyldithiophosphates (ZDDPS): characterisation and role in the lubricating oil, Tribology International, Volume 34, 6,389-395, 2001.
- [25] M. Kano, J.M. Martin, K. Yoshida, M. I. De Barros Bouchet, Super-low friction of ta-C coating in presence of oleic acid. Friction 2, 156–163, 2014; [25 bis] Y. Long, · J. Michel Martin · F. Dubreuil · M. De Barros Bouchet, Achieving Superlubricity of Ricinoleic Acid in the Steel/Si3N4 Contact Under Boundary Lubrication, Tribology Letters, 70: 109, 2022
- [26] C. Ye, W. Liu, Y. Chen, L. Yu, Room-temperature ionic liquids: a novel versatile lubricant, Chemical Communications, (21), -2245, 2001.
- [27] A. Arcifa, A. Rossi, N.D. Spencer, Adsorption and Tribochemical Factors Affecting the Lubrication of Silicon-Based Materials by (Fluorinated) Ionic Liquids. *Phys. Chem. C*, 121, 13, 7259–7275, 2017.

- [28] L. A. Jurado, H. Kim, A. Rossi, A. Arcifa, J. K. Schuh N. D. Spencer, C. Leal R. H. Ewoldt , R M. Espinosa-Marzal, Effect of the environmental humidity on the bulk, interfacial and nanoconfined properties of an ionic liquid, *Phys. Chem. Chem. Phys.*, 18, 22719-22730, 2016.
- [29] R. M. Espinosa-Marzal, A. Arcifa, A. Rossi, N. D. Spencer, Ionic Liquids Confined in Hydrophilic Nanocontacts: Structure and Lubricity in the Presence of Water, , *The Journal of Physical Chemistry C*, 118 (12), 6491-6503, 2014.
- [30] J.F.Watts, J. Wolstenholme, *An Introduction to Surface Analysis by XP Sans AES* ed. Wiley, 2003.
- [31] D.Briggs, J.T. Grant, *Surface Analysis by Auger and X-ray Spectroscopy* ed. IMPublications, 2003.
- [32] F. A. Stevie, C. L. Donley, *Introduction to x-ray photoelectron Spectroscopy*, *J. Vac. Sci. Technol. A* 38, 063204, 2020.
- [33] J. C. Vickerman, *Surface Analysis – The Principal Techniques*, Wiley (43-92) 1997
- [34] J.H. Scofield, *Journal of Electron Spectroscopy and Related Phenomena*, 8 (1976) 129 – 137.
- [35] M. P. Seah and W. A. Dench, *Surface and Interface Analysis* (1979) 1: 2–11.
- [36] J. F. Moulder, W. F. Stickle, P. E. Sobol, K. D. Bomben *Handbook of X Ray Photoelectron Spectroscopy: A Reference Book of Standard Spectra for Identification and Interpretation of XPS Data*, Physical Electronics, 1979.
- [37] NIST Standard Reference Database 20, Version 4.1, Last Update to Data Content: 2012, DOI: <http://dx.doi.org/10.18434/T4T88K>.
- [38] R.J Cole, J.A.D Matthew, P Weightman, Extra-atomic relaxation energy calculations using an extended potential model, *Journal of Electron Spectroscopy and Related Phenom.*, 72, 255-259,1995.
- [39] M. Olla, G. Navarra, B. Elsener, A. Rossi, Nondestructive in-depth composition profile of oxy-hydroxide nanolayers on iron surfaces from ARXPS measurement. *Surface and Interface Analysis: An International Journal devoted to the development and application of techniques for the analysis of surfaces, interfaces and thin films*, 38(5), 964-974, 2006.
- [40] M. A. Scorciapino, G. Navarra, B. Elsener, A. Rossi, Nondestructive Surface Depth Profiles from Angle-Resolved X-ray Photoelectron Spectroscopy Data Using the Maximum Entropy Method. I. A New Protocol, *The Journal of Physical Chemistry C*, 113 (51), 21328-21337, 2009.
- [41] M. A. Scorciapino, M. Fantauzzi, M. Crobu, G. Navarra, B. Elsener, and A. Rossi, *ACS Omega*, 2 (11), 7790-7802, 2017.
- [42] P.J. Cumpson, M.P. and Seah, *Elastic Scattering Corrections in AES and XPS. II. Estimating Attenuation Lengths and Conditions Required for their Valid Use in Overlay/Substrate Experiments. Surf. Interface Anal.*, Vol.25, p. 430, 1997.
- [43] S. Hofmann, G. Zhou, J. Kovac, S. Drev, S.Y. Lian, B. Lin, Y. Liu, J.Y. Wang, Preferential sputtering effects in depth profiling of multilayers with SIMS, XPS and AES, *Appl. Surface Science*, 483, 140-155, 2019.
- [44] G. Greczynski, L. Hultman, Towards reliable X-ray photoelectron spectroscopy: Sputter-damage effects in transition metal borides, carbides, nitrides, and oxides, *Appl. Surface Science*, 542, 148599, 2021.
- [45] A. Rossi, B. Elsener, XPS analysis of passive films on the amorphous alloy Fe70Cr10P13C7: effect of the applied potential. *Surface and interface analysis*, 18(7), 499-504, 1992."

Chapter 4. Thin Films on CuZn37

In this chapter the results obtained on the growth and characterization of thin films at the surface of the CuZn37 brass alloy in contact with three different formulations of artificial saliva are presented and discussed. In the first section it is provided a short introduction in order to present the state of the art and the scope of this work. Then the experimental details of electrochemical measurements and surface analysis are presented, and the results of the investigation are displayed and discussed.

Part of the results reported in this chapter have been published in [1-2].

4.1. Introduction

In recent studies on historical brass wind instruments from a collection hosted at the Burri museum (Bern, CH), a non-destructive electrochemical method was developed to provide information on the corrosion state inside the instruments. An electrochemical sensor to be used in-situ was developed [3]; this sensor was then applied to analyse both reference brass alloys [4] and historical brass wind instruments. [3]

The electrochemical sensor did not provide any information on the chemical composition of the patina inside the instruments, but the authors of those studies, combined the information obtained from electrochemical measurements on reference brass alloys in contact with artificial saliva solution, with XPS analyses of the surface of the alloys after the contact with the solution, in order to be able to develop a model that allows “*predicting*” the composition inside the instruments from non-destructive electrochemical measurements. [5-7]

Such studies were conducted using the formulation proposed by Tani and Zucchi [8] for artificial saliva. This formulation is one the most used artificial saliva solutions in electrochemical studies and it is mainly composed of inorganic salts (KSCN, NaHCO₃, KCl, NaH₂PO₄) with urea and small amounts of α -amilase as the only organic compounds. Despite its diffusion in corrosion studies, Tani Zucchi formulation does not contain any possible component that may act as a ligand for the metal ions present in the films formed at the surface of the alloys, that might potentially alter the corrosion behavior. In this study three different formulations for artificial saliva are considered for the corrosion studies of CuZn37 brass to evaluate the influence of the testing solutions on the composition and thickness of the film formed on brass and on its corrosion behavior. The three

different formulations here adopted will be called Darvell (D) [9], Carter-Brugirard (C-B) [10] and SALMO [11] in the following paragraphs. They are solutions of chlorides, thiocyanates, phosphates, carbonates, and urea, but in D uric acid, sodium citrate and lactic acids are also present. The results here obtained will be compared with previous studies that showed that the dissolution of the brass was under anodic control, that increasing the exposure time the corrosion rate decreased [5], and that the dissolution rate was controlled by the resistance of the protective film formed on the surface [7] that was mainly composed of CuSCN and $\text{Zn}_3(\text{PO}_4)_2$. [5]

4.2. Experimental

4.2.1. Materials and surface preparation

In this work brass alloy CuZn37 samples (Brütsch/Rüegger Werkzeuge AG, CH) were examined. The nominal composition of the brass was 63 wt% copper and 37 wt% zinc. The 'as received' samples (Figure 1) show various scratches, thus before the electrochemical measurements, they were mechanically polished (MP) with diamond paste to a 'mirror-like' finish following the steps reported in Table 1. This procedure removes the contamination and the oxide film naturally present at the surface of the samples and ensures that composition and roughness of the starting surface are similar among different samples before the exposure to the different formulations. An argon stream was used to dry the MP brass; the dried samples were then transferred to the fast entry chamber of the XPS spectrometer and analysed by XPS before the electrochemical tests.



Figure 1: picture of as received CuZn37 brass alloy sample.

Table 1: Mechanical polishing procedure

Step	Grinding		Polishing	
Surface	2400 SiC paper	4000 SiC paper	DP Dur cloth with 1 mm diamond paste	DP Dur cloth with ¼ mm diamond paste
Lubricant	Bi-distilled water	Ethanol	Ethanol	Ethanol
Time [min.]	5 - 10	5	5	5

4.2.2. Model solutions

The chemical composition of the saliva model solutions used in this work, Darvell (D), Carter-Brugirard (C-B) and SALMO [9-11] is reported in Table 2. These formulations were selected from those reported in the literature since they are similar to the previously adopted Tani-Zucchi [8] formulation as far as the thiocyanates, phosphates, chlorides and carbonates content, but they differ in the organic compounds content: C-B solution contains only urea, SALMO solution contains urea and glycine and D solution contains urea, trisodium citrate, uric acid and lactic acid. D and C-B are transparent and colourless solutions, while SALMO solution is turbid with suspended white particles. The solution pH is 6.81 (0.01), 7.26 (0.02) and 8.06 (0.01) for D, C-B and SALMO respectively. All reagents used were at least of ACS grade and double-distilled water with a specific conductivity of $1.1 \pm 0.1 \mu\text{S cm}^{-1}$ at 293.16 K was used to make up the solutions.

Table 2: Chemical composition (g / dm³) of saliva solutions. *Darvell solution was prepared by adding 10 cm³ of stock A, 20 cm³ of stock B and 10 cm³ of stock C in 1 dm³, following the procedure describe in literature [9]

D*	C-B	SALMO
Stock A (g / dm ³)	0.70 g / dm ³ NaCl	0.52 g / dm ³ NaCl
56 NaH ₂ PO ₄	1.20 g / dm ³ KCl	0.58 g / dm ³ KCl
150 NaCl	0.26 g / dm ³ KH ₂ PO ₄	0.23 g / dm ³ CaCl ₂
22 NH ₄ Cl	0.33 g / dm ³ KSCN	0.10 g / dm ³ MgCl ₂ · 6H ₂ O
2.2 Na ₃ C ₆ H ₅ O ₇ · 2 H ₂ O	0.19 g / dm ³ Na ₂ HPO ₄	0.19 g / dm ³ K ₂ SO ₄
7.0 lactic acid (C ₃ H ₆ O ₃)	1.50 g / dm ³ NaHCO ₃	0.11 mg / dm ³ NaF
Stock B (g / 2 dm ³)	0.13 g / dm ³ Urea	0.96 g / dm ³ NaHCO ₃
20.0 urea (CH ₄ N ₂ O)	(CH ₄ N ₂ O)	1.48 g / dm ³ K ₂ HPO ₄
1.5 Uric acid (C ₅ H ₄ N ₄ O ₃)		0.19 g / dm ³ NH ₄ Cl
0.4 NaOH		0.19 g / dm ³ KSCN
Stock C (g / dm ³)		0.03 g / dm ³ Glycine
60.0 NaHCO ₃		(C ₂ H ₅ NO ₂)
20.0 NaSCN		0.20 g / dm ³ urea (CH ₄ N ₂ O)

4.2.3. Optical microscopy (OM)

The morphology of brass surface was examined by optical microscopy. The optical micrographs were acquired by using an optical microscope Zeiss, Axiolab A (Carl Zeiss Jena GmbH). Digital images at various magnifications were taken by a camera connected to the optical microscope. The calibration was performed using a TEM grid with a hole size of about 56 μm as reference.

4.2.4. XRF analysis

The X-ray fluorescence spectroscopy (XRF) was exploited to obtain the bulk composition of the alloy by a hand-held standard-less- XRF spectrometer SPECTRO xSORT (Spectro Analytical Instruments GmbH, Kleve, Germany). The instrument is equipped with a miniaturized X-ray Rh-anode and in these measurements an acceleration voltage of 50 kV was applied. The analysis method used in this work was “precious metals”. The instrument calibration is carried out by the instrument, and it is based on the ICAL algorithm that determines the current detector resolution, calculates the spectrum-energy-correlation and furthermore the X-ray intensity. The experimentally determined composition calculated as mean value over three independent samples was: Cu = 64.5 (0.1) wt % and Zn = 35.5 (0.1) wt %.

4.2.5. Electrochemical tests

A plexiglass three-electrode cell [12-13], with a 0.785 cm² lateral porthole (\varnothing 1 cm), was used to perform the electrochemical tests. The MP samples were positioned and pushed against the o-ring sealing of the hole. 200 cm³ of the test solutions were used for each electrochemical measure. A potentiostat/galvanostat model VersaSTAT3 (Ametek Scientific Instruments Inc., USA) was employed, with a platinum counter electrode and a saturated calomel reference electrode ($E = + 0.241$ V vs. NHE). The reference electrode was placed into an intermediate vessel filled with a saturated KCl solution and inserted into a Haber-Luggin capillary filled with the test solution. This set-up was necessary in order to prevent the SCE from undergoing ion exchange with the saliva solutions. All potentials are referred to the saturated calomel electrode (SCE). The electrochemical tests were carried out at 25 ± 1 °C and the data are reported as mean value over at least three independent measurements; the standard deviation is given in parentheses. The scheme of the cell is shown in Figure 2 together with the picture of the potentiostat.

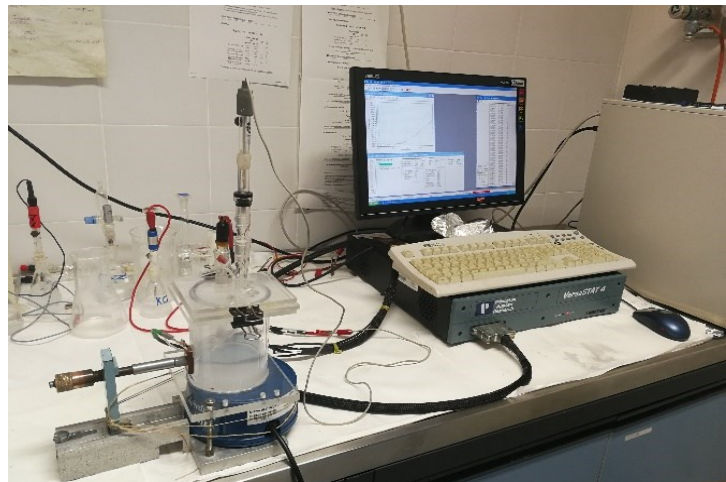
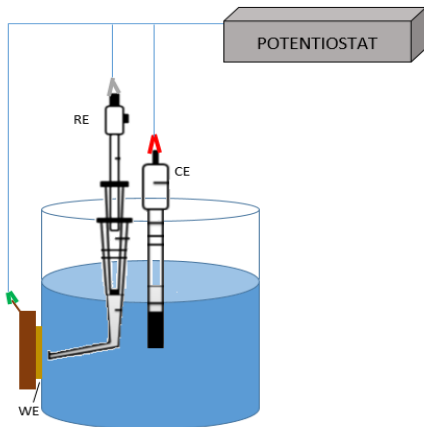


Figure 2: Scheme and picture of the cell.

Open Circuit Potential (OCP) and Linear Polarization resistance (LPR)

The open circuit potentials (OCP) of the brass samples were acquired open to air after 1 h, 3h and 16 h of contact with the three different artificial saliva solutions. At the end of OCP experiments, the linear polarization resistance (LPR) measurements were performed applying a potential of ± 20

mV vs OCP and with a scan rate equal to 0.2 mV s^{-1} . From these measurements it was possible to determine the polarization resistance values (R_p).

Cathodic and anodic polarization curves

Cathodic and anodic polarization curves were acquired with a scan rate of 0.2 mV s^{-1} , following the OCP measurements for 1 h of contact with the different formulations. For the cathodic potentiodynamic curves a potential of -250 mV vs OCP was applied and then the scan run to $+250 \text{ mV vs OCP}$ for the anodic potentiodynamic curves. The anodic (β_a) and cathodic (β_c) Tafel constants were extrapolated from the curves using Versa studio software [14].

4.2.6. XPS surface analysis

The surface composition was investigated by X-ray photoelectron spectroscopy (XPS) using a ThetaProbe spectrometer (ThermoFisher, East Grinstead UK) equipped with a monochromatic $\text{AlK}\alpha$ source ($h\nu = 1486.6 \text{ eV}$). The beam diameter used in this work was $400 \mu\text{m}$, operating at 6.7 mA and 15kV (100 W). Survey and high-resolution spectra were acquired with a step size of 1 eV and 0.05 eV respectively, in fixed analyser transmission mode (FAT). The pass energy was 200 eV for the acquisition of survey and 100 eV for the high-resolution (HR) spectra, in standard lens mode. In these conditions the full-width at half-maximum (fwhm) of the peak height for $\text{Ag } 3d_{5/2}$ was found to be $0.93 \pm 0.05 \text{ eV}$. The linearity of the binding energy scale was checked according to ISO 15472:2014 with an accuracy of $\pm 0.1 \text{ eV}$.

The instrument is equipped with an argon ion gun. For depth profile experiments an acceleration voltage of 1 kV and an ion current of 661 nA were used in this work. The sputtered area was $3 \times 3 \text{ mm}^2$. The sputtering rate was determined using a thin SiO_2 of $1.45 (0.07) \text{ nm}$ measured by ARXPS on a Si wafer and it was found to be 0.02 nm/seconds . The accuracy on the thickness value was calculated referring to a Au/Si sample of a thickness of 20 nm (determined by ellipsometry) and it was found to be $\pm 1.3 \%$, more details are reported in (Appendix A - Figure A.1). The value of thickness d , on the mechanically sample, was determined considering the seconds at the cross point of the curves of Zn (0) and O 1s and by knowing the etch rate. Moreover, high-resolution spectra were acquired in angle resolved lens mode at 16 emission angles, ranging from $24.88\text{--}83.13^\circ$, and a pass energy of 150 eV . The intensity vs angles response of the instrument was checked during the periodic calibration of the instrument by using a flat sputter-cleaned Ag [15].

Data were processed with CASA XPS software (v2.3.24, Casa Software Ltd., Wilmslow, Cheshire, UK). The Shirley-Sherwood background subtraction routine was applied before the curve fitting procedure [16]. The parameters Gaussian/Lorentzian ratio and width at half maximum of the signal of the model functions determined on spectra acquired on pure alloys and on analytical grade copper and zinc compounds, analysed under the same experimental conditions [6], were used for the curve fitting of the spectra of the analysed samples. The quantitative composition of the film was calculated on the basis of the first-principle method [17] assuming the sample homogeneity, thus, starting from the experimental areas (intensities) corrected for the sensitivity factors that take into account the Scofield ionization cross section [18], the asymmetry factor [18], the spectrometer transmission function [20] and the inelastic mean free path [21], (eq. 1-2).

$$X_A = \frac{\frac{I_A}{S_A}}{\sum_j \frac{I_j}{S_j}} \quad \text{eq. 1}$$

where I is the measured peak area in cps*eV and S is the sensitivity factor. The sensitivity factor is calculated for each element, using the following formula:

$$S = \sigma_{hv} \cdot L_A(\gamma) \cdot T(E_A) \cdot \Lambda_{MA} \quad \text{eq.2}$$

Where, σ_{hv} is the Scofield factor, $L_A(\gamma)$ is the asymmetry factor, $T(E_A)$ is the spectrometer transmission function and $\Lambda = \lambda \cos \theta$ is the attenuation length. λ is the inelastic mean free paths (IMFP) and the emission angle $\theta = 53^\circ$ for the Theta Probe when used in the standard lens mode.

Since Cu 2p and Zn 2p do not show chemical shift between Cu (0) and Cu (I) and between Zn (0) and ZnO, [6] it is not possible distinguishing the different chemical state of copper and zinc considering exclusively the binding energy of the photoelectron signals. The x-ray induced Auger signal (XAES) show clear shifts in kinetic energy (KE) and different shape for metals and oxide states [6]. Thus, in this work, the percentage of 2p areas of copper and zinc ascribed to oxidised species was calculated starting from the oxidised element/metal ratios (eq. 3) determined on the Auger signals, following the strategy developed in previous studies [6].

$$k = \frac{R_{ox}}{R_{met}} \quad \text{eq.3}$$

Where R_{ox} is the intensity ratio for the oxidized component and R_{met} is for metallic component calculated as (eq.4):

$$R = \frac{I_{2p}}{I_{LMM}} \quad \text{eq.4}$$

k is equal to 1.5 for copper and 0.8 for zinc.

4.3. Results

4.3.1. Morphology

The surface of the as received and mechanically polished samples was observed by an optical microscope. Some features such as several scratches are revealed on the as received alloy (Figure 3a), but following the mechanical polishing a less rough surface, with almost no detectable scars is obtained (Figure 3b), indicating a proper polishing of the samples for the subsequent XPS and electrochemical analyses.

The area of the CuZn37 surface after the contact with the saliva model solutions, using the electrochemical cell described in paragraph 3.2, was opaque and the presence of a film was clearly visible as it also appeared in the micrographs (Figures 1c-h). Crystallites are present on the CuZn37 samples exposed to the D solution: their size increase upon the exposure time (Figures 3c and 3d). The same effect was not observed on the samples exposed to C-B (Figures 3e and 3f) and SALMO (Figures 3g and 3h) formulations.

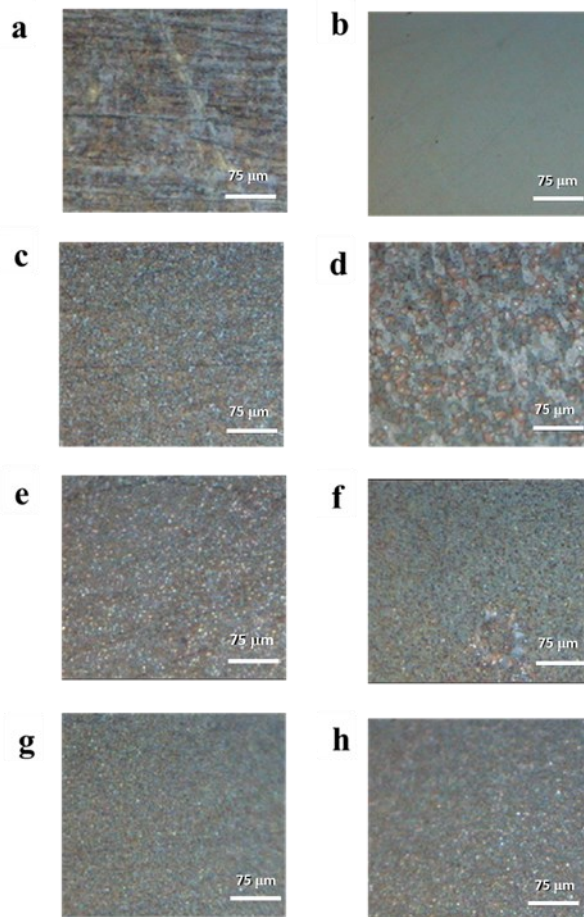


Figure 3: Optical micrographs of the brass surfaces - objective Epiplan 100 X / 0.75: a) CuZn37 as received; b) CuZn37 mechanically polished; c) CuZn37 after 1h in contact with D; d) CuZn37 after 16 h in contact with D; e) CuZn37 after 1h in contact with C-B; f) CuZn37 after 16h in contact with C-B; g) CuZn37 after 1h in contact with SALMO; h) CuZn37 after 16 h in contact with SALMO.

4.3.2. Electrochemical results

Open circuit potential (OCP)

The open circuit potential (OCP) of the mechanically polished CuZn37 alloy was measured for 1 h, 3 h and 16 h of exposure to the solutions in equilibrium with air and at ambient temperature ($25 \pm 1^\circ\text{C}$). The average values of the OCP at the various time are reported in Table 3.

Immediately after the contact of the CuZn37 samples to the model saliva solutions, the OCP decreased for few minutes (Figure 4a). This behaviour can be ascribed to the dissolution of the thin surface film developed during mechanical polishing procedure. After the initial decrease, in the case of the brass in contact with C-B and SALMO formulations the OCP significantly increased for about 4 h, then, after 7 hours a plateau is reached and the OCP stayed almost constant at -150 mV SCE

for C-B and at about -200 mV SCE for SALMO solutions up to 16 hours (Figure 4b and Table 3). The CuZn37 samples in contact with the D formulation show a decreasing of the OCP in the first hour, then it slowly increases reaching the value of -285 (18) mV SCE after 16 hours of exposure (Figure 4b, Table 3). The reason of this different behaviour will be clarified exploiting X-ray photoelectron spectroscopy (*vide infra*).

Table 3: OCP mean values (mV vs. SCE) of CuZn37 in contact with the artificial saliva solutions, recorded after t= 0 s (E₀), t = 1h (E_{1h}), t = 3 h (E_{3h}) and t = 16 h (E_{16h}). Standard deviations are given in parentheses. Adapted from [1]

Model solutions		Darvell	Carter-Brugirard	SALMO
OCP vs SCE (mV)	E ₀	-293 (11)	-301(13)	-309 (5)
	E _{1h}	-327 (1)	-311(1)	-282 (2)
	E _{3h}	-311 (8)	-303 (17)	-277 (19)
	E _{16h}	-285 (18)	-164 (6)	-190 (15)

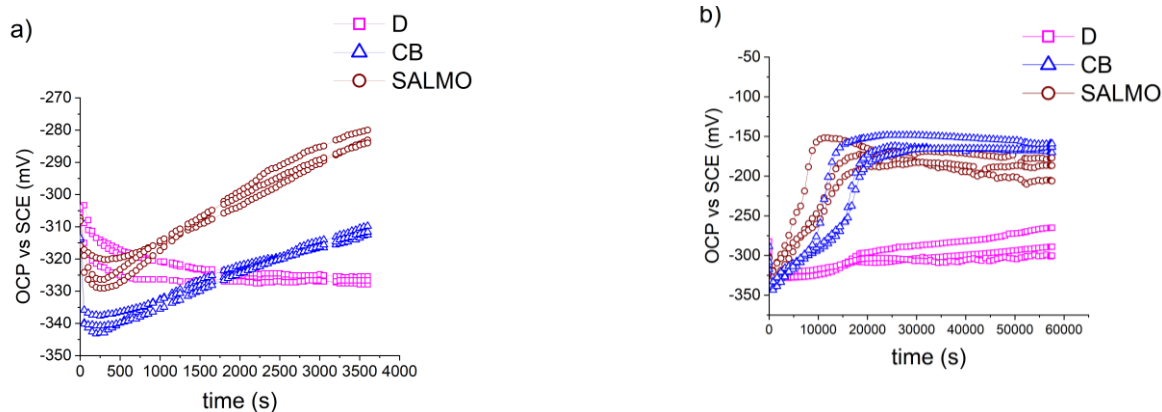


Figure 4: OCP vs time curves for CuZn37 in contact 1 h (a) and 16 h (b) to Darvell (D), Carter-Brugirard (C-B) and SALMO solutions. The results of three independent measurements are reported for each solution. Adapted from [1]

Potentiodynamic polarization curves (Tafel plot)

The polarization curves of CuZn37 samples exposed in all saliva model formulations examined (Figure 5) showed a cathodic branch, an active passive transition and an anodic region. The cathodic Tafel region showed β_c values of -195 (22) mV/dec for C-B, -207 (10) mV/dec for SALMO and -206 (14) for D respectively, thus quite similar. The anodic Tafel slopes (although not very pronounced) β_a were found to be equal to 60 mV/dec. These values allowed calculating the coefficient B, required to determine the corrosion current density from polarization resistance values (section 4.2.5.), according to eq. 1:

$$B = \frac{\beta_a \beta_c}{2.303(\beta_c + \beta_a)} \quad (1)$$

B values were found to be 20 (2) mV for the three artificial saliva solutions D, C-B and SALMO.

After the current maximum, an anodic plateau is observed; the current density for C-B and SALMO were in the range of 1.5 – 2.5 $\mu\text{A}/\text{cm}^2$ while the CuZn37 samples exposed to D solution showed a current density of 7 – 8 $\mu\text{A}/\text{cm}^2$ thus higher than in the other formulations.

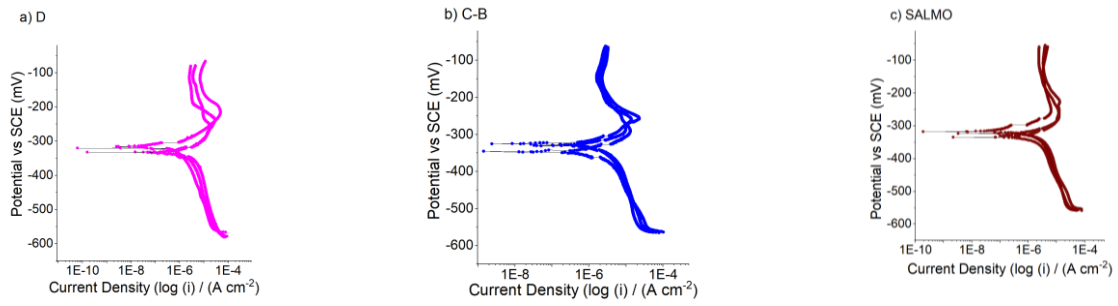


Figure 5: Potentiodynamic polarization curves of brass after 1 h of exposure to a) D, b) C-B and c) SALMO. The results of three independent measurements are reported for each solution. Adapted from [1]

Linear Polarization resistance (LPR) and corrosion rate

Following the OCP measurements, LPR measurements were carried out for each immersion time of 1 h, 3 h and 16 h. The linear polarization resistance measurements (Appendix A- Figure A.2) are curves characterized by a linear region at ± 20 mV around the OCP. The slope of the linear region provides the polarization resistance (R_p) values. In Table 4 the R_p values obtained for each immersion times and formulations are given. The R_p values increased upon the exposure time and, for each time, the values obtained with D solution were the lowest. The corrosion current density (i_{corr}) was calculated from the R_p measurements by equation proposed by Stern and Geary. [22] The constant B was experimentally calculated according to equation 1.

The average corrosion rates v_{corr} (Table 5) were calculated over three independent measurements for each immersion time by equation 8 in chapter 3 (Farady's law). The highest corrosion rate were observed the for the D solution and for each formulation it decreased upon immersion time.

Table 4: Polarization resistance (R_p) mean values at various immersion times for each model solution. Standard deviations are given in parentheses. Adapted from [1].

Model solutions	Darvell	Carter-Brugirard	SALMO
$R_{p_{1h}}$ [k Ω · cm ²]	4.8 (0.6)	8 (1)	16 (2)
$R_{p_{3h}}$ [k Ω · cm ²]	9 (4)	23 (10)	136 (54)
$R_{p_{16h}}$ [k Ω · cm ²]	89 (6)	256 (41)	338 (79)

Table 5: Corrosion rate (v_{corr}) mean values at various exposure times for each model solution. Standard deviations are given in parentheses. Adapted from [1].

Model solutions	Darvell	Carter-Brugirard	SALMO
$v_{corr_{1h}}$ [$\mu\text{m} / \text{year}$]	48 (11)	30 (8)	15 (2)
$v_{corr_{3h}}$ [$\mu\text{m} / \text{year}$]	27 (12)	10 (5)	1.8 (0.7)
$v_{corr_{16h}}$ [$\mu\text{m} / \text{year}$]	3.0 (0.3)	0.9 (0.2)	0.8 (0.2)

4.3.3. XPS results

CuZn37 mechanically polished

The XPS survey spectrum (Figure 6a) shows the presence of the Cu and Zn signals, that belong to the alloy, C and O due to the exposure of the brass surface to the ambient during the mechanical polishing procedure and the sample transfer to the spectrometer. The high-resolution spectra of copper and zinc show Cu $2p_{3/2}$ signal at 932.5 (0.1) eV and Zn $2p_{3/2}$ at 1021.7 (0.1) eV (Figure 6b and Figure 6c). As it is well known, that Cu 2p and Zn 2p signals do not show a chemical shift between Cu (0) and Cu (I), and Zn (0) and Zn(II) in ZnO at the energy resolution commonly available with laboratory XP-spectrometers. Nevertheless, the Auger electron signals [4-21] induced by the x-ray excitation of the material allows distinguishing them. The $\text{CuL}_3\text{M}_{4,5}\text{M}_{4,5}$ and $\text{ZnL}_3\text{M}_{4,5}\text{M}_{4,5}$ Auger signals have a quite complex shape since they consist of five and four components for Cu(0) and Cu (I) respectively, and of five components for both Zn (0) and ZnO. [6]; it is thus necessary to use a curve fitting procedure to separate the peaks in order to be able to determine the kinetic energy due to the various chemical states. In this work the approach proposed in [6] based on the parameters obtained by analysing reference materials was performed. In Figures 6b and 6c, the envelope of the components assigned to metallic copper and zinc are showed in blue while the envelope of the components assigned to Cu(I) and Zn (II) are showed in red. The energy values, FWHM and line shapes of both photoelectron and Auger peaks (GL ratio and tail function) are provided in Table 6. For both copper and zinc, the kinetic energy of the Auger peaks provided in Table 6 refers to the most intense ^1G component of the metal and oxides multiple peaks.[6]

The $\text{CuL}_{3\text{M}_{4,5}\text{M}_{4,5}}$ signal showed a major contribution of Cu (0) at 918.5 (0.1) eV (kinetic energy) and a weak component due to Cu (I) at 916.7 (0.1) eV (Figure 6d). The $\text{ZnL}_{3\text{M}_{4,5}\text{M}_{4,5}}$ signal (Figure 6e) showed the presence of two components ascribed to Zn (0) and to Zn (II) at 992.1 (0.1) eV and 987.9 (0.1) eV respectively [6-23-24] suggesting that a thin oxide layer mainly composed of ZnO is growth on the MP CuZn_{37} surface.

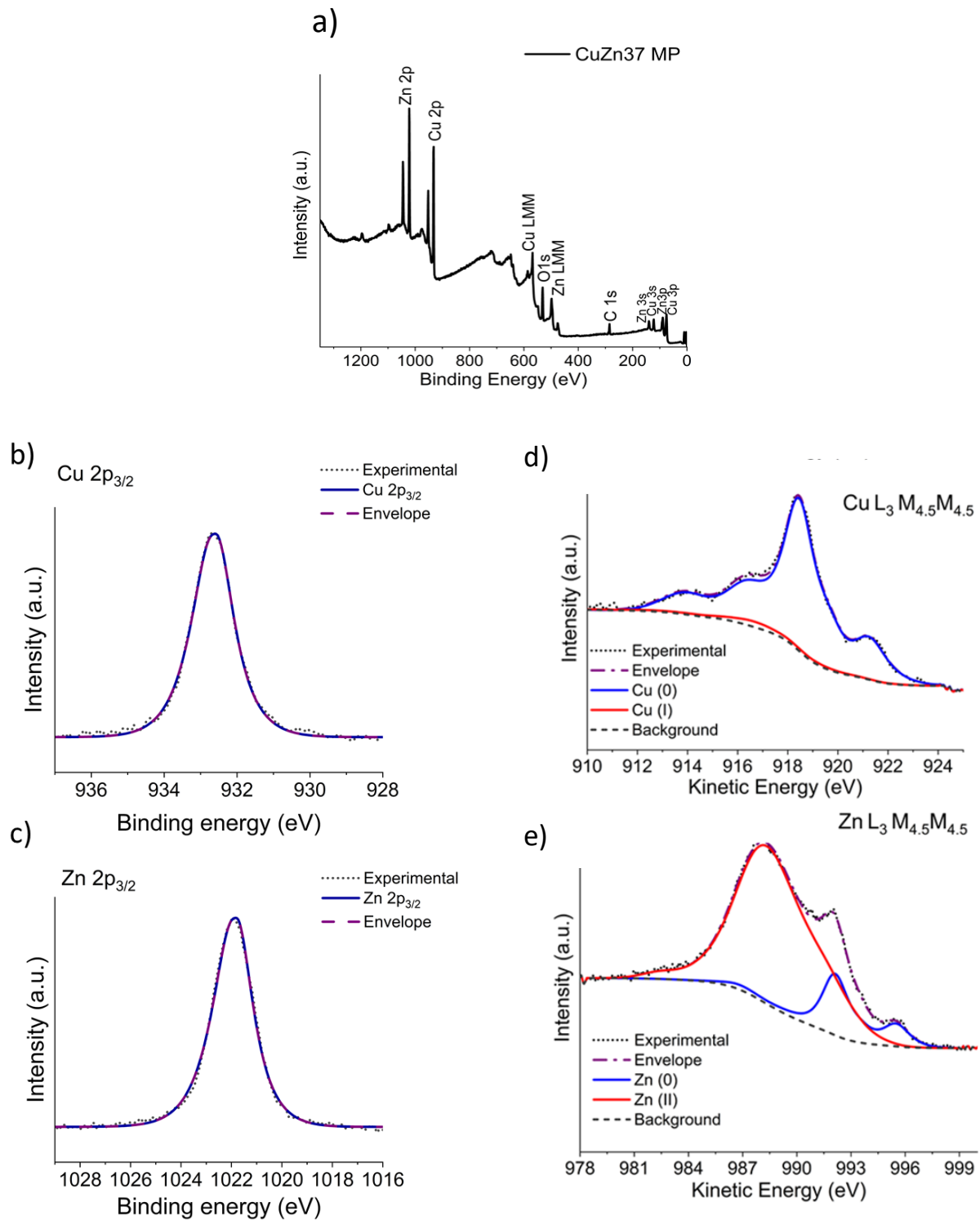


Figure 6: a) Survey spectrum of mechanically polished CuZn37. b) High-resolution spectra of Cu $2p_{3/2}$ of mechanically polished CuZn37 c) High-resolution spectra of Zn $2p_{3/2}$ of mechanically polished CuZn37 d) X-ray induced Auger spectra (XAES) of Cu $L_3 M_{4.5} M_{4.5}$ and e) of Zn $L_3 M_{4.5} M_{4.5}$ of mechanically polished CuZn37. Adapted from [2]

Table 6: Peak parameters for fitting the Cu 2p_{3/2}, Zn 2p_{3/2}, O 1s, Cu L₃M_{4,5}M_{4,5} and Zn L₃M_{4,5}M_{4,5} spectra of CuZn37 samples following mechanical polishing.

Brass CuZn37 alloy after mechanical polishing			
Peak	BE (eV ± 0.1)	FWHM (eV± 0.1)	Line shape
Cu 2p_{3/2}	932.5	1.4	GL (82)T(2.5)
Zn 2p_{3/2}	1021.7	1.7	GL (92)T(2)
O 1s	530.4	2.0	GL (45)
O 1s	532.0	2.0	GL (45)
O 1s	533.9	2.0	GL (45)
Signal	KE (eV ± 0.1)		
Cu L₃M_{4,5}M_{4,5} metal	918.5		
Cu L₃M_{4,5}M_{4,5} oxide	916.7		
Zn L₃M_{4,5}M_{4,5} metal	992.1		
Zn L₃M_{4,5}M_{4,5} oxide	987.9		

In order to determine the thickness of the film formed after mechanical polishing, both angle-resolved analyses and compositional depth profile by Argon ion etching were performed. The thickness of the layer is supposed to be in the nanometre range since the metallic component of copper and zinc were detected and the surfaces did not appear porous in the micrographs (Figure 3).

Since copper seems to be mostly present as Cu (0) and Zn is present both as Zn (0) and Zn (II), zinc is considered for thickness estimation by angle resolved XPS (ARXPS). The ARXPS results showed that the metallic zinc component was detectable even at high emission angles (Figure 7) substantiating the hypothesis of the presence of an oxide film less thick than the sampling depth in XPS analysis that is estimated to be about 2 nm for Zn (at 53° emission angle) (Appendix A -Figure A.3).

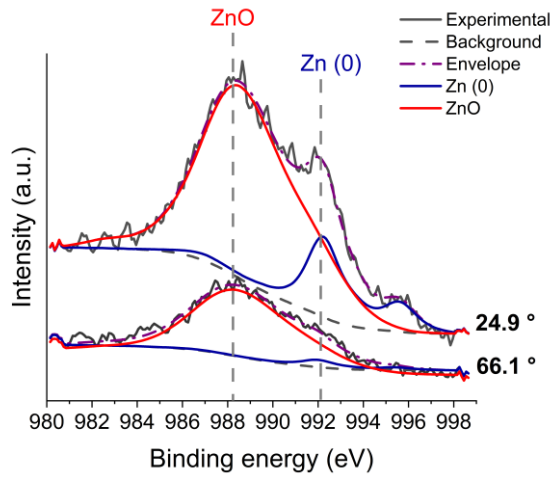


Figure 7: Zn $L_{3}M_{4,5}M_{4,5}$ XAES spectra acquired at two different emission angles 24.9° and 66.1° of a mechanically polished CuZn37 sample.

The spectra show the presence of two convoluted signals having the KE at 992.1 (0.1) eV and at 987.9 (0.1) eV assigned to Zn(0) and ZnO respectively.

The metal component decreases as the angle of emission increases, while the oxide component increases (Figure 8).

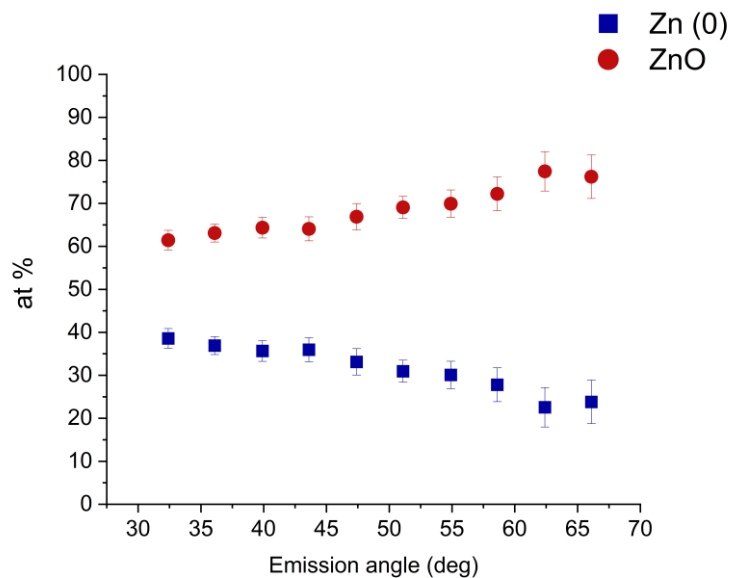


Figure 8: Angle resolved results acquired on mechanically polished CuZn37. Apparent concentrations in atomic percentage versus the emission angle are reported considering Zn(0) and ZnO. Mean and standard deviations were calculated over three independent measurements.

Different methods were used to determining the thickness, analysing the zinc spectra:

1. A more rigorous approach, recording a complete series of angle resolved data (16 angles were recorded, from 24.9° to 83.1°) and using the equation:

$$\ln [1+R/ R^\infty] = d/ (\lambda_{\text{ZnO}} \cos\theta) \quad \text{eq. 1}$$

where R is the ratio of intensities of metallic and oxide components experimentally determined and R^∞ is the ratio of the same intensities considering a thick sample (thickness > 100 nm) [17], d is the layer thickness considering the contamination layer.

The range between 24.9° and 66.1° was considered, because at higher emission angles the elastic scattering effects affect the spectra [17]. Thus, by plotting, for each angle, the left-hand side of this equation vs $(1/\cos\theta)$, it results in a straight line whose slope is equal to d/λ_{ZnO} , (where λ_{ZnO} is the attenuation length of the $\text{Zn}2p_{3/2}$ photoelectrons that move toward the surface through a ZnO layer calculated applying G1 equation [25] using the NIST Electron Inelastic-Mean-Free-Path Database [26]);

2. In the second method the intensities of the metallic zinc component I_m at two different emission angles, 24.9 ° (θ_1 = “bulk” angle) and 66.1 ° (θ_2 = surface angle) are considered by using the equation:

$$I_m(\theta_1)/I_m(\theta_2) = \exp [d \lambda_{\text{ox}} (1/\cos\theta_2 - 1/\cos\theta_1)] \quad \text{eq.2 [17, 27]}$$

being $\theta_{1,2}$ two emission angles, $I_m(\theta_1)$ and $I_m(\theta_2)$ are the intensities of the photoelectrons emitted by the metallic components (Zn(0) in Figure 6) at θ_1 and θ_2 , λ_{ox} is the inelastic mean free path of the zinc oxide and d is the total thickness of the overlayer equal to the sum of the contamination and the oxide layer thicknesses.

3. The equation (1) was also exploited to estimate the thickness considering only one angle (24.9°).
4. Compositional depth profile was obtained by bombarding the sample with Argon ions, the details are reported in section 4.2.6.

The values of the layer thickness and the respective standard deviations determined using the 1-3 methods are reported in table 7.

Table 7: Thickness values obtained by 1-3 methods. Standard deviations are reported in brackets.

Methods	Thickness (nm)
1 (ten emission angles from 24.9° to 66.1°)	1.3 (0.1)
2 (two different emission angles: 24.9° and 66.1°)	1.2 (0.4)
3 (one emission angle 24.9°)	1.4 (0.1)

The compositional depth profile is presented in Figure 9: the abscissa reports the sputtering time together with the estimated depth, the ordinate is the atomic fraction. The sputtering rate was determined using a SiO₂ layer on a silicon wafer and more details on the method followed here for determining the interface between the surface layer and the substrate alloy are provided in paragraph 4.2.6. After 20 seconds of ion-sputtering the C 1s signal is no more revealed, suggesting that this element belonged to the most outer layer also known as contamination layer; It is possible to estimate that the contamination layer is about 0.4 nm thick. The value of the thickness d is estimated to be about 1.6 nm, being d the total thickness, i.e. the sum of the outer layer and of the surface layer grown on the brass surface.

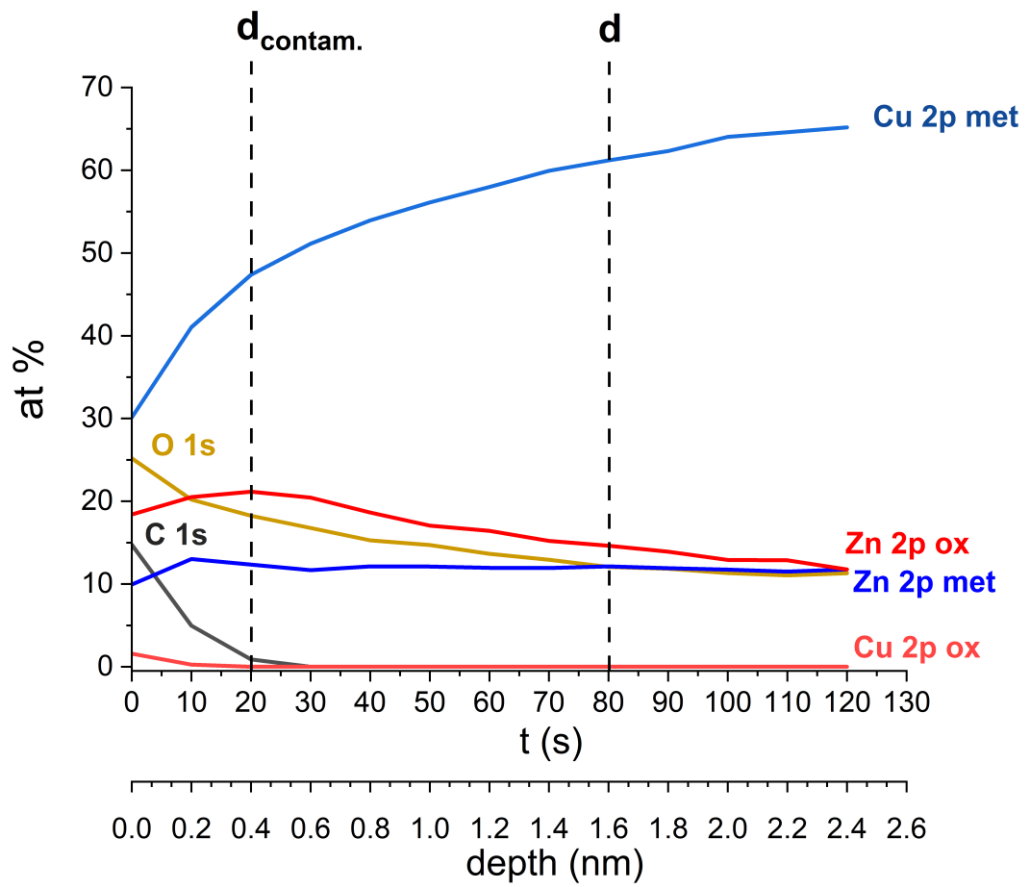


Figure 9: Example of a compositional depth profile obtained by Argon ion sputtering of a mechanically polished CuZn37 sample.

This value is in good agreement with the values obtained by ARXPS and with the thickness of the film on mechanically polished brass reported in previous works. [6,27]

CuZn37 exposed to saliva formulations

In all three saliva solutions a surface film visible to the naked eye was formed on the surface of the CuZn37 samples as shown in the micrographs (Figure 3). The XPS analysis was performed in small-area mode selecting the center of the exposed area to the solution and using a spot size of 400 μm in this condition the analysed area was reported to be 0.5 mm^2 . [28] In the contact area, in addition to Cu, Zn, C and O, sulphur and nitrogen signals were detected in the survey spectra of all the samples; on the surface of the brass samples exposed to C-B and SALMO model solutions, phosphorus signals were also detected, while P2p was not revealed on the sample exposed to D (Figure 10). In the samples exposed to SALMO calcium is also revealed.

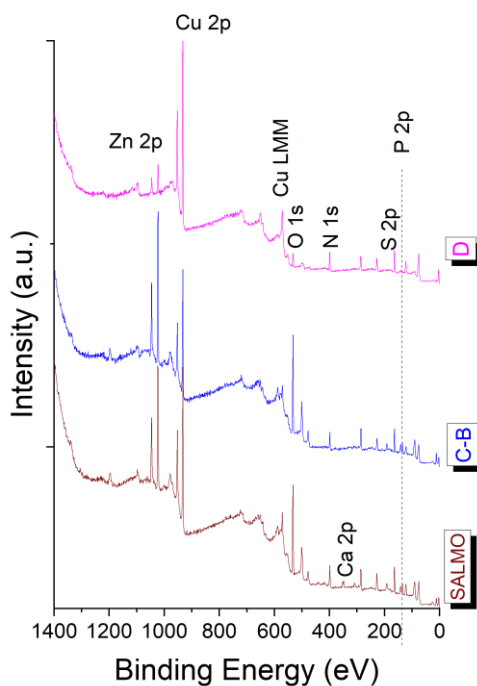


Figure 10: XPS Survey spectra of a mechanically polished CuZn37 alloy after 1 h of contact with D, C-B and SALMO saliva solutions. Adapted from [1]

The binding energy (BE) and the kinetic energy (KE) of the most intense photoelectron and Auger peaks are provided in Table 8. The Cu $2p_{3/2}$ signal showed a single peak at 932.5 (0.1) eV for all samples (Figure 11). The Zn $2p_{3/2}$ signal was found at 1021.7 (0.1) eV when the brass samples were exposed to D solution, This signal might contain Zn(0) and ZnO contributions. After 1h of exposure to SALMO and C-B solutions the Zn $2p_{3/2}$ signal was revealed at 1022.9 (0.1) eV and in

this case the signal was attributed to zinc-phosphate suggesting that on the surface a zinc phosphate film was grown during the contact with this saliva solution (Figure 11) [29-30]. The main component of the Zn $L_{3}M_{4,5}M_{4,5}$ Auger signals was found at 985.6 (0.1) eV. On the CuZn37 samples exposed to D formulation, only metallic zinc and oxide components were revealed (Figure 12a). The Auger signal was found at 987.8 (0.2) eV and it was assigned to ZnO according to the literature [4]. The main component in the Cu $L_{3}M_{4,5}M_{4,5}$ spectra was located at 915.5 (0.1) eV after 1 h of contact with SALMO and C-B. In the case of the samples exposed to D, the Cu(I) component was found at 916.0 (0.3) eV and it was attributed to CuSCN [5,7,27] (Figure 12b). The Auger parameters α' , were also calculated according to [31-33] and are listed in Table 8.

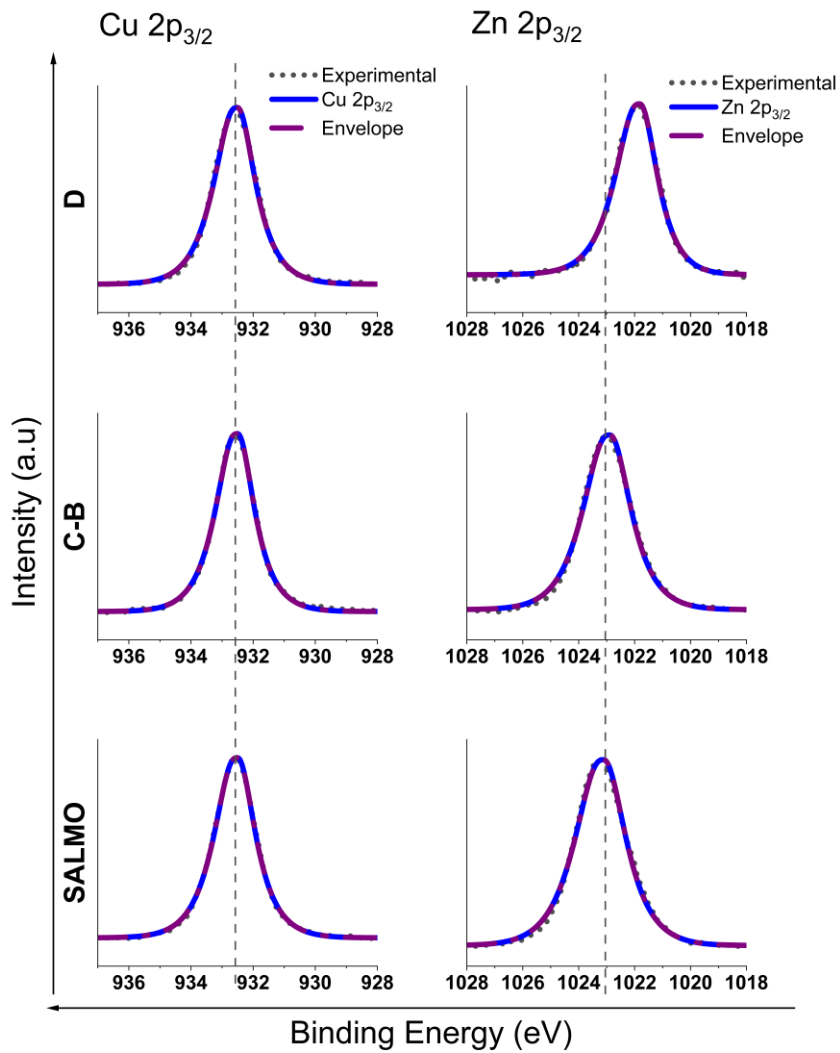
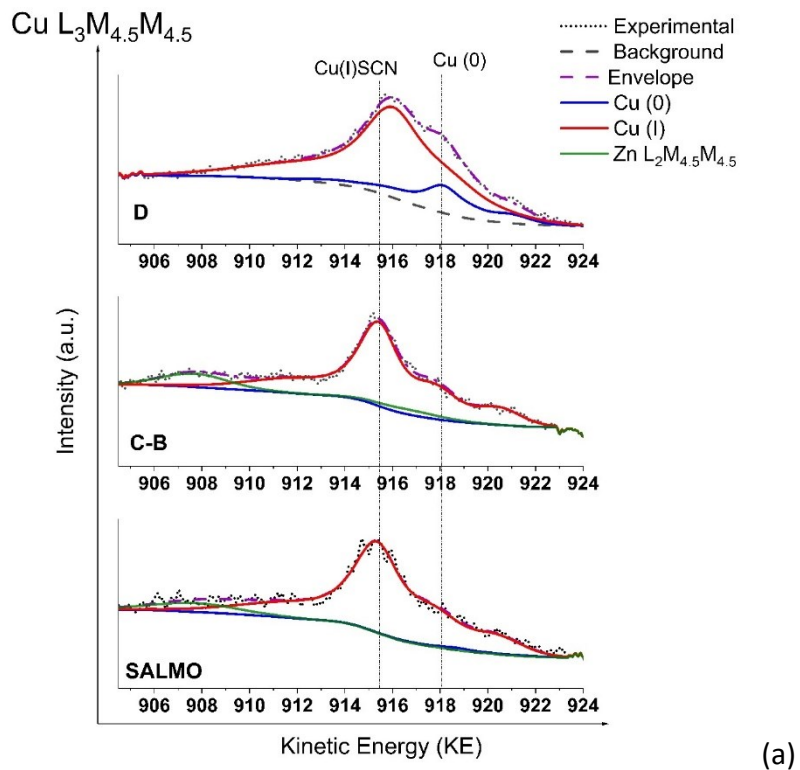
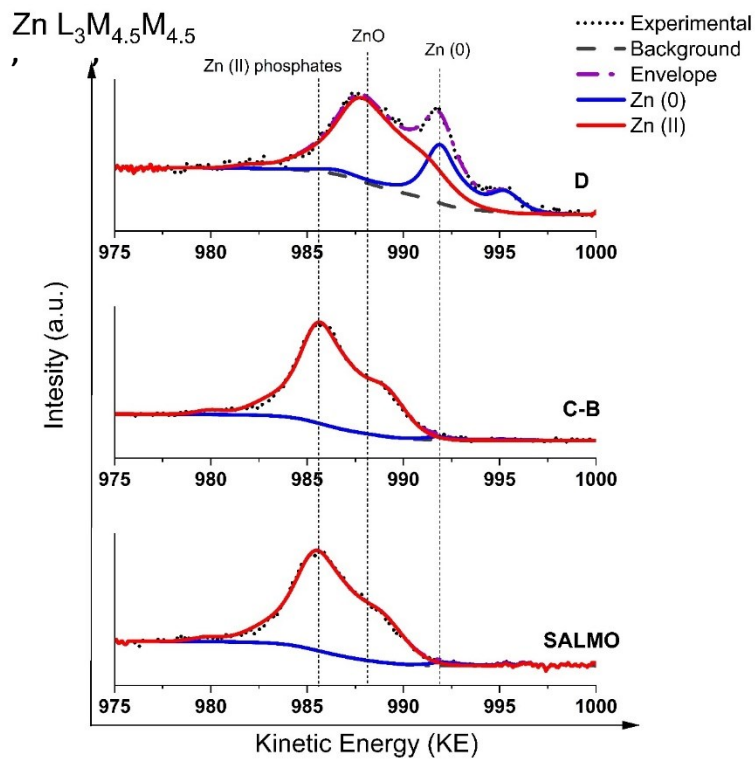


Figure 11: High-resolution XP-spectra on the left: Cu 2p_{3/2}, on the right: Zn 2p_{3/2} of CuZn37 alloy exposed for 1 h to D, C-B and SALMO (from top to down respectively). A Shirley-Sherwood background subtraction was applied prior curve-fitting.



(a)



(b)

Figure 12: a) High-resolution XP-spectra of $\text{Cu L}_3\text{M}_{4.5}\text{M}_{4.5}$ and b) $\text{Zn L}_3\text{M}_{4.5}\text{M}_{4.5}$ of CuZn37 alloy exposed for 1 h to D, C-B and SALMO (from top to down respectively). A Shirley – Sherwood background subtraction was applied before curve-fitting.

Table 8: Binding energy (BE) of the most intense photoelectron peaks, kinetic energy of Auger peaks of the elements detected on CuZn37 surface after 1h of contact with Darvell (D), Carter-Brugirard (C-B) and SALMO saliva model solutions. Auger parameters (α' = BE + KE) of Zn and Cu are also reported. Standard deviations are given in parentheses. Data reported in [2]

CuZn37	D 1h		C-B 1h		SALMO 1h	
	BE (eV)		BE (eV)		BE (eV)	
C 1s (-SCN)	285.8 (0.1)		286.0 (0.1)		286.1 (0.1)	
Cu 2p _{3/2}	932.5 (0.1)		932.5 (0.1)		932.5 (0.1)	
N1s	398.7 (0.1)		398.7 (0.1)		398.7 (0.1)	
N1s	400.2 (0.1)		400.2 (0.1)		400.2 (0.1)	
O1s	530.8 (0.2)		531.6 (0.1)		531.7 (0.2)	
O1s	532.0 (0.1)		532.5 (0.1)		532.5 (0.1)	
O1s	533.2 (0.3)		533.4 (0.2)		533.9 (0.2)	
S 2p _{3/2} (-SCN)	163.2 (0.1)		163.5 (0.1)		163.5 (0.1)	
S 2p (II)	161.9 (0.1)		-		-	
P 2p _{3/2}	-		134.2 (0.1)		134.4 (0.1)	
Ca 2p _{3/2}	-		-		348.7 (0.1)	
Zn2p _{3/2}	1021.7 (0.2)		1022.9 (0.1)		1022.9 (0.1)	
	KE (eV)	α'	KE (eV)	α'	KE (eV)	α'
Cu L ₃ M _{4,5} M _{4,5} film	916.0 (0.3)	1848.5 (0.2)	915.5 (0.1)	1848.0 (0.1)	915.5 (0.1)	1848.0 (0.1)
Zn L ₃ M _{4,5} M _{4,5} film	987.8 (0.2)	2009.5 (0.3)	985.7 (0.1)	2008.6 (0.1)	985.4 (0.1)	2008.3 (0.1)

Quantitative composition (at %) of the main elements detected and the Zn to Cu ratio on CuZn37 surface after 1h of contact with Darvell (D), Carter-Brugirard (C-B) and SALMO artificial saliva solutions are reported in Table 9. The Zn/Cu atomic concentration ratio differs on the surfaces exposed to the different formulations: the samples exposed to D formulation show a lower ratio than in the other cases.

Table 9: Quantitative composition (at %) of the main elements detected and Zn to Cu ratio on CuZn37 surface after 1h of contact with Darvell (D), Carter-Brugirard (C-B) and SALMO saliva model solutions. Standard deviations are given in parentheses. Data reported in [2]

CuZn37	D 1h	C-B 1h	SALMO 1h	SALMO 1h With calcium
	at %	at %	at %	at %
C 1s (-SCN)	19.0 (1)	14.8 (0.3)	13.4 (0.4)	13.0 (0.5)
Cu 2p _{3/2} film	28.0 (2)	10.0 (0.6)	12.4 (0.4)	12.1 (0.3)
N1s	13.0 (2)	7.4 (0.5)	8.7 (0.4)	8.5 (0.4)
N1s	2.1 (0.5)	0.7 (0.2)	0.7 (0.2)	0.7 (0.2)
O1s	12.0 (2)	32.0 (1)	31.3 (0.4)	30.6 (0.4)
S 2p _{3/2} (-SCN)	17.0 (3)	12.0 (0.5)	14.1 (0.5)	13.8 (0.5)
S 2p (II)	5.0 (2)	-	-	-
P 2p	-	7.4 (0.4)	7 (1)	7 (1)
Ca 2p	-	-	-	2.5 (0.7)
Zn2p _{3/2} film	4 (1)	15 (1)	12.0 (0.6)	11.7 (0.6)
	D 1h	C-B 1h	SALMO 1h	
Zn film / Cu film	0.15 (0.03)	1.5 (0.2)	0.97 (0.07)	

The S 2p high-resolution spectra (Figure 13a) show on all samples the presence of a doublet located at 163.4 (0.1) eV assigned to ⁻SCN. [3,5,7,27]. A second doublet with the peak maximum of the S 2p_{3/2} is at 161.9 (0.1) eV, is only found following the exposure of the CuZn37 alloy to D solution. The interpretation of this second component is provided in the Discussion section.

P 2p signal at 134.3 (0.1) eV was ascribed to a phosphate [5,7,27,29-30]. This signal was only present on the brass exposed to SALMO and C-B formulations. On the CuZn37 surface exposed to D formulation no P signal was revealed (Figure 13b).

The N 1s high-resolution spectra (Figure 13c) showed on all samples the presence of two components, one at 398.7 (0.1) eV attributed to a -SCN and the other one at 400.2 (0.1) eV that might be due to organic residuals, such as urea, according to the literature. [3,5,7,27]

The Ca 2p signal (Appendix A- Figure A.4) at 348.7 (0.1) eV was attributed a CaCl₂ [34] present in the SALMO formulation, no Cl signals were revealed.

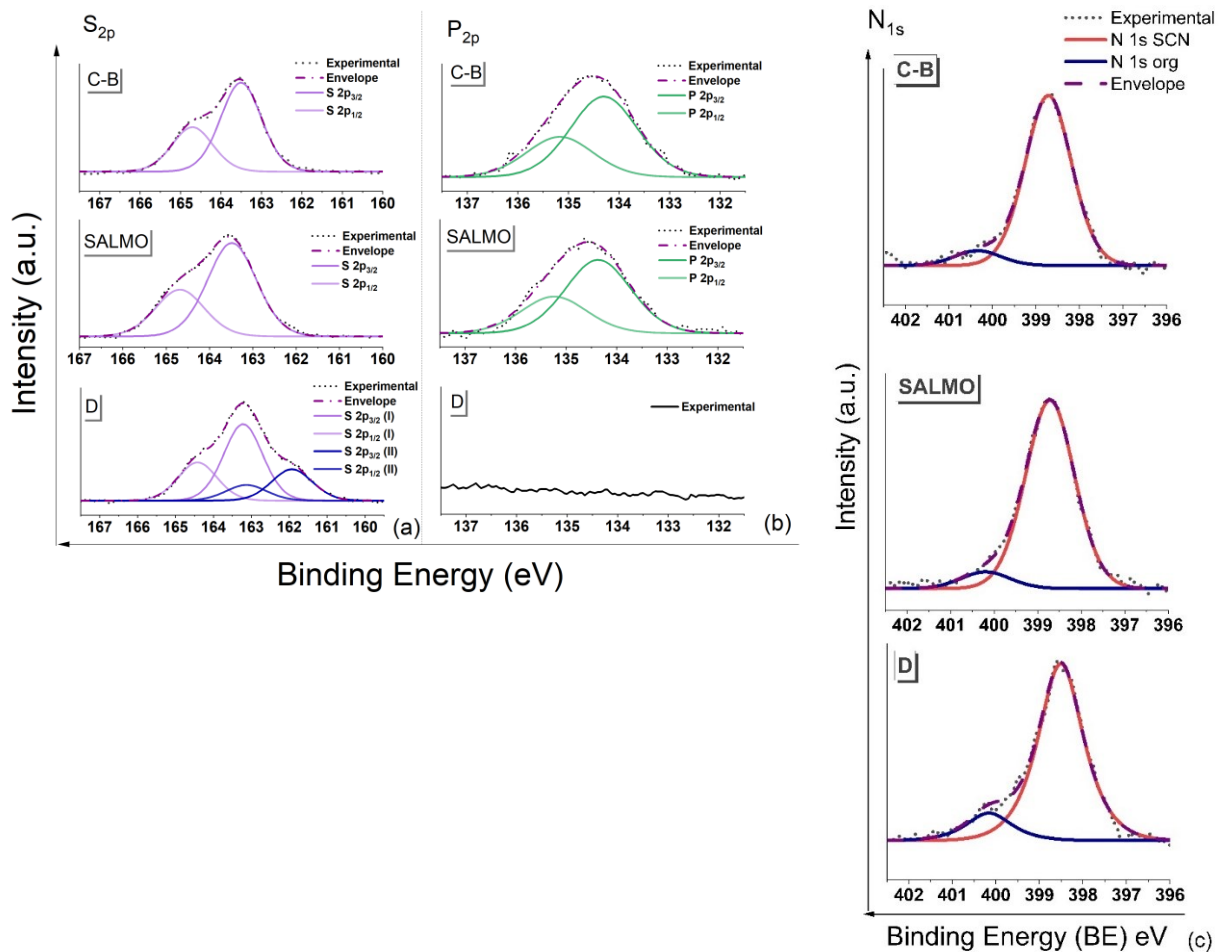


Figure 13: a) High-resolution spectra of S_{2p} and b) P_{2p} c) N_{1s} of CuZn₃₇ after 1 h of contact with (top to bottom) Carter-Brugirard (C-B), SALMO and Darvell (D) formulations. A Shirley – Sherwood background subtraction was applied before curve-fitting. Adapted from [2]

The angle-resolved analyses were also performed for the sample exposed to the saliva solutions. The apparent concentrations vs emission angles considering the film composition are reported in Figure 14.

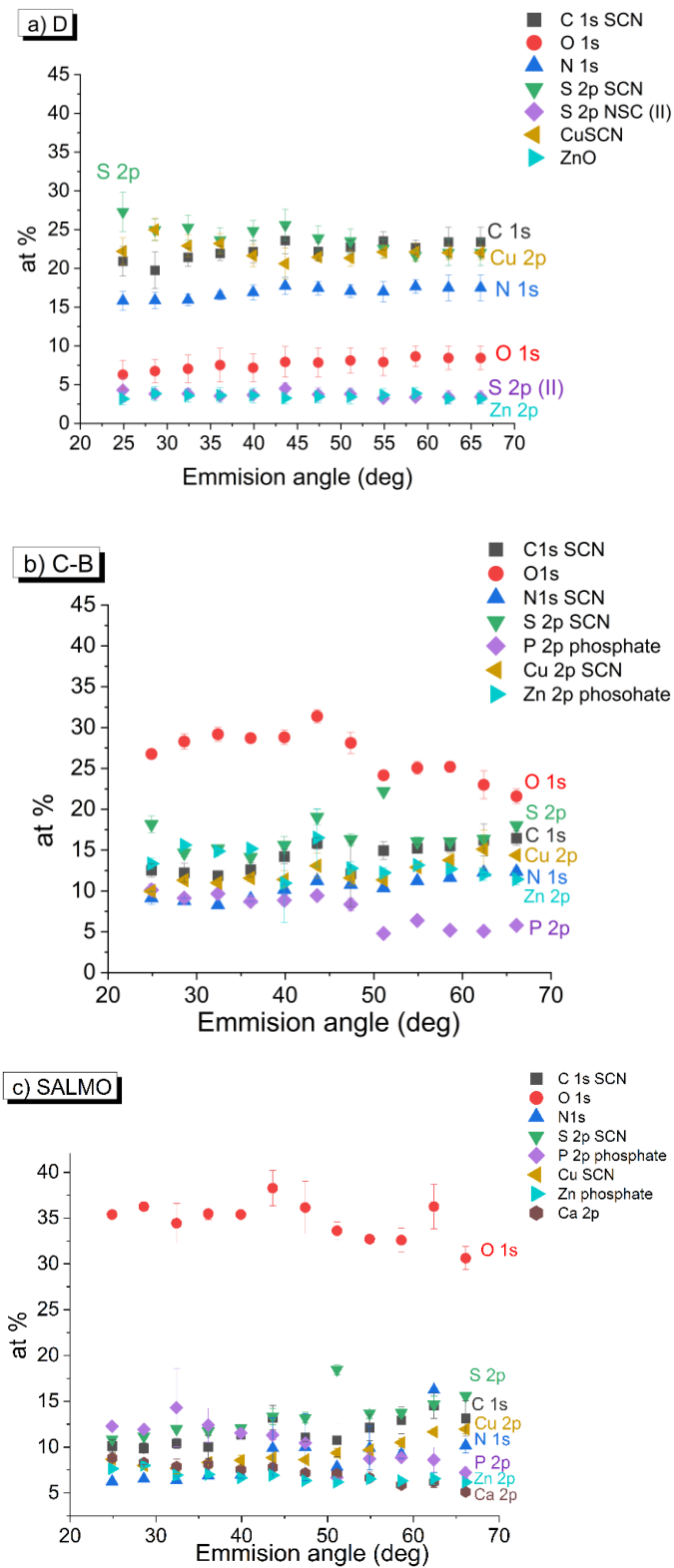


Figure 14: Angle resolved results acquired on samples exposed to a) D, b) C-B, c) SALMO. Apparent concentrations in atomic percentage versus the emission angle are reported, considering the film composition.

The apparent concentration vs angles plot for the sample exposed to Darvell solution (Figure 14 a) shows a quite homogenous film in composition at all angles, mainly composed of CuSCN, as reported

in Table 9. The film formed after the contact with C-B solution (Figure 14b) results enriched on near surface (66.1 °) in CuSCN: the atomic percentages of phosphorous, oxygen, and zinc (attributed to zinc phosphate) decrease with the increasing of the emission angle. In the case of the brass exposed to SALMO solution, also calcium was revealed (Table 9). Ca is detected also at small emission angle, suggesting that it is part of the film. Also in this case, the film results enriched on CuSCN at surface angles.

Since the samples exposed to Darvell show the presence of metallic copper and zinc component at all the considered angles, the thickness of the film by using 1-3 methods (eq. 1-2) was also determined and will be discussed in the next paragraph. (Figure 15). The metallic components markedly decrease with the increase of emission angles.

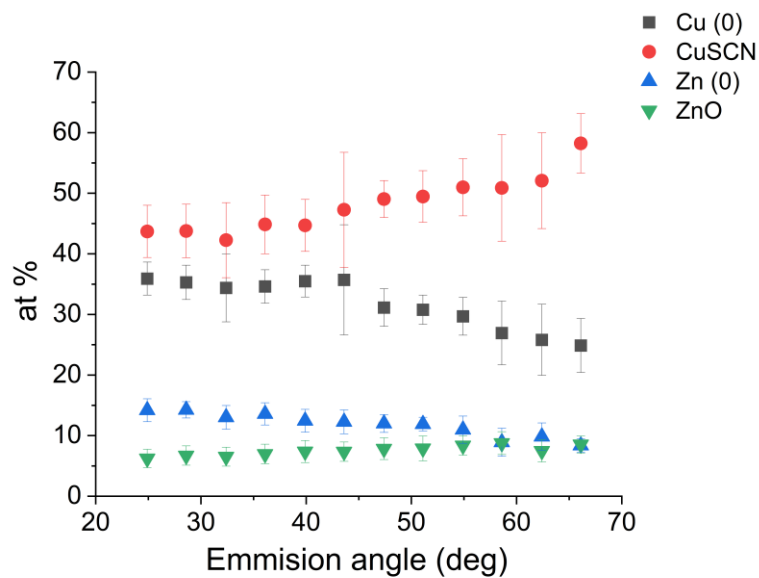


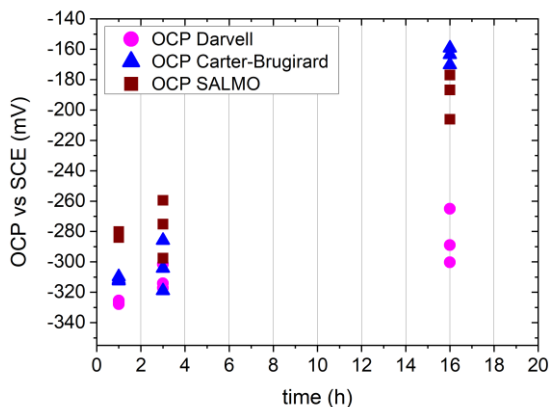
Figure 15: Apparent concentrations in atomic percentage versus the emission angle. Angle resolved results acquired on samples exposed to a) D. Metallic and oxidized zinc and copper components are reported.

4.4. Discussion

4.4.1. Effect of exposure time

No differences on the open circuit potential at the beginning of the exposure (E_0) were observed with the different formulations and it was found to be 301 (12) mV vs SCE. After few minutes of contact the OCP decreased (Figure 4) reaching a minimum due to the dissolution of the film formed at the surface of the brass upon mechanical polishing. [3,5,7,27] Increasing the exposure time, the open circuit potential becomes more positive in all the formulations (Figures 4b and 16a) and in the case of the C-B and SALMO, the OCP trend was similar to the trend observed for the CuZn37 in contact with Tani-Zucchi artificial saliva. [3,5,7,27] Upon contact between the brass and D solution, the OCP reached lower values in comparison with C-B and SALMO (Table 3 and Figure 16a). In parallel, a marked increase with exposure time of the polarization resistance, R_p , is observed for all the solutions (Figure 16b) being the R_p measured after 16 hours about 20 times higher than the R_p measured after 1 hour. This is probably due to the formation of a protective film that leads to a decrease of the corrosion rate.

a)



b)

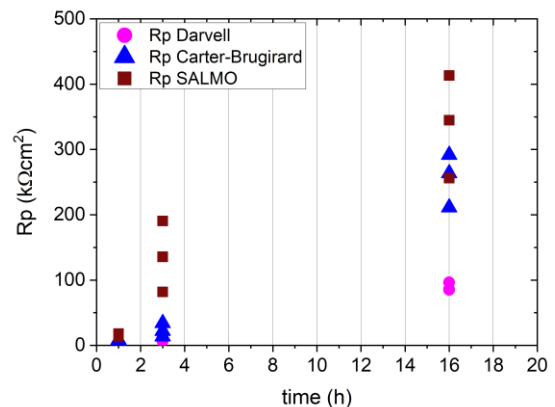


Figure 16: a) Open circuit potential versus time and b) polarization resistance (R_p) vs time for CuZn37 exposed for 1, 3 and 16 h to D, C-B and SALMO. Three independent measurements for each solution were performed. adapted from [1]

4.4.2. Dissolution mechanism

The log R_p vs OCP plot can be exploited with the aim of clarifying the electrochemical mechanism of dissolution of the brass CuZn37 in contact with the artificial saliva formulation (Figure 17). R_p increases exponentially with OCP resulting in a straight line in the log R_p vs OCP plot for all the

solutions here adopted; the same trend was observed also for CuZn37 in contact with the Tani-Zucchi formulation from previous works. [5,7,27] The exposure time increases from the left side to the right side of of figure 17. The slope of the line $\Delta \log R_p / \Delta OCP$ is positive, and it is about $120 \text{ mV decade}^{-1}$.

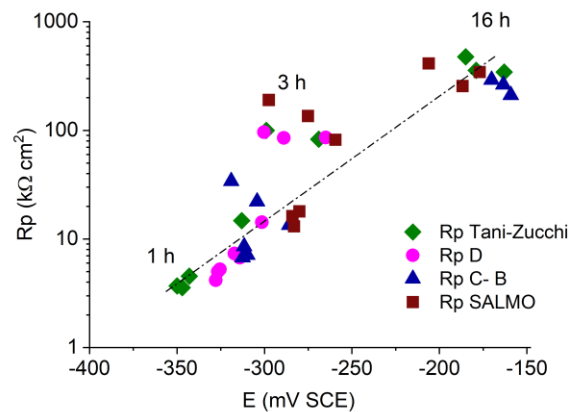


Figure 17: Diagram log R_p vs. OCP for CuZn37 after 1, 3 and 16 hours of contact with Darvell, SALMO and Carter-Brugirard. For comparison, the results previously obtained with Tani-Zucchi saliva are also reported [5,7,27]. Three independent measurements for each solution were performed. adapted from [1]

These results allow concluding that that the dissolution of the CuZn37 alloy is under anodic control for all the tested solutions: the rate of the anodic reaction decreases with exposure time due to the formation of a protective film that slows down the dissolution of the alloy, in agreement with [3,5-7,27]. EIS results on brass alloys with different composition exposed to Tani-Zucchi formulation [7] demonstrated that the corrosion rate was limited by the surface film formed following the brass dissolution.

4.4.3. Practical implications - corrosion rate

The corrosion current density (i_{corr}) decreased with exposure time (Figure 18) reaching values between 0.05 and $0.1 \mu\text{A} / \text{cm}^2$ after 16 hours. The proportionality factor of 12 was found between the corrosion rate and the i_{corr} ($1 \mu\text{A} / \text{cm}^2$ corresponds to $12 \mu\text{m}$ of section loss per year). The i_{corr} values after 16 hours of exposure to D solution were about three times than the i_{corr} measured after contact with C-B and SALMO. (Table 5). Even if the composition of human saliva were similar to that of the solutions here adopted, corrosion damage on brass wind instrument would show only after years of use. Furthermore, the results here presented were obtained on mechanically polished

CuZn37 samples; the presence of the natural patina on the surface of real brass wind instruments slows down the dissolution of the alloy.

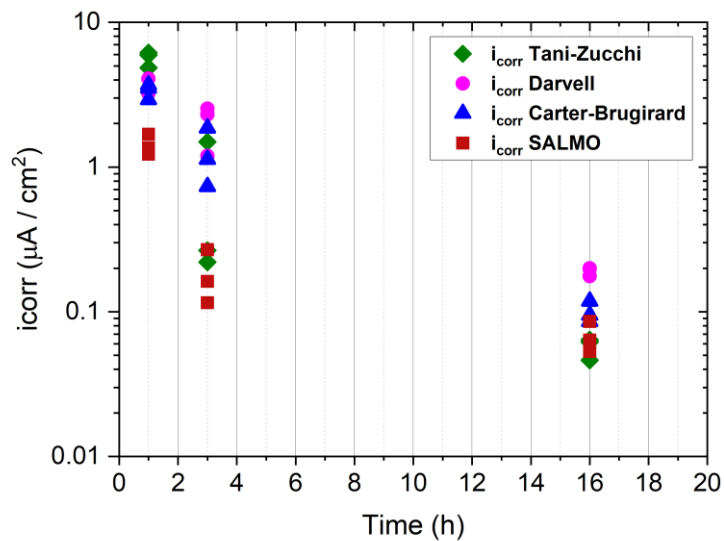


Figure 18: Corrosion density i_{corr} for CuZn37 after 1, 3 and 16 hours of contact with Darvell, SALMO and Carter-Brugirard. For comparison, the results previously obtained with Tani-Zucchi saliva are also reported [5,7,27]. Three independent measurements were performed for each solution. Adapted from [1]

4.4.4. Influence of saliva composition

The different corrosion behaviour of CuZn37 exposed to D can be related to the presence of sodium citrate, lactic acid and uric acid, together with urea in this formulation while in C-B and SALMO the main organic constituent was urea. the presence of these components seems to influence the corrosion rate, despite the low concentration. Also, in the Tani-Zucchi formulation, urea was the main organic constituent ad from previous XPS studies on CuZn37 exposed to Tani-Zucchi artificial saliva [5,7,27] the presence of a film mainly composed of copper (I) thiocyanate and zinc phosphate was reported.

4.4.5. Effect of citrate on film composition

Following the contact of the brass with the solutions for one hour, sulfur signals were detected in XPS survey spectra recorded on all the samples; P signals were only revealed on the samples exposed to C-B and SALMO (Figure 7) despite the phosphate concentration was similar in all the formulations. The absence of P signals and the lowest Zn/Cu ratio observed on CuZn37 exposed to Darvell solution allowed excluding the formation of zinc phosphate. In Darvell solution there are constituents that could act as ligand for Zn leading to the formation of a soluble zinc complex that might limit the growth of the protective films made of $Zn_3(PO)_4$ that was observed on the surface of CuZn37 exposed to SALMO and C-B solutions. Citrate and lactic acid might form soluble complexes with zinc, but from the formation constant values (Kf) [35] it can be seen that the formation of zinc citrate (Figure 19) is favoured (Table 10). To demonstrate the role of citrate ion, a mechanically polished CuZn37 sample was exposed for 1h to a solution of trisodium citrate dihydrate with the same concentration of trisodium citrate in D solution. Also, in this case the Zn/Cu ratio is about 3 times lower than on mechanically polished CuZn37 (Figure 20a and Table 11). Comparing the Zn $L_{3M_{4,5}M_{4,5}}$ (Figure 20 b and Figure 20 c) and C1s spectra (Figure 20d and Figure 20 e) of the sample exposed to the citrate solution and the MP sample, there are no great differences, thus confirming the hypothesis of the possible formation of the soluble zinc-citrate complex.

Table 10: Apparent dissociation constant K_{app} or conditional constants for zinc citrate and zinc lactate, referring to pH value 7,7 ; $K_d = 1/K_f$. [35]

Zinc ligands	K_d^{app} *
Citric acid (citrate)	$1,17 * 10^{-12} M^2$
Lactic acid (lactate)	$1,38 * 10^{-2} M$

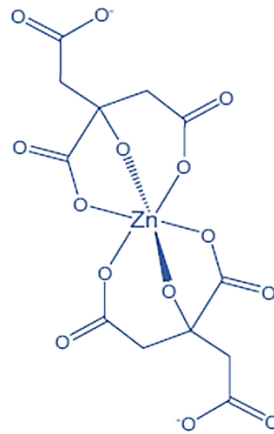


Figure 19: Zinc citrate complex structure, adapted from. [35]

Table 11: Zn/Cu atomic ratio for MP sample and the brass exposed to citrate.

Zn / Cu	
CuZn37 MP	0.90 (0.02)
CuZn37 Citrate	0.28 (0.02)

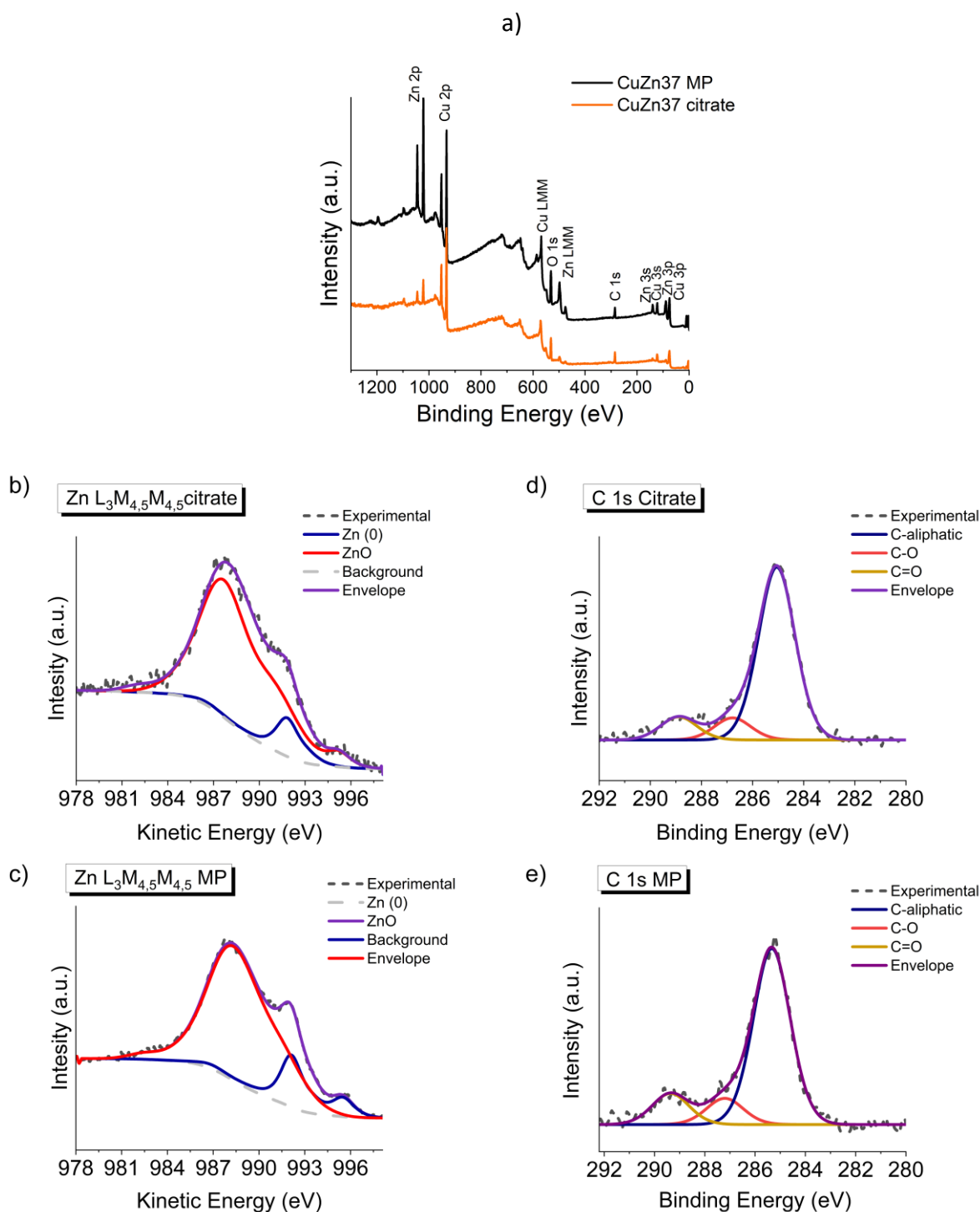


Figure 20: a) Survey spectra of mechanically polished (MP) CuZn37 and CuZn37 samples after 1h of contact to trisodium citrate solution; b) Zn L₃M_{4,5}M_{4,5} spectra of CuZn37 alloy after 1 h of contact to the citrate. solution; c) Zn L₃M_{4,5}M_{4,5} spectra of the MP CuZn37; d) C 1s spectra of CuZn37 alloy exposed for 1 h to the citrate solution; e) C 1s spectra of MP CuZn37. Adapted from [2]

4.4.6. Effect of uric acid

Cu (I) usually coordinates the SCN⁻ ion via sulphur atom, since it is soft Lewis acid [34] SCN⁻ ion is an ambidentate ligand and if it is the only ligand present, its mode of bonding generally follows the

hard (M-NCS) or soft (M-SCN) principle [34]. When other ligands are present, the metal can behave as hard- or soft ion resulting in different thiocyanate complexes [36-38]. The presence of a sulphur component at 161.9 eV might be explained with the presence of Cu (I) sulphide [38-40], or of a mixed complex where thiocyanate coordinates copper both via S and via N, in analogy with the results reported in literature in the presence of ligands as bipyridine with other metal ions. [43-45] To investigate the possible formation of the mixed complex due to the presence of uric acid in D solution, a pure copper sample was exposed for 1 h to a solution containing of NaSCN and uric acid with the same concentration as in D. The same experiment was repeated replacing the uric acid with lactic acid. When uric acid (Figure 21) and sodium thiocyanate were simultaneously present, the S2p showed the presence of the component at 161.9 (0.1) eV (Figure 22). This result corroborates the hypothesis of the formation of a mixed complex where SCN^- coordinates Cu (I) both via S- and via N- atoms due to the steric and electronic effects exerted by uric acid. The presence of Cu_2S can be ruled out if the chemical state plot of copper is taken into account.

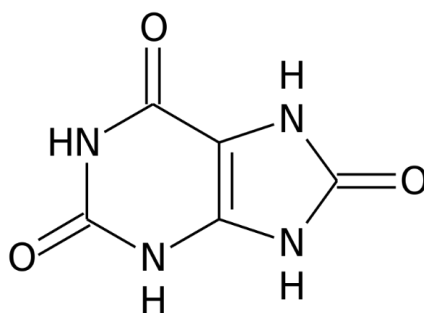


Figure 21 : uric acid structure. (Public domain, copyright not applicable)

a)

b)

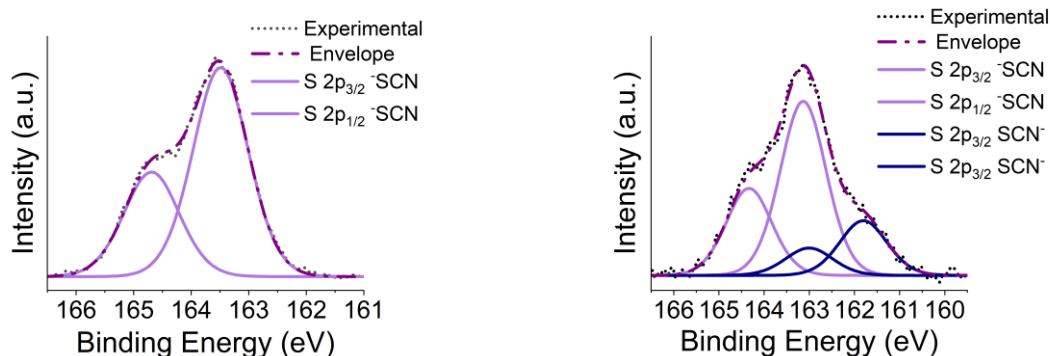


Figure 22: High-resolution spectra of S2p signal of a) pure copper exposed to NaSCN (0.20 g / dm^3) and lactic acid (0.07 g / dm^3) solution and b) pure copper exposed to NaSCN (0.20 g / dm^3) and uric acid (15 mg / dm^3) solution. Adapted from [2]

4.4.7. Wagner plots

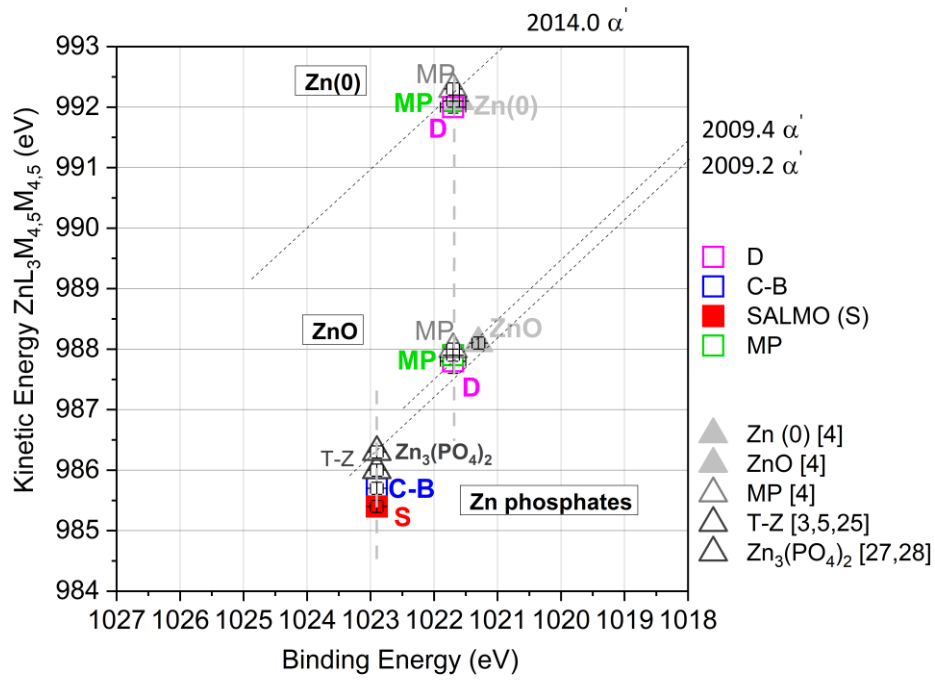
A powerful tool for determining the chemical state is the Wagner chemical state plot [31- 33, 34]: it combines the kinetic energy of the X-ray induced Auger lines (y-axis) and the binding energy of photoelectron lines (on the x-axis) of the same element. With the sum of them, another important parameter could be determined: the Auger parameter α' . This sum will be the same, independent of sample charging, and is found in the chemical state plot as a series of diagonal lines representing equal α' (Figure 23). The chemical state plot allows a more accurate assignment of the chemical state of the same element, in particular for copper and zinc compounds.

The points of Zn (0), ZnO and Zn-phosphate fall in different regions of Zn- chemical state plot (Figure 23a); also in the case of copper, Cu(0), Cu₂O and CuSCN are clearly distinguishable in the Wagner plot (Figure 23b). At the surface of the MP sample Cu (0), Zn (0), ZnO and Cu₂O are detected due to the presence of a thin oxide at the brass surface, confirmed also by the ARXPS and depth profile data (Table 9 and Figure 10). When CuZn37 is exposed to C-B and SALMO, Zn₃(PO₄)₂ and CuSCN are

the main constituents of the protective film, while only Zn (0) and ZnO are revealed upon the contact with D solution. The α' values of Zn for the CuZn37 exposed to C-B ($\alpha' = 2008.6$ (0.1) eV) and SALMO ($\alpha' = 2008.3$ (0.1) eV) are in agreement with those obtained for standard of $Zn_3(PO_4)_2$, while α' value for CuZn37 exposed to D ($\alpha' = 2009.5$ (0.3) eV) is close to the value reported for ZnO [4,46] and for $Zn(acac)_2$ and for Zn (Captopril). [31] Captopril, acetylacetonate and citrate ligands coordinate zinc atoms in a similar way, thus preventing the possibility of ruling out the presence of surface complexes in this case.

As far as copper, the Auger parameter values obtained for CuZn37 exposed to C-B and SALMO ($\alpha' = 1848.0$ (0.1) eV) are typical for copper thiocyanate where SCN- is bonded via sulphur in analogy with results obtained on CuZn37 exposed to Tani-Zucchi artificial saliva [5-7,27] and for the complexed of copper with 1-(D-3-mercapto-2-methylpropionyl)-L-proline (captopril, CAP) [46]. α' values for CuZn37 exposed to D ($\alpha' = 1848.5$ (0.2) eV) showed a slight positive shift that might be related to CuSCN where SCN- is bonded via S- and via N- due to the presence of uric acid. This slight positive shift of α' reflects differences in the extra atomic relaxation energies, determined by the differences of the polarizability of the ligand electronic cloud towards the core holes formed in copper atoms upon photo-emission in analogy with results reported by Battistoni et al [47] for copper polynuclear compounds.

a)



b)

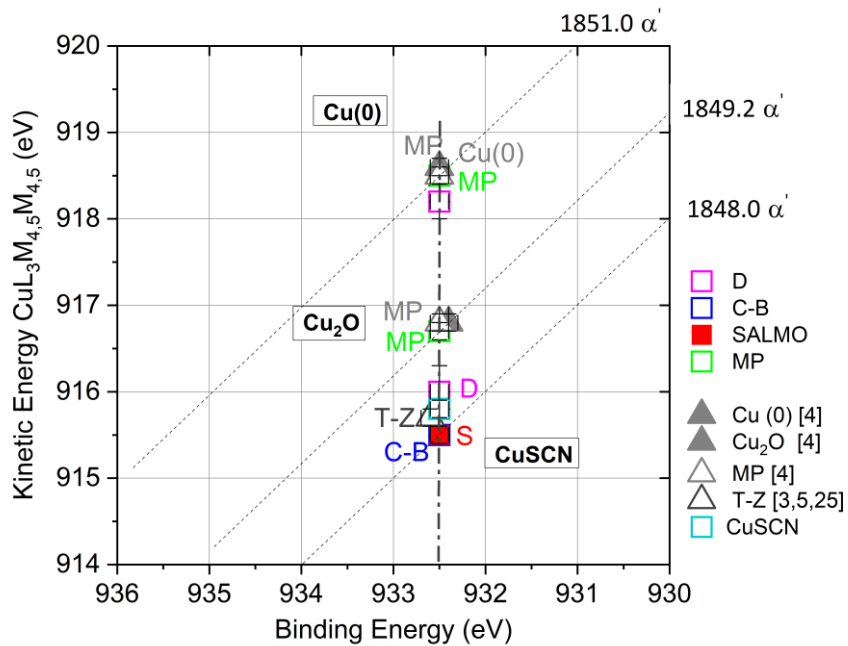


Figure 23: Wagner chemical state plot of a) zinc and b) of copper using data obtained in this work and data from literature [5-7,27, 29,30] for CuZn37 MP, exposed 1h to artificial saliva, and for reference materials (Zn(0), ZnO and Cu(0), Cu₂O, CuSCN).

4.4.8. Effect of the thickness

The thickness of film determined for the MP sample is in good agreement among the methods used and also with the literature [6,26]. For the samples exposed to Darvell solution, the presence of the metallic component on XAES spectra of Cu and Zn indicates the presence of a very thin film (Figure 9). The thickness of the film formed after 1 hour of exposure of Darvell solution was calculated by using three different methods starting from ARXPS data and the values are reported in Table 12. As for the MP sample, the ratio of ZnO and Zn(0) intensities was taking into account.

Table 12: Thickness values of film formed after 1 hour of brass exposure to D solution obtained by 1-3 methods. Standard deviations are reported in brackets.

Methods	Thickness (nm)
1 (different emission angles from 24.9° to 66.1°)	0.57 (0.05)
2 (two different emission angles 24.9° and 66.1°)	0.7 (0.2)
3 (one angle 24.9°)	0.57 (0.08)

For the samples exposed to C-B and SALMO solution, the metallic component was revealed only at a small emission angle. For this reason, the thickness can be estimated taking into account only the smallest emission angle, considering for R calculation the intensity ratio between Zn(0) and Zinc phosphate, and for R^∞ , the density the molar mass, and the λ value calculated for zinc phosphate. The thickness was found to be 5.2 (0.1) nm for SALMO and 6.6 (0.5) nm for C-B. Considering that the sampling depth ($3\lambda\cos\theta$) for metallic zinc at 53 ° is about 2 nm, the thickness obtained could be a reasonable value for the films formed in these samples. These facts could explain the high corrosion rate observed for brass exposed to the D solution: the film formed was less protective than the ones formed in SALMO and C-B solutions.

Despite the film thickness estimation taking into account a single emission angle is quick and useful, it is less accurate when complex systems are considered. Not only the acquisition and analysis of a complete set of ARXPS data allow obtaining a more accurate thickness estimation, but in the case of in-depth inhomogeneous layers it allows also highlighting the presence of gradients. The thickness estimation by equation 1 does not allow for distinguishing between the thickness of the film and of the organic contamination layer.

For multi-layered films, if the thickness of the layers has to be estimated, equation 1 cannot be applied due to the fact that it only allows obtaining the thickness of the whole film; in such cases, the reconstruction of the depth profiles from ARXPS data can be obtained by algorithms based for example on the maximum entropy method (MEM). [49-51]

4.5. Conclusions

On the basis of the results obtained in this work, the following conclusions can be drawn:

- The corrosion behaviour of brass and the composition of the surface film are strongly influenced by the composition of the model solution:
 - From OCP and R_p measurements it can be concluded that the dissolution mechanism of CuZn37 is under anodic control for all the considered formulations.
 - The corrosion rate varies in the order: D > C-B > SALMO and it significantly decreases upon the exposure time.
 - The corrosion rate depends on the presence of organic ligands in the model solutions: citrate ions in Darvell formulation favour zinc dissolution and hinder the precipitation of zinc phosphate that is found to play a protective role against further corrosion together with CuSCN.
 - The films thickness for the samples exposed to saliva solutions was found to be about 0.6 nm, for Darvell, and in the range of 7-9 nm for SALMO and C-B. These facts could explain the high corrosion rate observed for brass exposed to D solution: the film formed was less protective than the ones formed in the other solutions.
- The Auger parameters and chemical state plot allowed to unambiguously assign the chemical state of zinc and copper.
- The synergistic combination of electrochemical and surface analytical results allows us to correlate surface composition and corrosion rates.

References

- [1] “D. Biggio, B. Elsener, D. Atzei, A. Rossi, M. Fantauzzi, The effect of the saliva formulation on brass corrosion, 2022, *Materials and Corrosion*. <https://doi.org/10.1002/maco.202213476>
- [2] D. Biggio, M. Fantauzzi, B. Elsener, D. Atzei, A. Rossi, The role of organic compounds in artificial saliva for corrosion studies: evidence from XPS analyses, 2022, *Surface and Interface Analysis*. <https://doi.org/10.1002/sia.7149>.
- [3] B. Elsener, F. Cocco, M. Fantauzzi, A. Rossi, Determination of the corrosion rate inside historical brass wind instruments – proof of concept., *Mater. Corros.* 67, 1336–1343, 2016b.
- [4] B. Elsener, M. Alter, T. Lombardo, M. Ledergerber, M. Wörle, F. Cocco, M. Fantauzzi, S. Palomba, A. Rossi, A non-destructive in-situ approach to monitor corrosion inside historical brass wind instruments; *Microchem. J.* 124, 757–764, 2016a.
- [5] F. Cocco, M. Fantauzzi, B. Elsener B., A. Rossi, Dissolution of brass alloys naturally aged in neutral solutions – an electrochemical and surface analytical study, *RSC Adv.*, 6, 90654, 2016.
- [6] F. Cocco, B. Elsener, M. Fantauzzi, D. Atzei, A. Rossi, Nanosized surface films on brass alloys by XPS and XAES, *RSC Adv.*, 6, 31277, 2016.
- [7] M. Fantauzzi, B. Elsener, F. Cocco, C. Passiu, A. Rossi, Model Protective Films on Cu-Zn Alloys Simulating the Inner Surfaces of Historical Brass Wind Instruments by EIS and XPS, *Front. Chem.*, 8, 272, 2020.
- [8] G. Tani, F. Zucchi, Electrochemical valuation of the corrosion resistance of commonly used metals in dental prosthesis, *Minerva Stomatologica*, 16, 710-713, 1967.
- [9] B. W. Darvell., The development of an artificial saliva for *in vitro* amalgam corrosion studies, *J. of Oral Rehabil.*, 5, 41, 1978.
- [10] M. Andrei, B. Galateanu, A. Hudita, M. Costache, P. Osiceanu, J.M. Calderon Moreno, S.I. Drob, I. Demetrescu, Electrochemical comparison and biological performance of a new CoCrNbMoZr alloy with commercial CoCrMo alloy, *Mater. Sci. Eng. C*, 59, 346, 2016.
- [11] F. Crea, C. De Stefano, D. Milea, A. Pettignano, S. Sammartano, SALMO and S3M: A Saliva Model and a Single Saliva Salt Model for Equilibrium Studies, *Bioinorg. Chem. Appli., Bioinorg. Chem. and Appli.*, 2015, 267985, 2015.
- [12] B. Elsener, M. Crobu, M.A. Scorciapino, A. Rossi, Electroless deposited Ni–P alloys: corrosion resistance mechanism. *J Appl Electrochem* 38, 1053–1060, 2008.
- [13] M. Crobu, A. Scorciapino, B. Elsener, A. Rossi, The corrosion resistance of electroless deposited nano-crystalline Ni-P alloys, *Electroc. Acta*, 53, 3364, 2008.
- [14] VersaStudio 2.44.4, Princeton Applied Research, Ametek, 2015.
- [15] B. Barnard, P. Belcher, Theta probe spectrometer set up, March, 2003.
- [16] D. A. Shirley, *Physical Review B: Solid State*, 5, 4709, 1972.
- [17] D. Briggs and J. T. Grant, *Surface Analysis by Auger and X-ray Photoelectron Spectroscopy*, IM Publications and Surface Publication Data, West Sussex, 345, 2003.
- [18] J. H. Scofield, Hartree-Slater subshell photoionization cross-sections at 1254 and 1487 eV, *J. Electron Spectrosc. Relat. Phenom.*, 8, 129, 1976.
- [19] R.F. Reilman, A. Msezane, S.T. Manson, Relative intensities in photoelectron spectroscopy of atoms and molecules, *J. Electron. Spectrosc. Relat. Phenom.*, 8, 389, 1976.
- [20] M. Fantauzzi, A. Pacella, J. Fournier, A. Gianfagna, G.B. Andreozzi, A. Rossi, Surface chemistry and surface reactivity of fibrous amphiboles that are not regulated as asbestos, *Anal. Bioanal. Chem.*, 404, 821, 2012.
- [21] M. P. Seah, W. A. Dench, Quantitative electron spectroscopy of surfaces: A standard data base for electron inelastic mean free paths in solids, *Surf. Interface Anal.*, 1, 2, 1979.
- [22] M. Stern, A. L. Geary, *J. Electrochem. Soc.*, Electrochemical Polarization, 104,56, 1957.
- [23] M. C. Biesinger, W.M. Lau Leo, R. Gerson Andrea, St.C. Smart Roger, Resolving surface chemical states in XPS analysis of first row transition metals, oxides and hydroxides: Sc, Ti, V, Cu and Zn, *Appl. Surf. Sci.*, 257, 887, 2010.
- [24] J. F. Moulder, W. F. Stickle, P. E. Sobol and K. D. Bomben, *Handbook of X-ray Photoelectron Spectroscopy*, Perkin-Elmer Corp., *Physical electronics*, Minnesota, 1992.

- [25] W.H. Gries, A Universal Predictive Equation for the Inelastic Mean Free Pathlengths of X-ray Photoelectrons and Auger Electrons. *Surf. Interface Anal.*, 24: 38-50, 1996.
- [26] C. J. Powell, A. Jablonski, NIST Electron Inelastic-Mean-Free-Path Database, Version 1.2, National Institute of Standards and Technology, Gaithersburg, MD (2010).
- [27] F. Cocco, PhD thesis, Sustainability in cultural heritage: from diagnosis to the development of innovative systems for monitoring and understanding corrosion inside ancient brass wind, Università di Cagliari, 2016.
- [28] C. Passiu, A. Rossi, L. Bernard, D. Paul, J. Hammond, W.E. Unger, W. E., V.V. Nagaiyanallur, N. D. Spencer, Fabrication and microscopic and spectroscopic characterization of planar, bimetallic, micro- and nanopatterned surfaces. *Langmuir*, 33(23), 5657-5665, 2017.
- [29] M. Crobu, A. Rossi, F. Mangolini, N.D. Spencer, Chain-length-identification strategy in zinc polyphosphate glasses by means of XPS and ToF-SIMS. *Anal Bioanal Chem.*;403(5), 1415-32, 2012.
- [30] M. Crobu, A. Rossi, N.D. Spencer, Effect of Chain-Length and Countersurface on the Tribochemistry of Bulk Zinc Polyphosphate Glasses, *Tribol. Lett.*, 48, 393-406, 2012.
- [31] C.D. Wagner, Chemical shifts of Auger lines, and the Auger parameter, *Faraday Discuss. Chem. Soc.*, 60, 291-300, 1975.
- [32] Moretti G., Auger parameter and Wagner plot in the characterization of chemical states by X-ray photoelectron spectroscopy: a review., *J Electron Spectr. Related Phenom*, 95, 95-144, 1998.
- [33] C.D. Wagner, and A. Joshi. "The auger parameter, its utility and advantages: a review." *Journal of electron spectroscopy and related phenomena*, 47,283-313, 1988.
- [34] C.D. Wagner, Chapter 7 In 'Handbook of X-Ray and Ultraviolet Photoelectron Spectroscopy', D. Briggs, Editor, 1977.
- [35] A. Krężel, W. Maret, The biological inorganic chemistry of zinc ions, *Arch Biochem Biophys*, 19, 611-3, 2016.
- [36] R. G. Pearson, *Chemical Hardness*. Wiley-VCH Verlag GmbH, Weinheim, 1997.
- [37] J. Burmeister, Ambidentate ligands, the schizophrenics of coordination chemistry, *Coord. Chem. Rev.*,105, 77-133, 1990.
- [38] D. Aldakov, C. Chappaz-Gillot, R. Salazar, V. Delaye, K.A. Welsby, V. Ivanova, P.R. Dunstand, Properties of Electrodeposited CuSCN 2D Layers and Nanowires Influenced by Their Mixed Domain Structure. *J. Phys. Chem. C*, 118(29), 16095-16103, 2014.
- [39] D.W. Meek, P.E. Nicpon, V. Imhof Meek, Mixed Thiocyanate Bonding in Palladium (II) Complexes of Bidentate Ligands, *J. Am. Chem. Soc.*, 92, 5351-5359, 1970.
- [40] K. Gholivand, K. Farshadfar, S.M. Roe, M. Hosseini and A. Gholami, Investigation of structure-directing interactions within copper(I) thiocyanate complexes through X-ray analyses and non-covalent interaction (NCI) theoretical approach, *Cryst .Eng. Comm.*, 18, 7104-7115, 2016.
- [41] M. Fantauzzi, B. Elsener, D. Atzei, P. Lattanzi, and A. Rossi, The surface of enargite after exposure to acidic ferric solutions: an XPS/XAES study, *Surf. Interface Anal.*, 39, 908-915, 2007.
- [42] M. Fantauzzi, A. Rigoldi, B. Elsener, D. Atzei, A. Rossi, A contribution to the surface characterization of alkali metal sulfates, *J. Electron Spectrosc. Relat. Phenom.*, 193, 6-15, 2014.
- [43] M. Fantauzzi, G. Rossi, B. Elsener, G. Loi, D. Atzei, A. Rossi, An XPS analytical approach for elucidating the microbially mediated enargite oxidative dissolution, *Anal. Bioanal. Chem.*, 393, 1931-1941, 2009.
- [44] R.A. Walton, X-ray Photoelectron Spectra of Inorganic Molecules [11]. XXIII. On the Question of the Usefulness of XPS in Studying the Ambidentate Nature of the Thiocyanate Ligand, *Inorg. Chim. Acta*, 37, 231-240, 1979.
- [45] A. Bowmaker Graham and V.Z. Hanna John, IR Spectroscopy of Two Polymorphs of Copper(I) Thiocyanate and of Complexes of Copper(I) Thiocyanate with Thiourea and Ethylenethiourea, *Z. Naturforschung*, 64b, 1478-1486, 2009.
- [46] D. Atzei, C. Sadun, L. Pandolfi, X-ray photoelectron spectra of complexes with 1-(d-3-mercapto-2-methylpropionyl)-L-proline and Ni(II), Cd(II) and Cu(I): synthesis and LAXS study of Cu(I) derivative, *Spectr. Acta Part A: Mol. and Biomol. Spectr.*, 56,531-540, 2000.
- [47] C. Battistoni, G. Mattogno, E. Paparazzo, L. Naldini, An XPS and Auger study of some polynuclear copper compounds, *Inorg. Chim. Acta*, 102,1-3, 1985.
- [48] D. Atzei, D. De Filippo, A. Rossi, A. Lai, G. Saba, R. Bucci, IR, NMR, XPS study of 1-(D-3-mercapto-2-methylpropionyl)-L-proline and its zinc complexes, *Spectrochimica A*, 48, 911-919, 1992.

- [49] M. Olla, G. Navarra, B. Elsener, A. Rossi, Nondestructive in-depth composition profile of oxy-hydroxide nanolayers on iron surfaces from ARXPS measurement. *Surface and Interface Analysis: An International Journal devoted to the development and application of techniques for the analysis of surfaces, interfaces and thin films*, 38(5), 964-974, 2006.
- [50] M. A. Scorciapino, G. Navarra, B. Elsener, A. Rossi, Nondestructive Surface Depth Profiles from Angle-Resolved X-ray Photoelectron Spectroscopy Data Using the Maximum Entropy Method. I. A New Protocol, *The Journal of Physical Chemistry C*, 113 (51), 21328-21337, 2009.
- [51] M. A. Scorciapino, M. Fantauzzi, M. Crobu, G. Navarra, B. Elsener, and A. Rossi, *ACS Omega*, 2 (11), 7790-7802, 2017."

Chapter 5. Thin Films on stainless steel DIN 1.4456

This chapter shows the results obtained on the growth and characterization of thin films at the surface of the Ni-free 1.4456 stainless steel in contact with three different formulations of artificial saliva. The first section provides a short introduction aiming to explain the purpose of the work. Then, the experimental details of the electrochemical measurements and of surface analysis are presented. The results of the investigation are displayed and discussed in the last two sections.

The electrochemical experiments in this section are performed in collaboration with Giulia Usai, undergraduate student at the University of Cagliari, under my tutoring.

5.1. Introduction

Nickel allergy is the most common allergy in the world population and it is more common in women than in men with a prevalence of 17% and 3%, respectively. [1]. Due to the diffusion of Ni allergy, the European Commission in 1994, prohibited the use of products that allow a Ni release per week higher than $0.5 \mu\text{g}/\text{cm}^2$. [2]

In sensitized subjects, contact with nickel causes the appearance of dermatological symptoms, regardless the contact with the epidermis. In fact, these symptoms were also found in patients with dental or orthopedic prostheses. [1] For these reasons, Ni-bearing alloys used for implants have to be replaced with more suitable Ni-free materials.

In previous research [3], the stability and the reactivity of the Ni-free 1.4456 stainless steel in contact with a solution simulating human saliva, made up according to the formulation proposed by Tani and Zucchi (TZ), [4] was investigated by the combination of electrochemical techniques and x-ray photoelectron spectroscopy, in order to evaluate the possibility of exploiting this SS for orthodontics applications. The main inorganic constituent of TZ solution was KCl ($0.02 \text{ mol}/\text{dm}^3$) together with Na_2HPO_4 ($0.0014 \text{ mol}/\text{dm}^3$), NaHCO_3 ($0.0015 \text{ mol}/\text{dm}^3$) and KSCN ($0.0053 \text{ mol}/\text{dm}^3$). As far as the organic components, only urea ($0.017 \text{ mol}/\text{dm}^3$ and α -amilase ($0.1 \text{ g}/\text{dm}^3$) were present. The authors showed that for prolonged exposure time the passive film formed at the surface of the SS was enriched in chromium oxy-hydroxide and depleted in FeO and manganese. Manganese depletion was observed also on the alloy beneath the passive film. Since for the longest exposure

time the maximum corrosion rate was found to be 0.1 $\mu\text{m}/\text{year}$, the authors demonstrated that the 1.4456 can be used in orthodontics due to its good biocompatibility at 37°C. [3]

This part of the work studied the corrosion behavior of the same Ni-free 1.4456 stainless steel in contact with the same artificial saliva formulations exploited for the study on brass corrosion, thus Darvell (D) [5], Carter – Brugirard (C-B) [6] and SALMO [7]. Also in this case, the effect of the different organic constituents, especially in D formulation, on the corrosion behavior and on the composition of the films is analyzed and discussed.

5.2. Experimental

5.2.1. Materials and surface preparation

In this work stainless-steel DIN 1.4456 samples (Kretzschmann GmbH & Co. KG, Birkenfeld / Germany) were examined. The composition of the steel is reported in Table 1. The ‘as received’ samples (Figure 1) show various scratches, thus before the electrochemical measurements, they were polished with diamond paste to a mirror-like finish according to the procedure described in Table 2. The samples were washed with bi-distilled water after each grinding step, and with EtOH after each polishing step. The mechanically polished samples were washed with EtOH and dried under an argon stream, then, they were transferred to the fast entry air lock of the XPS spectrometer and analysed by XPS before the electrochemical tests.

Table 2: Composition (wt %) of the DIN 1.4456 stainless-steel.

Alloying elements	Fe	Cr	Mn	Mo	Ni	C	S	Si	N	P
wt %	60.1	17.9	18.4	1.9	0.18	0.06	0.04	0.9	0.8	0.025

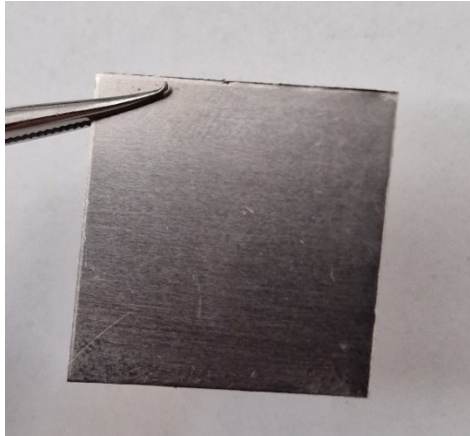


Figure 1: picture of as received stainless-steel DIN 1.4456 sample.

Table 2: Mechanical polishing procedure

Step	Grinding			Polishing		
Surface	500 SiC paper	1200 SiC paper	2400 SiC paper	DP Plus cloth with 3 μm diamond paste	DP Plus cloth with 1 μm diamond paste	DP Plus cloth with $\frac{1}{4}$ μm diamond paste
Lubricant	Bi-distilled water	Bi-distilled water	Bi-distilled water	Ethanol	Ethanol	Ethanol
Time [min.]	3	3	2	1.30	1	1

5.2.2. Model solutions

The artificial saliva formulations employed in this work are Darvell (D), Carter-Brugirard (C-B) and SALMO. [5-7] Their chemical composition is reported in Table 2 Chapter 4.2. All reagents used were at least of ACS grade and double-distilled water with a specific conductivity of $1.1 \pm 0.1 \mu\text{S cm}^{-1}$ at 293.16 K was used to make up the solutions.

5.2.3. Optical microscopy (OM)

The morphology of steel surfaces was examined by optical microscopy. The optical micrographs were acquired by using an optical microscope Zeiss, AxioLab A (Carl Zeiss Jena GmbH). Digital images at various magnifications were taken by a camera connected to the optical microscope. The calibration was performed using a TEM grid with a hole size of about 56 μm as reference.

5.2.4. XRF analysis

The X-ray fluorescence spectroscopy (XRF) was exploited to obtain the bulk composition of the alloy by a hand-held standard-less XRF spectrometer SPECTRO xSORT (Spectro Analytical Instruments GmbH, Kleve, Germany). The details on instrument set-up and calibration are provided in chapter 4 (§4.2.4). The results over three independent measurements are reported in table 3 and the experimentally determined composition is in very good agreement with the expected one (Table 1).

Table 3: stainless-steel composition by XRF.

Alloying elements	Fe	Cr	Mn	Mo	Ni
wt %	59 (1)	20 (1)	18.2 (0.1)	1.91 (0.05)	0.13 (0.03)

5.2.5. Electrochemical tests

A plexiglass three-electrode cell [8,9], with a 0.785 cm^2 lateral porthole (\varnothing 1 cm), was used to perform the electrochemical tests. The MP samples were positioned and pushed against the o-ring sealing of the hole. 200 cm^3 of the test solutions were used for each electrochemical measure. A potentiostat/galvanostat model VersaSTAT3 (Ametek Scientific Instruments Inc., USA) was used, with a platinum counter electrode and a saturated calomel reference electrode ($E = + 0.241$ V vs. NHE). The reference electrode was placed into an intermediate vessel filled with a saturated KCl solution and inserted into a Haber-Luggin capillary filled with the test solution. All potentials are referred to the saturated calomel electrode (SCE). The electrochemical tests were carried out at 25

± 1 °C and the data are reported as mean value over at least three independent measurements; the standard deviation is given in parentheses. The data are acquired using Versa studio software [10].

Open Circuit Potential (OCP) and Linear Polarization resistance (LPR)

The open circuit potentials (OCP) of the stainless-steel samples were acquired open to air after 1 h, 3h and 16 h of contact with the three different artificial saliva solutions. At the end of OCP experiments, the linear polarization resistance (LPR) measurements were performed applying a potential of ± 20 mV vs OCP and with a scan rate equal to 0.116 mV s^{-1} . From these measurements it was possible to determine the polarization resistance values (R_p).

Cathodic and anodic polarization curves

Cathodic and anodic polarization curves were acquired with a scan rate of 0.2 mV s^{-1} , following the OCP measurements for 1 h of contact with the different formulations. The scan was started applying a potential of -1400 mV vs OCP for the cathodic region and then run to the transpassive potential for the anodic potentiodynamic curves.

5.2.6. XPS surface analysis

The surface composition was investigated by X-ray photoelectron spectroscopy (XPS) using a ThetaProbe spectrometer (ThermoFisher, East Grinstead UK) equipped with a monochromatic $\text{AlK}\alpha$ source ($h\nu = 1486.6 \text{ eV}$). The beam diameter used in this work was $400 \mu\text{m}$, operating at 6.7 mA and 15kV (100 W). Survey and high-resolution spectra were acquired with a step size of 1 eV and 0.05 eV respectively, in fixed analyser transmission mode (FAT). The pass energy was set at 200 eV for the acquisition of survey and 100 eV for the high-resolution (HR) spectra in standard lens mode. In these conditions the full-width at half-maximum (fwhm) of the peak height for $\text{Ag } 3d_{5/2}$ was found to be equal to $0.93 \pm 0.05 \text{ eV}$. The linearity of the binding energy scale was checked according to ISO 15472:2014 with an accuracy of $\pm 0.1 \text{ eV}$.

High-resolution spectra were acquired in angle-resolved lens mode at 16 emission angles, ranging from 24.88 – 83.13° , and a pass energy of 150 eV . The angular response of the instrument was checked by using a flat sputter-cleaned Ag and the intensity vs angles data were collected during the angle signature acquisition procedure [11].

Data were processed with CASA XPS software (v2.3.24, Casa Software Ltd., Wilmslow, Cheshire, UK). The Shirley-Sherwood background subtraction routine was applied before the curve fitting procedure [12]. The quantitative composition of the film was calculated on the basis of the first-principle method [13] assuming the sample homogeneity. The experimental areas are corrected for Scofield ionization cross section [14], the asymmetry factor [15], for the spectrometer Intensity/energy response function and for $\Lambda = \lambda \cos \theta$ where λ is the inelastic mean free paths (IMFP) calculated according to [16] and θ is the emission angle; $\theta = 53^\circ$ for the Theta Probe spectrometer when used in the standard lens mode. More details are provided in chapter 4 (§ 4.2.6).

5.3. Results

5.3.1. Morphology

The surface of the as received and mechanically polished samples was observed at the optical microscope. Surface defects, such as scratches, are revealed on the as received alloy (Figure 2a), the mechanical polished sample, indeed, shows a less rough surface, with almost few scars (Figure 2b). Following the contact with the model solutions using, the area of the brass surface was slightly opaque and the presence of a film was visible as it also appeared in the micrographs (Figures 2c-h). All samples show the presence of small particles on the surface. These particles are bigger in the samples exposed to D solution after 1 hour and their amount increases significantly upon the exposure time (Figures 2c and 2d). The same effect was not observed on the samples exposed to C-B (Figures 2e and 2f) and SALMO (Figures 2g and 2h) formulations.

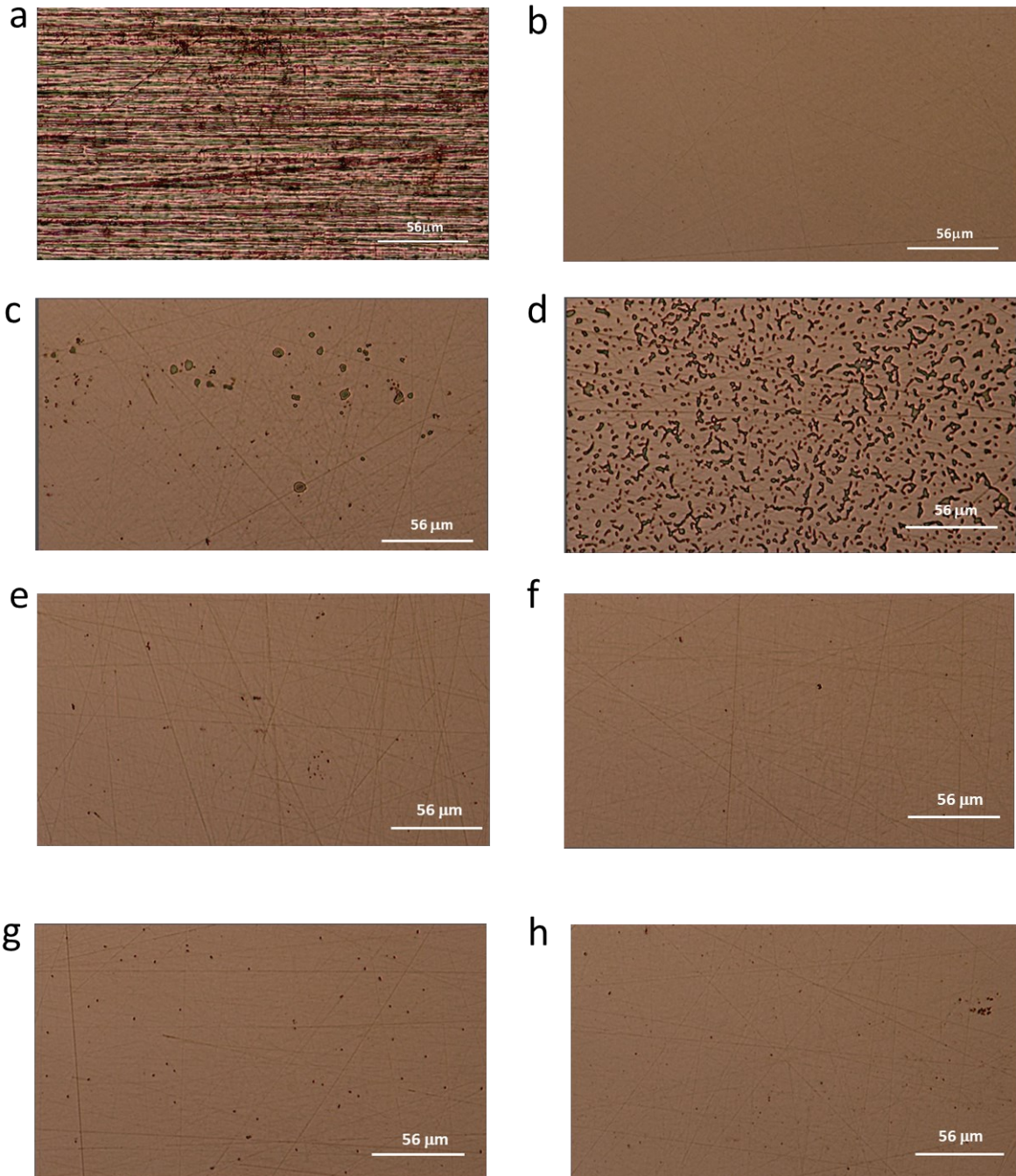


Figure 2: Optical micrographs of the stainless-steel DIN 1.4456 surfaces - objective Epiplan 100 X / 0.75: a) as received stainless-steel; b) mechanically polished stainless-steel; c) stainless-steel after the exposure to D for 1h; d) stainless-steel after the exposure to D for 16 h; e) stainless-steel after the exposure to C-B for 1h; f) stainless-steel after the exposure to D for 16h; g) stainless-steel after the exposure to SALMO for 1h; h) stainless-steel after the exposure to SALMO for 16h.

5.3.2. Electrochemical Results

Open circuit potential (OCP)

The open circuit potential (OCP) of the mechanically polished stainless steel was measured for 1 h, 3 h and 16 h of exposure to the solutions in equilibrium with air and at ambient temperature ($25 \pm 1^\circ\text{C}$). The average values of the OCP at the various times are reported in Table 4. Immediately after the exposure of the samples to the artificial saliva solutions, the OCP decreases reaching a minimum after few minutes, suggesting the dissolution of the thin surface film formed during mechanical polishing (Figure 3); The OCP in the samples exposed to D, at the first hour increases more slowly than the others (Figure 3a). For all samples, after 16 hours the OCP values rise toward positive values, indicating the growth and the increasing stability of the passive film (Figure 3b).

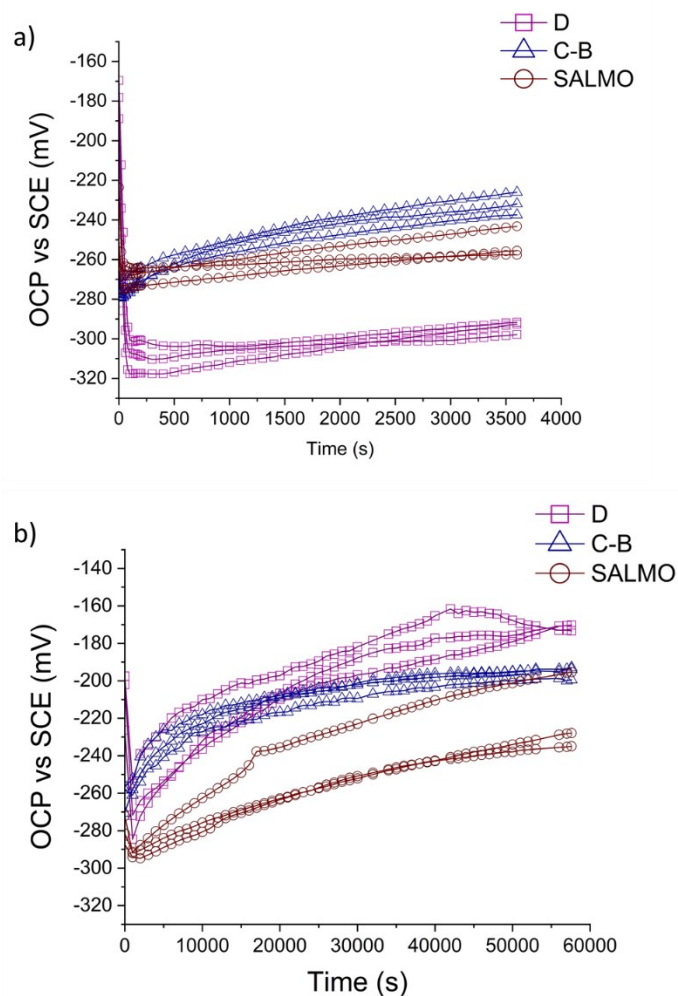


Figure 3: Open circuit potential versus time curves for stainless-steel DIN 1.4456 exposed for 1 h (a) and 16 h (b) to Darvell (D), Carter-Brugirard (C-B) and SALMO solutions. Three independent measurements for each solution were performed and in this picture all measurements are shown.

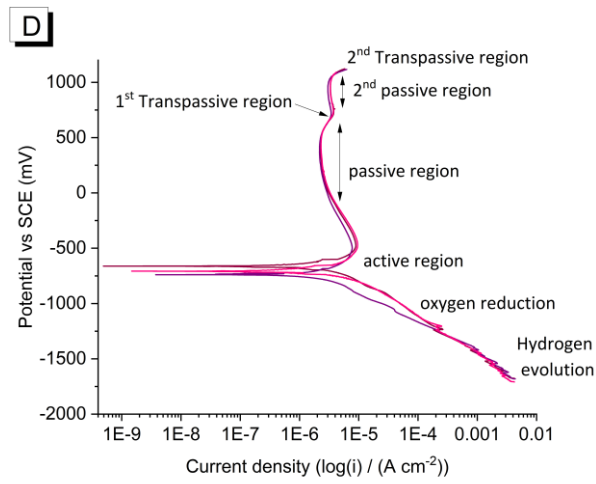
Table 4: Open circuit potential mean values (mV vs. SCE) of stainless-steel DIN 1.4456 exposed to model solutions, recorded after t= 0 s (E_0), t = 1h (E_{1h}), t = 3 h (E_{3h}) and t = 16 h (E_{16h}). Standard deviations are given in parentheses.

Model solutions	OCP vs SCE (mV)			
	E_0	E_{1h}	E_{3h}	E_{16h}
Darvell	-198 (20)	-294 (3)	-258 (18)	-171 (2)
Carter-Brugirard	-263 (9)	-232 (6)	-221 (1)	-195 (3)
SALMO	-265 (27)	-252 (8)	-241(3)	-217 (19)

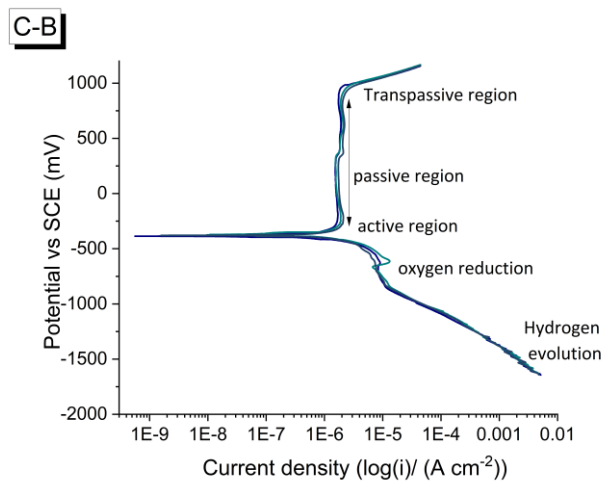
Potentiodynamic polarization curves (Tafel plot)

The polarization curves of stainless-steel DIN 1.4456 samples in all saliva solutions tested (Figure 4) showed a cathodic branch, an active passive transition and a broad passive range. A similar behaviour of anodic and cathodic curves of the Tafel plot was observed for samples exposed to D, C-B and SALMO (Figure 4a, 4b and Figure 4c) while the samples exposed to D solution showed a difference in the anodic curve at about 600 mV vs SCE an increase in current density is observed.

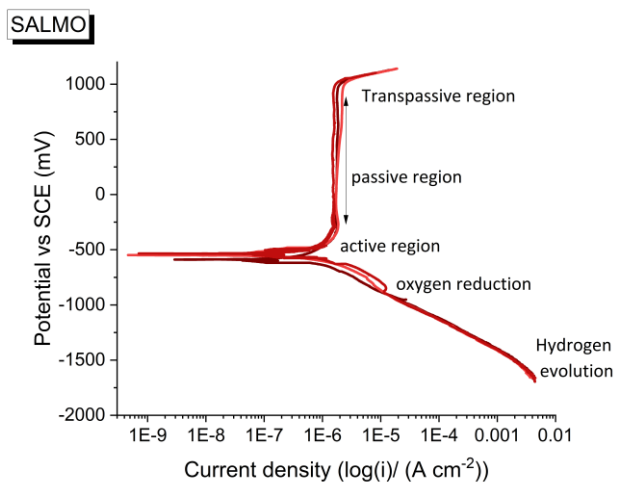
The cathodic curves show, for all samples, a shoulder at low cathodic current density of about $8 \cdot 10^{-6}$ A/cm² due to diffusion limited oxygen reduction. Then the current density increases exponentially again at more negative potential from -860 mV vs SCE to -1600 mV vs SCE when hydrogen evolution occurs.



(a)



(b)



(c)

Figure 4: Potentiodynamic polarization curves of stainless-steel DIN 1.4456 after 1 h of contact to a) D, b) C-B and c) SALMO. Three independent measurements for each solution were performed.

Linear Polarization resistance (LPR) and corrosion rate

Linear polarization resistance measurements were carried out at the end of the OCP measurements for each exposure period of 1 h, 3 h and 16 h. The LPR plots measured (Appendix A-Figure A.5) in saliva solutions are curves characterized by a linear region at ± 20 mV around the OCP, and the R_p values are determined from the slope of the linear region. The average R_p values and standard deviation for each formulation and for the different exposure times are reported in Table 5. The R_p values increased with longer exposure times and, for each time, the values of the different solutions were similar. The corrosion current density (i_{corr}) was estimated from the R_p measurements applying the Stern–Geary equation [17] (eq. 7 Chapter 3). As the anodic Tafel constant was difficult to determine, a value of $B= 52$ mV usually assumed for steel in the passive state was used. [18]

The corrosion rates v_{corr} were calculated for the different model solutions at the various exposure times by using Faraday's law; the conversion factor is $i_{corr} 1\mu\text{A}/\text{cm}^2 = 11.7 \mu\text{m}/\text{year}$ considering the density and molar mass of iron. The average values and standard deviation are reported in Table 6. The corrosion rate values decreased upon time for all solution. The high value was obtained for C-B after 1 hour, but for prolonged exposure it decreased markedly compared to the others. After 16 hours the values were found to be quite similar among the solutions.

Table 4: Polarization resistance (R_p) mean values at various exposure times for each model solution. Standard deviations are given in parentheses.

Model solutions	$R_{p_{1h}}$ [$M\Omega \cdot \text{cm}^2$]	$R_{p_{3h}}$ [$M\Omega \cdot \text{cm}^2$]	$R_{p_{16h}}$ [$M\Omega \cdot \text{cm}^2$]
Darvell	0.42 (0.06)	0.6(0.1)	1.2 (0.1)
Carter-Brugirard	0.3 (0.1)	1.1 (0.2)	1.9 (0.6)
SALMO	0.38 (0.02)	0.6 (0.2)	1.2 (0.3)

Table 6: Corrosion rate (v_{corr}) mean values at various exposure times for each model solution. Standard deviations are given in parentheses.

Model solutions	v_{corr} 1h [μm / year]	v_{corr} 3h [μm / year]	v_{corr} 16h [μm / year]
Darvell	1.5 (0.2)	1.0 (0.2)	0.5 (0.1)
Carter-Brugirard	2 (1)	0.6 (0.1)	0.3 (0.1)
SALMO	1.6 (0.1)	1.1 (0.5)	0.5 (0.2)

5.3.3. XPS results

Stainless steel DIN 1.4456 mechanically polished

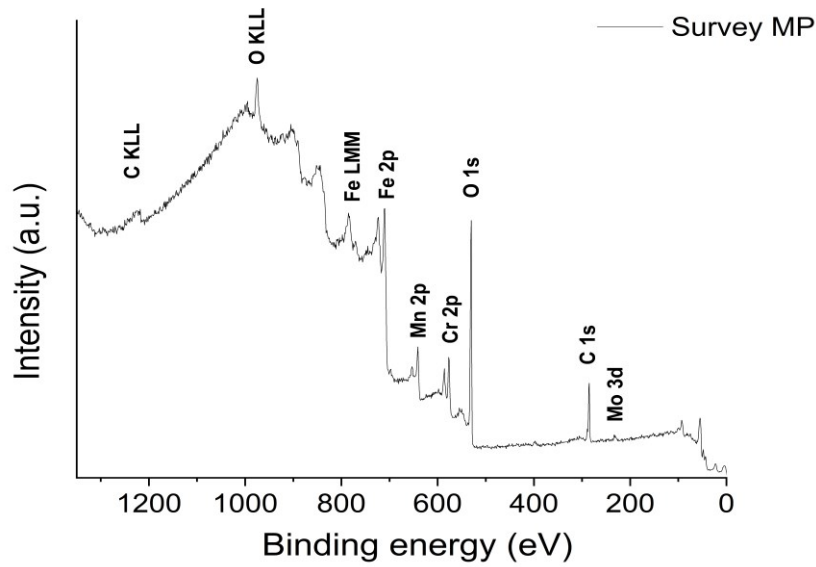
The samples were mechanically polished using the protocol described in Table 2 and characterized by XPS. The XPS survey spectra (Figure 5a) show the presence of iron, manganese, chromium and molybdenum belonging to the alloy, oxygen due to the oxidation of the surface of the sample, and carbon due to organic contamination layer. The high-resolution spectra of Fe2p, Cr2p, Mn2p and Mo3d are showed in Figure 5 and in Table 7 the binding energy of the photoelectron lines and the curve fitting parameters are listed.

- The Fe 2p_{3/2} signal shows four components (Figure 5b); the component at 707.0 (0.1) eV is assigned to metallic iron while, as far as the oxidized components, Fe (II) is found at 709.7 (0.1) eV with its satellite at 715.2 (0.1) eV, Fe (III) oxide at 710.9 (0.1) eV and the oxy-hydroxide component at 712.4 (0.1) eV. (Table 7)
- The Cr 2p_{3/2} signal consists of three components (Figure5c): metallic chromium at 574.0 (0.1) eV, Cr (III) oxide at 576.5 (0.1) eV and Cr (III) hydroxide at 578.1 (0.1) eV.
- The manganese Mn 2p_{3/2} spectra show five contributions (Figure 5d): the metallic manganese at 638.7 (0.1) eV, Mn (II) oxide at 640.9 (0.1) eV and the Mn (IV) oxide at 642.5 (0.1) eV.
- Molybdenum 3d peak (Figure 5e) is complex due to the lower signal-to-noise ratio and the superposition of two contributions of the spin-orbit doublet (3d_{5/2} and 3d_{3/2} with a difference

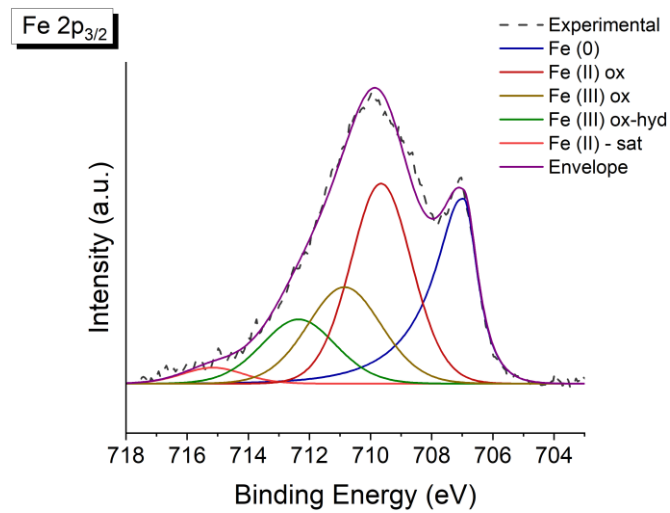
in binding energy of 3.15 eV . The metallic component was found at 227.9 (0.1) eV, the Mo (IV) oxide at 231.0 (0.1) eV and Mo (VI) hydroxide at 232.7 (0.1) eV.

The binding energies of the revealed components for the main constituents of the stainless steel are in agreement with the literature. [3, 18-23]

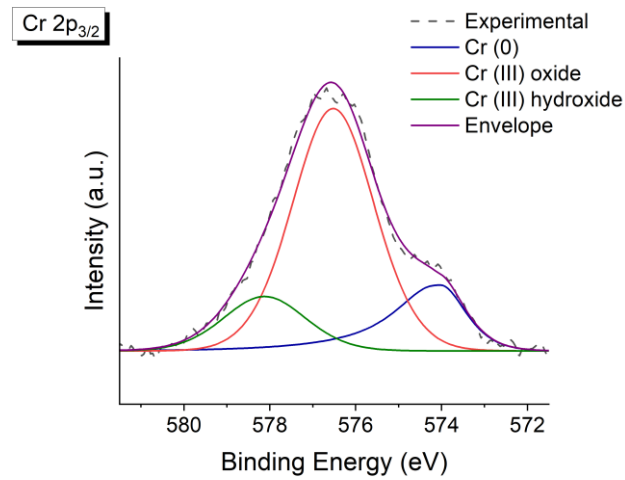
a)



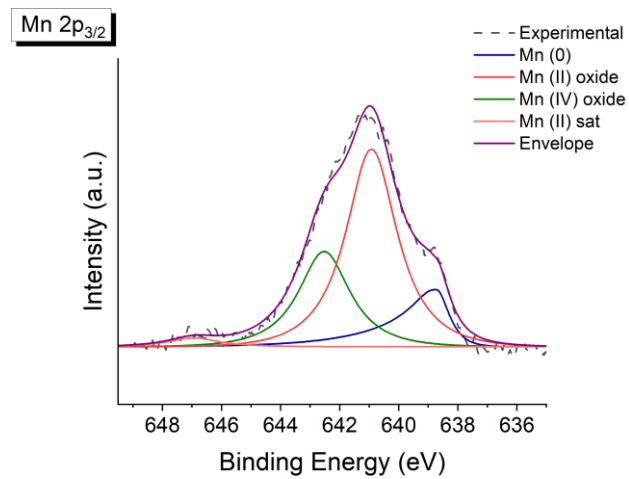
b)



c)



d)



e)

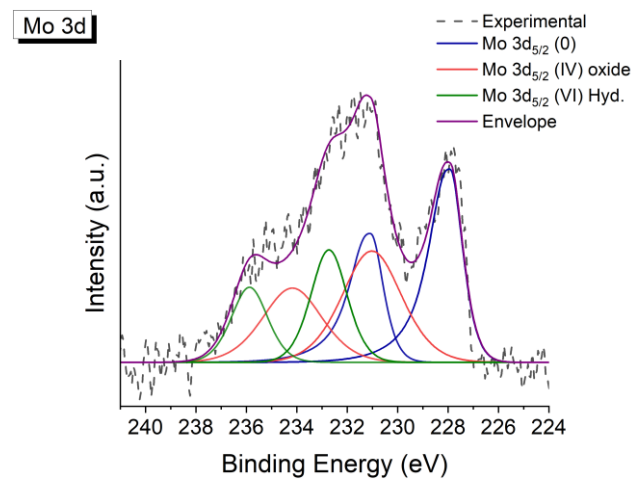


Figure 5: Stainless steel DIN 1.4456 mechanically polished a) Survey; High-resolution spectra of b) Fe $2p_{3/2}$ c) Cr $2p_{3/2}$ d) Mn $2p_{3/2}$ e) Mo 3d. A Shirley-Sherwood background subtraction was applied prior curve-fitting.

Table 7: Peak parameters for fitting Fe 2p, Cr 2p, Mn 2p and Mo 3d spectra of stainless-steel.

Peak	BE (eV ± 0.1)	Fwhm (eV ± 0.1)	Line shape
Fe 2p_{3/2} met.	707.0	1.2	GL(85)T(0.80)
Fe 2p_{3/2} (II) oxide	709.7	2.6	GL(30)
Fe 2p_{3/2} (II) sat.	715.2	2.6	GL(30)
Fe 2p_{3/2} (III) oxide	710.9	3.1	GL(30)
Fe 2p_{3/2} (III) oxy-hydroxide	712.4	3.1	GL(30)
Cr 2p_{3/2} met.	574.0	1.4	GL(65)T(1)
Cr 2p_{3/2} (III) oxide	576.5	2.2	GL(30)
Cr 2p_{3/2} (III) hydroxide	578.1	2.2	GL(30)
Mn 2p_{3/2} met.	638.7	1.0	GL(80)T(0.55)
Mn 2p_{3/2} (II) oxide	640.9	2.1	GL(90)
Mn 2p_{3/2} (II) sat.	647.0	2.1	GL(90)
Mn 2p_{3/2} (IV) oxide	642.5	2.1	GL(90)
Mo 3d_{5/2} met.	227.9	1.2	GL(60)T(1.2)
Mo 3d_{5/2} (IV) oxide	231.0	2.8	GL(45)
Mo 3d_{5/2} (VI) oxide	232.7	1.7	GL(45)

Stainless steel DIN 1.4456 exposed to saliva solutions

The survey spectra of the stainless-steel exposed to the saliva solutions are reported in Figure 6. In all sample the Fe, Cr, Mn, Mo, C, O and P signals were revealed. On the samples exposed to SALMO also calcium was revealed.

The survey spectra (Figure 7) show different ratio Fe/Cr among the samples: the film formed on the samples exposed to D solution is enriched in chromium.

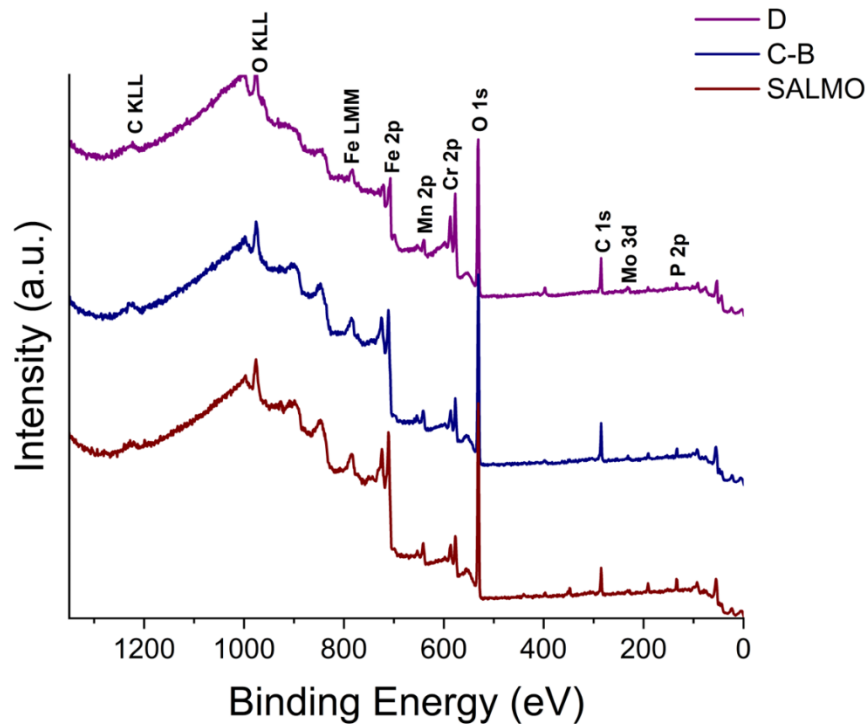


Figure 6: Survey spectra of stainless-steel DIN 1.4456 exposed for 1 h to D, C-B and SALMO (S) saliva solutions (from top to bottom respectively).

The binding energy (BE) of the most intense photoelectron peaks are provided in Table 8.

- The Fe $2p_{3/2}$ signal shows for all samples (Figure 8a) six components: the metallic component at 706.9 (0.1) eV, the FeO at 709.5 (0.1) eV, and its satellite at 715.1 (0.1) eV. The at Fe_2O_3 710.8 (0.1) eV and the Fe(III)–OOH component at 712.3 (0.1) eV. The component ascribed to $FePO_4$ was found to be at 713.8 (0.1) eV.

In the sample exposed to D solution (Figure 7a top) the signal is mainly composed of the metallic component. The phosphate component is less intense compared to the signal from the samples exposed 1 h to C-B and SALMO (Figure 7a centre and bottom respectively).

- The Cr $2p_{3/2}$ signal shows for all samples (Figure 7b) four components: The Cr(0) component at 574.0 (0.1) eV, the Cr (III) oxide at 576.5 (0.1) eV. The $CrPO_4$ component was found to be at 577.1 (0.1) eV according to [24], then the Cr(III) hydroxide at 578.1 (0.1) eV.

The samples exposed to D solution (Figure 7a top) are strongly enriched in Cr(III) oxi-hydroxide and phosphate (Table 9). The contribution of $CrPO_4$ relative to Cr(III) oxi-hydroxide is higher as compared to the samples exposed to C-B and SALMO (Figure 7b centre and bottom respectively).

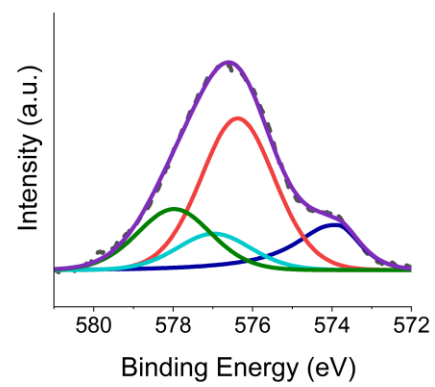
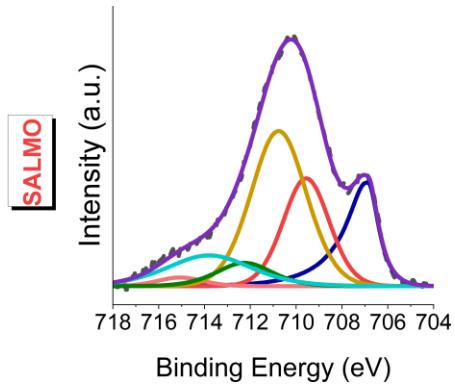
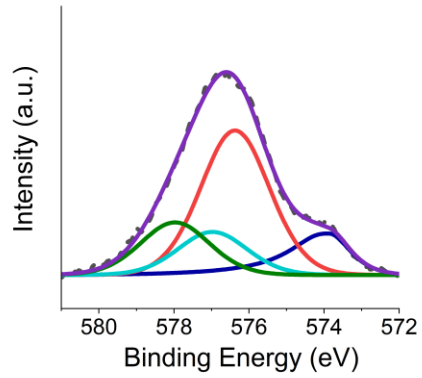
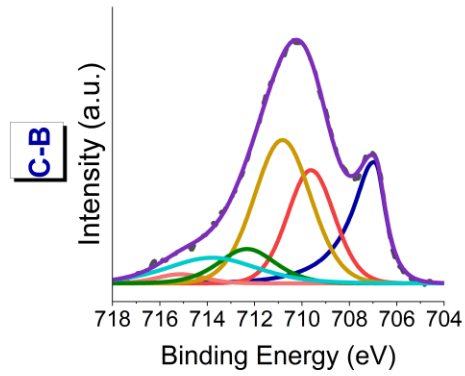
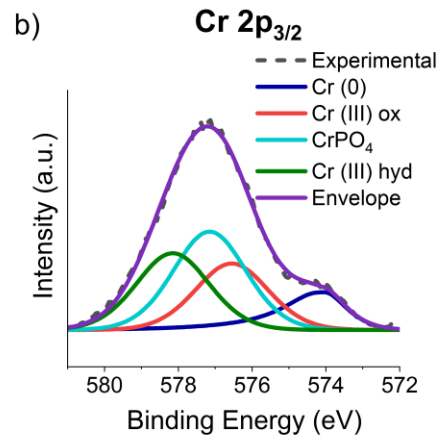
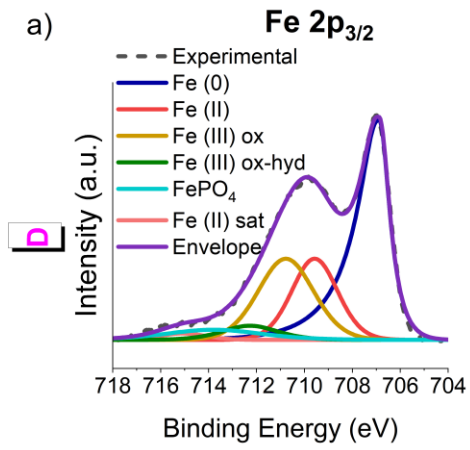
- The Mn $2p_{3/2}$ peak shows for all samples (Figure 7c) three components: the metallic one at 638.6 (0.1) eV, the Mn(II) oxide at 641.0 (0.1) eV and the Mn (IV) oxide at 642.3 (0.1) eV.

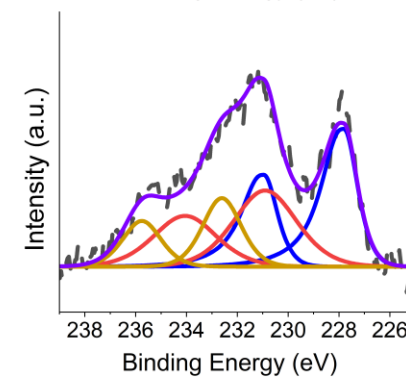
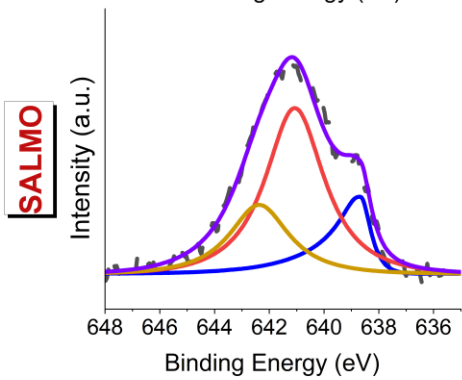
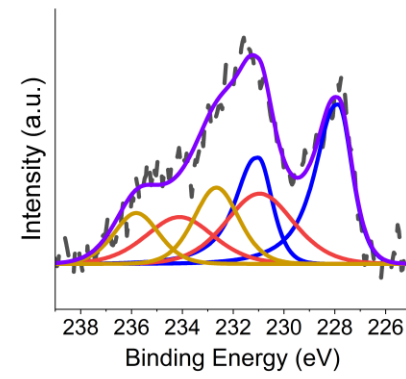
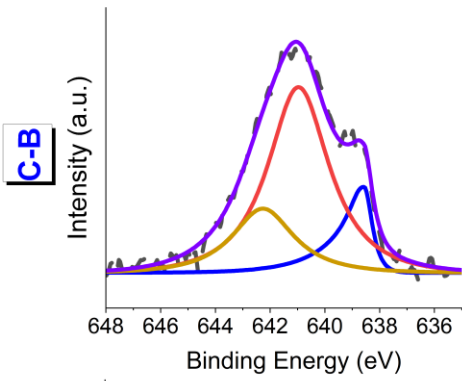
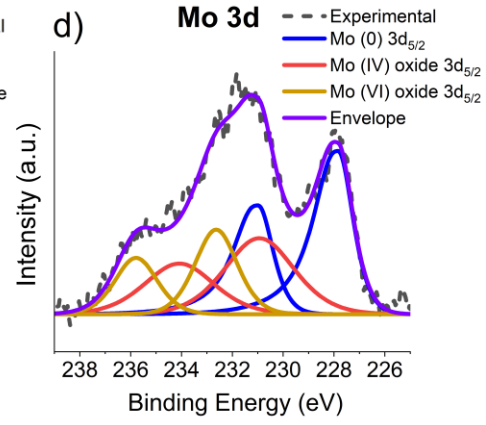
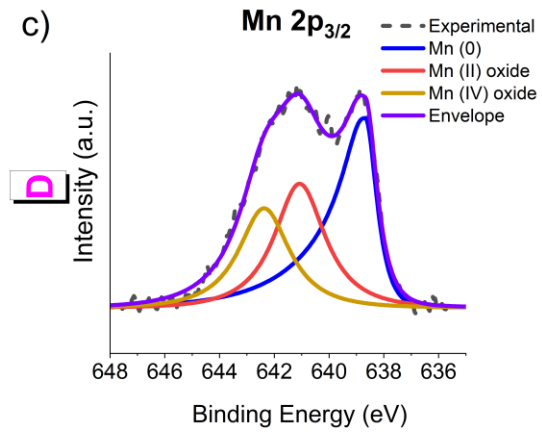
Also in this case, the sample exposed to D (Figure 7c top) show a high contribution of the metallic component compare the Mn $2p_{3/2}$ signal observed for the samples exposed to C-B and SALMO (Figure 7c centre and bottom respectively). For these sample the major contribution derived from the MnO component.

- The Mo 3d peak (Figure 7d) shows three components: the binding energy for the metallic component was 227.8 (0.1) eV; for Mo (IV) oxide it was 230.9 (0.1) eV and in the case of the Mo (VI)oxide the peak was found at 232.6 (0.1) eV.

For this peak, there are no great differences among the samples.

- The P 2p signal (Figure 7e) shows the P $2p_{3/2}$ peak at 133.5 (0.1) eV for all samples, ascribed to Fe and Cr phosphates and probably also to calcium phosphate in the case of samples exposed to SALMO, since when the stainless steel is exposed to this formulation, the only one containing calcium ions due to the presence of CaCl_2 , Ca $2p_{3/2}$ peak at 347.8 (0.1) eV is detected (Appendix A-Figure A.6).





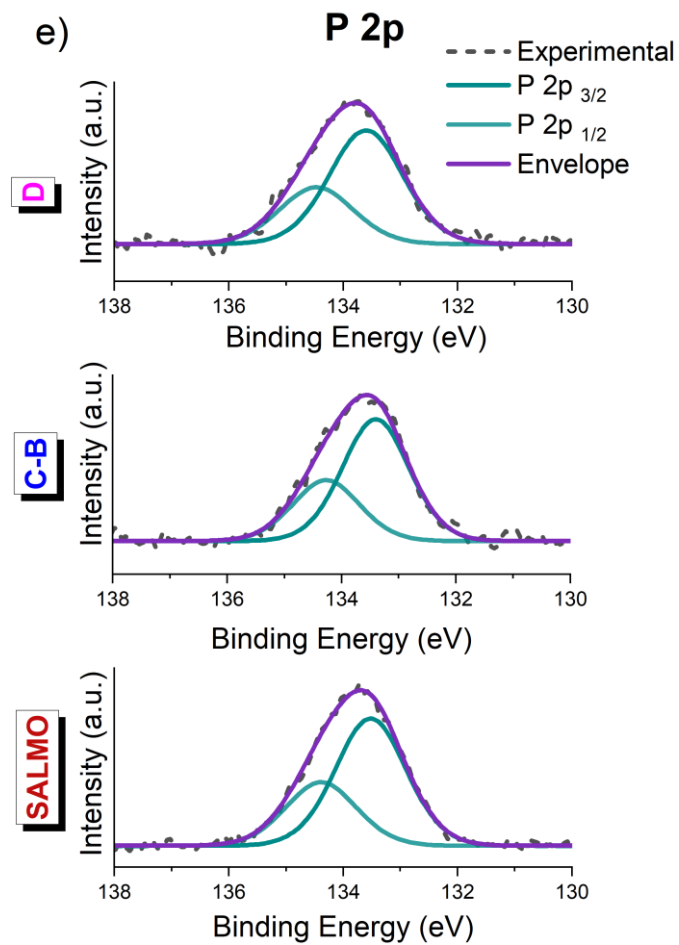


Figure 7: High-resolution spectra of a) Fe 2p_{3/2}; b) Cr 2p_{3/2}; c) Mn 2p_{3/2}; d) Mo 3d; e) P 2p of stainless-steel exposed for 1 h to D, C-B and SALMO (from top to down respectively). A Shirley-Sherwood background subtraction was applied prior curve-fitting.

Table 8: Average binding energy (eV) of the intense photoelectron peaks of the element detected on stainless-steel DIN 1.4456 after 1h of exposure to D, C-B and SALMO saliva model solutions.

Peak	BE (eV ± 0.1)
Fe 2p_{3/2} met.	706.9
Fe 2p_{3/2} (II) oxide	709.5
Fe 2p_{3/2} (II) sat.	715.1
Fe 2p_{3/2} (III) oxide	710.8
Fe 2p_{3/2} (III) oxy-hydroxide	712.3
FePO₄	713.8
Cr 2p_{3/2} met.	574.0
Cr 2p_{3/2} (III) oxide	576.5
CrPO₄	577.1
Cr 2p_{3/2} (III) hydroxide	578.1
Mn 2p_{3/2} met.	638.6
Mn 2p_{3/2} (II) oxide	641.0
Mn 2p_{3/2} (IV) oxide	642.3
Mo 3d_{5/2} met.	227.8
Mo 3d_{5/2} (IV) oxide	230.9
Mo 3d_{5/2} (VI) oxide	232.6
P 2p_{3/2}	133.5
Ca 2p_{3/2} *	347.8

*Calcium detected only for the samples exposed to SALMO.

Quantitative composition (at %) of the main elements detected on stainless-steel DIN 1.4456 surface after 1h of exposure to Darvell (D), Carter-Brugirard (C-B) and SALMO saliva model solutions are reported in Table 9.

The main result observed is that samples exposed to Darvell solution show a much higher concentration of Cr(III) oxide and phosphate components compared to SALMO and C-B solution. The Fe oxide and phosphate components, indeed, were higher on the samples exposed to C-B and SALMO than in samples exposed to D. The high at % determined on the steel exposed to SALMO solution for the phosphorous signal might be ascribed to the presence of calcium, as calcium phosphate. The Mn (0) component resulted higher in the samples exposed to D compared to the other samples.

This is seen more clearly when calculating the composition of the film (all oxidized components) separately from the metallic substrate beneath (Table 10). The passive film of samples exposed 1h to D solutions is enriched in Cr(III) and depleted in Fe(II) and Fe(III); these results are in agreement with those observed for the potentiodynamic curves (Figure 4a).

The composition of the alloy beneath the oxide film formed after 1h of immersion in C-B and SALMO results approximately close to the bulk composition, with a slight depletion in manganese. Moreover, the composition of the alloy beneath the oxide film formed after the exposure to the D solution results depleted in iron and enriched in molybdenum.

Table 9: Quantitative composition (at %) of the main elements detected on stainless-steel DIN 1.4456 surface after 1h of exposure at Darvell (D), Carter-Brugirard (C-B) and SALMO saliva model solutions. For all elements the metallic (met.) contribution, the sum of oxides and hydroxides contribution (ox.) and the phosphate contribution are reported. Standard deviations are given in parentheses. *Calcium is detected only in the samples exposed to SALMO.

	At % D	At % C-B	At % SALMO
O 1s	68 (1)	68 (1)	67 (2)
Cr 2p_{3/2} met.	1.9 (0.4)	1.0 (0.1)	0.9 (0.1)
Cr 2p_{3/2} ox.	7.4 (0.9)	5.1 (0.4)	4.1 (0.3)
CrPO₄	4.2 (0.7)	0.8 (0.3)	0.6 (0.2)
Fe 2p_{3/2} met.	4.7 (0.8)	3.3 (0.2)	2.8 (0.4)
Fe 2p_{3/2} ox.	4.3 (0.6)	10.6 (0.8)	11 (1)
FePO₄	0.3 (0.2)	1.1 (0.4)	1.9 (0.5)
Mn 2p_{3/2} met.	1.3 (0.3)	0.5 (0.1)	0.4 (0.1)
Mn 2p_{3/2} ox.	1.6 (0.3)	2.4 (0.3)	2.4 (0.2)
Mo 3d_{5/2} met.	0.43 (0.04)	0.29 (0.02)	0.22 (0.03)
Mo 3d_{5/2} ox.	0.55 (0.07)	0.40 (0.02)	0.32 (0.02)
P 2p_{3/2}	4.9 (0.4)	6.2 (0.6)	8.3* (0.8)

Table 9: Composition of the substrate and of the film formed at the surface of the 1.4456 stainless steel after one hour of contact with the three formulations. The compositions of the substrate and of the film are calculated taking into account the metallic components of Cr, Fe, Mn and Mo signals and the oxidized components of the same elements as the sum of oxides, hydroxides and phosphate (for Cr and Fe). Standard deviations are given in parentheses.

Substrate composition (at%)			
	D	C-B	SALMO
Cr - met	23.1 (0.7)	20.2 (1.1)	20.0 (0.4)
Fe - met	56 (1)	64.1 (1.0)	66 (2)
Mn - met	15 (1)	10.0 (1.7)	9 (1)
Mo - met	5 (1)	5.7 (0.6)	5.0 (0.4)
Film composition (at)			
	D	C-B	SALMO
Cr – ox +P	64 (5)	29 (3)	23 (1)
Fe – ox+P	25 (4)	57 (3)	63 (2)
Mn - ox	9 (1)	12 (1)	12 (1)
Mo - ox	3.0 (0.4)	2.0 (0.1)	1.6 (0.1)

5.4. Discussion

Dental alloy materials should have good mechanical properties and a high corrosion resistance to be biocompatible. The biocompatibility (IUPAC definition) “is the ability to be in contact with a living system without producing an adverse effect” [25]. The corrosion of metals and alloys may release allergenic, toxic/cytotoxic or carcinogenic (e.g., Ni, Co, Cr, V, Al) species that cause the failure of implants. [26,27] The oral cavity is a potentially highly corrosive environment for the materials used for dental alloys, such as stainless steels, thus, they have to show only negligible corrosion rates.

In the following, the effect of the exposure time on the corrosion rate and the effect of the model solutions on the film composition are discussed.

Influence of exposure time

The present section of this work investigates the corrosion behaviour of the nickel-free stainless-steel DIN 1.4456 after exposure to different artificial saliva solutions for 1h, 3 h and 16 h. The obtained results clearly indicate that a passive film is formed on the nickel-free stainless-steel DIN 1.4456 in all artificial saliva model solutions.

The OCP values tend to increase with the exposure time (Figure 8).

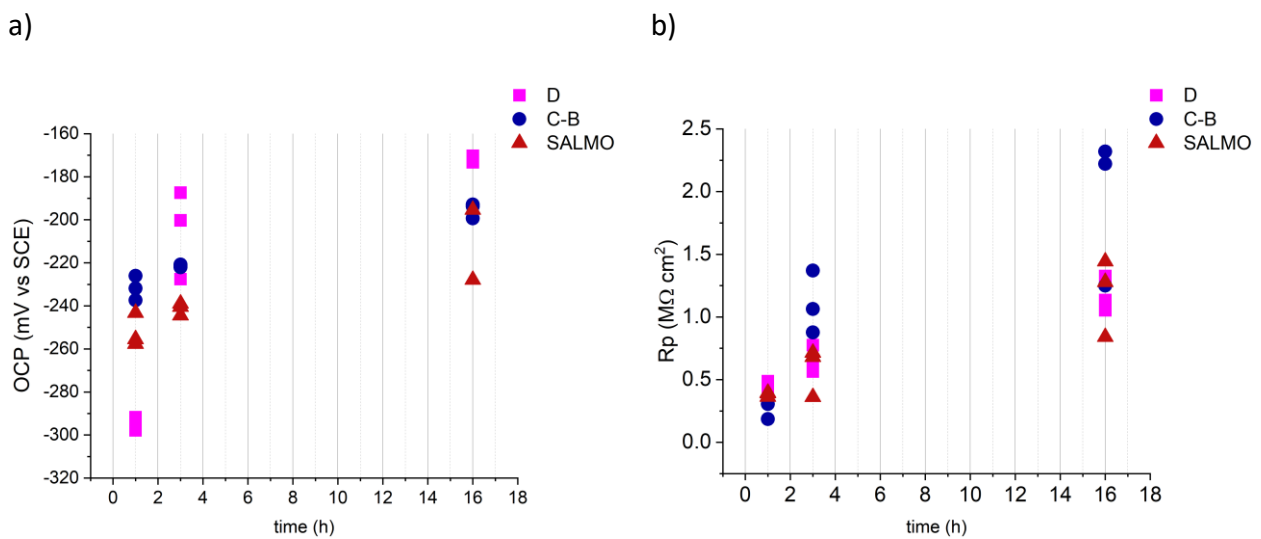


Figure 8: Open circuit potential versus time and b) polarization resistance (Rp) vs time for DIN 1.4456 exposed for 1, 3 and 16 h to D, C-B and SALMO. Three independent measurements for each solution were performed.

The increase of the OCP passing from 1 h to 16 h is more pronounced for the samples exposed to Darvell solution compared to the samples exposed to C-B and SALMO. This trend in OCP with exposure time is typical for the formation of the passive film and it was also observed for the same Ni-free stainless steel in contact with Tani-Zucchi formulation both at 25 °C [28] and at 37 °C [3]. Together with the increase of the OCP values, also the increase in the polarization resistance (Figure 8b) is observed and, consequently, the corrosion rate values show a marked decrease with exposure time (Figure 9).

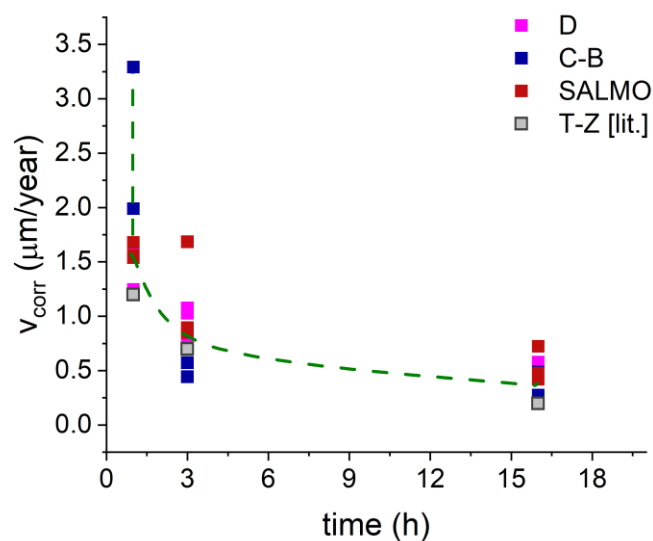


Figure 9: Evolution of the corrosion rate vs exposure time for the DIN 1.4456 stainless steel exposed to D, C-B and SALMO formulations. Data from [28] for the same material exposed to Tani-Zucchi solution at 25°C are reported from comparison.

Furthermore, the corrosion rate values are in agreement with those reported after contact with Tani-Zucchi for 1h, 3 h and 16 h at 25°C [28] (Figure 9) and they are comparable with the results obtained when the nickel-free stainless-steel DIN 1.4456 is in contact with Tani-Zucchi formulation at 37°C. [3,29]

Observing the i_{corr} vs OCP (mV) graph it is possible to appreciate that is occurring the same mechanism (anodic control) for the Ni-free DIN 1.4456 in contact with all the three solutions here adopted (Figure 10) and this is also the same mechanism observed for the same stainless steel exposed to Tani-Zucchi at the same temperature adopted in this work (25°C) [28]. The findings of a previous study demonstrated that the same mechanism also occurs after the contact with Tani-Zucchi at 37°C [3.]

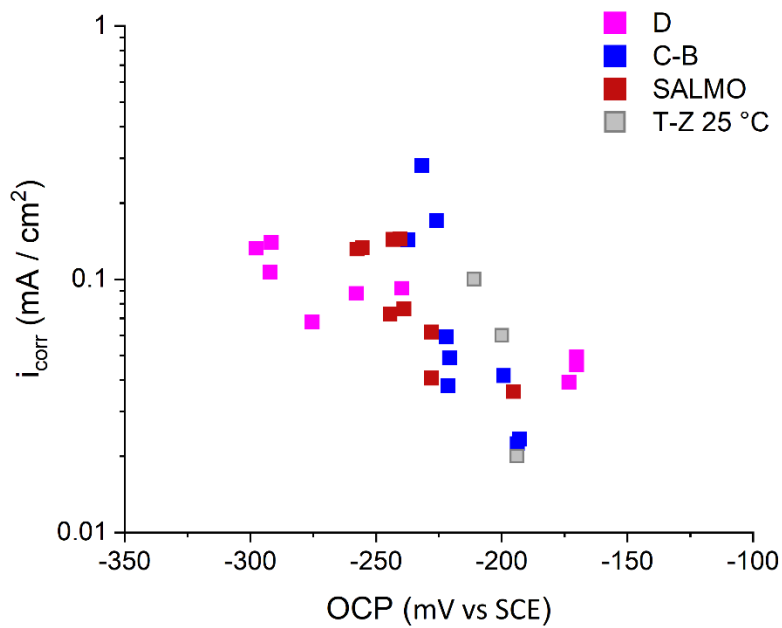


Figure 10: corrosion current density, i_{corr} , versus open circuit potential, OCP. DIN 1.4456 exposed to D, C-B and SALMO at 25°C. Data from [28] are reported as a comparison (grey squares).

Effect of model solutions on the film composition

Despite the fact that there were no significant differences in terms of corrosion rate among the samples exposed to D, C-B and SALMO, the Tafel plots showed different behaviour for the sample exposed to D. The Tafel plots recorded on the samples exposed for 1h to C-B and SALMO solutions, in fact, show a typical behaviour of a steel in the passive state [3, 18-21] with a dynamic passive current density of about $2 \cdot 10^{-6} \text{ A/cm}^2$. The samples exposed to D solution (Figure 4a), however, showed an increase in the current density at ca. 600 mV SCE, typical for chromium-enriched steels and this is due to the oxidation of chromium (III) to chromium (VI).

The presence of a Cr (III) enriched film formed after the contact with D solution at the open circuit potential (ca. -250 mV SCE, in the passive range) is confirmed by the XPS results (Figure 7, Table 9). In figure 11 the composition of the film determined taking into account only the oxidized components of Fe, Cr, Mn and Mo in 1.4456 after 1h of contact with D, C-B and SALMO, is compared with the bulk composition obtained by XRF and with the composition of the film reported for the same stainless steel after the contact for 1h with Tani-Zucchi formulation [3,29].

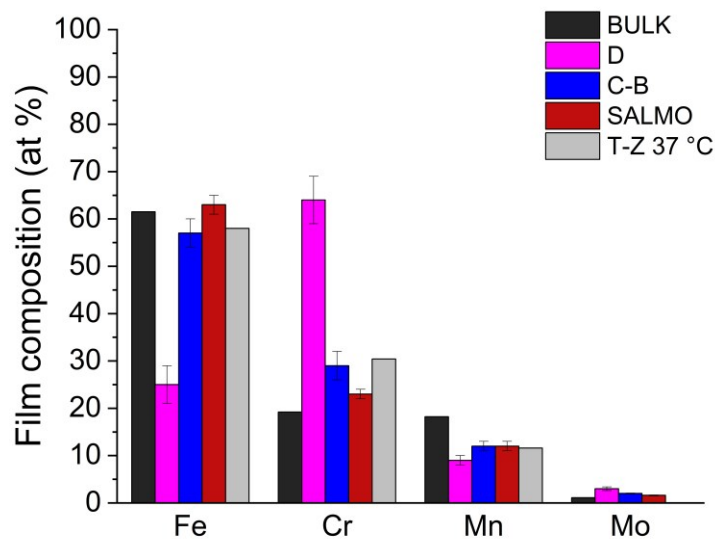


Figure 11: composition (at %) of the film determined taking into account only the oxidized components of Fe, Cr, Mn and Mo in 1.4456 after 1h of contact with D, C-B and SALMO, compared with the bulk composition obtained by XRF and with the composition of the film reported for the same stainless steel after the contact for 1h at 37 °C with Tani-Zucchi formulation. [3,29]

A dramatic increase in oxidized Cr content is found in the case of D solution compared to both the Cr content in the alloy and to Cr content in the film formed following the contact with other formulations. In parallel, a strong iron and manganese depletion is observed (Figure 10). In the case of Mn, the pronounced depletion was observed also by Elsener et al. [3] together with an iron content in the oxide slightly lower than in the bulk. The quantitative composition here obtained with C-B and SALMO are in pretty good agreement with those observed with Tani- Zucchi.

This result supports the hypothesis that also in the case of DIN 1.4456 stainless steel, the organic components of D solution play an important role in the film composition, similarly to what was observed for brass. While C-B, SALMO and Tani-Zucchi have a similar composition as far as the organic compounds, being the urea the major organic constituent, and no possible ligands are present, in D solution sodium citrate, uric acid and lactic acid are present. All these three compounds might form soluble complexes with iron [30-32] and this might be confirmed by the presence of the intense contribution of the metallic component in Fe 2p_{3/2} peak (Figure 8a bottom) when 1.4456 is in contact with D. In this case, the Fe/Cr atomic ratio in the film is about 7 times lower than the ratio calculated for the films formed upon contact with C-B and SALMO.

Estimated weight loss

From the corrosion rate values, the weight loss (WL: $\mu\text{gcm}^{-2}\text{week}^{-1}$) can be estimated by the formula:

$$\text{weight loss} = \frac{v_{\text{corr}} \times A \times D \times 100}{52}$$

Where v_{corr} is the corrosion rate ($\mu\text{m}/\text{year}$), $A = 0.785 \text{ cm}^2$ is the area of the porthole, $D = 7.874$ is the density (g/cm^3), 52 is the number of weeks per year and 100 is a factor that takes into account the conversion of μm to cm and of g to μg .

The weight loss calculated taking into account the v_{corr} after 16 h of exposure (Table 6) is reported in Table 10.

Table 10: v_{corr} and weight loss calculated for the Ni- free DIN 1.4456 stainless steel exposed to D, C-B and SALMO for 16 hours.

	v_{corr} ($\mu\text{m}/\text{year}$)	Weight loss ($\mu\text{g}/\text{cm}^2\text{week}$)
DARVELL	0.52 (0.06)	6.2 (0.7)
C-B	0.3 (0.1)	4 (2)
SALMO	0.5 (0.2)	6 (2)

The weight loss values observed for D- C-B and SALMO are comparable taking into account the uncertainty on the measurements. It is noteworthy that the steady state, after 16 hours, might have not been already reached. The literature data indicate, after 16 [29] hours and 24 hours [3] of exposure to Tani-Zucchi at 37°C , a weight loss of $9 \mu\text{g}/\text{cm}^2\text{week}$ and $3 \mu\text{g}/\text{cm}^2\text{week}$ respectively. Therefore, it is plausible that also in the present case, for prolonged times and in steady state conditions, the weight loss decreases.

Furthermore, it has to be considered that the data of this work are referred to a mechanically polished surface. According to literature, the amount of released iron, chromium and nickel from an abraded 316L stainless steel after 168 hours of contact with an acidic simulated body fluid was found to be four times higher than the amount of released ions from the as received steel. [33] Consequently, the use of Ni-free DIN 1.4456 stainless steel in the real conditions seems to meet the requirements of biocompatibility and good resistance to corrosion for application in orthodontics.

5.5. Conclusions

From the combination of electrochemical and XPS analyses on the Ni-free DIN 1.4456 stainless steel in contact with three different formulations of artificial saliva, the following conclusions can be drawn:

- The corrosion behaviour of the DIN 1.4456 is similar, despite the different composition of the three solutions, especially regarding the organic components.
- The corrosion resistance of the stainless-steel increases upon time due to the formation of a passive film.
- Despite the presence of possible ligands for iron in one of the three solutions, which seems to promote iron dissolution from the DIN 1.4456, the corrosion behaviour of stainless steel is comparable with the results observed with the solutions that do not contain organic ligands.
- When organic ligands are present, the passive film is strongly enriched in chromium oxi-hydroxide and it protects the stainless steel from further oxidation.

References

- [1] "P. Falagiani, M. Di Gioacchino, L. Ricciardi, P. L. Minciullo, S. Saitta, A. Carni, G. Santoro, S. Gangemi, M. Minelli, M.P. Bozzetti, S. Massari, S. Mauro, D. Schiavino, Systemic nickel allergy syndrome (SNAS): A review, *Rev. Port. Imunoalergologia*, 16(2), 135-147, 2008.
- [2] European Communities. European Dir. 94/27/EC of 30 June 1994, amending the 12th time Dir. 76/769/EEC on the approximation of the laws, regulations and administrative provisions of the Member States relating to restrictions on the marketing and use of dangerous substances. *Official J Eur Communities*, 37: 1-2. 1994.
- [3] B. Elsener, M. Pisu, M. Fantauzzi, D. Addari and A. Rossi, Electrochemical and XPS surface analytical study on the reactivity of Ni-free stainless steel in artificial saliva, *Materials and Corrosion*, 67, 591, 2016.
- [4] G. Tani, F. Zucchi, Electrochemical valuation of the corrosion resistance of commonly used metals in dental prosthesis, *Minerva Stomatologica*, 16, 710-713, 1967.
- [5] B. W. Darvell., The development of an artificial saliva for *in vitro* amalgam corrosion studies, *J. of Oral Rehabil.*, 5, 41, 1978.
- [6] M. Andrei, B. Galateanu, A. Hudita, M. Costache, P. Osiceanu, J.M. Calderon Moreno, S.I. Drob, I. Demetrescu, Electrochemical comparison and biological performance of a new CoCrNbMoZr alloy with commercial CoCrMo alloy, *Mater. Sci. Eng. C*, 59, 346, 2016.
- [7] F. Crea, C. De Stefano, D. Milea, A. Pettignano, S. Sammartano, SALMO and S3M: A Saliva Model and a Single Saliva Salt Model for Equilibrium Studies, *Bioinorg. Chem. Appli.*, *Bioinorg. Chem. and Appli.*, 2015, 267985, 2015.
- [8] B. Elsener, M. Crobu, M.A. Scorciapino, A. Rossi, Electroless deposited Ni-P alloys: corrosion resistance mechanism. *J Appl Electrochem* 38, 1053–1060, 2008.
- [9] M. Crobu, A. Scorciapino, B. Elsener, A. Rossi, The corrosion resistance of electroless deposited nano-crystalline Ni-P alloys, *Electroc. Acta*, 53, 3364, 2008.
- [10] VersaStudio 2.44.4, Princeton Applied Research, Ametek, 2015.
- [11] B. Barnard, P. Belcher, Theta probe spectrometer set up, March, 2003.
- [12] D. A. Shirley, *Physical Review B: Solid State*, 5, 4709, 1972.
- [13] D. Briggs and J. T. Grant, *Surface Analysis by Auger and X-ray Photoelectron Spectroscopy*, IM Publications and Surface Publication Data, West Sussex, 345, 2003
- [14] J. H. Scofield, Hartree-Slater subshell photoionization cross-sections at 1254 and 1487 eV, *J. Electron Spectrosc. Relat. Phenom.*, 8, 129, 1976.
- [15] R.F. Reilman, A. Msezane, S.T. Manson, Relative intensities in photoelectron spectroscopy of atoms and molecules, *J. Electron. Spectrosc. Relat. Phenom.*, 8, 389, 1976.
- [16] M. P. Seah, W. A. Dench, Quantitative electron spectroscopy of surfaces: A standard data base for electron inelastic mean free paths in solids, *Surf. Interface Anal.*, 1, 2, 1979.
- [17] M. Stern, A. L. Geary, *J. Electrochem. Soc.*, *Electrochemical Polarization*, 104, 56, 1957.
- [18] B. Elsener, Corrosion rate of steel in concrete—Measurements beyond the Tafel law, *Corrosion Science*, 47 (12), 3019-3033, 2005.
- [19] A. Rossi, B. Elsener, Role of the interface oxide film/alloy composition and stability of stainless steels, *Materials and Corrosion*, 63, N°12, 2012.
- [20] B. Elsener, D. Addari, S. Coray, A. Rossi Nickel-free manganese bearing stainless steel in alkaline media—Electrochemistry and surface chemistry, *Electrochimica Acta*, 56 (12), 4489-4497, 2011.
- [21] D. Addari, B. Elsener, A. Rossi, Electrochemistry and surface chemistry of stainless steels in alkaline media simulating concrete pore solutions, *Electrochimica Acta*, 53 (27), 8078–8086, 2008.
- [22] D. O. Scanlon, G. W. Watson, D. J. Payne, G. R. Atkinson, R. G. Egdell, and D. S. L. Law, Theoretical and Experimental Study of the Electronic Structures of MoO₃ and MoO₂, *The Journal of Physical Chemistry C* 114 (10), 4636-4645, 2010.
- [23] M.C. Biesinger, B. P. Payne, A.P. Grosvenor, L. W.M. Lau, A.R. Gerson, R. St.C. Smart, Resolving surface chemical states in XPS analysis of first row transition metals, oxides and hydroxides: Cr, Mn, Fe, Co and Ni, *Appl. Surface Science*, 257, 2717–2730, 2011.

- [24] K. Prabakaran, S. Rajeswari, Electrochemical, SEM and XPS investigations on phosphoric acid treated surgical grade type 316L SS for biomedical applications, *J. Appl. Electrochem.*, 39, 887–897, 2009.
- [25] M. Vert, Y. Doi, K.H. Hellwich, M. Hess, P. Hodge, P. Kubisa, R. Przemyslaw, M. Rinaudo, F. Schué, "Terminology for biorelated polymers and applications (IUPAC Recommendations 2012)" *Pure and Applied Chemistry*, vol. 84, no. 2, 377-410, 2012.
- [26] N. Eliaz, Corrosion of Metallic Biomaterials: A Review. *Materials*, 12(3), 407, 2019.
- [27] MA. Hussein, A.S. Mohammed, N. Al-Aqeeli, Wear Characteristics of Metallic Biomaterials: A Review. *Materials*, 8(5),2749-2768, 2015.
- [28] F.C. Carta, Studio della stabilità di superficie di leghe dentali attraverso indagine XPS ed elettrochimica, Master thesis in Materials Science, University of Cagliari, 2008 (in italian).
- [29] M. Pisu, Stability of dental alloys in artificial saliva: an electrochemical and XPS investigation, PhD Thesis, 2013.
- [30] J. Pierre, I. Gautier-Luneau, Iron and citric acid: A fuzzy chemistry of ubiquitous biological relevance. *Biometals* 13, 91–96 (2000).
- [31] K. J. Davies, A. Sevanian, S.F. Muakkassah-Kelly, P. Hochstein, Uric acid-iron ion complexes. A new aspect of the antioxidant functions of uric acid. *The Biochemical journal*, 235(3), 747–754, 1986,
- [32] I.P. Pozdnyakov, F. Wu, A.A. Melnikov, V. P. Grivin, N. M. Bazhin, S. V. Chekalin, V. F. Plyusnin, Photochemistry of iron(III)-lactic acid complex in aqueous solutions. *Russ Chem Bull* 62, 1579–158, 2013.
- [33] G. Herting, I. O. Wallinder, C. Leygraf, Metal release rate from AISI 316L stainless steel and pure Fe, Cr and Ni into a synthetic biological medium- a comparison, *J. Environ. Monit.*, 10, 1092–1098, 2008."

Chapter 6. Thin films on Si_3N_4

In this chapter the tribochemical behaviour of Si_3N_4 tribopair in the presence of a hydrophilic ionic liquid: [EMIM EtSO₄] is presented together with the results obtained adding to the IL 2 %wt of oleic acid and EMIM oleate. After a short introduction, the experimental details used in the characterization of the thin films present on Si_3N_4 before and after mechanical tests are presented. The effect of the RH% and of the water absorption is also investigated and discussed.

The NMR spectra were acquired by Dr. E. Benetti at ETH, Zurich and they were interpreted by myself.

6.1. Introduction

Many investigations have been carried out since 2001 [1-2] on the lubrication capabilities of Ionic Liquids. This class of compounds appeared to be very promising because they can contain imidazolium, phosphonium, or ammonium cations and sulphate, sulphonates and fluorinated anions just to mention few of the possible combinations within the rich number of organic compounds that are available. Tribological tests carried out using steel tribopairs [3] and silicon pairs [4] showed that they can lower the coefficient of friction to very low values. In those works the role of environmental humidity on the lubrication of the pairs was highlighted together with the influence of the structure of the IL.

The presence of long chain lengths in the alkyl attached to the imidazolium ring has been demonstrated to have a beneficial effect for lubrication while the thermo-oxidative stability is reduced. The results obtained using hydrophobic ionic liquids as the fluorinated ones provided evidence of degradation and led to the conclusion that the product of degradation could be so aggressive to corrode the material. These results pointed out that the tribochemistry in the presence of ILs is rather complex and X-ray photoelectron spectroscopy can be used for gaining very useful information on the tribolayer composition and growth as to rationalize the tribological data.

So far few papers report tribological results using Si_3N_4 despite the fact that ionic liquids have a beneficial effect on the running in of this material when added to water (see for example the work of [5]). Furthermore, Si_3N_4 ceramics are very interesting materials because they have low density (3.2 g/cm³); high fracture toughness (7 MPam^{1/2}), operating temperature 1300°C and it has been reported that hydrodynamic lubrication is promoted by tribochemical wear. [6-8]

In this investigation the tribological measurements are carried out at various levels of relative humidity (RH), measuring the viscosity of the ionic liquid EMIM EtSO₄ and the blend obtained adding oleic acid and EMIM oleate as friction modifier. There are also performed tribological tests in a very controlled manner, the XPS measurements, using the small-area mode, in order to be sure that the obtained information is from the contact and non-contact areas of the samples.

6.2. Experimental

6.2.2. Materials

The balls (2 mm \varnothing) and the disks (25 mm \varnothing) used in the pin-on-disk tribological tests were made of Si₃N₄ (Toshiba, Japan). The ionic liquid (IL), 1-ethyl-3-methyl imidazolium ethylsulfate, [EMIM] EtSO₄ with purity $\geq 95\%$, purchased from Sigma Aldrich, Darmstadt, Germany, was tested for the lubrication of Si₃N₄ tribopairs. The [EMIM] EtSO₄ $\geq 95\%$ (pH 7.7 in water) was dehydrated by placing about 4 cm³ into a sealed vessel connected to a rotary pump ($\sim 10^{-2}$ mbar) at ambient temperature ($T = 23 \pm 2$ °C) for about 1 hour. Oleic acid (FluoroChem, England), purity $\geq 99\%$ and an equimolar mixture of oleic acid and [EMIM] oleate (synthesized at UniPi [9], Italy) were used as an additive.

The IL and the [EMIM] oleate were characterized by attenuated-total-reflection Fourier-transform infrared spectroscopy (ATR – FTIR, Alpha-P Bruker) and by nuclear magnetic resonance (NMR, Bruker BioSpin GmbH, 300 MHz) (see Appendix-A Figure A.7 and Figure A.8). The viscosity of the dried [EMIM] EtSO₄ $\geq 95\%$ and of the blend ([EMIM] EtSO₄ $\geq 95\%$ + 2 wt % of equimolar oleic acid/[EMIM] oleate) was measured using an Anton Paar viscometer SVM 3000 Stabinger. The viscosities were found to be 91.4 (0.2) mPa*s and 89.4 (0.1) mPa*s for dried IL and the dried blend respectively. In addition, c.a. 1 cm³ of the dried IL and c.a. 1 cm³ of the dried blend were equilibrated at relative humidity (RH) of 45% (23 ± 2 °C) into a sealed vessel using a saturated solution of potassium carbonate for about 1 week. In these conditions the water uptake (measured by weighting) was 7.9 (0.5) % for IL and 9.8 (0.8) % for the blend.

6.2.3. Surface preparation

To obtain a smooth surface, the disks were polished using a rotating polishing machine LaboPol-25 (Struers GmbH, Germany), diamond bonded grinding disks and polishing suspension (Struers GmbH, Germany) (Table 1). Milli-Q water (conductivity at 25 °C, 0.055 $\mu\text{S cm}^{-1}$, Merck, Millipore, Billerica, Massachusetts, USA) was used as a lubricant throughout all the steps. Between each step the disks were sonicated in milli-Q water for 5 min to avoid contamination of the disk with abrasive residues. The disks were dried under a nitrogen stream. The last step of the polishing protocol with DP-Mol cloth was carried out by hand to avoid possible contaminations before the tribological and the XPS tests.

Table 3: Mechanical polishing procedure for Si_3N_4 samples.

Cloth	Diamond paste	Lubricant	Speed	Time
MD-Piano 80	-	Water	300 rpm	5'
MD-Piano 220	-	Water	300 rpm	5'
MD-Allegro 9 μm	DiaPro 9 μm	Water	300 rpm	5'
MD-Allegro 6 μm	DP-Spray P 6 μm	Water	300 rpm	5'
MD-Allegro 3 μm	DP-Spray P 3 μm	Water	300 rpm	5'
MD-Allegro 1 μm	DP-Spray P 1 μm	Water	300 rpm	5'
DP-Mol cloth	-	Water	-	-

6.2.4. Optical microscopy and Profilometry

Optical images of Si_3N_4 tribopairs were acquired by using an AXIO 10 Imager M1m (Carl Zeiss AG, Oberkochen, Germany) in bright-field mode, equipped with a CCD camera and processed with the AxioVs40 software (v4.5.0.0). To investigate the topography of the samples a Sensofar PLu NEOX 3D profilometer (Sensofar-Tech S.L., Terrassa, Spain) was used (Figure 1). Data were acquired by using SensoSCAN software (Sensofar-Tech, SL) and processed by SensoMAP software (Digital Surf,

Besancon, France) and by Gwyddion 2.55 software (Czech Metrology Institute). The 2D images of the disks were acquired in phase-shifting interferometry (PSI) mode, using a DI 50X-N and DI 10X-N objective. The 2D images of the spheres were acquired in confocal mode, using an EPI 20X-N objective and 10X-N in PSI mode.



Figure 1: Sensofar PLu NEOX 3D profilometer.

6.2.5. Tribological tests

The mechanical tests were carried out using a UMT-2 tribometer (Bruker Nano Inc., Campbell, CA, USA) operating in pin-on-disk mode (Figure 2a). A load cell with a maximum capacity of 20 N and a resolution of 0.001 N (manufacturer's data) was used for all the experiments. The planarity was adjusted by placing metal foils of known thicknesses between the sample holder and rotational drive. The running-in was carried out in water under an applied load of 4.5 N.

All the experiments were carried out using 300 μ L of sample at relative humidity RH = 43.5-55% ($T = 23 \pm 2$ °C) equilibrated in the custom-made system built on top (Figure 2 b) of the tribometer cup. In order to investigate the transition from hydrodynamic- to mixed- and boundary lubrication regimes, ramp tests consisting of a sequence of steps in which the speed gradually decrease from 200 mm/s to 0.1 mm/s were performed. The Stribeck curves were repeated one after the other in

the same track. The RH% was monitored by a sensor and the test started when the RH% value was constant – usually the waiting time did not exceed five minutes. Each time mechanically polished disks were checked by XPS for the contamination before the tribological test. After the ramp test the balls and disks were washed three times with milli-Q water and then with 2-propanol and dried by using powder free paper wipes (Kimtech, Kimberley Clark, United States). Slow tests of 2 minutes at 6 mm / s with water and without liquid (dried) were also performed after the ramp test.

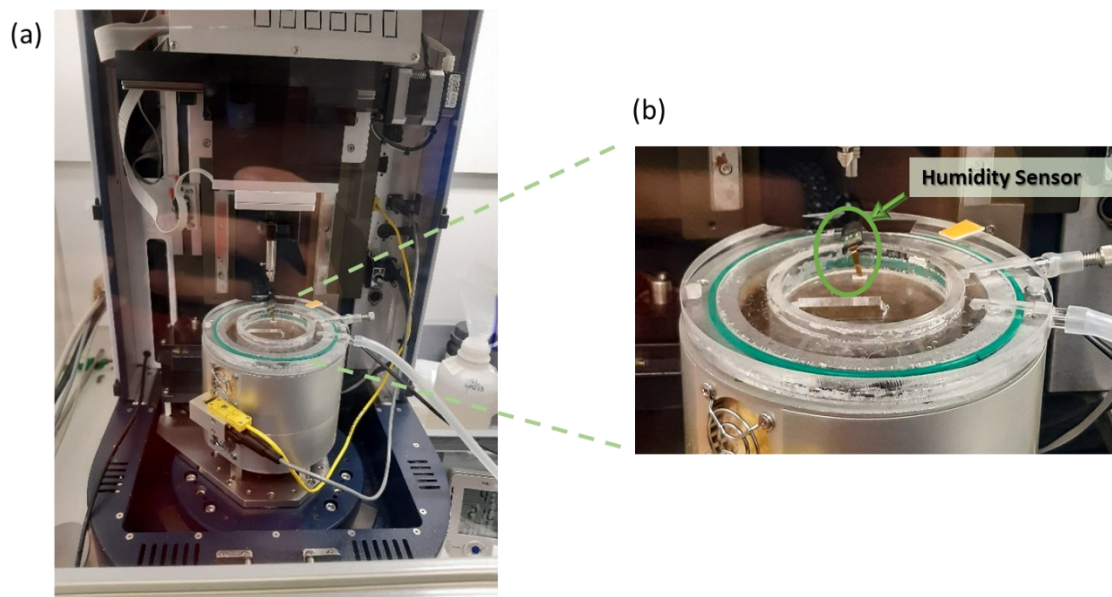


Figure 2: a) UMT-2 tribometer in pin-on-disk mode; b) custom made humidity chamber with sensor.

6.2.6. XPS surface analysis

The XPS spectra of Si₃N₄ disks mechanically polished and tribopairs after the tribological test were acquired with a PHI QuanteraSXM (ULVAC-PHI, Chanhassen, MN, USA). Analyses were carried out with a monochromatic AlK α source ($h\nu = 1486.6$ eV), using a beam diameter of 100 μm for the mechanically polished disk and 50 μm for the tribostressed tribopairs (ball and disk) with the purpose of analyzing the track area (contact area). Constant-analyzer energy (CAE) mode was selected for the spectra acquisition. The high-resolution spectra were recorded using pass energy and the step size of 69 eV and 0.125 eV, respectively. The energy resolution given as full width at half-maximum (fwhm) of the peak height of the Ag 3d_{5/2} was 0.7 eV. Survey spectra were acquired setting the pass energy at 280 eV and using a step size of 1 eV. In both cases, the emission angle was 45°. The linearity of the binding energy scale was checked following the ISO 15472:2014 and it was found an accuracy of ± 0.1 eV. The analyses were carried out while using a low-voltage argon ion source/electron neutralizer to compensate for possible sample charging [10]. The X-ray-excited secondary-electron images (SEI) were also collected in order to select the points in the contact area on the ball and on the disk, following tribological tests. The high-resolution spectra were processed using CasaXPS software (v.2.3.24, Casa Software Ltd., Wilmslow, Cheshire, UK). The Shirley-Sherwood background subtraction routine was applied before the curve fitting procedure [11]. The parameters Gaussian/Lorentzian ratio and width at half maximum of the signal of the model functions were used as reported in the literature [4, 10] and are reported in the section 6.3.4 of the present work.

6.3. Results

The Ionic liquids characterization for its use in the tribotest are presented in this section.

6.3.1. Viscosity

The mean values of the viscosity measurements at 25 °C of [EMIM] EtSO₄ and of the blend [EMIM] EtSO₄ + 2 wt % equimolar oleic acid/[EMIM] oleate are given in table 1. The IL and the blend were dried before the measurements as described in section 6.2.2. The density and the kinematic viscosity were also measured.

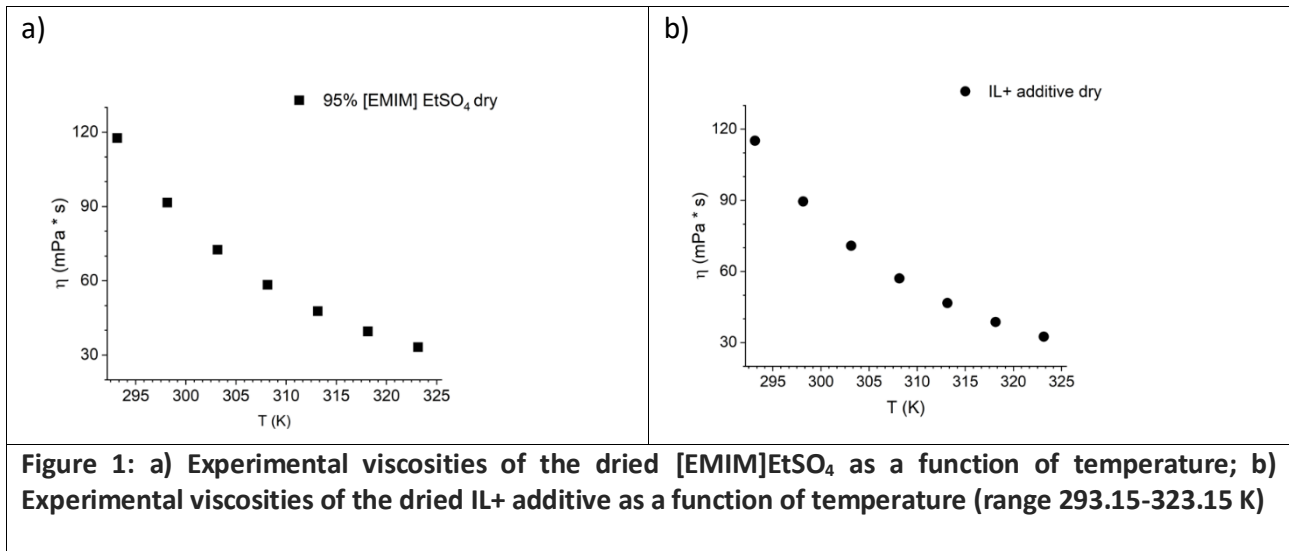
Table 1: Experimental viscosity, kinematic viscosity and density at 25 °C and relative standard deviation of dried IL and blend.

	Dried	
	[EMIM] EtSO ₄	Blend
Viscosity η (mPa * s)	91.4 (0.2)	89.4 (0.1)
Kinematic Viscosity ν (mm ² * s ⁻¹)	74.0 (0.2)	72.4 (0.1)
ρ (g * cm ⁻³)	1.2354 (0.0001)	1.2347 (0.0001)

The results are in agreement with the literature data [12] and the effect of the additive on the viscosity seems to be negligible. The viscosity of the dried IL and of the IL + additive blend was also measured at different temperatures, in the range 293.15 K – 325.15 K and the results are reported in Table 2 and in Figure 1.

Table 2: Experimental viscosities of dried IL and IL + additive as a function of temperature.

[EMIM] EtSO ₄ – Dried		IL + additive – Dried	
T (K)	η (mPa * s)	T (K)	η (mPa * s)
293.15	117.6	293.15	115.1
298.15	91.6	298.15	89.5
303.15	72.5	303.15	70.9
308.15	58.4	308.15	57.1
313.15	47.7	313.15	46.7
318.15	39.6	318.15	38.7
323.15	33.2	323.15	32.5



As illustrated, in the temperature range considered (293.15 – 323.15 K), the viscosity drastically decreases with the increase of the temperature.

6.3.2. Morphology

Si₃N₄ mechanically polished

Following the mechanical polishing, the sample morphology and topography were characterized by optical microscopy and by profilometry (Figure 2). The roughness was checked and was found Sq = 2.6 (0.7) nm and Sa = 1.7 (0.3) nm (Figure 2b). The Rq value is calculated with a Gaussian filter 0.025, was found to be equal to 0.9 (0.3) nm (Figure 2c). Where Sq is the “root mean square height of the surface”, Sa is the “arithmetical mean height of the surface” and the Rq value is “root mean square roughness” according to ISO 25178: Geometrical Product Specifications (GPS) – Surface texture: areal.

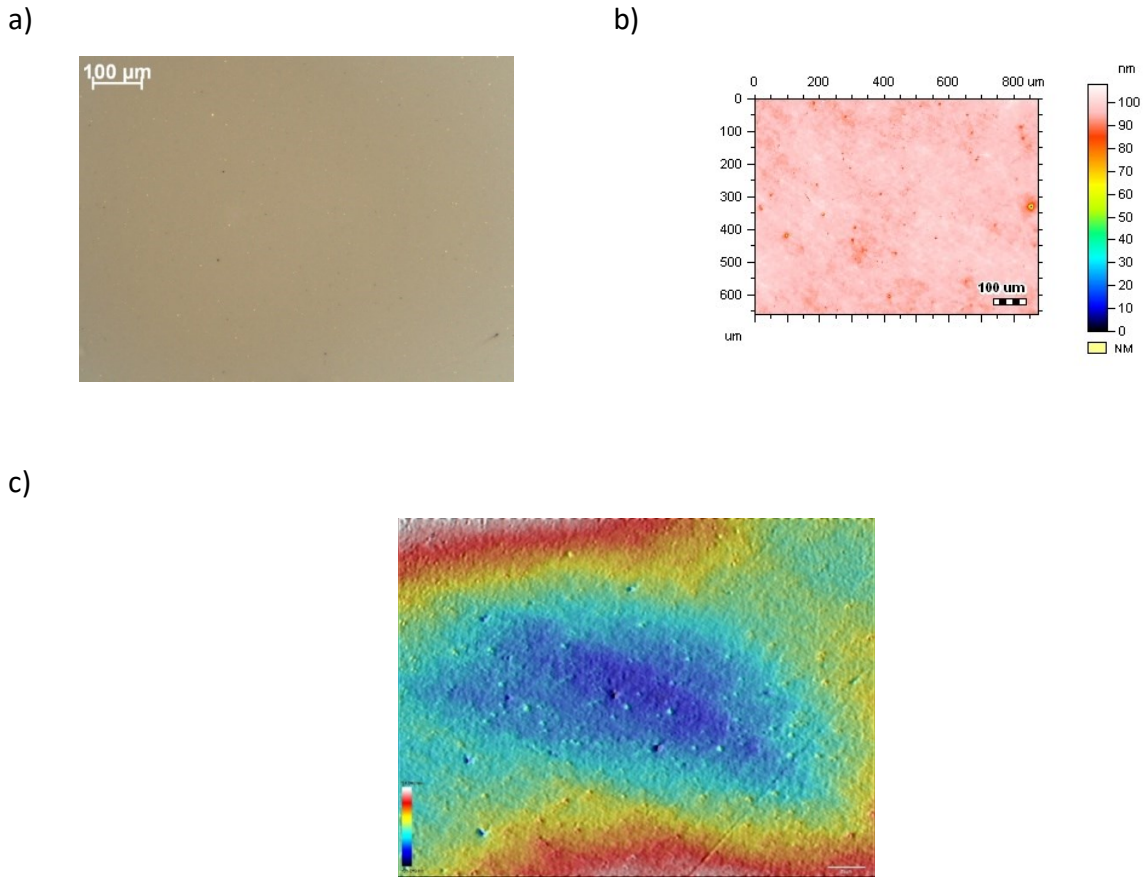
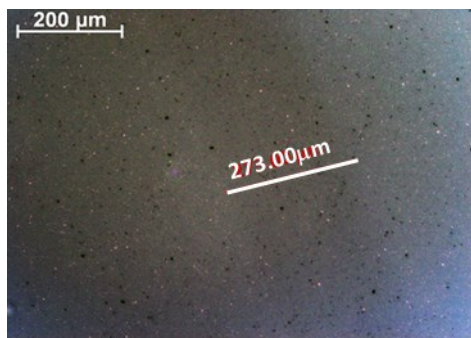


Figure 2: a) Optical image of Si_3N_4 mechanically polished- objective 10x; b) Topography of Si_3N_4 Mechanically polished. Objective 50X; c) Roughness topography of Si_3N_4 mechanically polished, gaussian filter 0.025.

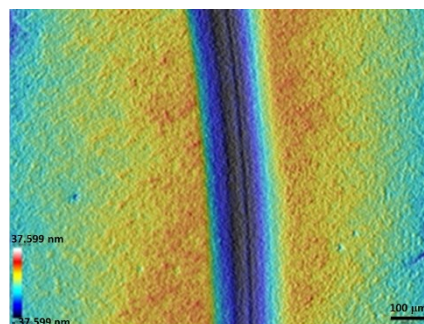
Si_3N_4 disk and the pin after Stribeck Tests in the presence of $[\text{EMIM}]\text{EtSO}_4$

The morphology and topography of the disk (fig.3) and pin (fig.4) after the tribotest in the presence of $[\text{EMIM}]\text{EtSO}_4$ were characterized by optical microscopy and by profilometry. The track size in the presence of $[\text{EMIM}]\text{EtSO}_4$ was found to be 274 (2) μm and 284 (2) μm for the disk and the pin respectively. The minor differences between the samples tested with IL and IL + additive are probably attributable to the running in. The running-in procedure, in fact, generates smooth contact surfaces and during this procedure the majority of wear occurs.

a)



b)



c)

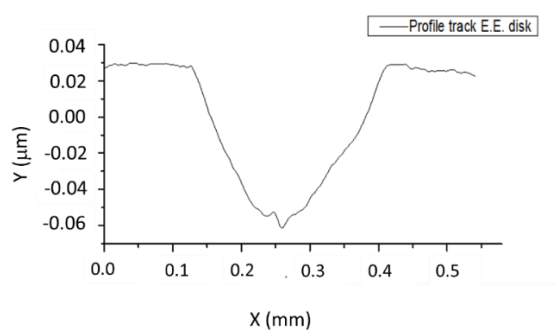


Figure 3: a) Optical image of Si_3N_4 disk after tribotest in the presence of $[\text{EMIM}]\text{EtSO}_4$ - objective 10x; b) Topography of Si_3N_4 disk after tribotest in the presence of $[\text{EMIM}]\text{EtSO}_4$. DI 10X-N PSI mode; c) Profile on the disk track after tribotest in the presence of $[\text{EMIM}]\text{EtSO}_4$.

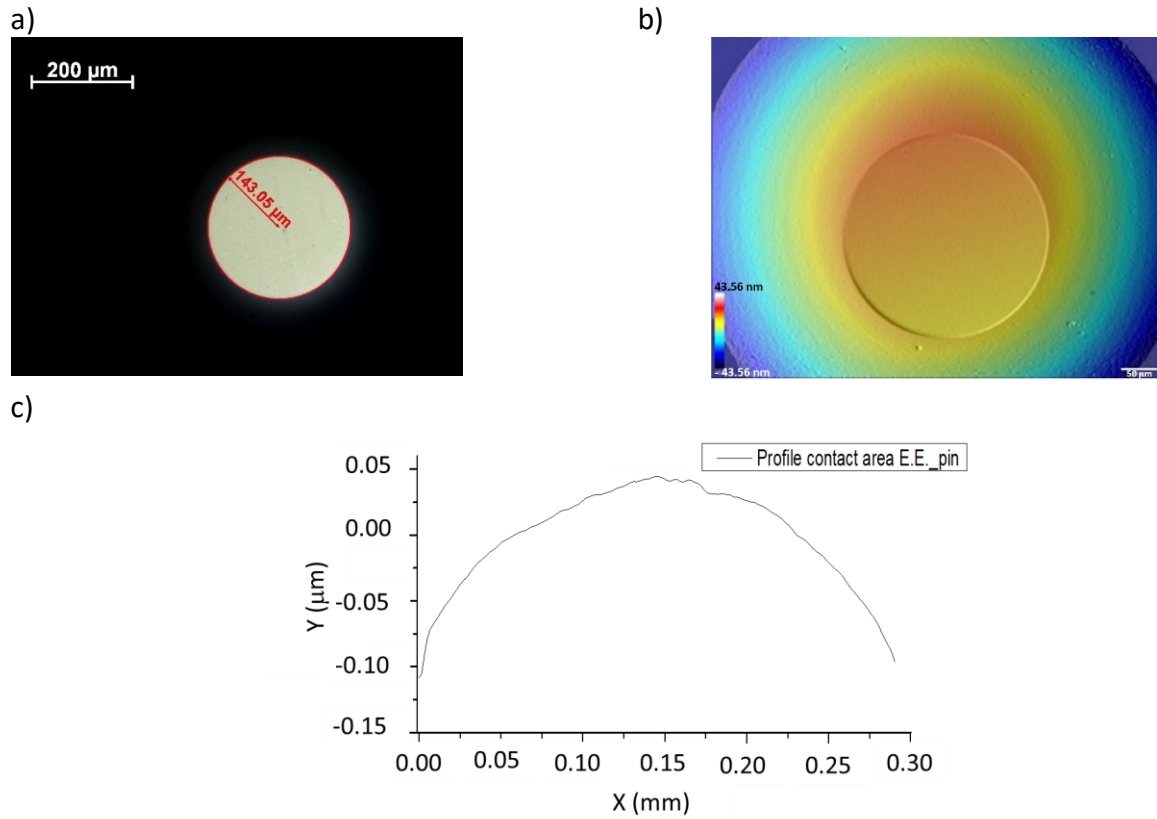


Figure 4: a) Optical image of Si₃N₄ pin after tribotest in the presence of [EMIM]EtSO₄ - objective 10x; b) Topography of Si₃N₄ pin after tribotest in the presence of [EMIM]EtSO₄ - DI EPI-20X confocal mode; c) Profile pin track after tribotest in the presence of [EMIM]EtSO₄.

Si₃N₄ disk and the pin after Stribeck Tests in the presence of [EMIM]EtSO₄ + 2 wt % Oleic acid/[EMIM]oleate 50/50

The morphology and topography of the disk (fig.5) and pin (fig.6) after the tribotest in the presence of [EMIM]EtSO₄ + 2 wt % Oleic acid/[EMIM]oleate 50/50 was characterized by optical microscopy and by profilometry. The track size was found to be of 302 (1) μm and 306 (2) μm for the disk and the pin respectively. These minor differences between the sample tested with IL and IL+ additive are probably attributable to the running-in procedure (section 6.2.5).

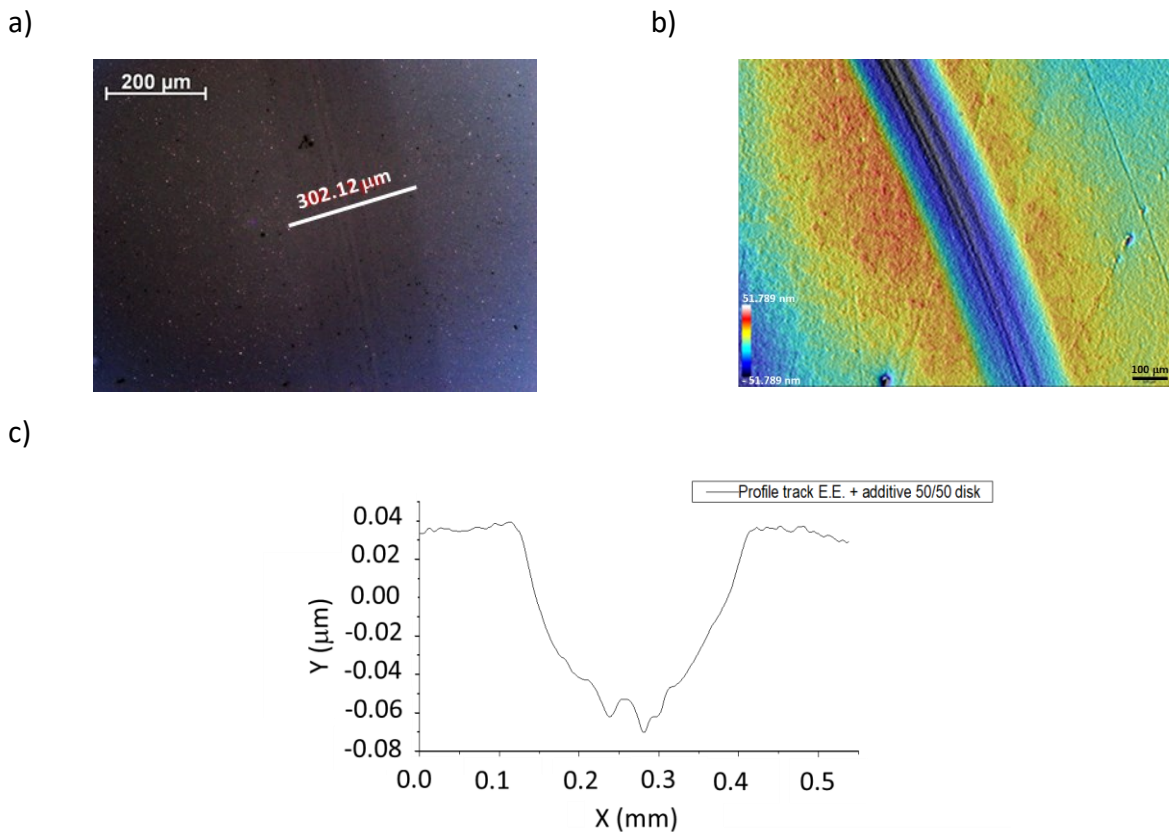


Figure 5: a) Optical image of Si₃N₄ disk after tribotest in the presence of the blend- objective 10x; b) Topography of Si₃N₄ disk after tribotest in the presence of the blend; DI 10X-N PSI mode c) Profile pin track after tribotest in the presence of the blend

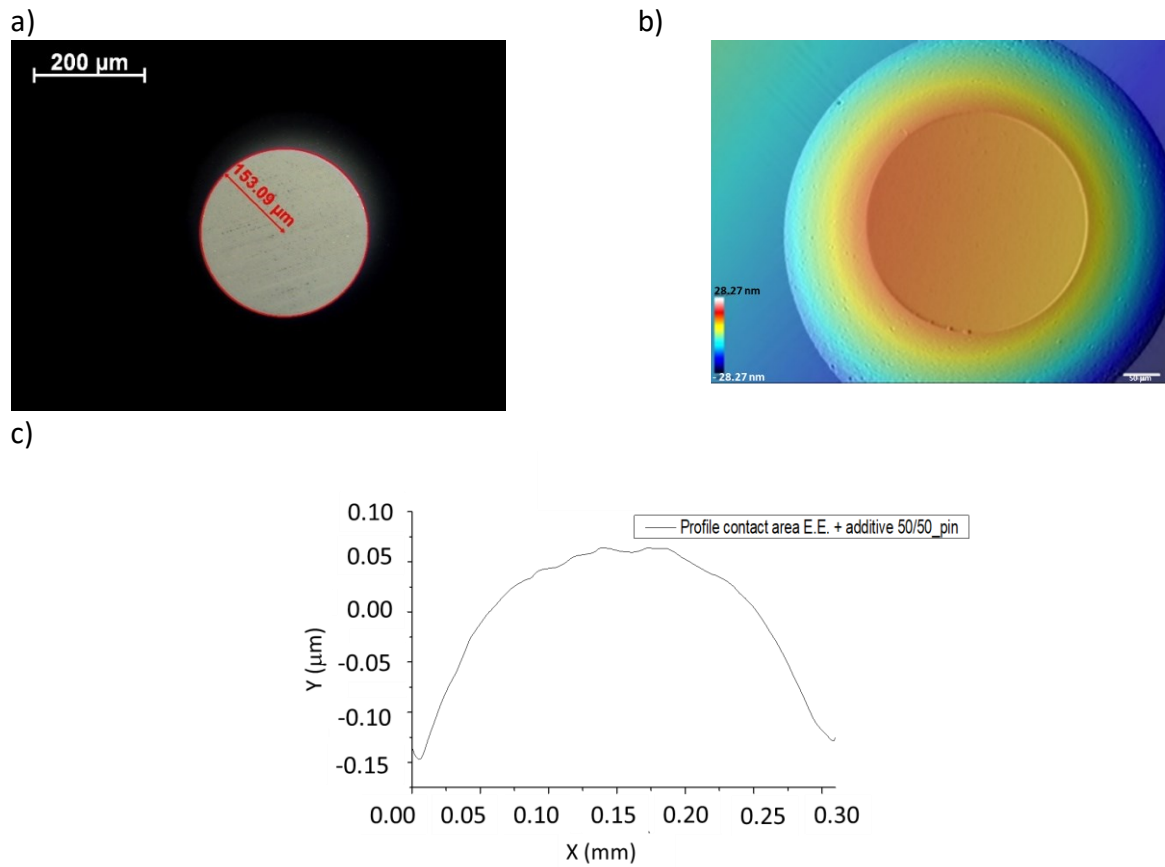


Figure 6: a) Optical image of Si₃N₄ pin after tribotest in the presence of the blend - objective 10x; b) Topography of Si₃N₄ pin after tribotest in the presence of the blend- DI EPI-20X confocal mode; c) Profile pin track after tribotest in the presence of [EMIM]EtSO₄.

6.3.3. Tribological results

Stribeck curves in the presence of dried and equilibrated [EMIM]EtSO₄

The CoF vs speeds trends observed using the dried [EMIM] EtSO₄ and the equilibrated [EMIM] EtSO₄ are reported in Figure 7.

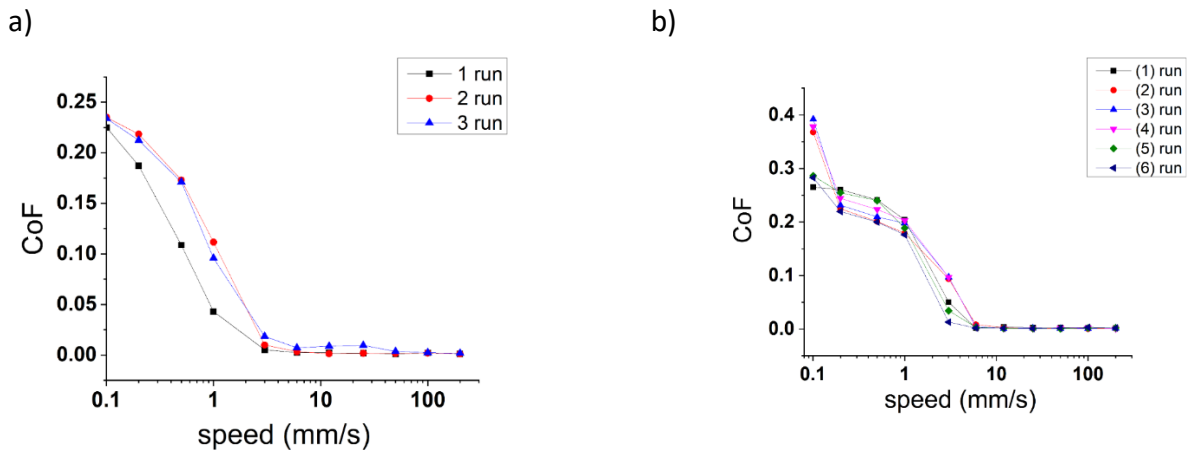


Figure 7: Coefficient of friction (CoF) vs speed (mm / s). Ramp test: decreasing sliding speed from 200 mm/s to 0.1 mm/s. a) Stribeck curves in the presence of dried [EMIM]EtSO₄ - RH % (during the tests) = 45.0- 55.0 % - T= 25° C - applied load 4.5 N; b) Stribeck curves in the presence of equilibrated [EMIM]EtSO₄ - equilibrated for 1 week at 45% RH, water uptake* = 7.9 (0.5) % - RH % (during the tests) = 43.5- 54.0 % -T= 25° C - applied load 4.5 N.

The vast majority of wear occurs during the running-in in water: it results in hydrodynamic bearing-like contact. The viscosity increases from 1 mPa*s (water) to 10-100 mPa*s depending on the water amount in the IL. Regarding the case of the test in the presence of dried [EMIM]EtSO₄, an increase of the coefficient of friction at lowest speeds from the first to the third run due to the water absorption was observed (Figure 7a). Comparing the test with dried [EMIM]EtSO₄ and the test with equilibrated [EMIM]EtSO₄ (Figure 7b), it is possible to observe the increase of CoF values at lowest speeds and the shift of the curves in the transition from HDL to mixed regime.

Stribeck curves in the presence of dried and equilibrated [EMIM]EtSO₄ + 2 wt% Oleic acid/[EMIM]oleate 50/50

The CoF vs speeds trends observed using the dried blend and the equilibrated blend are reported in Figure 8. Also in this case, in the presence of the dried blend (Figure 8a) the increase of the coefficient of friction at lowest speeds from the first to the third run due to the water absorption is observed. Comparing the test carried out in dried blend and the test with the blend following 1 week

at RH % = 45 (equilibrated) (Figure 8b), it is possible to observe the increase of CoF values at lowest speeds and the shift of the curves in the transition from HDL to mixed regime.

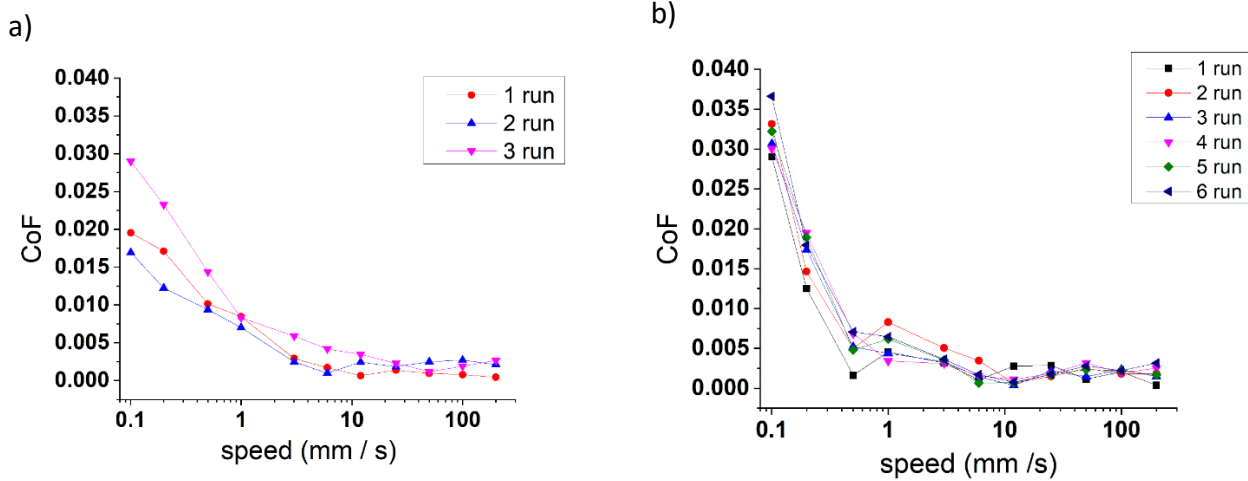
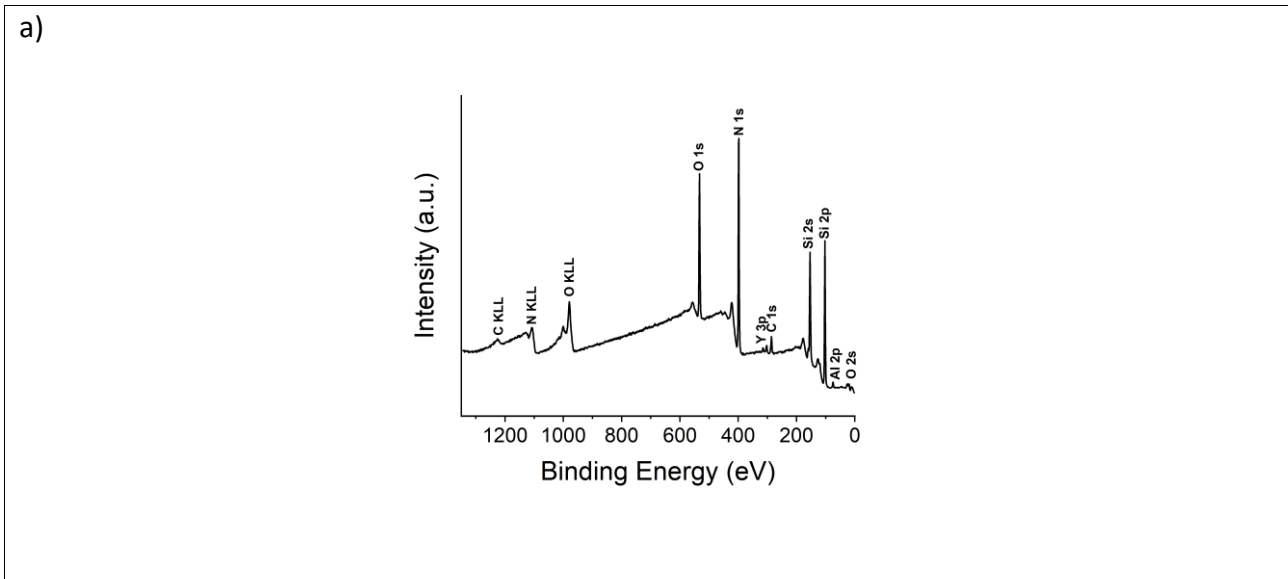


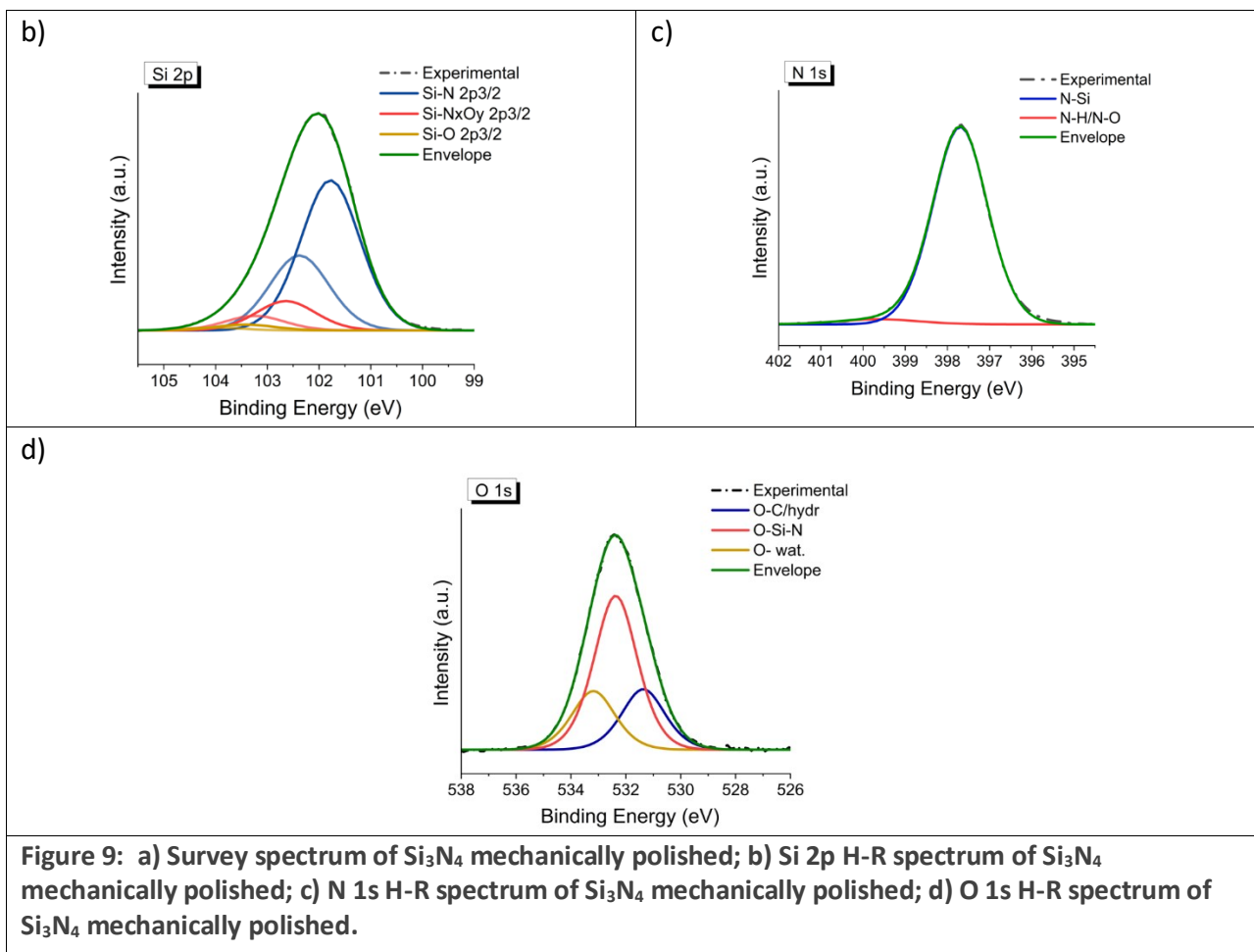
Figure 8: Coefficient of friction (CoF) vs speed (mm / s). Ramp test: decreasing sliding speed from 200 mm/s to 0.1 mm/s. a) Stribeck curves in the presence of dried blend - RH % (during the tests) = 45.0- 55.0 % - T= 25° C - applied load 4.5 N; b) Stribeck curves in the presence of equilibrated blend - equilibrated for 1 week at 45% RH, water uptake* = 9.8 (0.3) % - RH % (during the tests) = 44.7- 54.7 % -T= 25° C - applied load 4.5 N.

6.3.4. XPS results

Si₃N₄ disk mechanically polished

The Survey spectrum (Figure 9a) of the mechanically polished Si₃N₄ disk showed the photoelectron Si 2p, Si 2s, N 1s, C 1s, O1s and Auger N KLL, C KLL, O KLL peaks expected for the substrate, oxide and the contamination layer. The Al 2p and Y 3p were also detected: these elements are often present in Si₃N₄ ceramics as additives for improving the mechanical properties of the material.





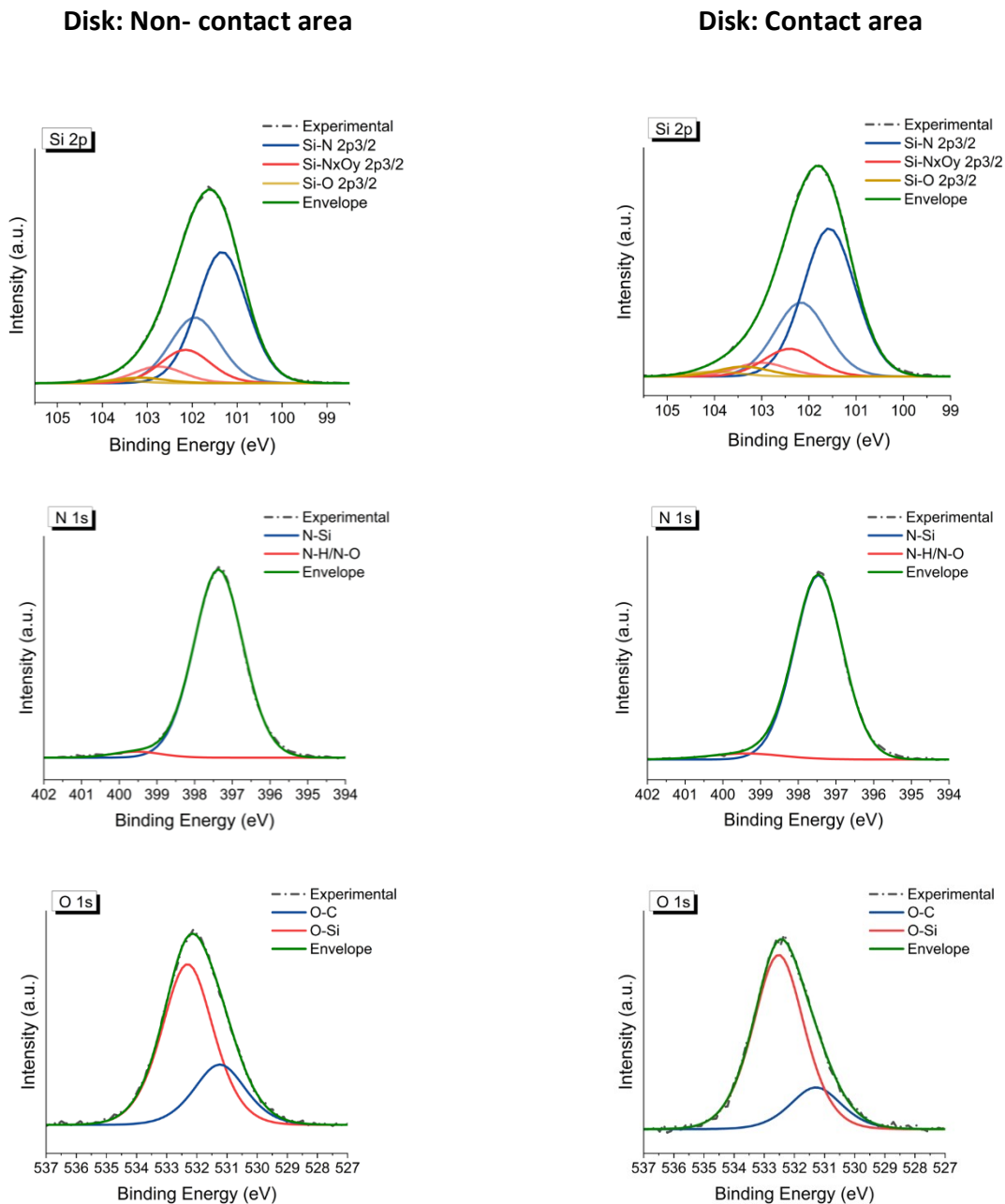
The high-resolution Si 2p spectrum shows three components (Figure 9b). The Si 2p_{3/2} peaks at 101.7 (0.1) eV and at 102.5 (0.1) eV, can be assigned to a Si-N component and to a Si-N_xO_y component respectively. According to the literature [13-15], the other contribution at 103.5 (0.2) can be assigned to the Si-O bond, The N 1s spectrum consists of an intense component ascribed to Si-N bonds in Si_3N_4 contribution at 397.6 (0.1) eV and of a low intensity shoulder at 399.7 (0.1) eV due to the NH₂/N-O contribution, as reported by Bertoti et al. [14]. The O 1s spectrum consists of a major contribution at 532.4 (0.1) eV, assigned to the Si-O bond. An additional contribution at 531.4 (0.1) eV can be attributed to hydroxides. A final contribution to the O1s spectrum at 533.1 (0.2) eV can be ascribed to adsorbed water remaining from the cleaning process. The peak parameters and the binding energies of Si 2p_{3/2}, N1s and O1s are reported in Table 3.

Table 3: Peak parameters of Si 2p_{3/2}, N1s and O1s spectra of mechanically polished disk. Standard deviations are reported in parentheses

	Line Shape	Component	Disk MP	FWHM (eV)
			BE (eV)	
Si 2p_{3/2}	GL(30)	Si-N	101.7 (0.1)	1.4 (0.1)
		Si-NxOy	102.5 (0.1)	1.4 (0.1)
		Si-O	103.5 (0.1)	1.4 (0.1)
N 1s	GL(30)	N-Si	397.6 (0.1)	1.6 (0.1)
		N-H/N-O	399.7 (0.1)	2.3 (0.1)
O 1s	GL(50)	O-H	531.4 (0.1)	2.0 (0.1)
		O-Si	532.4 (0.1)	2.0 (0.1)
		O-cont. water	533.1 (0.1)	2.0 (0.1)

Si₃N₄ disk and pin after the test in the presence of equilibrated [EMIM]EtSO₄

The high-resolution Si 2p, N 1s, O 1s and S 2s spectra recorded on the disk and the pin after the test in the presence of equilibrated [EMIM]EtSO₄, both in the contact area and in the non-contact one, are reported in Figure 10 and Figure 11 respectively. The peak-fitting was performed by applying to the synthetic components the same parameters adopted for the mechanically polished sample.



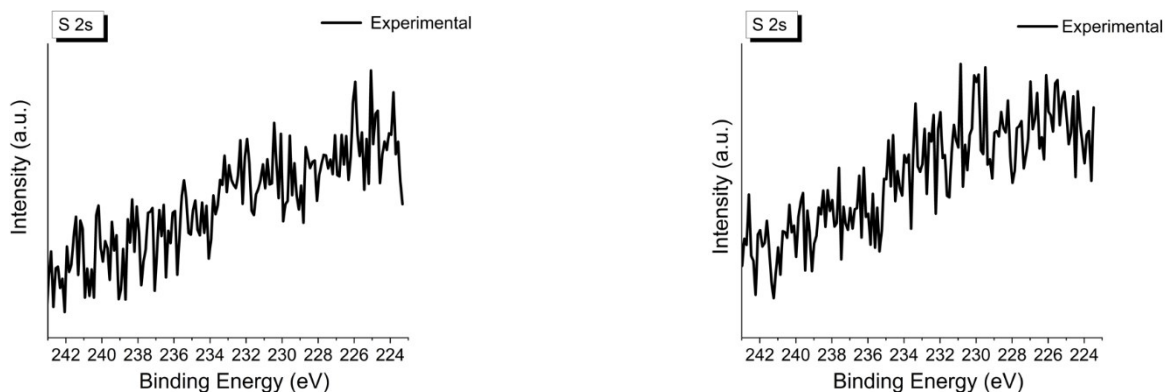
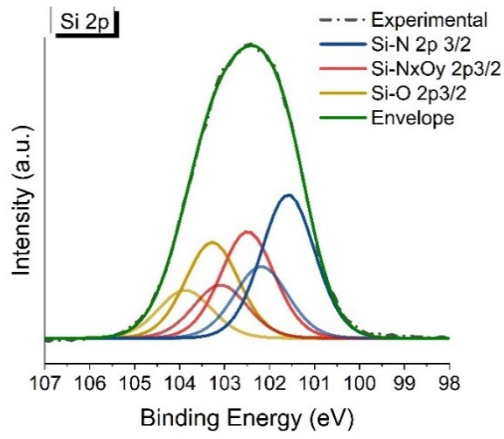


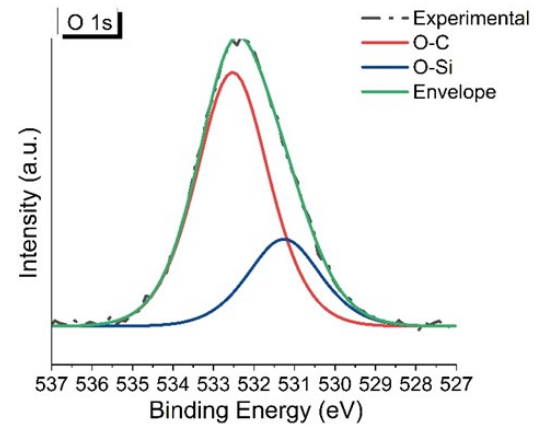
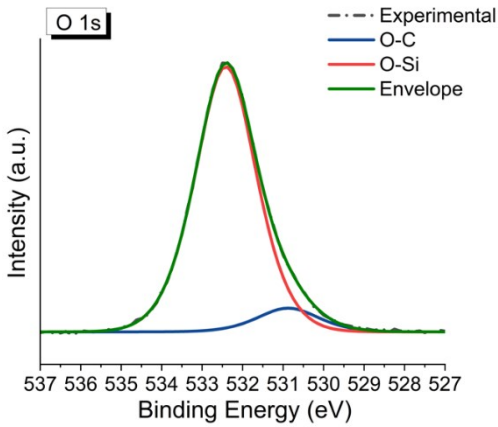
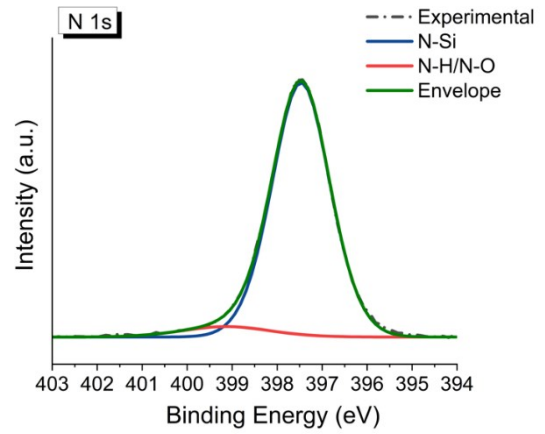
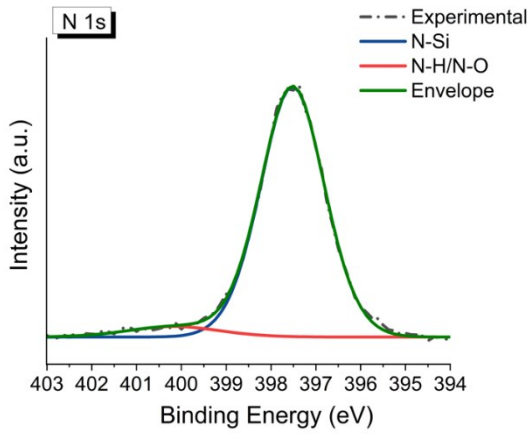
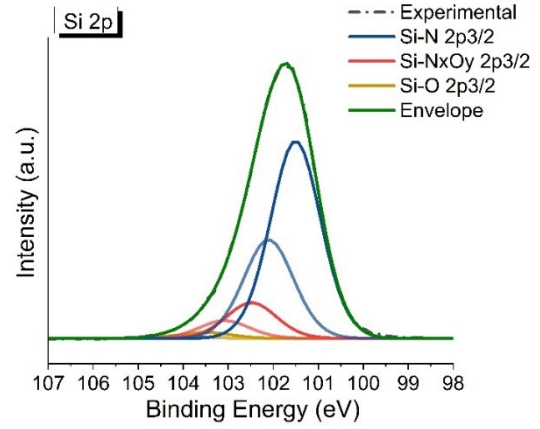
Figure 10: XPS spectra of Si_3N_4 disk after the test in the presence of equilibrated $[\text{EMIM}]\text{EtSO}_4$; Left : Non-contact area; right: Contact area; from top to down: Si 2 p spectrum; N 1s spectrum; O 1s spectrum; S 2s spectrum.

As far as the Si_3N_4 disk after the test, no significant differences between the non-contact area (Figure 10 left panel) and contact area (Figure 10 right panel) are observed (Table 4). The Si 2p_{3/2} components at 101.5 (0.1) eV and at 102.3 (0.1) eV and at 103.3 (0.1) eV can be assigned to Si-N, to Si-N_xO_y and to Si-O respectively, for both areas. The N 1s spectra showed the presence of the Si_3N_4 contribution at 397.4 (0.1) eV and a shoulder at higher binding energy 399.4 (0.1) eV corresponding to the NH₂/N-O contribution. The O 1s spectrum consisted of a major contribution at 532.5 (0.1) eV, in contact area and 532.3 ± 0.1 eV out the contact area, corresponding to the Si-O bond. An additional contribution at 531.3 (0.1) eV, more intense in the contact area than in the non-contact one, can be attributed to hydroxide or carbonate bonded to a NH₃ species. No S 2s signal is detected.

Pin: Non- contact area



Pin: Contact area



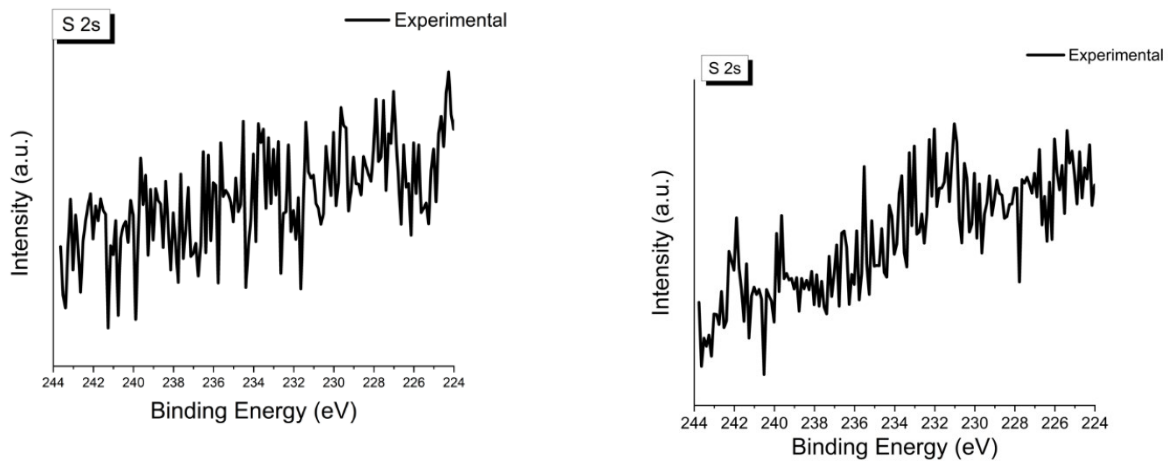


Figure 11: XPS spectra of Si_3N_4 pin after the test in the presence of equilibrated $[\text{EMIM}]\text{EtSO}_4$; Left : Non-contact area; right: Contact area; from top to down: Si 2 p spectrum; N 1s spectrum; O 1s spectrum; S 2s spectrum.

The spectra of the pin after the test in the presence of equilibrated $[\text{EMIM}]\text{EtSO}_4$ show a different shape on the Si 2p and O 1s signals when comparing non-contact area and contact area (Figure 11). The Si 2p spectrum of the contact area shows the main component at 101.4 (0.1) eV and at 101.6 \pm 0.1 eV in the non-contact area attributable to Si-N component. Two other components were revealed: at about 102.3 (0.1) eV attributed to SiN_xO_y and to Si-O component at 103.4 (0.1) eV for both areas. The two components at ascribed to SiN_xO_y and the Si-O are markedly less intense in the contact area, after the test, than in the non-contact area.

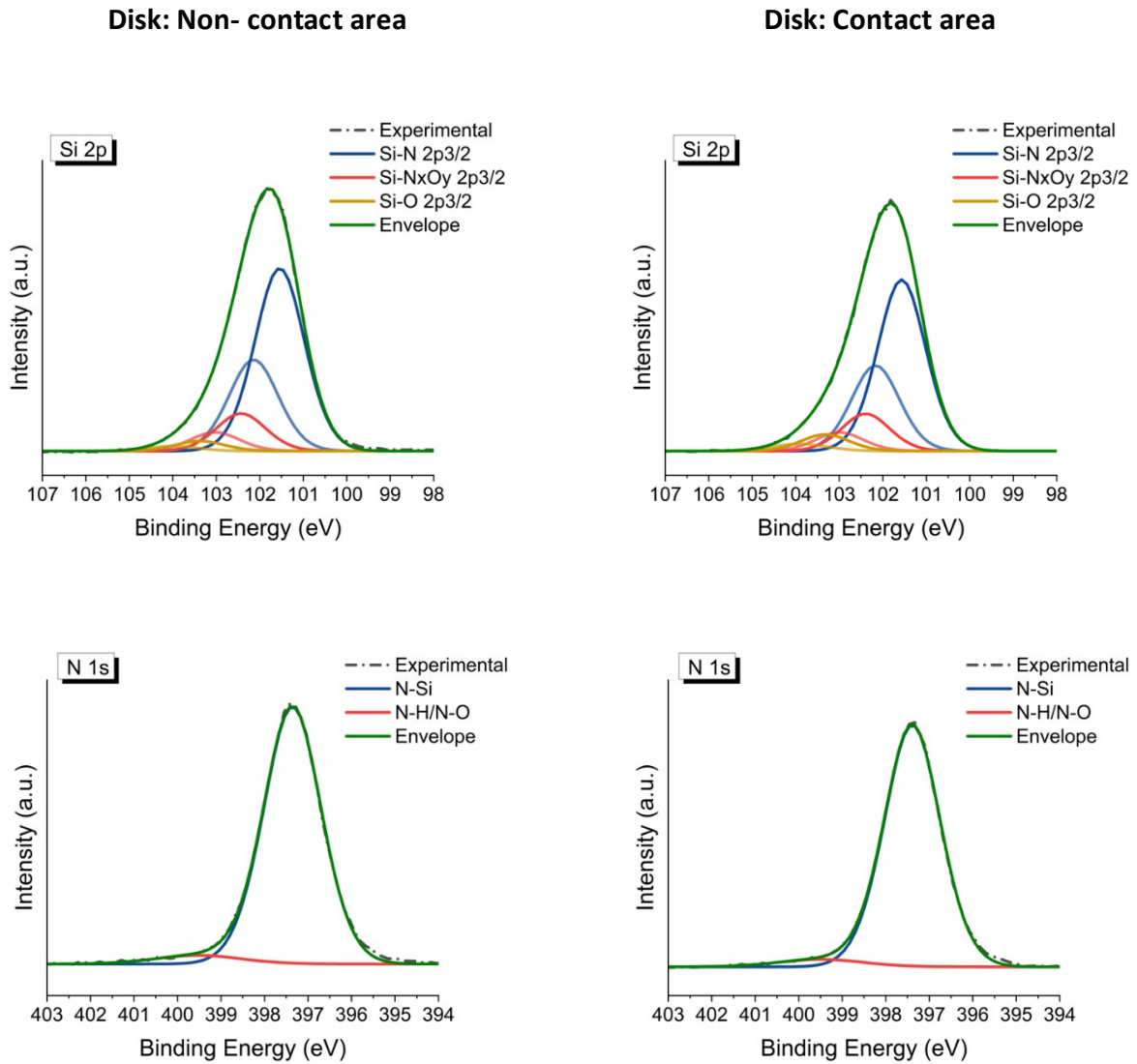
The N 1s spectrum contained a major contribution of N-Si component at 397.5 (0.1) eV and the N-H/N-O component was found at 399.1 (0.1) eV. The S 2s signal could not be processed due to its low signal to noise ratio, but it might be present in the contact area. These data are summarized in Table 4.

Table 4: Peak parameters of Si 2p_{3/2}, N1s and O1s spectra of disk and pin after the test in the presence of equilibrated [EMIM]EtSO₄. Standard deviations are reported in parentheses.

	Component	Disk out	Disk	Pin out	Pin
		contact area	tribostressed in the presence of [EMIM]EtSO ₄	contact area	tribostressed in the presence of [EMIM]EtSO ₄
		BE ± 0.1(eV)	BE (eV)	BE ±0.1 (eV)	BE (eV)
Si 2p_{3/2}	Si-N	101.4	101.5 (0.1)	101.6	101.4 (0.1)
	Si-NxOy	102.2	102.3 (0.1)	102.4	102.3 (0.1)
	Si-O	103.2	103.3 (0.1)	103.4	103.5 (0.1)
N 1s	N-Si	397.3	397.5 (0.1)	397.5	397.5 (0.1)
	N-H/N-O	399.3	399.4 (0.1)	399.1	399.1 (0.1)
O 1s	O-H	531.2	531.3 (0.1)	531.2	531.4 (0.1)
	O-Si	532.3	532.5 (0.1)	532.4	532.4 (0.1)

Si₃N₄ disk and pin after the test in the presence of equilibrated [EMIM]EtSO₄ + 2 wt % Oleic acid/[EMIM]oleate 50/50

The high-resolution Si 2p, N 1s, O 1s and S 2s spectra of the disk and pin after the test in the presence of equilibrated blend are reported in Figure 12 and Figure 14 respectively for the contact and non-contact area.



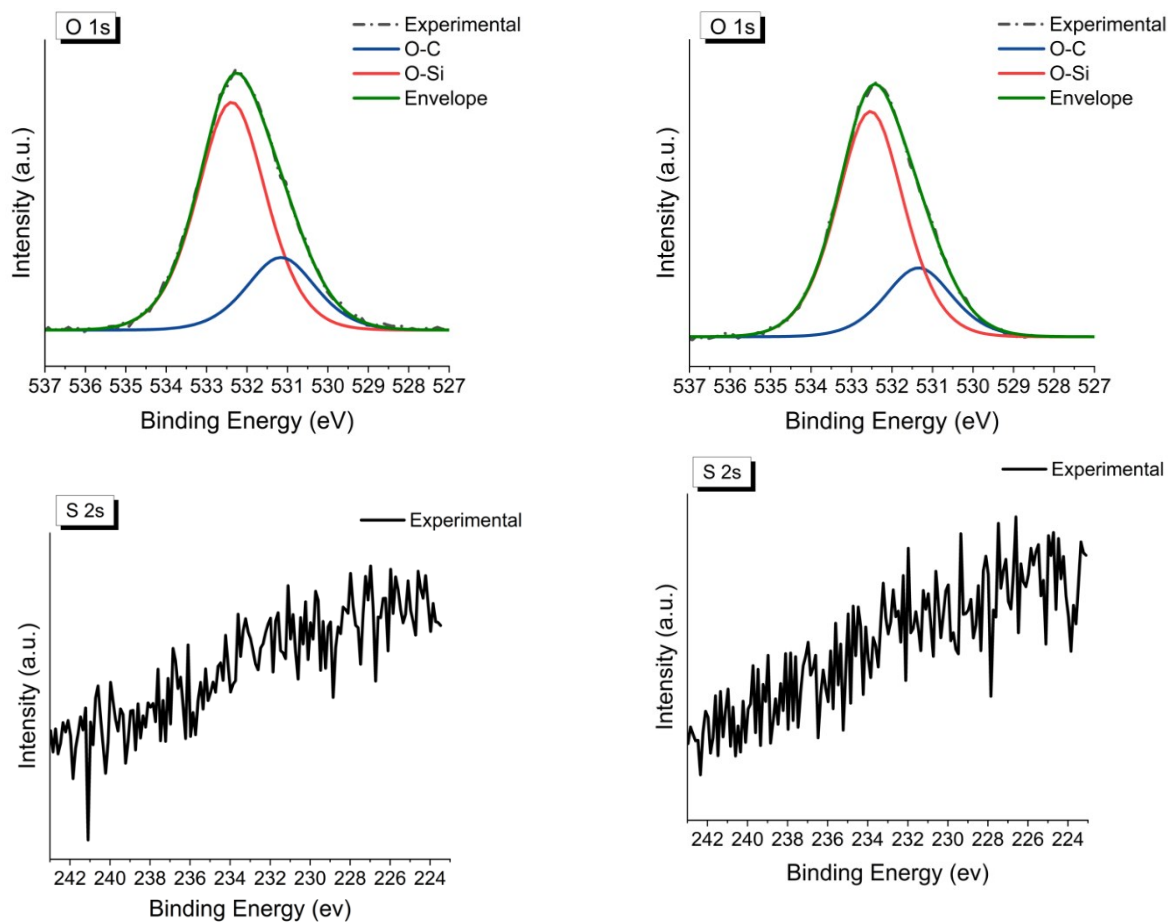


Figure 12: XPS spectra of Si_3N_4 disk after the test in the presence of equilibrated $[\text{EMIM}]\text{EtSO}_4 + 2 \text{ wt } \% \text{ Oleic acid}/[\text{EMIM}]\text{oleate } 50/50$; Left: Non-contact area; right: Contact area; from top to down: Si 2 p; N 1s; O 1s; S 2s.

Also in this case, the high-resolution spectra of the Si_3N_4 disk after the test in the presence of equilibrated $[\text{EMIM}]\text{EtSO}_4 + 2 \text{ wt } \% \text{ Oleic acid}/[\text{EMIM}]\text{oleate } 50/50$ show no significant differences between the non-contact area (Figure 12 – left panel) and contact area (Figure 12 – right panel). The Si $2p_{3/2}$ peaks at 101.5 (0.1) eV and at 102.3 (0.1) eV and at 103.3 (0.2) eV can be assigned to a Si-N component, to a $\text{Si-N}_x\text{O}_y$ and to Si-O component respectively, for both areas. The N 1s spectrum exhibited the presence of the Si_3N_4 contribution at 397.5 (0.1) eV and a shoulder at 399.4 (0.1) eV that might be assigned to the $\text{NH}_2/\text{N-O}$ contribution [14]. The O 1s spectrum consisted of a major contribution at 532.5 (0.1) eV, which is assigned to the Si-O bond. An additional contribution at 531.2 (0.2) eV can be attributed to hydroxides. No S 2s signal is detected.

Significant changes in the XPS were revealed in the C 1s spectra during the acquisition of the spectra (Figure 13). The comparison of C1s signal of the contact area acquired at the beginning and at the

end of the XPS experiment, allows observing that the intense shoulder detected at 286.5 ± 0.1 eV, this signal in the C1s acquired at the beginning of the experiment (Figure 13 a) and ascribed to C-OH component, is no longer detected at the end (Figure 13 b). A less intense peak shifted towards low binding energy values (285.8 ± 0.1 eV) is observed. This behaviour is probably attributable to soft X-ray damage that occurs during the experiment.

The damage process seems to be fast, since if the C1s signal is acquired as a second region, therefore after about 1.2 minutes of X-ray exposure, the shape of the signal coincides with that shown in Figure 13b.

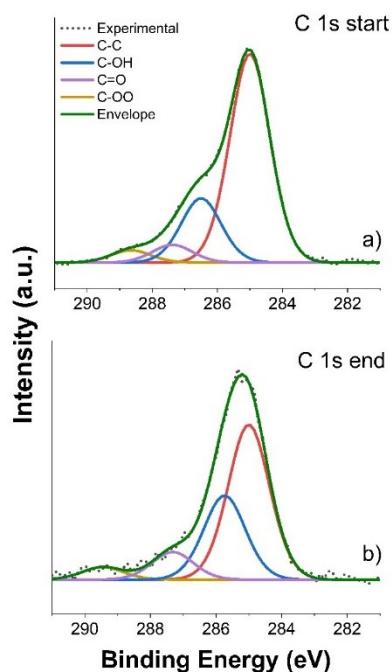


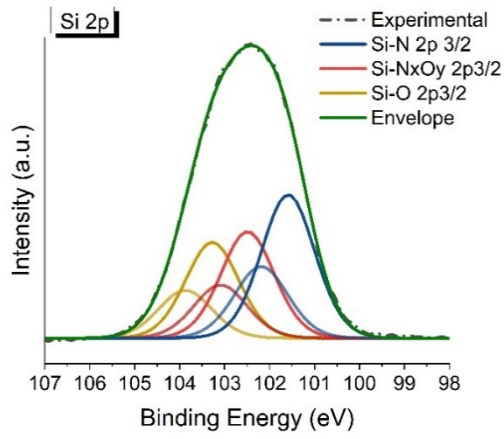
Figure 13: a) C1s signal acquired at the beginning of the XPS experiment; b) C1s signal acquired at the end of the XPS experiment.

The spectra of the pin after the test in the presence of equilibrated blend show a different shape Si 2p and O 1s signals comparing non-contact area and contact area (Figure 14). The Si 2p spectrum shows the main component at $101.6 (0.1)$ eV Si-N in both areas. The SiN_xO_y component was found at about $102.4 (0.1)$ eV and the Si-O component was found at $103.4 (0.1)$ eV for both areas.

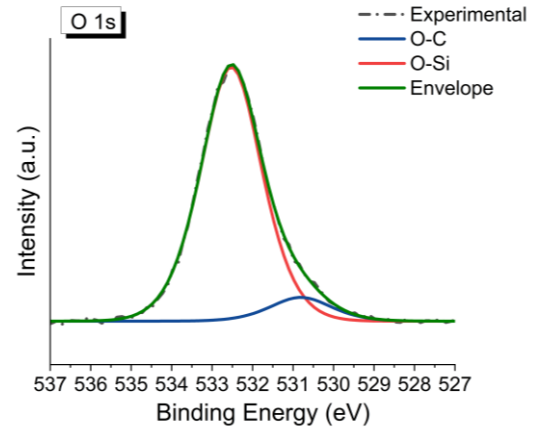
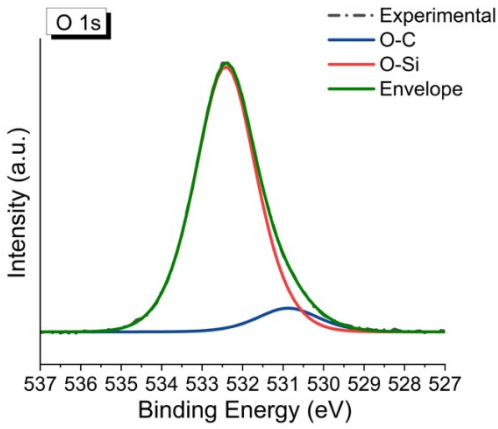
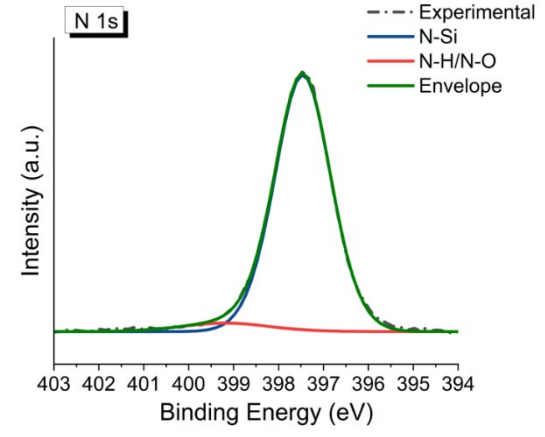
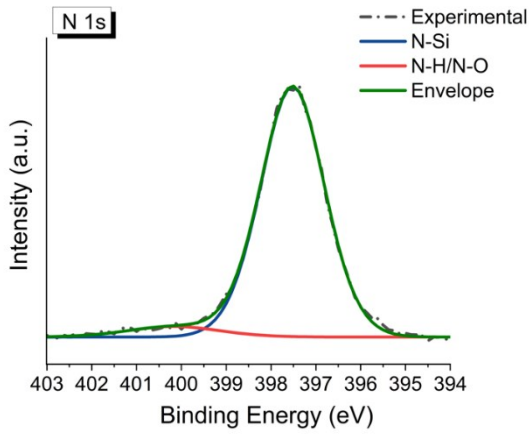
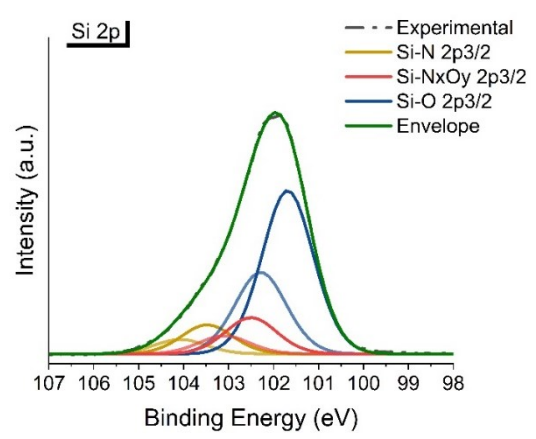
The N 1s spectrum contained a major contribution of N-Si component at $397.5 (0.1)$ eV and the N-H/N-O component at $399.3 (0.1)$ eV in contact area and at 399.1 ± 0.1 eV in non- contact area.

The O 1s spectrum shows the major contribution at 532.5 (0.1) in both contact and non-contact areas. The S 2s signal is not detectable. The binding energy of Si2p, N1s and O1s for all samples are reported in Table 5.

Pin: Non- contact area



Pin: Contact area



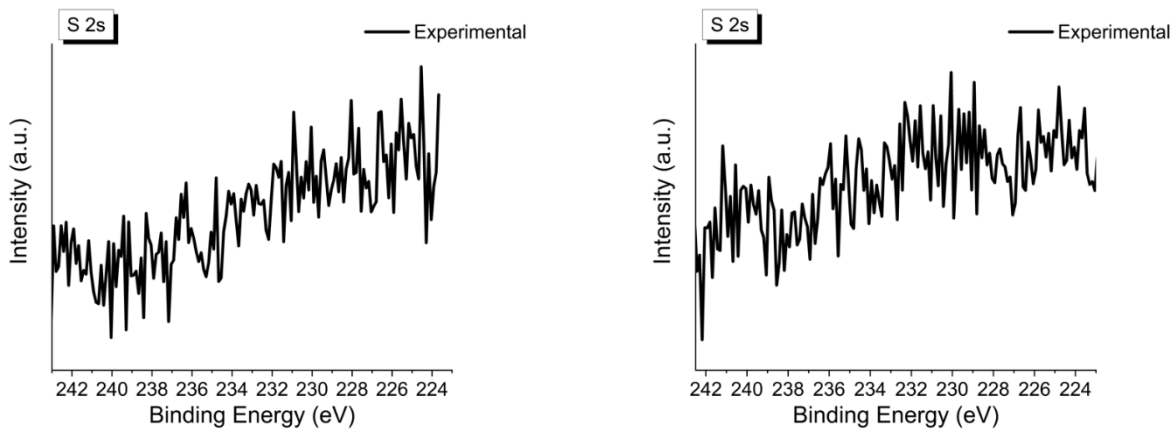


Figure 14: XPS spectra of Si_3N_4 pin after the test in the presence of equilibrated $[\text{EMIM}]\text{EtSO}_4 + 2 \text{ wt } \% \text{ Oleic acid}/[\text{EMIM}]\text{oleate } 50/50$; Left: Non-contact area; right: Contact area; from top to down: Si 2 p H-R spectrum; N 1s H-R spectrum; O 1s H-R spectrum; S 2s H-R spectrum.

Table 5: Peak parameters of Si 2p_{3/2}, N1s and O1s spectra of disk and pin after the test in the presence of equilibrated blend.

	Component	Disk out contact area	Disk tribostressed in the presence of The blend	Pin out contact area	Pin tribostressed in the presence of The blend
		BE (eV) ±0.1	BE (eV)	BE (eV) ±0.1	BE (eV)
Si 2p_{3/2}	Si-N	101.5	101.5 (0.1)	101.6	101.6 (0.1)
	Si-N _x O _y	102.4	102.4 (0.1)	102.4	102.5 (0.1)
	Si-O	103.3	103.3 (0.2)	103.4	103.3 (0.1)
N 1s	N-Si	397.4	397.5 (0.1)	397.5	397.6 (0.1)
	N-H/N-O	399.4	399.4 (0.1)	399.1	399.3 (0.1)
O 1s	O-C	531.2	531.2 (0.2)	531.2	531.3 (0.1)
	O-Si	532.5	532.5 (0.1)	532.4	532.5 (0.1)

6.4. Discussion

The profilometer traces of the disk and pin showed no remarkably differences between the tests in the presence of [EMIM]EtSO₄ and in the presence of [EMIM]EtSO₄ + Oleic acid/[EMIM]oleate 50/50, since the vast majority of wear occurs during the running-in in water. It is reported [8,16] that the running-in procedure generates smooth contact surfaces, thus preventing the occurrence of micro fracture and debris formation. In this work the running-in procedure was carried out before the test in order to obtain the hydrodynamic bearing-like contact and to evaluate the effect of the lubricant and additive in the boundary lubrication.

6.4.1. Effect of the water content on lubrication

Water seems to play a critical role on lubrication mechanism since the water content influences the viscosity of the investigated lubricants (Table 6). The comparison of Figures 7a-b, and 8a-b allows observing an increase of the coefficient of friction at low speeds with the adsorption of water in the case of both the dried IL and the dried blend during the test. In addition, the shift of the curve observed in the transition from HDL to mixed lubrication between the dried and the equilibrated lubricants can be assigned to the change in viscosity: from about 100 mPa * s (for dried IL and blend) to c.a. 10 mPa * s (for equilibrated IL and blend). The water molecules coordinate the ionic liquid and this leads to the direct contact between the surfaces of the disk and the sphere, consequently, the coefficient of friction increases, influencing the lubrication.

Table 6: Water content and experimental viscosity after 1 week at 45 % RH of [EMIM]EtSO₄ and [EMIM]EtSO₄ + Oleic acid/[EMIM]oleate 50/50.

Lubricant	Water content after 1 week at 45 % RH	Viscosity η (mPa * s) at 45 % RH
[EMIM]EtSO ₄	7.9 (0.5) %	12.2 (0.1)
[EMIM]EtSO ₄ + Oleic acid/[EMIM]oleate 50/50	9.8 (0.3) %	12.3 (0.1)

6.4.2. Effect of the blend composition on lubrication

During the tribological tests in the presence of IL and in the presence of the blend, two possible mechanisms can occur [17]:

- 1) tribochemical wear effect, in which the interactions between the two surfaces take place in the form of asperities colliding and smoothing with each other;
- 2) tribochemical film effect, with chemical reactions between lubricant molecules and surfaces that usually accompany such collisions producing a tribofilm.

The XPS and the tribological results obtained in this work suggest that the tribochemical wear effect probably prevails during the running-in in water and in the presence of equilibrated IL. In fact, there are no changes in the XPS spectra after the test with the [EMIM]EtSO₄ and no sulphur signals are detected. R.S. Gate & S.M. Hsu [17] showed that the substituted imidazoline reduced wear and friction, but no visible film was found in the wear scar after the test, and the same was observed for Si₃N₄ in contact with sulfurized fatty acids. Thus, it is observed the absence of tribofilm on the surface after the test and the cleaning before the XPS analyses.

The tribochemical effect, indeed, probably predominates when the IL + additive is present. The tribological results showed that the CoF significantly decreases of about ten times in the presence of the additive at the lowest speeds. In addition, the shift of the Stribeck curve observed in the mixed lubrication regime in the presence of additive, is not due to the change in viscosity (as observed in the case of water absorption) but it suggests a different lubrication mechanism. The XPS data of the pin following the tribotests with the IL and the blend showed different shape of the Si

2p signal between no-contact area and contact area (Figure 11 and Figure 14). These findings can be explained by the oxidation of the Si_3N_4 surface after the interaction with the environment and this oxide film is partially removed during the tribotest, as showed by the decrease in intensities of the Si-NxOy and Si-O component (Figures 11 and 14).

Interesting results were observed in the presence of the additive: the Si 2p signal showed higher intensities of Si-O component compare to the IL presence case. This can be associated to the interaction between oleic acid/ [EMIM] oleate and the surface, that probably leads to the formation silyl ester (Figure 14). These reactions might explain why the acid functional groups can lubricate Si_3N_4 . [17] These results, in addition with the degradation of C1s signal observed in the disk after the test with the blend, suggest the formation of a thin tribofilm in the presence of additive.

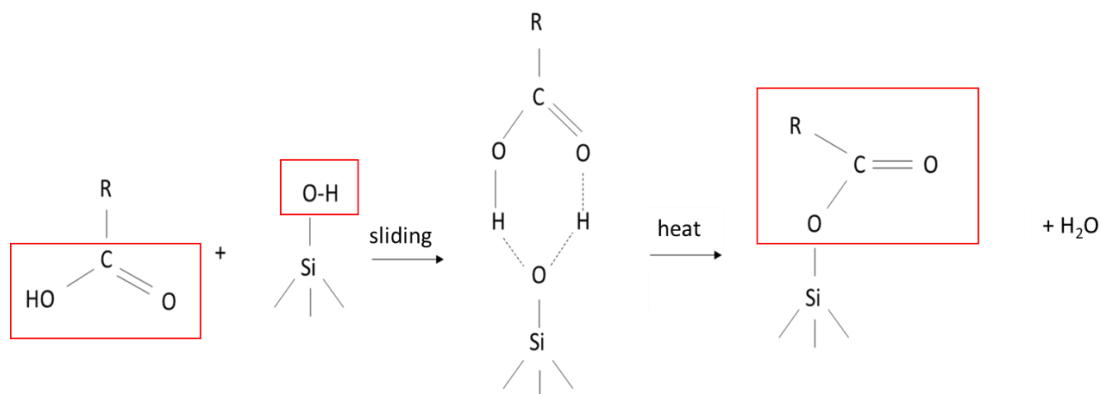


Figure 14: possible reaction that could occur in the presence of additive, adapted from [17].

6.4.3. Slow tests: tribochemical film effect

Slow tests for 2 minutes at 5 mm / s in water and without liquid (dried) were performed following the mechanical tests, in order to evaluate the effect and the presence of the tribofilm (Figure 15).

The slow test in water shows that as the CoF increase up to a value ca. 0.9 between 0 – 60 s. Then, there are peaks whose intensity and amplitude increase upon time (Figure 15b). Indeed, in the test without liquid, it is possible to observe how the CoF value ranges between about 0.1 and 0.27 (Figure 15d). These values are close to those obtained with the ionic liquid as lubricant. This might suggest and confirm the formation of a tribofilm on the surface in the contact area between the two counterparts, also without lubricants conditions, that play a role in the lubrication mechanism of Si_3N_4 .

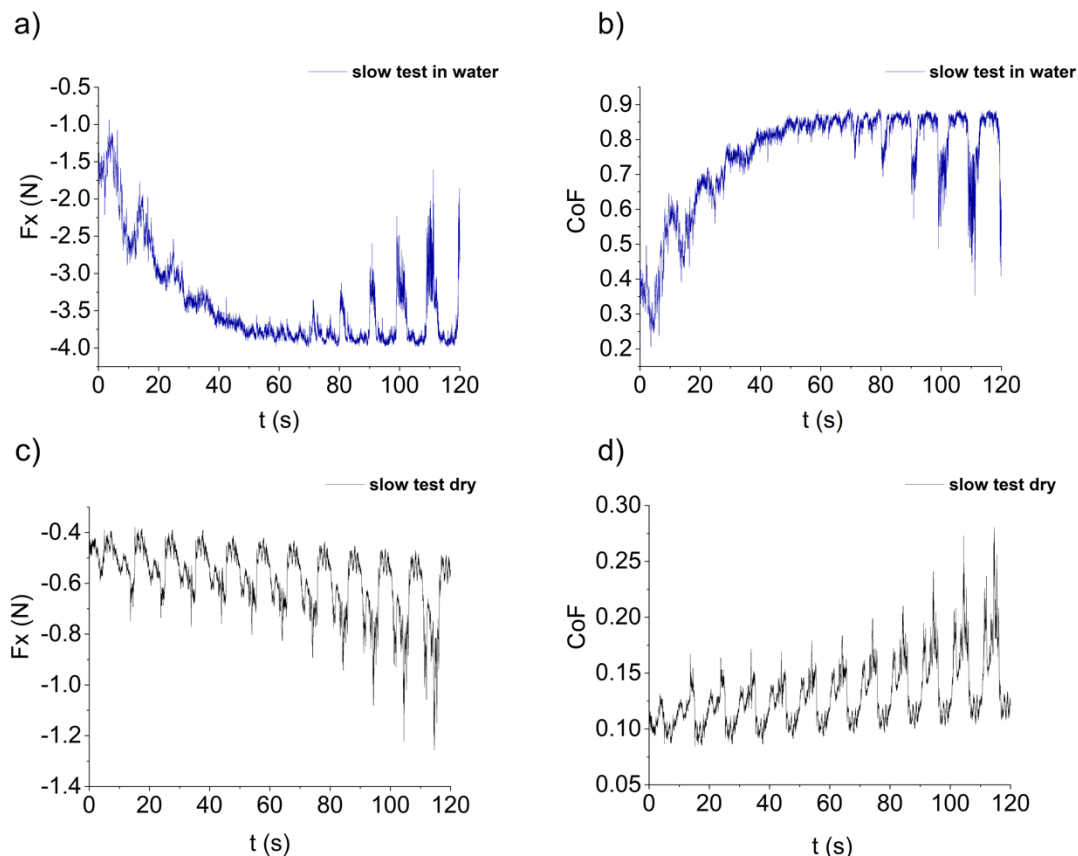


Figure 15: slow test 2 minutes at 6 mm / s. a) test in water (blu line): Force (x) vs time (s) and b) CoF vs time; test in dried conditions (black line): c) Force (x) vs time (s) and d) CoF vs time (s).

6.5. Conclusions

The tribological behaviour of Si_3N_4 tribopairs lubricated with $[\text{EMIM}]\text{EtSO}_4$ and with the blend $[\text{EMIM}]\text{EtSO}_4 + 2 \text{ wt } \% \text{ Oleic acid}/[\text{EMIM}]\text{oleate } 50/50$ has been investigated, and it is possible to draw the following conclusions:

- The vast majority of wear occurs during the running-in in water: it results in hydrodynamic bearing-like contact.
- Tribological data showed that the water content significantly influences the lubrication mechanism and the CoF increases. The water played an important role in the lubrication behavior since water influences the viscosity of the IL; the water molecules coordinate the ionic liquid leading to the direct contact between the asperities of the disk and the sphere and consequently the friction increases, influencing the lubrication.
- The mechanism probably predominant in the presence of equilibrated $[\text{EMIM}]\text{EtSO}_4$ is a smoothing of asperities; no film formation is observed by XPS.

- In the presence of oleic acid and [EMIM] oleate 50/50, the lubrication mechanism is different: the CoF is about 0.04 at the lowest speeds. This is probably explained by the formation of a film due the mechanical stress, also confirmed by the XPS and the slow test.

References

- [1] "M.D. Bermudez, A. Jimenez, J. Sanes, F. Carrion, Ionic Liquids as Advanced Lubricant Fluids, *Molecules* 2009, 14(8), 2888-2908;
- [2] M. Cai, Q. Yu, W. Liu, F. Zhou, Ionic liquid lubricants: when chemistry meets tribology, *Chemical Society Review*, 2020, 49, 7753-7818
- [3] L.A. Urtis, A. Arcifa, P. Zhang, J. Du, M. Fantauzzi, D. Rauber, R. Hempelmann, T. Kraus, A. Rossi, N.D. Spencer, Influence of Water on Tribolayer Growth When Lubricating Steel with a Fluorinated Phosphonium Dicyanamide Ionic Liquid, *Lubricants* 2019, 7(3), 27-42
- [4] A. Arcifa, PhD thesis, On the Mechanism of Ionic-Liquid-Mediated Lubrication of Silicon-Based Materials: A Combined Tribological and Spectroscopic Investigation ETH Zuerich, 2016.
- [5] H. Xiao, Ionic Liquid Lubricants: Basics and Applications, *Tribology Transactions*, 2017, 60.
- [6] C. Ye, W. Liu, Y. Chen, L. Yu, Room-temperature ionic liquids: a novel versatile lubricant, *Chemical Communications*, 2001: 2244-2245.
- [7] H. Tomizawa, T.E. Fischer, *Wear* 105.1 (1985): 29-45; 11.
- [8] H. Tomizawa, T.E. Fischer, Friction and wear of silicon nitride and silicon carbide in water: hydrodynamic lubrication at low sliding speed obtained by tribochemical wear. *ASLE transactions*, Vol. 30 (1), p. 41, 1987.
- [9] A. Mezzetta, L. Guazzelli, M. Seggiani, C. S. Pomelli, M. Puccini, C. Chiappe, A general environmentally friendly access to long chain fatty acid ionic liquids (LCFA-ILs), *Green Chemistry*, 19(13), 3103, 2017.
- [10] A. Arcifa, A. Rossi, A., N.D. Spencer, Adsorption and Tribochemical Factors Affecting the Lubrication of Silicon-Based Materials by (Fluorinated) Ionic Liquids. *J. Phys. Chem. C*, 121 (13), 7259, 2017.
- [11] D. A. Shirley, *Physical Review B: Solid State*, 5, 4709, 1972.
- [12] J. S. Torrecilla, T. Rafione, J. García, F. Rodríguez, Effect of Relative Humidity of Air on Density, Apparent Molar Volume, Viscosity, Surface Tension, and Water Content of 1-Ethyl-3-methylimidazolium Ethylsulfate Ionic Liquid, *Journal of Chemical & Engineering Data*, 53 (4), p. 923, 2008.
- [13] W. Hartung, A. Rossi, A., S. Lee, N.D. Spencer, Aqueous Lubrication of SiC and Si₃N₄ Ceramics Aided by a Brush-like Copolymer Additive, Poly(L-lysine)-graft-poly(ethylene glycol). *Tribol Lett.*, Vol. 34, p. 201, 2009.
- [14] I. Bertóti, G. Varsányi, G. Mink, T. Székely, J. Vaivads, T. Millers, J. Grabis, XPS characterization of ultrafine Si₃N₄ powders. *Surf. Interface Anal.*, Vol.12, p. 527, 1988.
- [15] C.D. Wagner, A.V. Naumkin, A. Kraut-Vass, J.W. Allison, C.J. Powell, J.R.Jr. Rumble, NIST Standard Reference Database 20, Version 3.4 (web version) (<http://srdata.nist.gov/xps/>).
- [16] J. Xu, K. Kato, T. Hirayama, The transition of wear mode during the running-in process of silicon nitride sliding in water, *Wear*, Vol. 205, p. 55, 1997.
- [17] R.S. Gates, S.M. Hsu, Silicon nitride boundary lubrication: lubrication mechanism of alcohols, *Tribol. Trans.*, Vol. 38, p. 645, 1995."

Conclusions and outlooks

In this thesis a method for the study of growth, characterization and functional properties of thin films formed on brass, steel and ceramic substrates was developed and the following conclusions can be drawn:

- The presence of small quantities of organic compounds in the near neutral saliva model solutions affect the corrosion behaviour of the material exposed to them and consequently the composition of the surface film formed after the exposure.
- The corrosion rate of both CuZn37 and Ni-free 1.4456 alloys exposed to different saliva solution formulations decreases with time, the corrosion mechanism is anodic control. In the case Ni-free steel the corrosion rates determined are markedly lower than those observed in CuZn37. This difference is due to the formation of a passive film in the Ni-free stainless-steel surface.
- The increasing of the CoF in the case of Si₃N₄ tribopair lubricating with dry IL ([EMIM] EtSO₄) can be explained by the water absorption, with the consequently decrease of viscosity and lubricant leakage, which led to the contact of surface asperities. Similar behaviour was observed with the dry blend of IL and oleic acid/[EMIM] oleate.
- The presence of oleic acid / [EMIM] oleate as additive, markedly influences the mixed and boundary lubrication mechanism. A significant decrease of the coefficient of friction was observed.
- The XPS analyses allow explaining the different corrosion behaviour of the alloys and the different lubrication mechanism observed with pure IL and the IL + additive since XPS provides the chemical evidence of different thin film composition:

- The higher corrosion rate observed on the CuZn37 exposed to D compared to C-B and SALMO solution can be explained by a formation on a thinner film compared to the brass exposed to the other solutions. In addition, the film results enriched in CuSCN and depleted in zinc and phosphate, indicating a pronounced dissolution of zinc due to the presence of ligands in the formulation;
- The different anodic Tafel curve behaviour observed in the case of the Ni-Free steel exposed to D solution is typical for a passive film enriched in chromium, showing the oxidation of Cr (III) to Cr (VI). This is confirmed by the XPS analysis: the film results enriched in chromium and depleted in iron.
- The different lubrication mechanism of the Si₃N₄ observed in the presence of IL and additive might be explained with the probable formation of a silyl-ester thin tribofilm.

The analytical method developed in this work is proved to be effective in studying the growth, the characterization, and the functional properties of thin films formed on different substrates tested in various media (saliva model solutions and ionic liquids). The combination of in-situ and ex-situ techniques provided insight into corrosion and wear phenomena.

In the case of brass and steels in contact with a saliva formulation, it has been shown that in the presence of organic compounds, the corrosion rate and consequently the film thickness and composition are affected.

This work is innovative in studying the corrosion resistance of brass in the presence of sodium citrate, uric acid and lactic acid. In order to evaluate the effects even after a long exposure time (16 h), it would be interesting not only to analyse the surface composition, but also the concentration in the solution of zinc and copper after 16 h in the presence of these organic compounds.

Tests could also be performed by exposing for 16 hours the brass to solutions containing the different organic compounds, by using a microcell. After the exposure, in addition to the determination of the surface composition of the brass by XPS, the solutions could be analysed by using spectroscopic techniques, such as inductively coupled plasma optical emission spectroscopy

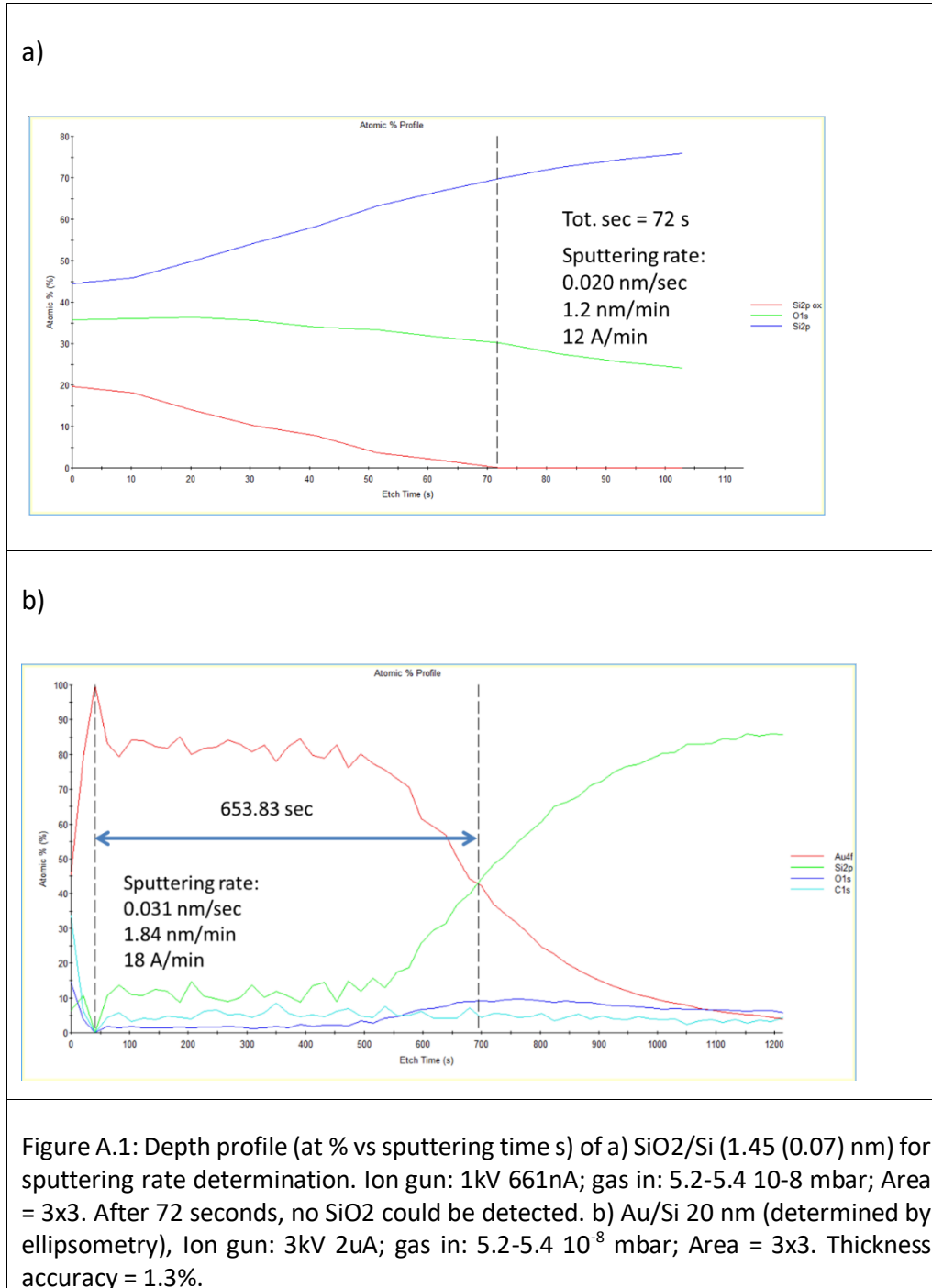
or inductively coupled plasma mass spectrometry (ICP -OES or ICP-MS), in order to measure the release rate of zinc and copper.

Usually, model salivary formulations consist mainly of inorganic salts, but real human saliva also contains organic compounds and proteins. The results obtained in this thesis could pave the way for new analytical investigations, especially in the orthodontic field. In fact, as observed for organic compounds, the presence of proteins in the saliva formulation could also influence the corrosion behaviour of the materials and thus their biocompatibility. For this reason, would be interesting to include proteins in the formulations to evaluate their role in corrosion mechanism.

The same considerations can be made for the case of lubrication phenomena. This work has shown how the addition of an additive (oleic acid/[EMIM] oleate) in ionic liquids seems to greatly influence boundary lubrication. Furthermore, through surface investigations, it was possible to reveal the formation of a thin film that preserves lubrication conditions over time. This work provides the guidelines for the interpretation of the phenomena that could occur in the presence of novel lubricants and demonstrates that the formulation of lubricants plays a role in lubrication mechanism. Moreover, would be interesting to evaluate the properties of different blends, with different ILs/ additives ratio.

Appendix A

Chapter 4 - Section 4.2.6. Details about sputtering rate determination. Depth profile of SiO₂/Si sample (Figure A.1a) and of Au/Si sample (Figure A.1b).



Chapter 4 – Section 4.3.2. Linear Polarization Resistance (LPR) of the brass samples exposed to D, C-B and SALMO 1h Figure A.2 (a1-3), 3h Figure A.2 (b-1-3) and 16h Figure A.2 (c1-3).

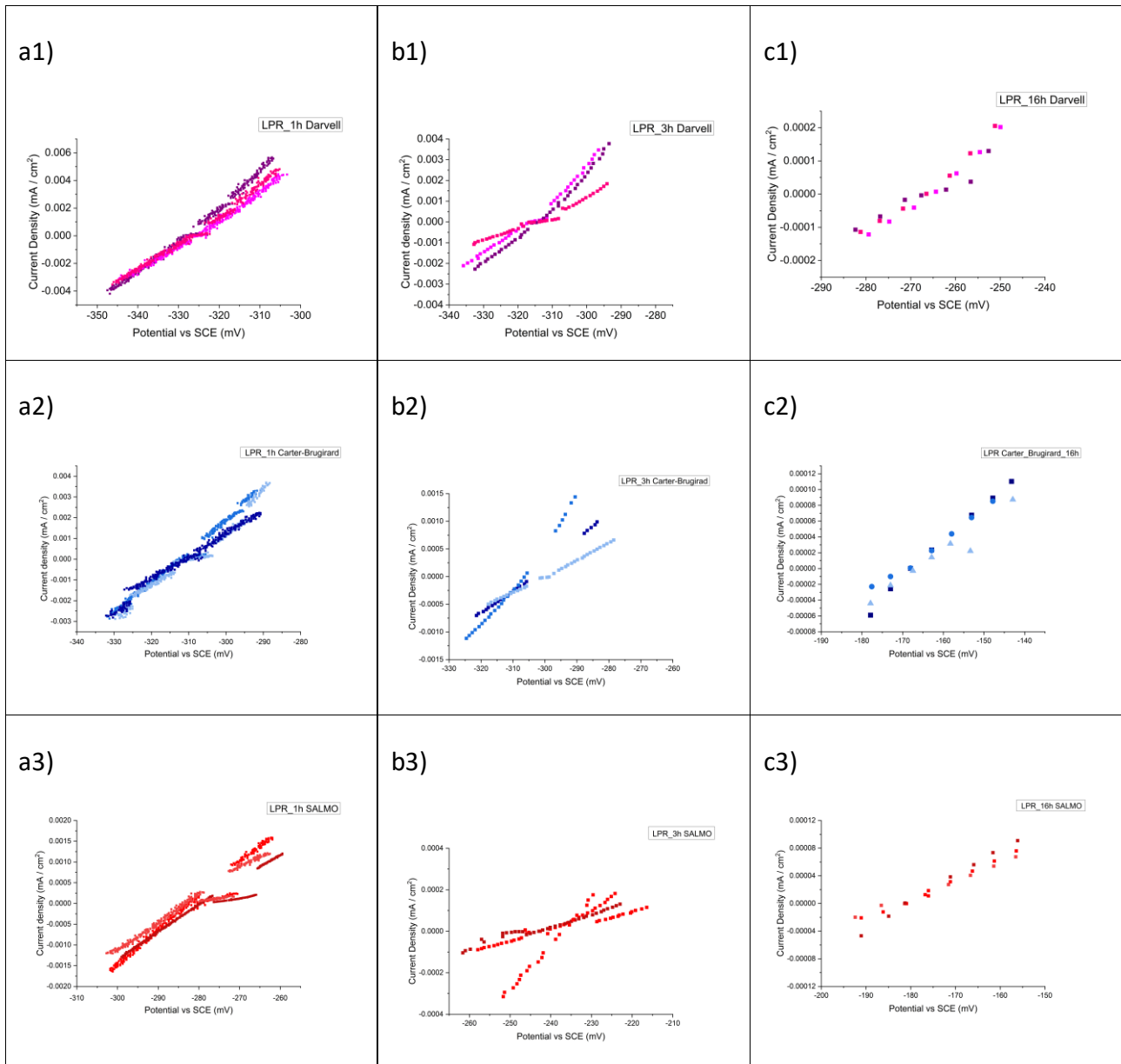


Figure A.2: LPR plots current density (mA cm⁻² vs potential vs SCE mV) of CuZn37 after: 1 h of exposure to a1) D; a2) C-B; a3) SALMO; 3 h of exposure to b1) D; b2) C-B; b3) SALMO; 16 h of exposure to c1) D; c2) C-B; c3) SALMO;

Chapter 4 – Section 4.3.3. Angle resolved – XPS analysis of MP CuZn37 (ARXPS)

Angle resolved results acquired on mechanically polished (MP) CuZn37. Apparent concentrations in atomic percentage versus the emission angle are reported considering the film and the contamination (Figure A.3).

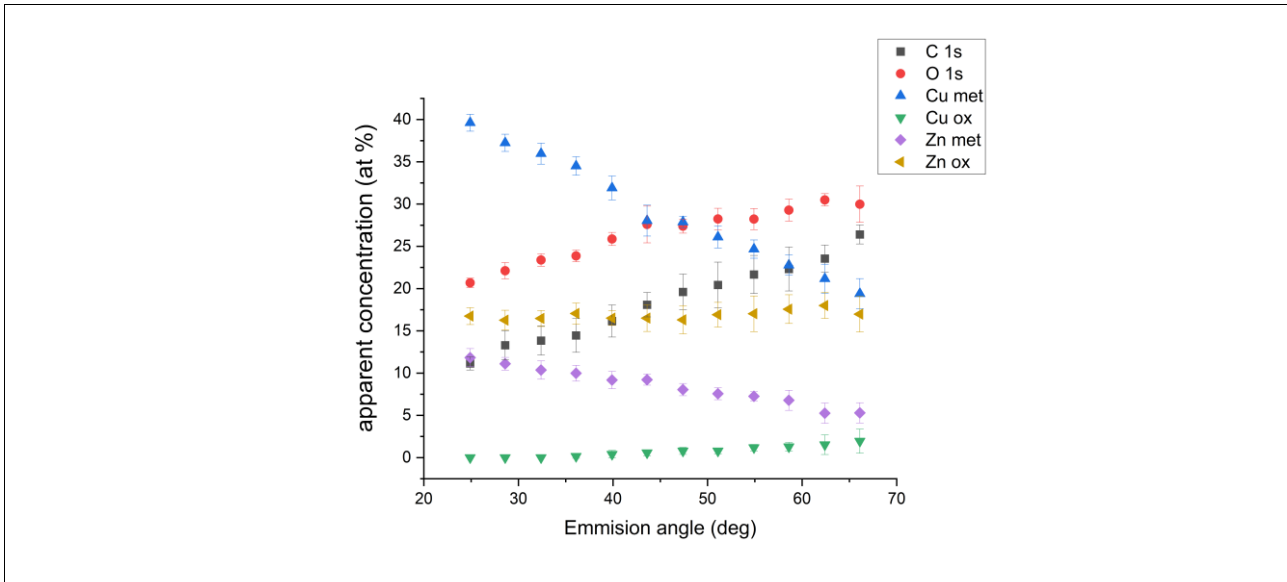


Figure A.3: Angle resolved results acquired on mechanically polished CuZn37. Apparent concentrations (at %) versus the emission angle are reported considering the film. Mean and standard deviations were calculated over three independent measurements.

Chapter 4 – Section 4.3.3. CuZn37 exposed to saliva formulations.

High-resolution spectrum of Ca 2p in CuZn37 exposed 1h to SALMO (Figure A.4)

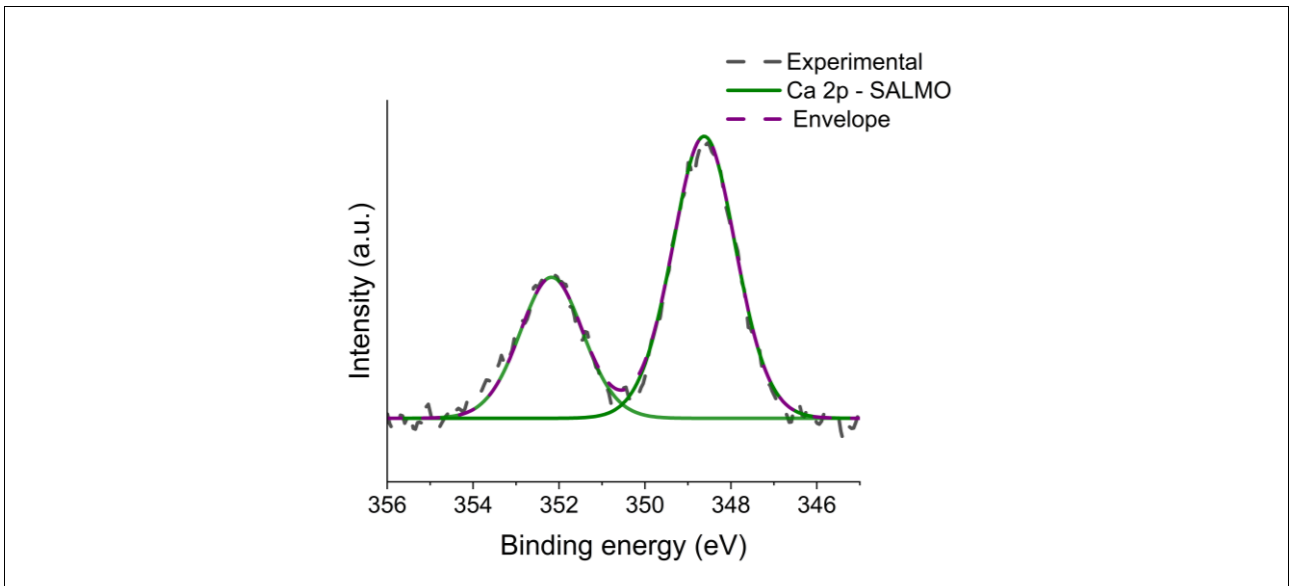


Figure A.4: High-resolution spectra of Ca 2p of CuZn37 after 1 h of contact with SALMO formulation. A Shirley – Sherwood background subtraction was applied before curve-fitting.

Chapter 5 – Section 5.3.2. Linear Polarization Resistance (LPR) of the steel samples exposed to D, C-B and SALMO 1h Figure A.5 (a1-3), 3h Figure A.5 (b1-3) and 16h Figure A.5 (c1-3).

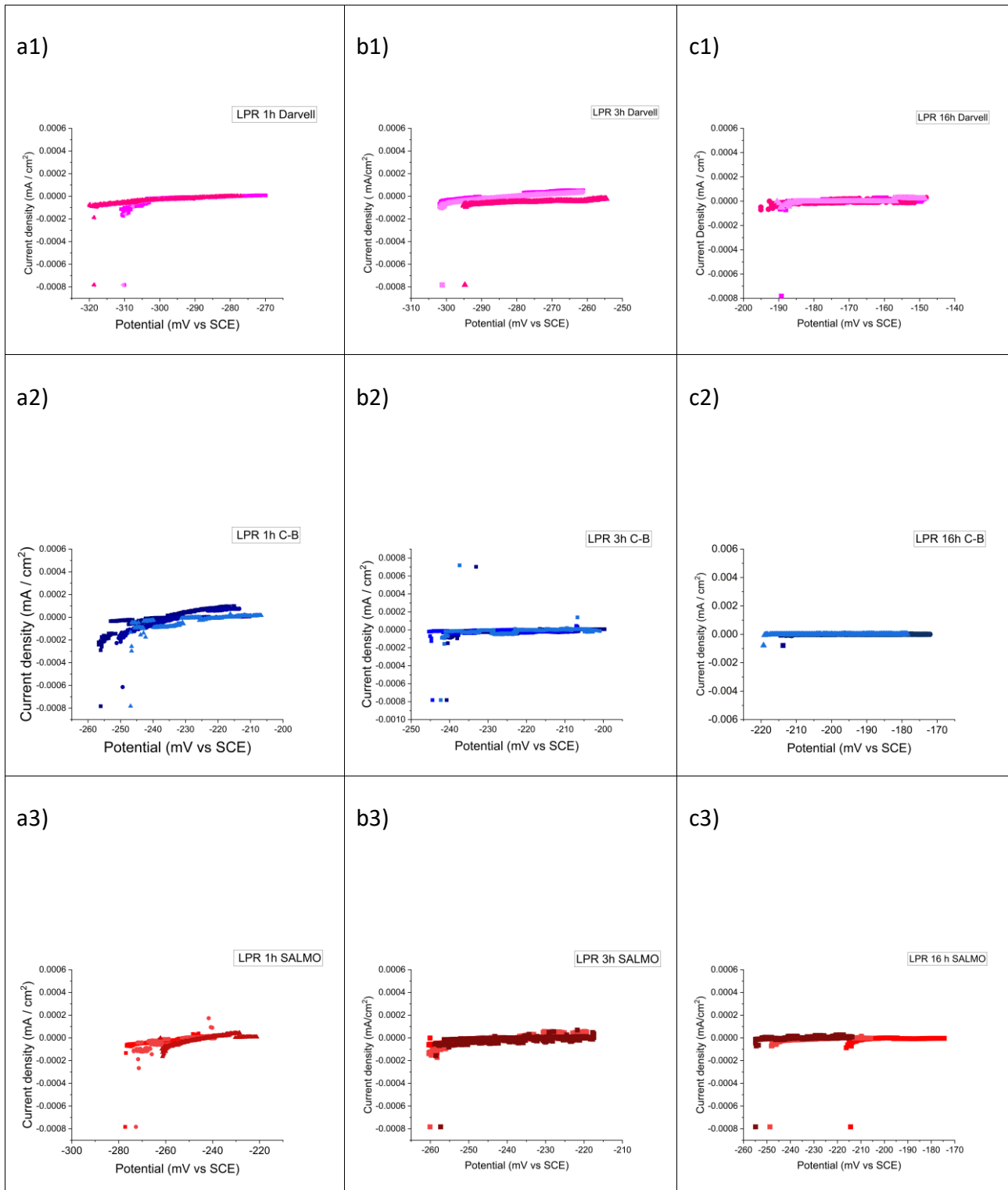


Figure A.5: LPR plots current density (mA cm⁻² vs potential vs SCE mV) of stainless-steel DIN 1.4456 after: 1 h of exposure to a1) D; a2) C-B; a3) SALMO; 3 h of exposure to b1) D; b2) C-B; b3) SALMO; 16 h of exposure to c1) D; c2) C-B; c3) SALMO;

Chapter 5 – Section 5.3.3. Stainless-steel exposed to saliva formulations.

High-resolution spectrum of Ca 2p in Stainless-steel exposed 1h to SALMO (Figure A.6)

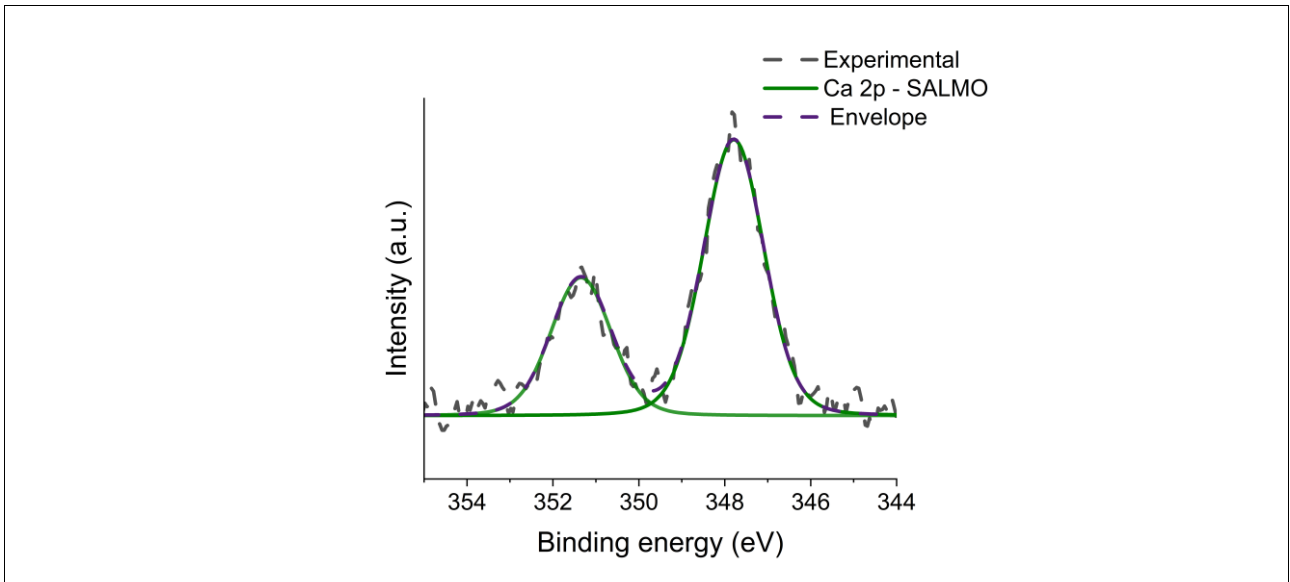
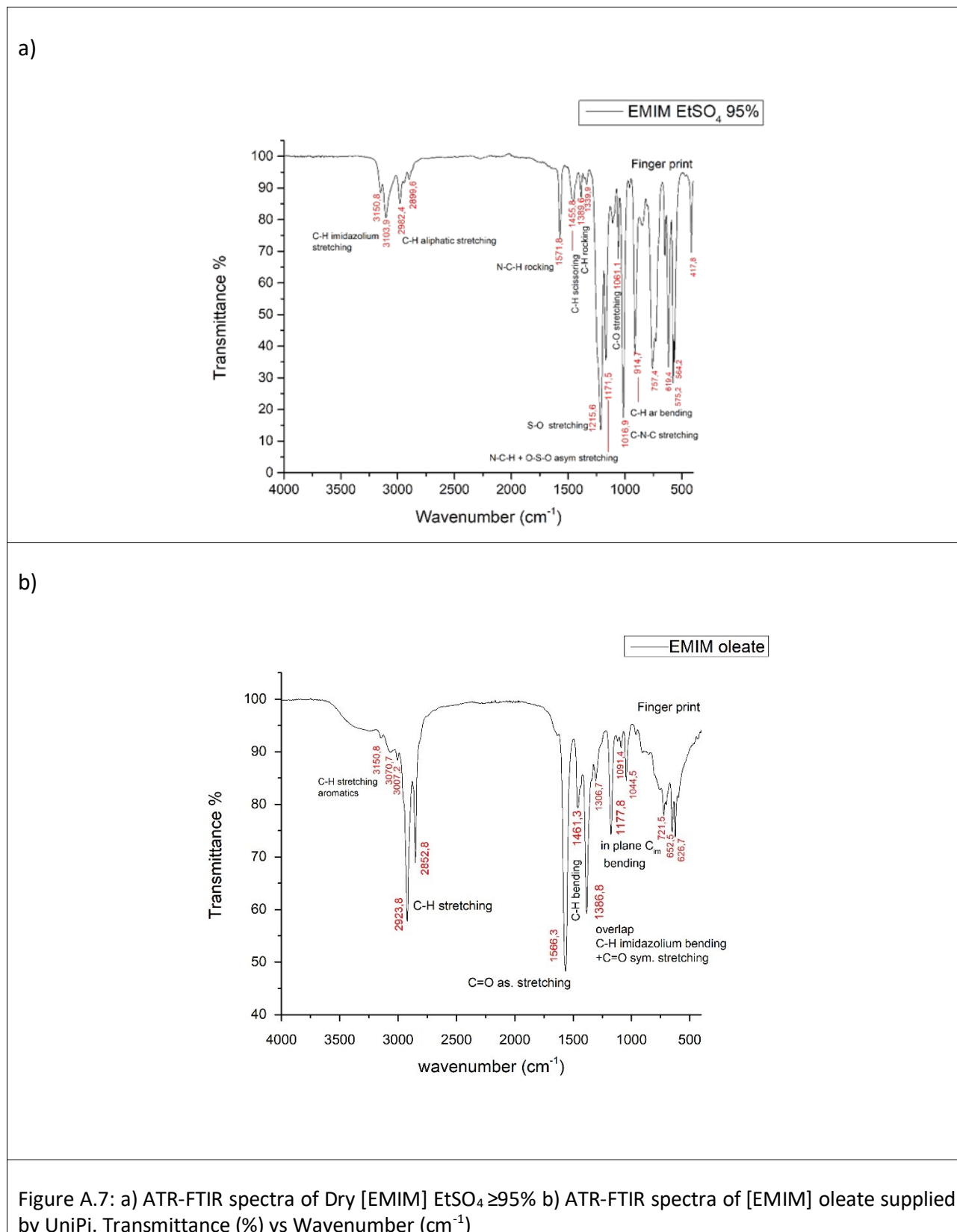


Figure A.6: High-resolution spectra of Ca 2p of CuZn37 after 1 h of contact with SALMO formulation. A Shirley – Sherwood background subtraction was applied before curve-fitting.

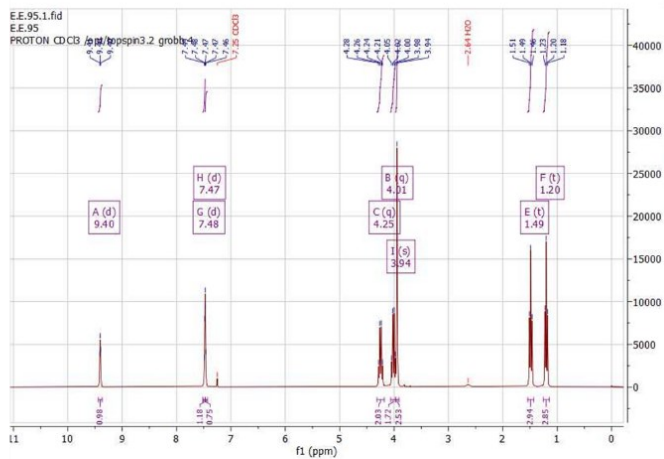
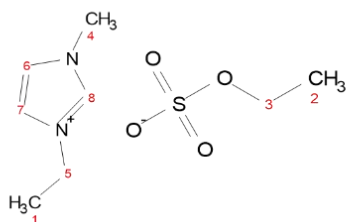
Chapter 6 – Section 6.2.1. Characterization of [EMIM]EtSO₄ and [EMIM] oleate by attenuated-total-reflection Fourier-transform infrared spectroscopy (ATR – FTIR, Alpha-P Bruker) (Figure A.7) and by nuclear magnetic resonance (NMR, Bruker BioSpin GmbH, 300 MHz) (Figure A.8).



a1)

δ ppm

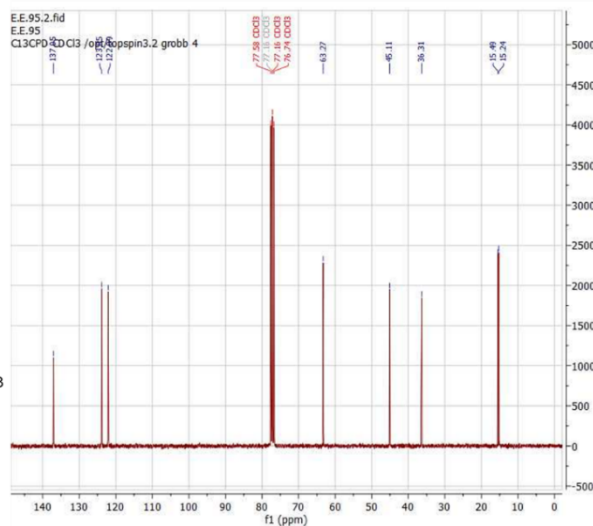
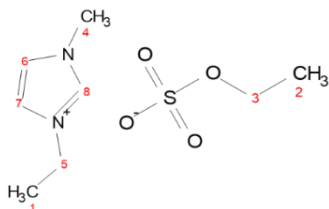
- 8 9.40 (d, $J = 1.8$ Hz, 1H),
- 6 7.48 (d, $J = 1.5$ Hz, 1H),
- 7 7.47 (d, $J = 2.0$ Hz, 1H),
- 5 4.25 (q, $J = 7.4$ Hz, 2H),
- 3 4.01 (q, $J = 7.1$ Hz, 2H),
- 4 3.94 (s, 3H),
- 2 1.49 (t, $J = 7.3$ Hz, 3H),
- 1 1.20 (t, $J = 7.1$ Hz, 3H).



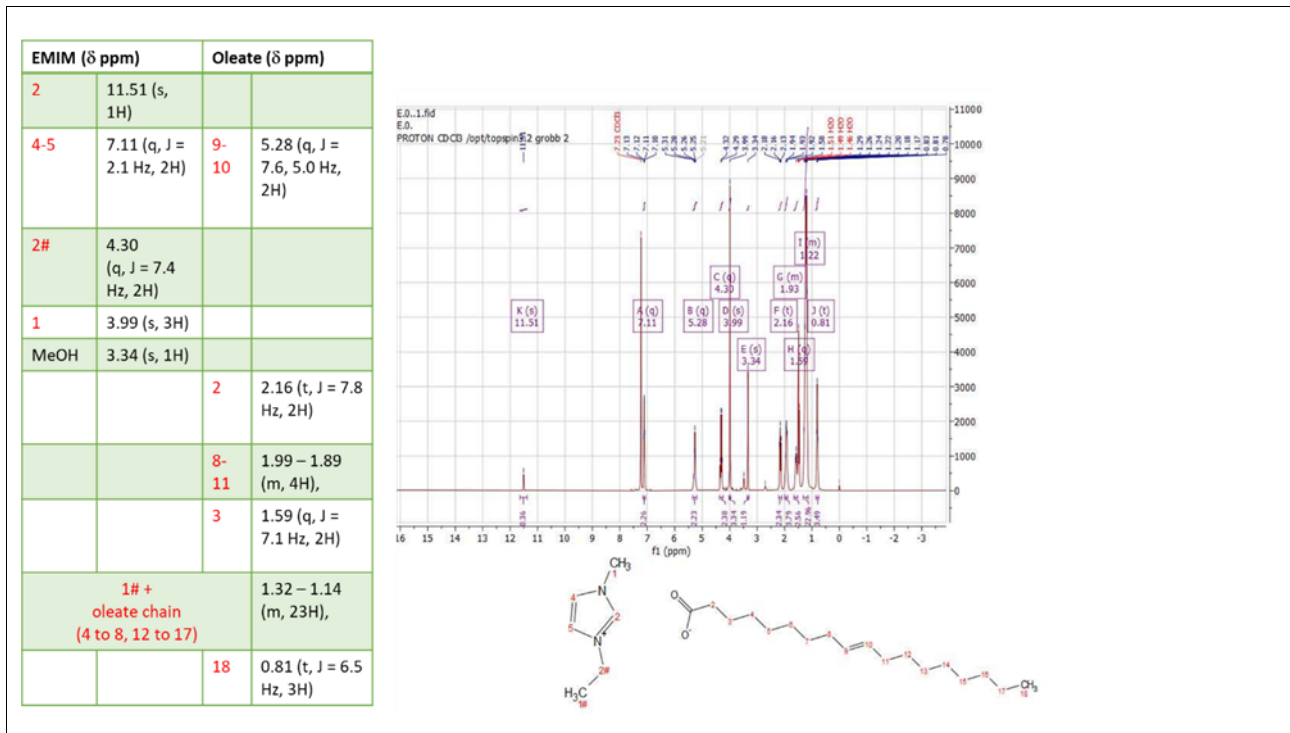
a2)

δ ppm

- 8 137.05,
- 6 123.85,
- 7 122.09,
- CDCl₃ 77.58-76.74,
- 3 63.27,
- 5 45.11,
- 4 36.31,
- 2 15.49,
- 1 15.24.



b1)



b2)

EMIM (δ ppm)		Oleate (δ ppm)	
		C(1)OO	181.10
		C(9-10)H	130.07-129.87
C(4)H	122.54		
C(5)H	120.58		
CDCl ₃ , CHCl ₃	77.59-76.74		
MeOD	50.00		
C(2#)H ₂ chain	45.03	C(2)H ₂	39.47
C(1)H ₃	36.30	C(3)H ₂	31.97
		C(chain)H ₂ 4-7 + 12-15	30.17-29.47
		C(16)H ₂	29.39
		C(11)H ₂	27.35
		C(8)H ₂	27.29
		C(17)H ₂	22.74
C(1#)H ₃ chain	15.59	C(18)H ₃	14.18

Figure A.8) a1) ¹H NMR (300 MHz, CDCl₃) spectra of [EMIM] EtSO₄; a2) ¹³C NMR (76 MHz, CDCl₃) spectra of [EMIM] EtSO₄ ≥95 %; b1) ¹H NMR (300 MHz, CDCl₃) spectra of [EMIM] oleate; b2) ¹³C NMR (76 MHz, CDCl₃) spectra of [EMIM] oleate.

Curriculum Vitae



Name and surname: Deborah Biggio

Address: via Giudice Mariano, 47 – Cagliari, CA, Italy

Nationality: Italian

Date and place of birth: 21/04/1994, Nuoro (Nu), Italy

Languages: Italian (Native speaker), English (B2 level)

Educational and training

1/11/2019– to date	PhD in Chemical Sciences and Technologies at the Department of Chemical and Geological Sciences at the Università degli Studi di Cagliari.
1/11/2019 al 30/06/2020	Training at the Laboratory for Surface Science and Technology (LSST), Department of Materials, ETH Zurich, Zurich, Switzerland.
19/07/2019	Master Degree in Chemical Sciences at the Università degli Studi di Cagliari - 110/110 e lode
24/02/2017	Beachelor degree in Chemistry at the Università degli Studi di Cagliari 106/110

Teaching and supervising Experience

15/03/2021- 30/06/2021	Lab assistant within the course "Chimica Analitica II e laboratorio", in Chimica L-27, SSD CHIM/01, SC 03/A1, (40 h) Università Degli Studi Di Cagliari.
5/03/2021- 30/06/2021	Lab assistant within the course "Chimica Analitica II e laboratorio", in Chimica L-27, SSD CHIM/01, SC 03/A1, (40 h) Università Degli Studi Di Cagliari.
13/09/2019- 31/10/2019	Scientific Assistant at Laboratory for surface science and technology (LSST), ETH, Zurich, Svizzera.

Publications

2022	Biggio D., Elsener B., Atzei D., Rossi A., Fantauzzi M., The effect of the saliva formulation on brass corrosion, Mater. Corros., 2022, https://doi.org/10.1002/maco.202213476
2022	Biggio D., Fantauzzi M., Elsener B., Atzei D., Rossi A., The role of organic compounds in artificial saliva for corrosion studies: evidence from XPS analyses, Surf. Inter. Anal.,

	2022; https://doi.org/10.1002/sia.7149
2021	F. Savino, V. Fanos , A. Noto, D. Biggio, C. Fattuoni, L. Barberini, Urinary metabolome of infants with colic treated with Lactobacillus reuteri DSM 17938: a pilot randomized trial, Minerva Pediatr 2021 Jan 13. doi: 10.23736/S0026-4946.20.06128-9.

Oral Presentations

14-23/09/2021	<i>Surface characterization of CuZn37 alloys in contact with artificial saliva: the role of organic compounds</i> , D. Biggio, M. Fantauzzi, B. Elsener, A. Rossi, XXVII CONGRESSO NAZIONALE DELLA SOCIETÀ CHIMICA ITALIANA
12-15/09/-2022	<i>Oleic acid/[EMIM] oleate as additives to [EMIM] EtSO4 for the lubrication of a Si₃N₄ tribopair</i> , Deborah Biggio, A. Arcifa, L. Guazzelli, R. Flury, A. Rossi, N. D. Spencer, WTC (WORLD TRIBOLOGY CONGRESS) 2022
29/05-3/06/2022	<i>The role of organic compounds in artificial saliva for corrosion studies: evidence from XPS analyses</i> . D. Biggio, M. Fantauzzi, B. Elsener, A. Rossi, ECASIA (European Association on Application of Surface And Interface Analysis)2022
11-15/09/22	<i>The effect of the artificial saliva composition for Corrosion studies: evidence from XPS analyses</i> . D. Biggio, M. Fantauzzi, B. Elsener, A. Rossi, XXIX Congresso della Divisione di Chimica Analitica La Chimica Analitica verso un futuro verde e sostenibile

Poster presentations

4-5/11/22	<i>Surface characterization of brass exposed to simulated biofluids</i> , D. Biggio, M. Fantauzzi, B. Elsener, D. Atzei, A. Rossi, NGCHEM Next Generation Chemist.
-----------	--

Acknowledgments

After these 3 years, here I am writing my acknowledgements...

I would like to express my gratitude to all the people who supported me and contributed to this project.

First of all, I would like to thank my supervisors: Prof.ssa Marzia Fantauzzi and Prof.ssa Antonella Rossi.

I would like to thank Prof. Marzia Fantauzzi, for motivating me over the years to achieve every goal, with her enormous passion for this work and her great intelligence. For helping me in my work but also in the growth of myself, during these not always easy years. If I am here writing these thanks, it is mainly thanks to her.

I am very grateful to Prof. Antonella Rossi for spurring me on all these years to give my best, guiding me through the world of analytical chemistry as only she knows how.

I deeply thank Professor Bernhard Elsener, who guided and supported me in learning the basics of corrosion and throughout my journey with stimulating and constructive discussions.

I am truly grateful to all of them for always believing in me even before me.

I would like to express my gratitude to Professor N.D. Spencer for giving me the opportunity to work in his Laboratory for Surface Science and Technology (LSST) group, at ETH Zurich. I would like to thank Josephine Baer for her support in administrative matters and for her kind patience. For welcoming and helping me as one of the LSST group. I'm also grateful to Dr. Andrea Arcifa for introducing me in the tribological issue and for the interesting discussions. Roman Flury I thank for the collaboration during my period at ETH.

I would especially like to thank all my family, who have been close to me over the years, always supporting me even in the most difficult moments. To them I owe everything.

To the whole "The office group", who brightened the days between scientific but above all a little less scientific discussion. You have been fundamental in these months. Thanks to Paola and Giulio, my travelling companions, who have always listened and supported me.